Document Version
Final published version

Citation (APA)
Hendrix, H. B. (2026). *Ageing of cementitious materials: Pathfinding study on ageing of cementitious materials for concrete structures.* [Dissertation (TU Delft), Delft University of Technology]. https://doi.org/10.4233/uuid:73a155a2-18cf-4413-89d5-2234ab19c6c3

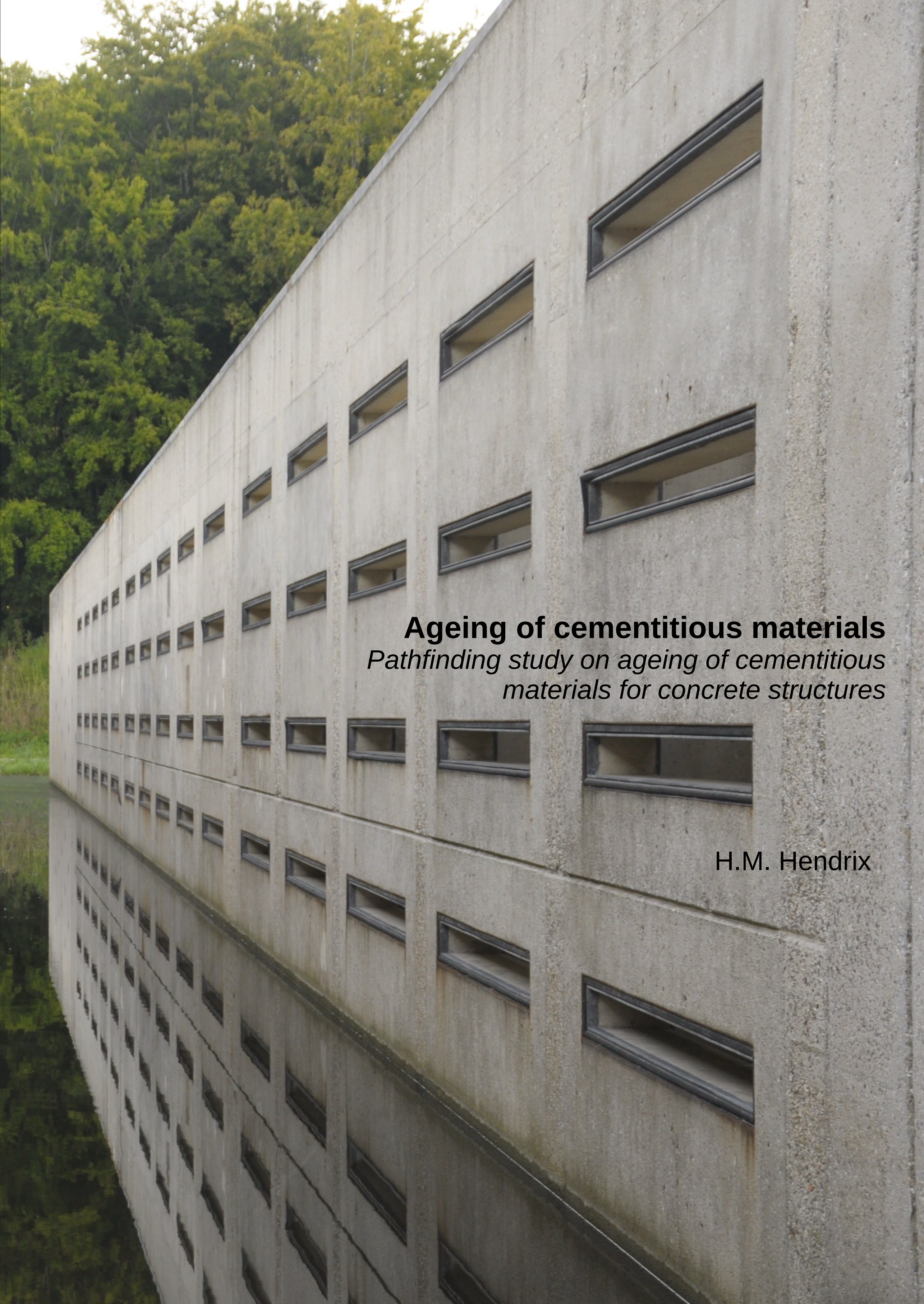

Ageing of cementitious materials

Pathfinding study on ageing of cementitious materials for concrete structures

H.M. Hendrix

Ageing of cementitious materials

Pathfinding study on ageing of cementitious materials for concrete structures

Ageing of cementitious materials

Pathfinding study on ageing of cementitious materials for concrete structures

Dissertation

for the purpose of obtaining the degree of doctor
at Delft University of Technology
by the authority of the Rector Magnificus
prof. dr. ir. H. Bijl
chair of the Board for Doctorates

to be defended publicly on
Thursday 5 March 2026 at 12:30 o'clock

by

Hubertus Maria HENDRIX

Master of Structural Engineering,
Technische Universiteit Delft, the Netherlands
Born in Geleen, the Netherlands

This dissertation has been approved by the promotors.

Composition of the doctoral committee:

Rector Magnificus	chairperson
Em. prof. dr. ir. K. van Breugel	Delft University of Technology, promotor
Prof. dr. ir. H.E.J.G. Schlangen	Delft University of Technology, promotor

Independent members:

Prof. dr. A. Cwirzen	Luleå University of Technology
Dr. ir. M. Boutz	SGS Intron
Prof. dr. ir. L.J. Sluijs	Delft University of Technology
Em. Prof. ir. A.Q.C. van der Horst	Delft University of Technology
Dr. B. Šavija	Delft University of Technology
Prof. dr. H.M. Jonkers	Delft University of Technology, reserve member

This research was funded by Rijkswaterstaat, the Executing organ of the Ministry of Infrastructure and Water Management

Keywords: ageing, digital image correlation, long-term performance
Printed by: Proefschriftspecialist
Cover design: Bart Hendrix

ISBN/EAN: 978 94 6384 873 2 (printed version)
978 94 6518 178 3 (pdf version)

To my beloved wife and children

Contents

Appendices:

Appendix A	Durability in Dutch Standards for structural concrete – an overview
Appendix B	Samples from existing structures
Appendix C	Composition and structural properties of laboratory samples
Appendix D	XRD results
Appendix E	Theoretical backgrounds chapter 6
Appendix F	ESEM tests, mean deformations from DIC analysis
Appendix G	Optical microscopy tests, mean deformations from DIC analysis

List of Figures

List of tables

Summary

Owners of concrete structures for civil infrastructure face ageing objects in their area of ownership. These objects are subject to physical ageing. The mechanism behind ageing in concrete - or more generally in cementitious materials - is not known yet, which hinders to some extent the assessment of the remaining service life. Well-known mechanisms in cementitious materials like carbonation and reinforcement corrosion are recognised and quantified when assessing a structure. Ageing – an intrinsic material-specific change in a material over time – is still largely unknown.

The problem statement is as follows: “Ageing, a material-inherent decay phenomenon, in concrete (or cementitious materials in general) is not understood well. It is yet unknown to what extent ageing plays a role in degradation phenomena and in limitations of service life. The use of binder materials with very low clinker content (for sustainability reasons) increases, while the effects of these binders on the long-term performance are insufficiently known. This lack of knowledge may result in – from a durability point of view – vulnerable designs of concrete structures because of poor prediction of the long-term performance of the structures.”

A literature study was performed about ageing of different materials. In material disciplines of plastics, metals and alloys and microprocessors, ageing is well understood. Gradients in the material lead to diffusion phenomena (transport or flow of energy) that may lead to changes in the material. These inherent changes in the material are interpreted as ageing.

In this study it is attempted to trace ageing phenomena in cementitious materials. Two research tracks are considered to focus on ageing. In the first track the focus was on microscopic scale deformations in cementitious material when exposed to cycles of wetting and drying and how the response of the material to those cycles changed over time. The second track consists of an investigation of changes in the mineralogy of cementitious material over time.

Deformations in the material were studied in an ESEM and with an optical microscope. Ageing phenomena in cementitious materials occur at a slow rate. To accelerate ageing, it was decided to expose the specimens to humidity changes with or without temperature changes. Due to the humidity changes large gradients occurred in the specimens, which may lead to changes in the cement paste. Specimens were tested in four test cycles with approximately 15 weeks in between. Between tests, the specimens were stored under different climate conditions (dry, wet, temperature cycles and wet-dry cycles).

Changes in the mineralogy were investigated by X-ray diffractometry (XRD). To detect changes, a reference test and a test on exposed specimens was conducted. The latter were stored in four different climate conditions (dry, wet, temperature cycles and wet-dry cycles) for about 40 weeks before testing.

The study was carried out on binders commonly used in the Netherlands (CEM I, CEM III/B, CEM III/B with fly ash and CEM III/C), with the former as a reference and the latter as a look-through for application of new binders.

In this study it was attempted to find changes in the deformational behaviour at the microscopic scale over time in cement paste upon exposure to changing relative humidity (from 50% RH to 100% RH and back). No changes in the deformational behaviour of the material were found that could be attributed to ageing. However, interesting findings were done with regard to the order of magnitude of the microscopic scale deformations in cement paste of the specimens.

From the XRD study it appears that at the exposure conditions used in this study, CEM I is a binder which is less prone to change than blended cements (CEM III) when exposed to similar exposure conditions. The observed changes were, however, not interpreted as ageing.

Samenvatting

Eigenaren van betonnen constructies voor de civiele infrastructuur worden geconfronteerd met verouderende objecten in hun areaal. Deze objecten zijn onderhevig aan fysieke veroudering. Het mechanisme achter veroudering in beton - of meer in het algemeen van cementgebonden materialen - is nog niet bekend. Dit bemoeilijkt de beoordeling van de resterende levensduur. Vaak worden bekende aantastingsmechanismen in cementgebonden materialen, zoals carbonatatie en wapeningscorrosie, herkend en gekwantificeerd bij de beoordeling van een constructie. Over veroudering – de intrinsieke materiaalspecifieke verandering in een materiaal in de loop van de tijd – is nog steeds veel onbekend.

De probleemstelling in deze studie is als volgt geformuleerd: "Veroudering, een materiaaleigen degradatieverschijnsel, in beton of cementgebonden materialen in het algemeen wordt nog niet goed begrepen. Het is nog onbekend in hoeverre veroudering een rol speelt bij degradatiemechanismen en welke gevolgen het heeft voor de levensduur. Het gebruik van bindmiddelen met een zeer laag klinkergehalte (vanwege duurzaamheidsredenen) neemt toe, terwijl de effecten van deze bindmiddelen op de lange termijn prestaties onvoldoende bekend zijn. Dit gebrek aan kennis kan - vanuit het oogpunt van levensduur - leiden tot kwetsbare ontwerpen van betonconstructies vanwege onvoldoende kennis van de lange termijn prestaties van het materiaal.".

Er is een literatuurstudie uitgevoerd naar het begrip veroudering in verschillende materiaaldisciplines. Over veroudering van o.a. kunststoffen, metalen en legeringen en microprocessors is veel bekend. Gradiënten in het materiaal leiden tot diffusie-verschijnselen (transport, overdracht van energie) welke kunnen leiden tot veranderingen in het materiaal. Deze inherente veranderingen in het materiaal worden geschaard onder veroudering.

In dit onderzoek is gepoogd om verouderingsfenomenen op te sporen in cementgebonden materiaal. Er zijn twee onderzoekstrajecten uitgewerkt, gericht op veroudering. In het eerste spoor lag de nadruk op vervormingen van cementgebonden materialen op microscopische schaal bij blootstelling aan cycli van bevochtigen en drogen en hoe de respons van het materiaal op die cycli veranderde in de tijd. Het tweede spoor bestaat uit een onderzoek naar veranderingen in de mineralogie van cementgebonden materialen in de tijd.

Vervormingen in het materiaal werden geobserveerd in een ESEM en met een optische microscoop. In cementgebonden materiaal ontwikkelen verouderingsfenomenen zich in

zeer traag. Om veroudering te versnellen zijn de proefstukken belast met vochtwisselingen al dan niet in combinatie met temperatuurwisselingen. Hierdoor worden de proefstukken aan grote gradiënten blootgesteld, welke aanleiding kunnen geven tot veranderingen in de cementpasta. De proefstukken werden getest in vier testcycli met ongeveer 15 weken tussentijd. Tussen de tests zijn de proefstukken opgeslagen in verschillende klimaatomstandigheden (droog, nat, temperatuurcycli en nat-droogcycli).

Veranderingen in de mineralogie werden onderzocht met behulp van röntgendiffractometrie. Om veranderingen op te sporen werden een referentietest en een test op blootgestelde proefstukken uitgevoerd. Deze laatste werden gedurende ongeveer 40 weken voorafgaand aan de test in verschillende klimaatomstandigheden (droog, nat, temperatuurcycli en nat-droogcycli) opgeslagen.

Het onderzoek werd uitgevoerd op in Nederland gangbare bindmiddelen (CEM I, CEM III/B, CEM III/B met vliegas en CEM III/C), waarbij de eerste als referentie en de laatste als doorkijk voor toepassing van nieuwe bindmiddelen werd gebruikt.

In deze studie is gepoogd om veranderingen in de tijd te vinden van het vervormingsgedrag op microscopische schaal van cementpasta, blootgesteld aan veranderende relatieve vochtigheid (van 50% naar 100% en terug) al dan niet in combinatie met temperatuurwisselingen. Er werden in het microscopisch onderzoek geen veranderingen in het vervormingsgedrag waargenomen die duiden op verouderingsfenomenen. Er werden echter wel interessante observaties gedaan met betrekking tot vervormingen op microschaal in de proefstukken.

Uit het mineralogisch onderzoek blijkt dat bij de in dit onderzoek gebruikte blootstellingsomstandigheden er in proefstukken met CEM I bindmiddel minder veranderingen optraden dan in proefstukken met gemengde cementen (CEM III) bij blootstelling aan vergelijkbare omstandigheden. De waargenomen veranderingen worden niet als verouderingsfenomenen gezien.

1 Introduction

1.1 Asset management – owner's perspective

For an asset owner, the service life expectancy of each individual asset (i.e. a steel structure, a concrete structure or a structure made of any other material) should be known, so that capital investments for refurbishment or replacement can be predicted accurately and incidental expenses are avoided. With regard to the long-term performance of structures, different asset management strategies can be used for dealing with existing structures.

Asset management can be categorised into five different strategies, with increasing 'maturity', as indicated in Figure 1.1. 'Classical' asset management can be categorized as reactive and/or prepared; an asset owner only comes into action when a defect occurs or when the desired function can no longer be ensured. This kind of asset management might lead to high costs during the service life because unexpected damage and repairs do not only involve direct repair costs, but also lead to costs associated with interruption in operations.

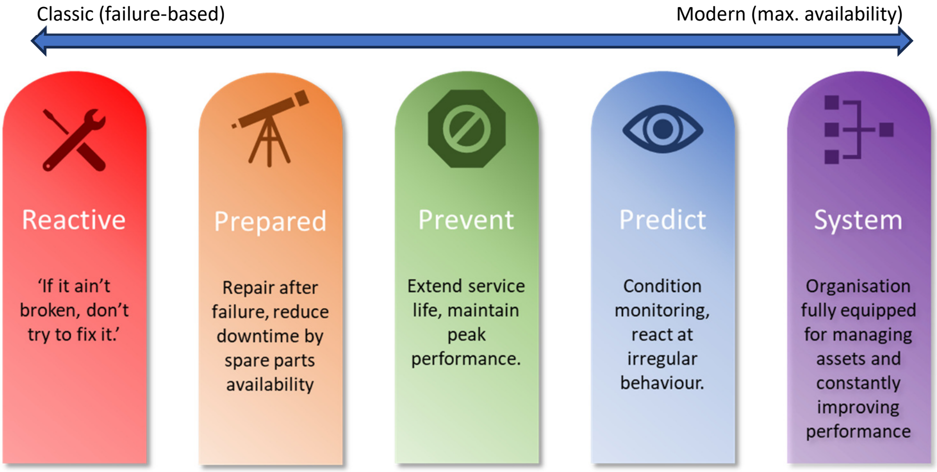

Figure 1.1: Degrees of maturity in asset management (deducted from [63]).

Modern asset management is focussed on preventive and predictive maintenance and aims for systematic maintenance (as indicated in Figure 1.1), with the organisation set up to optimise[1] asset performance through asset monitoring and damage repair during scheduled maintenance periods. These organisations use an integral approach for managing their assets.

1.2 The time-degradation relationship

The long-term performance of concrete structures can be conceptualised as a function of – among other things – time and degree of degradation, as illustrated in Figure 1.2.

Shortly after the origin of the horizontal branch of the time-degradation relationship in Figure 1.2, the structure is put into use. After a structure is put into use, the structure functions as it was planned to do. From that moment on, the structure becomes exposed to all sorts of mechanical and environmental loads.

After a certain period of time, the structure starts to show signs of degradation (e.g. cracking caused by (over)loading or time-dependent effects, corrosion of reinforcement with consequential cracking and spalling of the concrete cover). Degradation of the structure is usually connected with reduction of the cross-section of the reinforcement, caused by reinforcement corrosion. Without preventive maintenance, the degree of degradation increases up to the point where the structure can no longer carry the loads it was designed for. After renovation, the structure (partly) regains structural strength and after some time the degree of degradation increases again until the next renovation. A structure is decommissioned based upon a decision. The structure can in most cases be renovated to be brought up to an acceptable structural level. Functional requirements and the financial aspect of ongoing renovations are considerations that lead to the decision for either decommissioning or repeated renovation.

When considering the long-term performance of concrete structures, many different processes in the material should be taken into account (e.g. ongoing hydration of the binder, time-dependent deformation behaviour, crack formation, transport properties, etc.). As the performance of a structure depends on the state of the material, this study focusses on the state of the *material*.

---

[1] Optimised asset performance: maximised availability with lowest operational cost and societal impact.

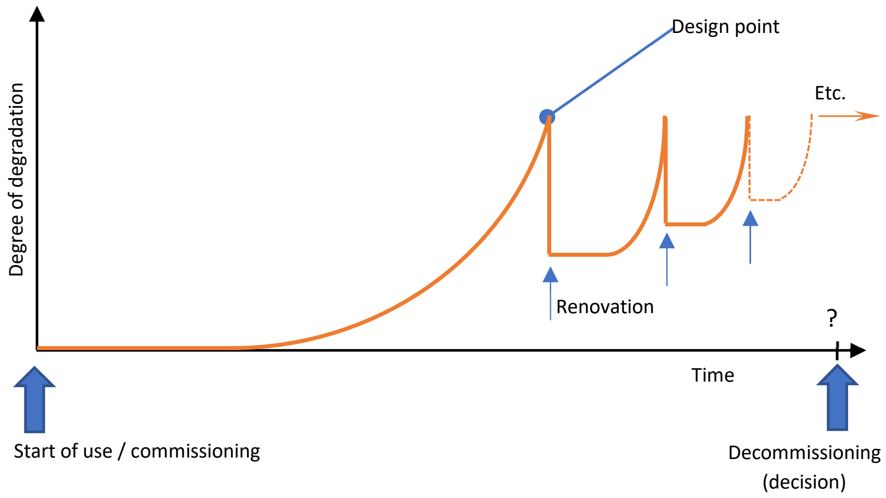

Figure 1.2: Conceptualized time - degradation relationship. At the design point, the structural strength is equal to the design load, i.e.: the structural integrity of is compromised and measures are necessary. After renovation the structure (partly) regains structural strength.

1.3 Change of performance with time – ageing

Over the years, research has been carried out on many degradation mechanisms in cementitious materials. There are, however, material inherent alteration phenomena that are not yet fully understood. Ageing of cementitious materials, for instance, has not yet been studied in detail until now. Gaining insight in ageing phenomena in these materials is useful with regard to service life prediction.

To illustrate the ageing phenomenon, the following examples are given:

- Plastic composites, and polymers in general, are known to be sensitive to ageing. Over time, without being influenced by any loading, the structure of a plastic composite or polymer changes. This change in structure may cause, as yet invisible, decay of the material. The most probable changes in performance usually are an increase in permeability or an increased brittleness and decreasing strength.
- A (reinforced) concrete structure is subjected to mechanical and environmental loads during its service life. The structure was designed to withstand these loads. However, over time the performance of the material decreases (increased deformations, superficial damage, cracking). Most structures are only inspected

superficially and only the visible signs of decay are recorded during such an inspection. There may be underlying, not yet identified, mechanisms that lead to decay of cementitious materials.

As yet, little is known about the origin of autonomous decay of cement-based materials and to which extent such decay should be considered as ageing.

1.4 Scope of long-term material and structural performance

In Figure 1.3 the subsequent stages of the performance over time of any system are presented [1]. After an initial period of solving teething problems and increasing performance, a material will perform on the desired level for a long time without showing any visually observable signs of change or decay.

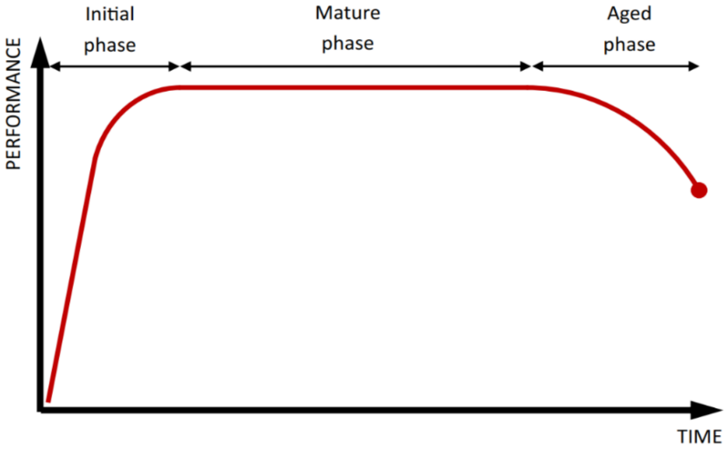

Figure 1.3: Inverted 'bathtub curve' for performance of a system in time. Adapted from [1]

At a certain point in time, the system will start to degrade and the performance of the system will start to decrease gradually (e.g. increasing deformations, cracks, leaks, etc.) until the system is affected in such a way that it is not functional anymore and needs to be repaired, refurbished or even replaced. This is marked in Figure 1.3 by the dot at the right hand side end of the curve.

The time until the performance of the system starts to decrease is affected by environmental exposure conditions and external loading and by the initial material properties. For new structures with known materials, Standards, guidelines and detailing rules are available. When these are applied correctly, a new structure is deemed to reach its designed service life. However, when using materials that are yet unfamiliar, service life predictions based upon Standards and guidelines may be less accurate (i.e.: the Standards and guidelines are not yet optimized for that particular material). For the prediction of the residual service life of existing structures, an accurate and reliable method must be available, which is not the case yet. As a result, the effects resulting from said exposures and loads can only be treated through reactive or prepared maintenance (according to Figure 1.1).

Figure 1.4 shows in four images the different levels of detail at which the condition of an object can be considered. When a concrete structure is viewed from a distance (Figure 1.4a) the structure looks sound and undamaged. Looking closer at the concrete

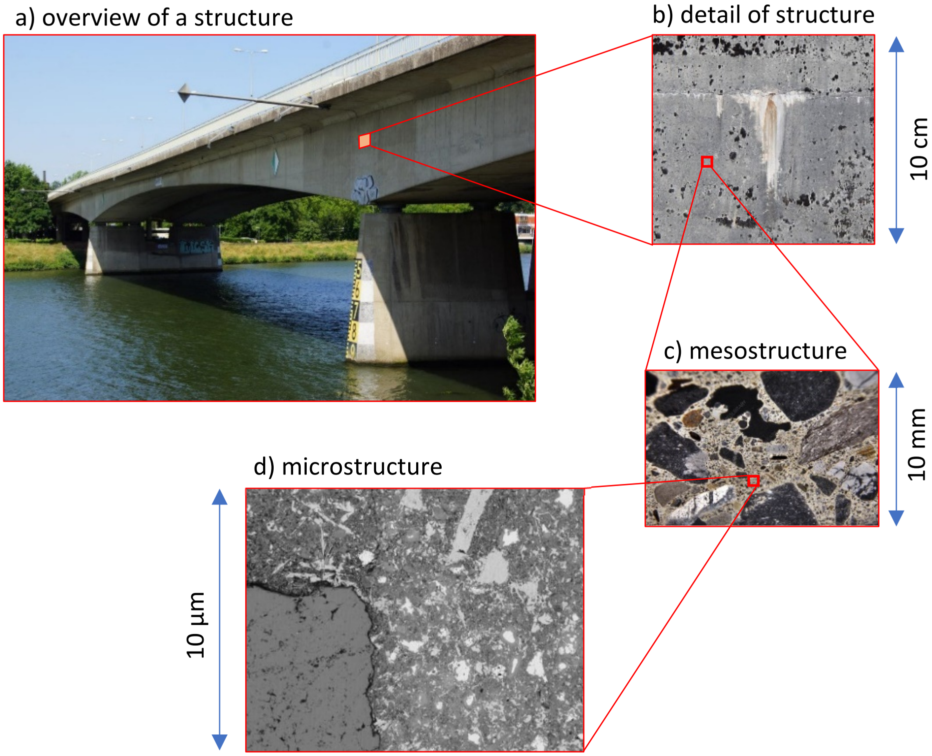

Figure 1.4: Zooming in on a structure. From a) to d) the level of detail increases.

surface, one may notice cracks, traces of leaching or other signs of degradation on the concrete surface (Figure 1.4b). Zooming in even further on the material, the individual aggregate grains become visible with the cement paste in between (Figure 1.4c).

When zooming in even further on the cement paste, the reaction products in the conglomerate of particles in the microstructure can be distinguished (Figure 1.4d). To study ageing of cementitious material in the mature phase (according to Figure 1.3), the material is analysed on the microscopic scale (Figure 1.4d).

1.5 Environmental issues – CO_2 emissions

New structures are designed for a desired service life, with sustainability gaining importance in recent years. Awareness about environmental issues and climate change are omnipresent in societal and political discussions. This also applies for the concrete construction industry.

For the production of 1000 kilograms of Portland cement, approximately 800 kilograms of CO_2 are emitted, CO_2 being a greenhouse gas. In Figure 1.5, the CO_2 emissions from cement production are shown in relation to global CO_2 emissions.

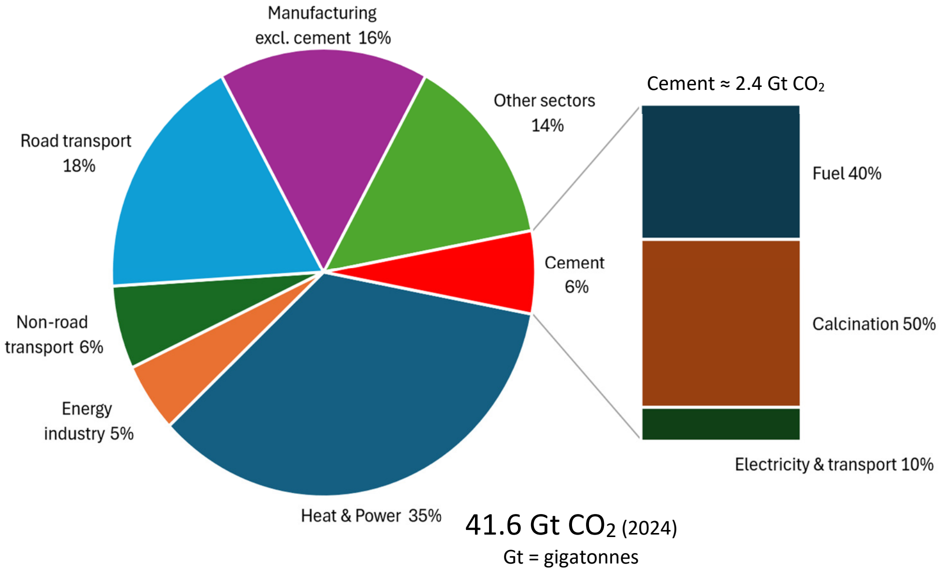

Figure 1.5: Total global CO_2 emissions in relation to cement production emissions, adapted from [64-66]

Driven by the need for CO_2 reduction, the concrete construction industry is looking for ways to reduce the carbon footprint of concrete structures. Production of Portland cement clinker[2] is the main cause for the high carbon footprint of concrete. Therefore, binder types with (very) low clinker content are already being used and there is a tendency to promote the use of binder types with even lower clinker content. In the Netherlands, the use of CEM III binder with clinker content < 35% of the total binder weight is common. Yet, there is little experience with the ageing and long-term performance of binder types with clinker content < 20% in concrete structures for infrastructure. When using binder types with an unknown or insufficiently known long-term performance – with respect to durability – the duration of the service life may be compromised. This is a potential risk for an asset owner. The consequences are not only that major repair or even replacement of the asset may be required earlier than expected, thus leading to extra costs. Also the consequences for all stakeholders (i.e. road or rail users, society) must be considered – and this is not always accounted for in Standards and regulations. For assets with a high utilisation rate and/or as part of a dense traffic network, the effects of major repair or replacement are highly unwanted. Another risk is, that the initial environmental benefit of CO_2 reduction is negated when a structure needs to be replaced earlier than originally planned. This underlines the necessity of a thorough understanding of the long-term performance (>50 years) of concrete with known and less known binder types for structures with a desired long service life (i.e. infrastructural facilities like bridges, tunnels, ship locks, etc.).

1.6 Problem statement

The problem statement for this thesis is now defined as follows:

- Ageing, a material-inherent decay phenomenon, in concrete or cementitious materials in general is not understood well. It is yet unknown to what extent ageing plays a role in degradation phenomena and in limitations of service life.
- The use of binder materials with very low clinker content (for sustainability reasons) increases, while the effects of these binders on the long-term performance are insufficiently known. This lack of knowledge may result in – from a durability point of view – vulnerable designs of concrete structures because of poor prediction of the long-term performance of the structures.

---

[2] Clinker: sintered limestone. Clinker nodules are ground to fine powder and are used as binder in cement products.

To improve the management of their capital investments, asset owners should set up systematic maintenance strategies for their assets. For these strategies, a thorough understanding of the long-term material performance under prevailing exposure conditions is required because the state of the material is decisive for the long-term performance of their assets.

To find a balance between the sustainability and the durability of concrete structures, it is important, if not a prerequisite, to understand the long-term material performance of the material. This thesis is a path-finding study in which an understanding of ageing of cementitious materials is pursued with the aim to more reliably estimate the materials proneness to future decay.

1.7 Research outline

The results of the study are presented in 9 chapters in this thesis. In chapter 1, the background, motivation and problem statement for the study are given. In chapter 2, a literature survey is given on ageing and long-term performance of cementitious materials. The literature survey also includes an overview of how the design service life of concrete structures is addressed in building codes and Standards over time. An overview of the differences and parallels between ageing in cementitious and other materials is given in this chapter. In chapter 3, the research hypothesis and research question are stated and the research strategy is presented. Chapter 4 describes the materials and methods used in this study and the research method of the microscopy research is described. In chapter 5, the results of the XRD analysis are described. The aim of the XRD analysis is to find differences in the mineralogy of cementitious material after prolonged exposure to simulated climatic conditions. The results of both the reference analysis and the analysis of the exposed specimens are compared and the differences are pointed out and discussed. Chapter 6 describes the microscopy research and Digital Image Correlation (DIC), which is used to analyse deformations in the cement paste of mortar and concrete specimens. Subsequently, in chapters 7 and 8 the measurement data and the results of the DIC analysis are described for ESEM specimens and optical microscopy specimens, respectively. In chapter 9, the outcome of the microscopy research is evaluated, interpreted and discussed and the work in this study is summarised and conclusions are drawn from the findings in the study. Also, the contributions of this research to science and practise are given, together with recommendations for further study.

2 Literature survey on ageing

This chapter provides an overview of the available knowledge regarding ageing in general and in cementitious materials.

First a literature survey is given with an overview of the development over time of Standards and regulations that cover long-term effects in concrete structures. This is followed by a literature survey on ageing of materials different from cementitious materials (e.g. metals/alloys, plastics/composites and semiconductors). The findings from the literature review are evaluated and discussed. Finally, a list of definitions is given of terminology used in this study.

2.1 Generic description of ageing in literature

Ageing is a term that is used in different disciplines and in relation to different scale levels. Colloquially, the term ageing is used to indicate that an object or a person has reached a certain age [source: Wikipedia]. In that context, the time scale is the known quantity. However, the phenomenon is not yet linked to a measurable quantity of the object or person itself.

Ageing is an inherent material-specific change in the material over time – for better or worse. In materials science, ageing refers to physical or chemical transformations in a material, whether or not of spontaneous origin [2]. These transformations can alter the engineering properties, affect the chemical characteristics or change the physical characteristics of the material.

Changes never occur spontaneously; there must be a cause, a driving force, for changes in the material to take place, which eventually leads to ageing of the material [2]. Temperature or humidity gradients or differences in the concentration of dissolved substances are considered to be precursors for change and thus for ageing of a material [2]. Depending on the rate of change in the material, ageing processes can occur at different time scales. Ageing processes take seconds, or even centuries to develop, depending on the material and the circumstances.

In materials technology, the chemical reactions involved in the development of a material during production are often referred to as ageing. In this study, however, only ageing in the mature and aged phases (as indicated in Figure 1.3) of the material are considered, because the state of the material and the performance of the structure or structural element during its service life is of primary interest.

In material disciplines other than that of cementitious materials, the concept of ageing is more common and dealing with ageing is more common practice. In polymers (especially long-chain polymers), for instance, ageing is relatively well understood [3], [4] and to some extent also in metals [5] and semiconductors [6, 7].

2.2 Ageing in non-cementitious materials

2.2.1 Ageing of metals and alloys

In metallurgy, the term ageing commonly refers to *weathering* of the material, to point out the formation of an oxide layer at the surface [5]. An oxide layer that developed over a long period of time is sometimes referred to as patina, and can be considered as a visual representation of the effect of time on the material [8]. The oxide layer can also be formed by manipulation of the surface material (forced ageing) [5].

Ageing in metals is promoted by the presence of dislocations of atoms in the crystal structure of the material. In alloys, but also in metals with impurities, ageing can seriously affect the material behaviour. When vacant crystal positions in a metal are taken by impurities or admixtures, the crystal matrix can become ‘clogged’; solid state diffusion is no longer possible in the crystal structure [5,9]. Consequently, the local material behaviour becomes different from the overall material behaviour. This, in turn, leads to a local restraint of deformations and stress concentrations.

In the crystal structure of metals, vacancies or defects are present caused by the fabrication process. When an external load is applied, defects or vacancies may lead to creep or cold flow in the material [4]. Typically, creep deformations in metals only become noticeable at elevated temperatures or at high stress levels.

2.2.2 Ageing of polymers

In polymer chemistry and physics, the term ageing is used in conjunction with physical ageing (no chemical reactions involved), and in connection with thermal conditioning (chemical alterations occurring at elevated temperatures) or weathering (the effects of ultraviolet (UV) light, water, pollutants and temperature changes) [3]. Often, multiple causes of ageing occur simultaneously and/or interactively.

Physical ageing in polymers occurs mainly in thermoplastics. After shaping, the material is cooled rapidly, which prevents the material from reaching thermodynamic equilibrium. Due to rapid cooling, the molecules are not in a state of optimal dispersion at low temperature. The molecules lose their freedom of movement and become fixed in the solidifying polymer matrix. This phenomenon can be illustrated by looking at the evolution of the density of the material. Shortly after cooling, the density of the material is equal to the density of the material at a high temperature. Over a long period of time, the density of the polymer increases due to shrinkage and creep [3]. This is caused by the material striving for the lowest thermodynamic state [10].

When polymers are exposed to elevated temperatures in the presence of an aggressive chemical agent, chemical reactions may occur which would not occur at ambient temperatures, or only at a very low rate. In thermosets, for instance, elevated temperatures cause an increase in the reaction rate of unreacted particles in the material (‘post-cure’). In thermoplastics, elevated temperatures can lead to accelerated physical ageing if no stabilisers are added.

Weathering, also called photochemical ageing or sometimes natural ageing, is the degradation of polymers caused by exposure to outdoor environments. The main causes of weathering are: exposure to ultraviolet (UV) radiation, exposure to airborne or precipitation-dissolved pollutants, exposure to moisture, elevated temperatures and temperature changes. Exposure to UV radiation and exposure to high humidity in combination with elevated temperatures are the most common causes of weathering.

2.2.3 Ageing in semiconductors

Since the invention of the transistor in 1948 and the integrated circuit (IC) in 1955, semiconductors have become an integral part of our society. Semiconductors are made of silicon. Depending on the required properties they can be doped with small amounts of metals (in the order of 0.01 ppm).

Evolution in the size of IC’s

Over time, the size of transistor circuits (process nodes) on an IC halved every 4 years, in 2025 the smallest achievable size is 2 nm. Smaller transistors lead to shorter calculation times and higher calculation power. This is especially beneficial for complicated modelling.

Origin of ageing in IC’s & semiconductors

There is, however, a downside to this miniaturisation. The performance of modern-day IC’s degrades over a much shorter period of time than in the past, well before the expected service life [7]. The ‘switches’ in the semiconductor become smaller, nearing one order of magnitude larger than silicon atoms. Amongst other issues, the temperature of IC’s increases in high-performance applications. It is well known that increased temperatures lead to a larger probability of changes in the state of the material.

Although ageing in semiconductors is still under investigation, it has become clear that changes originate at interfaces in the material due to electrons being driven through the transistors. This leads to faulty behaviour of the IC.

Ageing has always played a role in IC’s. In the past, however, IC’s were built much more robust. As the designed service life of IC’s used to be short, performance issues only occurred long after the designed service life of the IC, if at all [7]. In modern day IC’s, however, miniaturisation and the demand for an increase in performance of IC’s lead to faults and early failure.

2.2.4 Summary of ageing in non-cementitious materials

As described above, the term ageing is used differently in different material disciplines. In metallurgy, ageing mainly occurs in the form of (surface) oxidation of the material. Load-induced ageing in metallurgy mainly occurs during the manufacturing process, or as creep or cold flow in the case of defects in the material.

In polymer science, both autonomous ageing and so-called strain-induced ageing are well-known phenomena. In polymer science ageing has since long been part of research, not in the least because of the wide variety of plastics. In polymers (especially long-chain polymers), for instance, ageing is relatively well understood [3,4].

With regard to metals, terms like weathering, cold flow and forced ageing are used, whereas in polymers, terms like physical ageing and thermal conditioning are used. These terms can be classified into two categories:

- Autonomous ageing, which leads to a change in the performance of the material without any loading other than self-weight, and
- Load-induced ageing, which leads to a change in the performance of the material under external loading. The change in performance is supposed similar to that of autonomous ageing, however, the rate of change is higher.

2.3 Evaluation and discussion

Ageing in cementitious materials

Ageing is an inherent material-specific change in a material. In a concrete structure or structural element that seems to be 'at rest' on macroscopic scale, gradients will be present at the mesoscale level (e.g. temperature & moisture differences in the cross-section, density variations), leading to transport phenomena (e.g.: moisture and ions, temperature amongst others). On microscopic scale, the material consists of a conglomerate of different reaction products, unhydrated binder grains and pores, which can be (partially) filled with moisture. Differences in the concentrations of dissolved substances in the pore solutions and local differences in relative humidity lead to diffusion of moisture through the microstructure, which causes (differential) strains and stresses in the microstructure.

With regard to cementitious materials, the term ageing is used in different ways. On the one hand, the expression is used to denote the 'coming of age' of a *structure*. Analogously, the term ageing is used in Standards and durability models as an empirical quantity to account for (exposure) time. Time-dependent changes of hardened cementitious *materials,* on the other hand, are also called ageing. It is clear, however, that these changes in the material generally adversely affect the long-term performance of a structure. The description of the time-dependent alteration of cementitious material is coherent with the terminology used for ageing in metallurgy, polymer chemistry and physics.

The microstructure of cement paste in cementitious materials is heterogeneous. It consists of crystals and amorphous phases, all with different size and different shapes. Various conglomerates of particles, i.e. different reaction products, react differently to a changing RH. Besides the different nature of the 'building blocks' in the cement paste, the particle size distribution of these building blocks in the microstructure of cementitious materials influences the displacement pattern in the microstructure.

When ageing of concrete, or cementitious materials in general, is described in literature, an often used definition is "age-related degradation mechanisms caused by prolonged exposure to loads" [11-14]. This contrasts with another common use of the term ageing in cementitious materials, namely to refer to the initial phase of the material [15].

From a certain point in time onwards, the term ageing is used in a different way [16]; as an inherent change of the material over time. This change can occur with or without the presence of external loads. Whatever the conditions under which ageing occurs, with or without the presence of external stimuli, the origin of ageing of cementitious materials is not clear yet.

The performance of a structure or system (as depicted with the curve in Figure 1.3) is usually not noticeably affected by ageing during the mature phase. At some moment in time the point is reached when the effects of degradation mechanisms become noticeable (onset of curvature in the performance curve in Figure 1.3 at the end of the horizontal 'mature phase' line), either visually or by other detection devices.

Two types of autonomous ageing in cementitious material are indicated during the life span, as indicated in Figure 2.1:

a) Fast ageing; this type of ageing occurs in the first period after casting during setting and hardening of cementitious material. Large gradients occur in the material due to several processes occurring simultaneously. After a period of maturing, the material can be exposed to its design loading.
b) Slow ageing occurs after maturing of the material. Gradients in the material are smaller than in the phase of fast ageing. Gradients lead to any type of flow in the material. This flow is directed by temperature gradients and/or by differences in concentrations of pore solution and moisture equilibration with the environment.

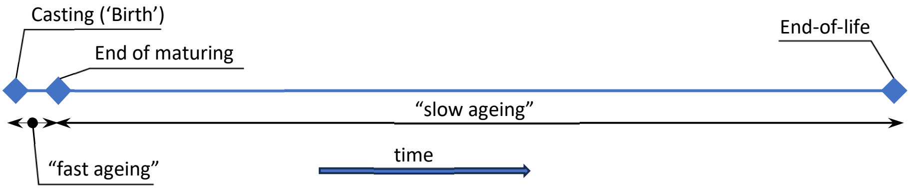

Figure 2.1: Types of ageing during the life span of cementitious material.

During the period denoted as "slow ageing" in Figure 2.1, autonomous ageing as referred to in this study takes place. In autonomous processes no external energy is added to the system. Chemical reactions will occur very slowly. Multiple equilibrium states are established in the microstructure over time (e.g.: moisture, ions, temperature amongst others). Each will lead to flow and a probability of chemical reactions. These reactions may lead to changes in the material. The effects of these changes to the performance of the material are only partially known (e.g.: ongoing hydration leads to a denser cement paste). These changes may lead to dimensional incompatibilities. Dimensional incompatibilities may lead to stresses and strains, of which the magnitude depends on relaxation and creep properties of the microstructure.

Activation energy

Ageing is supposed to occur as a result of ‘internal gradients’ and/or stress concentrations [2,3], without external loads. As long as the activation energy threshold is not met, chemical reactions only take place at a very slow rate or not at all. The rate of reaction is mainly regulated by the presence of any inherent instability or temperature change [17], i.e.: the probability that reactants have an encounter under the right circumstances.

Using thermodynamics, the basis for ageing in materials can be explained. According to the second law of thermodynamics, “energy spontaneously disperses, if it is not hindered. When it does so, entropy increases in the combination of system plus surroundings” [18]. In other words: a system always strives for optimal dispersion. This may be a distribution of heat or a dispersion of particles in solution [18]. Both are examples of energy that is dispersed. Depending on the nature of the dispersed energy, either an amount of energy is dispersed (e.g. heat dispersion) or energy is dispersed over a larger volume (e.g. concentrations of solvents in solute) [18]. These thermodynamic principles hold for all scale levels [19] and can, therefore, be considered useful for understanding ageing.

For a (chemical) reaction to take place, a minimum amount of energy must be provided for the reactants to start the reaction[3], as illustrated in Figure 2.2. Before a reaction takes place the system is at a certain energy level. After the reaction has taken place, the system is at a lower energy level. To start the transformation of the reactants into reaction products a minimum amount of energy is required. The activation energy acts as a threshold that actually regulates the rate of reaction of chemical reactions. Without this energy threshold, all chemical reactions would occur instantaneously [17].

Ageing is supposed to occur at a slow rate. It takes time for changes in a material to become noticeable. Depending on the kind of material, this may take longer. Ageing is supposed to be driven by internal gradients. This indicates that changes in the material are induced by a (macroscopically!) merely unnoticeable dispersion of energy that leads to small changes that – in itself – do not lead to an immediately noticeable change in the material, depending on the observed scale. On macroscale (e.g.: building structures), changes or decay may only become noticeable when a certain minimum number of changes have occurred. On microscale or nanoscale, a change may become noticeable after one occurrence (e.g.: semiconductors)

---

[3] More accurately: adding energy increases the probability that reactants will actually react with each other, allowing a chain of reactions to occur.

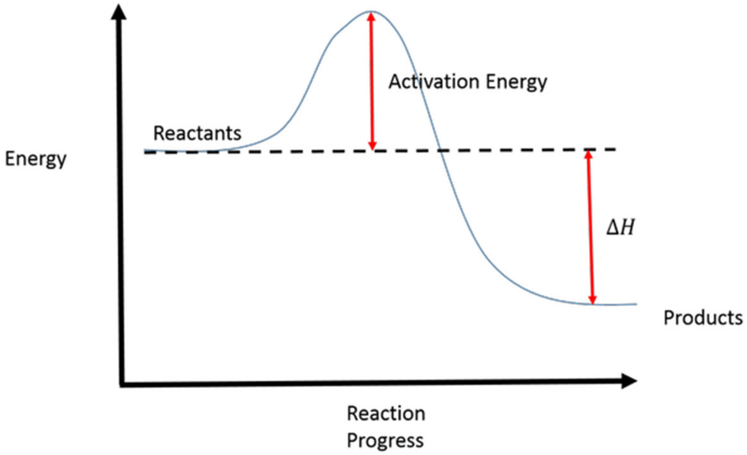

Figure 2.2: Energy of reaction and activation energy for an exothermal reaction .

Ageing in heterogeneous materials

Ageing is more likely in heterogeneous materials. In heterogeneous materials, the response to changes of different constituents differs due to different physical behaviour of the constituents (e.g.: adhesion, surface tension, solubility amongst others). As a result of changes, non-linearities occur in the material. At sites where nonlinearities occur it is likely that the necessary activation energy for local change in the material becomes available and changes actually occur.

As mentioned before, the occurrence of any reaction (either physical or chemical) in the microstructure of a material depends on the probability of reactants to interact [18]. Diffusion of reactants in solids, for instance, is much slower than in liquids. When reactants eventually come together, it depends on the available amount of energy at what rate a chemical reaction takes place.

2.4 Design service life in Dutch Standards and guidelines

Ageing in cementitious materials is considered a slow process which affects the long-term performance. Standards and guidelines contain rules and concepts based on both scientific and empiric knowledge. The following literature survey describes how the design service life of concrete structures is has been interpreted in the history of Dutch Standards and guidelines.

Although great improvements in materials science and material modelling have taken place over the past decades, service life predictions of concrete structures (or cementitious materials in general) remain problematic because of knowledge gaps in the time-dependent material behaviour of cementitious materials. In Codes and Standards service life design is, therefore, still approached deterministically.

By following Standards and guidelines, a required performance of concrete structures is ensured. Traditionally, the emphasis is on performance in terms of, mainly, structural safety and less on durability. Standards for the design and execution of concrete works have been developed from the moment that the use of structural concrete became common practice in the construction industry.

For concrete structures, structural safety and durability are strongly interconnected because the long-term structural behaviour strongly depends on the long-term material behaviour. In Appendix A, an overview of the history of Dutch Standards for structural concrete is given. The main conclusions that can be drawn from that overview is that the majority of these Standards have a ‘deemed-to-satisfy’ character and are either experience-based or based on experiments. These experience-based values, or experimental values, are incorporated in a probabilistic design approach. The contributions of research institutions, universities, clients and binder production companies to Standards committees, as well as European and global co-operation (e.g. FIB, ACI, etc.), have led to a coherent set of Standards in which experiences and knowledge are secured. The probabilistic design approach, however, offers little guidance for the application of materials with which less experience is available.

Now that civil engineering structures are gaining age, the importance of quantifying the effects of increasing age and long-term exposure to an outdoor climate is growing. Up to now, neither Standards nor technology provide sufficient rules or techniques for the assessment of the health of a structure at a scale lower than macroscopic scale.

2.5 Conclusion

2.5.1 Reflection on literature

Regarding cementitious materials, ageing has yet rarely been the subject of in-depth studies. One of the reasons for this is, that ageing was not considered as an inherent material property that can lead to changes in the performance of cementitious materials. As the use of new binder materials becomes more common, a more thorough understanding of ageing in cementitious materials is necessary to gain insight into the long-term performance of concrete structures or elements with new binders.

2.5.2 Aim of this study

The aim of this study is to detect ageing in cementitious material and to determine whether ageing leads to a significant decay of cementitious material.

2.6 Definitions

The *performance of a structure* is defined as the structure's response to the loads (both mechanical as well as environmental) where the structure was originally designed for. As long as the structure is not subjected to these loads, the structure has a performance *potential*.

The *state of a material* is defined as the actual capacity to accommodate mechanical stresses and strains caused by mechanical or environmental loads and/or deformations and chemical attack. The state of a material is observed on the microscopic scale. When the material decays, the performance of the structure is affected.

Degradation or *decay* is a detrimental process that leads to a decrease in performance.

The *design service life* (according to ISO 16204:2012) is the assumed period for which a structure or part of it can be used for its intended purpose with anticipated maintenance but without major repair being necessary. In the EN 1990 [20] this term is referred to as design working life.

Ageing[4] is an inherent material-specific change in the material over time (supposed to be associated with internal gradients). The topic of this thesis is autonomous, slow ageing as mentioned in sections 2.2.4, 2.3 and Figure 2.1.

The *concrete cover* is the layer of concrete which protects the reinforcement against influences from the external environment and which takes part in the transfer of forces from the reinforcement to the concrete and vice versa. The protective function is of interest in this thesis because the durability of a concrete structure depends mainly on the quality of the concrete cover zone.

---

[4] In North America and Canada, the common spelling is *aging*, which refers to the same notion.

3 Research questions and research strategy

3.1 Research hypothesis & research question

In this study, the performance of cementitious materials is studied in detail. Ageing is defined as follows:

Ageing: *an inherent material-specific change in the material over time*

Service life predictions in concrete structures mainly focus on the concrete cover layer, which is most intensively exposed to environmental loads. Further away from the concrete surface - where the influence of environmental actions is limited - ageing occurs as well (in the form of autonomous ageing). There, the rate of autonomous ageing is much lower.

Based upon the above, the following *research hypothesis* is formulated:

> *Understanding ageing phenomena is a prerequisite for estimating the long-term performance of cementitious materials*

Based on this hypothesis, the following *research question* was formulated:

> *Which changes in cementitious materials can be visualised and quantified and can be referred to as ageing?*

3.2 Research strategy

Changes in cementitious materials as a result of ageing are most likely to be found in the microstructure of cement paste. Due to the highly heterogeneous microstructure and the multitude of interfaces in the microstructure, large gradients occur. Gradients may lead to changes or decay in the microstructure of the cement paste. If change or decay occurs, the hypothesis is that it should become noticeable from differences in the deformational behaviour over time. Other indicators for change or decay as a result of autonomous ageing may be found in the mineralogy of the cement paste.

Because ageing occurs at a very low rate, the process needs to be sped up due to time constraints. Therefore, gradients are increased by loading specimens with humidity changes that mimic an outdoor environment. As a result of increased stressing of the specimens, it is considered more likely that change or decay occurs.

With these considerations in mind, ageing is studied by:

1. Visualising the deformational behaviour in cementitious materials at the microscopic scale while the material is exposed to changes in relative humidity and temperature;
2. Determination of changes in the mineralogy of cementitious material after prolonged exposure to different climatic conditions.

3.2.1 Deformations at the microscale

3.2.1.1 Description of test cycles and data-analysis

It is presumed that gradients and heterogeneities in the material promote ageing of a material. Gradients in a cementitious specimen, e.g. temperature and moisture gradients, will lead to stresses and strains in the material which may enhance the rate of ageing. Based upon that, attention is drawn to the work of Neubauer et al. (2000) [21,22]. Neubauer et al. measured deformations in the microstructure of cement paste when exposed to variations in relative humidity. In their work, a new Deformation Mapping Technique (DMT) was used to demonstrate deformations in the microstructure of cement paste when exposed to changes in relative humidity.

With the work of Neubauer et al. in mind, a path to the visualisation of microscopic deformations in cementitious materials is explored. Cement paste is studied in an environmental scanning electron microscope (ESEM), where the specimens are exposed to a changing relative humidity. Pictures of the microstructure are taken at different relative humidity. These pictures are then analysed with Digital Image Correlation (DIC) software. To demonstrate differences in deformations over time, the cementitious material is observed in four test cycles with approximately 10-15 weeks between subsequent test cycles. When notable differences occur between the deformational response of a specimen in subsequent test cycles, these are attributed to ageing.

Between test cycles, the cementitious material is stored in four different climate conditions (dry, wet, temperature cycles and alternating wet-dry).

From the analysis of deformation data it should be possible to visualise microstructural changes in the material. Because of the number of specimens and the amount of data that is gathered from the specimens during the tests, a qualitative comparison between the results of subsequent test cycles and between specimens made with different types of cement can be made.

3.2.1.2 Two-dimensional images in relation to the third dimension

In the microscopy study, the surface of a cementitious specimen is observed with an ESEM or an optical microscope. From the DIC analysis on subsequent images, two-dimensional deformations are gathered.

The deformations at the surface of an element are influenced by the material below the observed surface. In chapter 4, the layout of the microscopy specimens is discussed more in detail. The dimensions of the field-of-view in relation to the specimen size and specimen thickness make that the observations in the microscopy research, although only two dimensional, provide an insight in the deformation behaviour of the cement paste during consecutive tests.

3.2.1.3 Stress and strain

In this study only deformations are considered, no strength parameters. The calculated mean shrinkage and swelling strains in this study are measured over a small field-of-view (0.4 x 0.3 mm²) on small specimens (area of about 10 x 10 mm²). These mean strains are not to be interpreted as engineering properties. They are, however, suitable for a comparison of deformations in different specimens at different age.

Local strains are calculated at an even lower scale than the mean strains; the resolution at which local strains are calculated is in µm range. As a result, local strains are no longer representative for bulk material behaviour. A local strain represents the differential deformation per unit of measurement between two fictitious points in an image (hence they are so-called fictitious local strains). A local strain may be measured on one particle in the microstructure but often between two different particles with different properties. Therefore, these strains can only be used to indicate differences between different specimens rather than indicating engineering properties.

When strains are hindered, stresses occur in the material. Depending on the observed scale, different restraints occur. Specimens may be macroscopically unrestrained or partially restrained. At lower scale, the effect of a macroscale restraint may be much less pronounced. As a result, the definition of stress becomes diffuse at low scale levels.

3.2.1.4 Shrinkage and swelling in relation to specimen size

The response to humidity changes of a thick macroscale specimen leads to a moisture gradient and an associated stress gradient over the depth of the specimen. Figure 3.1 shows the development of (eigen)stresses and strains in thick (> 10 mm) and in thin (about 1 mm) unrestrained specimens. Because the specimens are macroscopically unrestrained, moisture gradients do not lead to stresses in the specimen, except for eigenstresses. In macroscale specimens it takes more time to reach equilibrium over the specimen than in thin specimens.

Thick specimen

Over time, shrinkage and swelling stresses in thick sections decrease as a result of creep [23-25]. Drying from the top of the specimen leads to eigenstresses as indicated in Figure 3.1. Over time, the moisture gradient slowly develops over the specimen and the eigenstresses disappear.

Thin specimen

In a thin specimen moisture equilibrium is reached much sooner than in a thick specimen ($\frac{t_{thick}\,[mm]}{t_{thin}\,[mm]}$ times faster as per Fick’s law; the thickness of the specimen affects the diffusion flux in a linear rate). A change of humidity almost immediately affects the whole specimen. Therefore, it leads to a rapid response without any substantial restraint by adjacent material. For this reason shrinkage and swelling in thick specimens are smaller than in thin specimens.

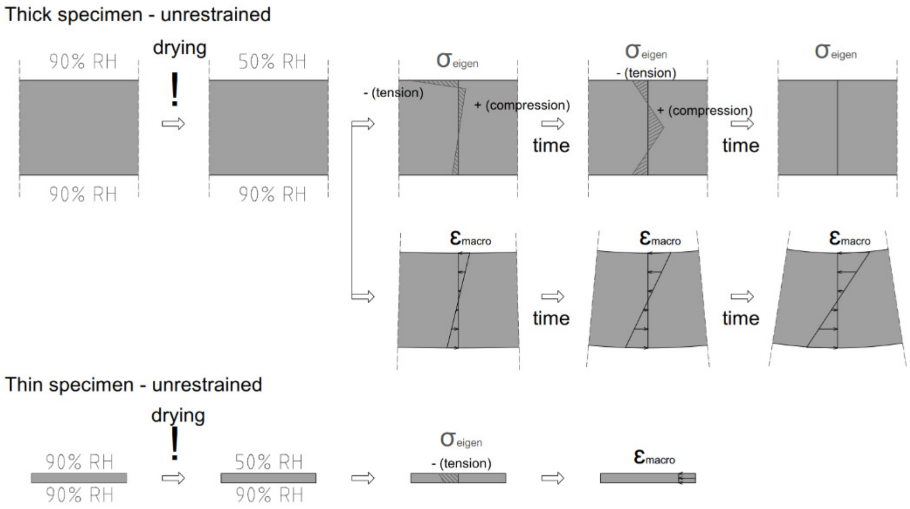

Figure 3.1: Development of shrinkage stress and mean (macroscale) strain in thick (top) and thin (bottom) optical microscopy specimen.

3.2.2 Change of the mineralogy of the material

Under prolonged exposure to environmental conditions, changes will occur in the microstructure of cementitious materials. To determine whether mineralogical changes in the material could be referred to ageing, two XRD analyses are carried out on specimens from the same material at different times. The first XRD analysis is carried out directly after specimen preparation. The material for the second XRD analysis is stored for 37-40 weeks under the same conditions as the material for microscopy tests. After this period, the second XRD analysis is carried out. By comparing XRD analyses at different ages, possible changes in the mineralogy that might indicate signs of ageing may be found.

3.3 Expected outcome

With the experimental work outlined above, an attempt is made to find effects of ageing in cementitious material, more specifically in cement paste of concrete and mortar specimens. It is expected that differences in the deformational behaviour of the microstructure are found by comparing microscopic images of specimens at subsequent ages. With XRD tests differences in the mineralogy of specimens are shown between specimens of different age. The expected results of the experimental work provide information that can be used to answer the research question defined in section 3.1.

4 Materials & methods

In this chapter materials and methods are described with the relevant test parameters and limitations. Relevant choices, assumptions, simplifications and limitations of the experimental studies are clarified.

4.1 Binder types and materials

The binder types that are used in this research are similar to those used in the majority of civil engineering structures in the Dutch infrastructural network. It was found, that the majority of structures is built with one of the following binder types:

- CEM I (ordinary Portland cement, mostly in older precast structural elements);
- CEM III/B (blast furnace slag cement), the most common binder in civil engineering works in The Netherlands. The slag content varies between 66% and 80% of the cement weight;
- CEM III/B + Fly ash (blast furnace slag cement with added fly ash). This binder with fly-ash is included in the research to illustrate the effect of fly-ash with regard to ageing;
- CEM III/C (blast furnace slag cement with a slag content between 81% and 95%). This binder is included in the research with the aim to illustrate the effect of low-carbon binder with regard to ageing.

New (mortar) specimens are produced with these four binder types. In order to ensure a link with existing structures, specimens are prepared from material taken from existing (concrete) structures in which nominally the same binder was used. There may be differences between the binder of new specimens and the binder of specimens from existing structures as sources and production methods may have changed over time.

4.2 Origin of specimens

4.2.1 Specimens from existing structures

For the preparation of specimens from existing structures (so-called “old” specimens), samples were taken from these structures by core drilling. The year of construction of the four existing structures varies between 1985 and 2014. Two of the four existing structures are shown in Figure 4.1.

It was decided to perform tests on core concrete (not exposed to outdoor environment until specimen preparation). Drilled core samples were taken from a greater depth from the exposed surface, as shown in Fig. 4.2. As a result, the influence of environmental exposure on the specimens is minimised.

The locations of the structures from which the cores were taken are described in Appendix B.

Motorway viaduct ‘Grollegat’

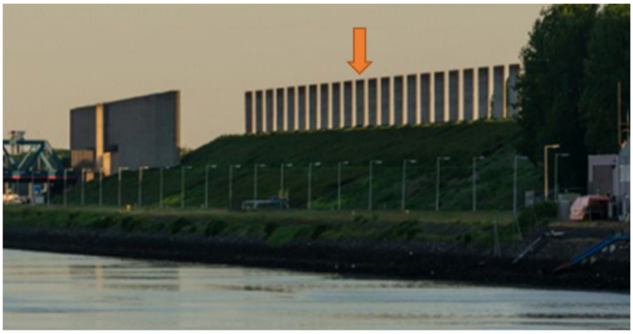

Wind deflecting structure Caland channel

Figure 4.1: Existing structures from which samples were taken for this study.

The specimens for both the microscopy tests and the XRD tests were taken from a certain distance from the exposed surface larger than the thickness of the concrete cover zone (> 55 mm), as shown in Figure 4.2.

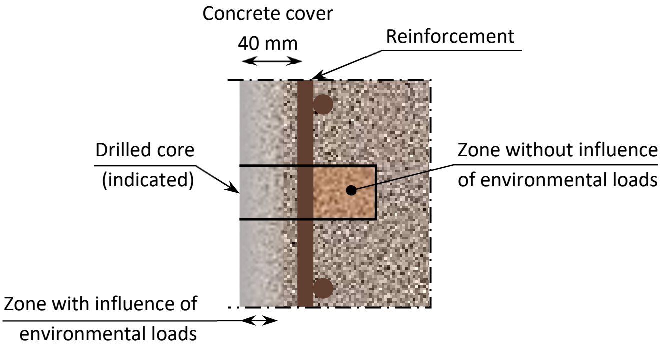

Figure 4.2: Illustration of drilled cores for material specimens of existing structures. The material behind the reinforcement (as seen from the exposed side) is considered optimally cured and unaffected by environmental loads.

4.2.2 Laboratory specimens

Mortar specimens (so-called “young” specimens) are made with nominally the same binder types as the specimens from the existing structures. For the microscopy tests and the XRD tests, specimens were taken from mortar beams with dimensions 40 x 40 x 160 mm^3. These mortar beams are made with a standard mortar mix after NEN-EN 196-1:2016 [26], with CEN Standard sand. Mortar is chosen for the microscopy specimens because of the small size of the specimens.

In Table 4.1 an overview of the composition and mechanical properties of the mortar specimens is presented. In Appendix C, the measurement data from the mortar specimens are listed.

Table 4.1: Compressive and flexural strength of mortar specimens

Binder & material type	Compressive strength [MPa]	Flexural strength [MPa]
CEM I – mortar	36.1	8.4
CEM III/B – mortar	44.2	10.2
CEM III/B+FA – mortar	42.0	9.0
CEM III/C – mortar	31.0	9.3

4.3 Storage conditions

The specimens for microscopy tests were stored under four storage conditions during the periods between consecutive tests (so-called interim storage). The storage conditions are based on high and low mean values of temperature and relative humidity in the Netherlands. The selected conditions are presented in Table 4.2.

Table 4.2: Storage conditions of specimens during period between testing (interim storage)

Storage condition	Temperature (range) [°C]	Relative humidity [%]
Dry	20	50
Wet	25	100
Temperature cycles	10 – 50 – 10 per 24 hrs	Var. 50 - 95
Wet-dry	8 hours wet	100
	328 hours dry	50

For XRD tests, a reference set of specimens was tested 29 days after casting, i.e.: 1 day after specimen preparation. A second set of specimens was stored under four storage conditions (the same conditions as for the specimens for microscopy tests) for 37-40 weeks before testing.

In Figure 4.3, the timeline for the microscopy tests and the XRD tests is presented. Between microscopy tests, the specimens are stored in four different storage conditions.

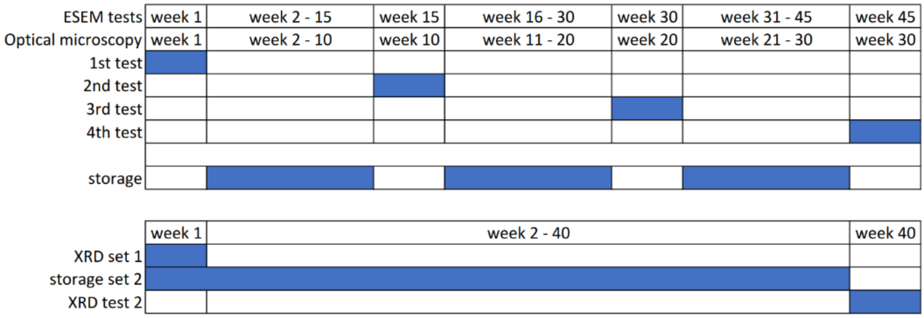

ESEM tests	week 1	week 2 - 15	week 15	week 16 - 30	week 30	week 31 - 45	week 45
Optical microscopy	week 1	week 2 - 10	week 10	week 11 - 20	week 20	week 21 - 30	week 30
1st test	■						
2nd test			■				
3rd test					■		
4th test							■
storage		■		■		■	

	week 1	week 2 - 40	week 40
XRD set 1	■		
storage set 2	■	■	
XRD test 2			■

Figure 4.3: Timeline for microscopy tests with interim storage periods (top part) and test moments for sets of XRD specimens (bottom part) with storage period.

The temperature cycles mimic the extreme temperature variations to which a concrete structure can be exposed during a summer day. The average air temperature in the Netherlands according to [27] is about 10°C and temperatures of 50°C are not uncommon at the concrete surface under the asphalt pavement on a viaduct or bridge on a warm summer day. The time scheme for the alternating wet-dry climate are taken from the Dutch CUR report 90-3 [28], in which a scheme of “4 hours wet, 164 hours dry” is defined that mimics the average Dutch climate. For practical reasons, the experimental work was carried out in a bi-weekly cycle. Therefore, the duration of the wet-dry scheme was doubled. Frost-thaw attack is a specific damaging mechanism that is left out of consideration in this study.

Storage until first test cycle

After specimen preparation, the specimens are stored under water for a maximum duration of five days until the first test cycle is carried out.

4.4 Preparation of test specimens

4.4.1 Specimens for XRD research

For the XRD tests, both concrete and mortar specimens are used. Five sets of eight specimen cubes with dimensions of approximately 10 x 10 x 10 mm^3 are cut from drilled cores (concrete specimens) and from mortar beams (mortar specimens) as shown in Figure 4.4.

Table 4.3: Characteristics of the specimens. An extended characterisation is included in Appendices B and C.

Specimen type	**Casting year**	**Age at t = 0 [years]**	**Water-cement ratio [-]**	**Fly ash [kg/m^2]**
CEM I – concrete	1999	21	< 0.45	-
CEM III/B – concrete	1997-1998	22	0.47	-
CEM III/B + FA – concrete	1985	35	< 0.55	30
CEM III/C – concrete	2014-2015	5	0.37	-
CEM I – mortar	2020	0	0.5	-
CEM III/B – mortar	2020	0	0.5	-
CEM III/B + FA – mortar	2020	0	0.5	30
CEM III/C – mortar	2020	0	0.5	-

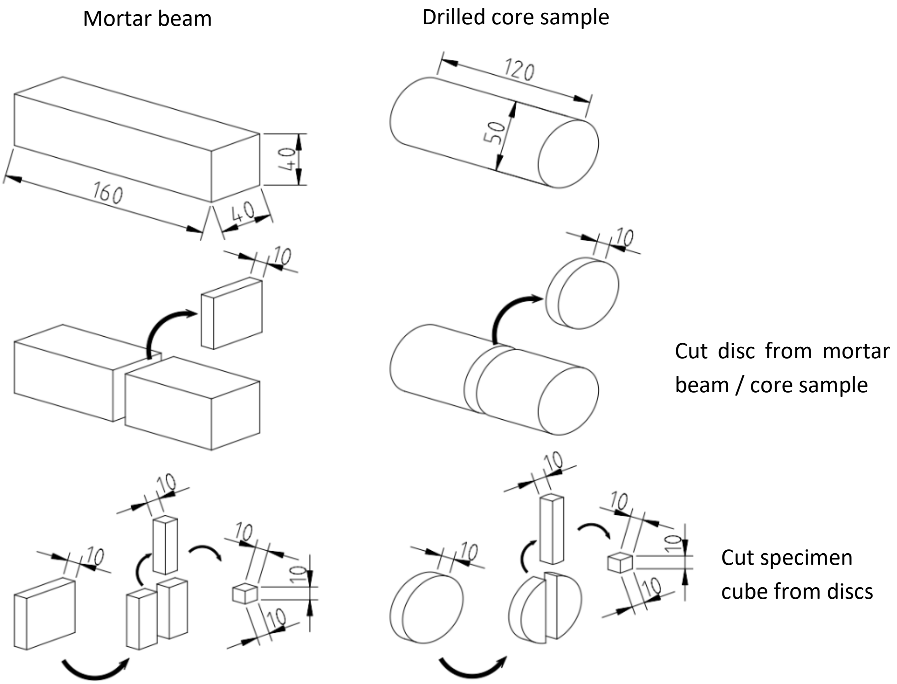

Figure 4.4: Cutting process for the preparation of XRD specimens.

Of each specimen type mentioned in Table 4.3, a specimen is exposed to one of the climatic conditions mentioned in Table 4.2. Therefore, for each specimen type five sample cubes are prepared. As indicated in Figure 4.5, one of these five specimens per specimen type is tested shortly after cutting of the sample cubes (for mortar samples this is at an age of 29 days). This reference test is defined as t = 0 [weeks]. The other four samples are stored and exposed to four simulated climatic conditions as described in section 4.3 and summarized in Table 4.2. The XRD analysis after exposure is carried out at t = 37-40 weeks (see chapter 5 or Appendix D for test dates).

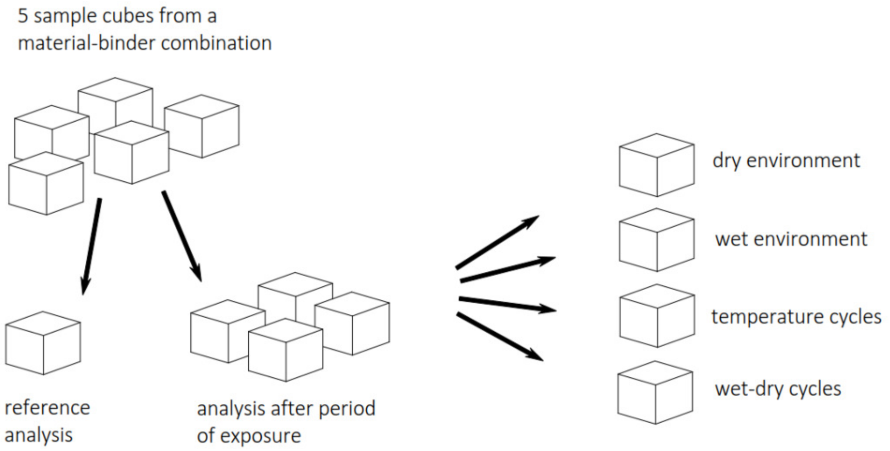

Figure 4.5: Destination of specimens: from each of the existing concrete specimens or mortar beams, five sample cubes are cut. One of the sample cubes is used for the reference analysis, the other four samples are stored in the four different simulated climate conditions.

None of the specimens were kept sealed in addition to those exposed to climate conditions. The effects of ageing must be distinguished from the effects of exposure to the climate conditions. However, when the age of the specimens from existing ('old') concrete structures at t = 0 is considered (see Table 4.3), it is expected that - given the low rate of ageing – only few changes in the mineralogy occur due to autonomous ageing between t = 0 and t = 37-40 weeks. In the mortar ('young') specimens, the changes in mineralogy due to the transition from 'fast ageing' to 'slow ageing' (see Figure 2.1) between t = 0 and t = 37-40 weeks are expected to be significant. This is mainly the result of continued hydration. Since this study focusses on the change in mineralogy and thus on occurring differences, in spite of the above, some differences can be observed between the changing mineralogy of the specimens with different binders and within the binder category between the specimens with different exposure conditions.

The specimens from existing concrete structures are taken at a depth > 50 mm from the surface. The specimens were not checked beforehand on carbonation (e.g. with a phenolphthalein test), although the probability that carbonation penetrates to such depth is small unless the exposure conditions were constantly dry (≤ 65% RH). The material at this depth from the surface is not exposed to short-cycle climatic changes. Young specimens from (laboratory) mortar beams are taken from the core of the beams.

For XRD analysis, the hydration reaction in the specimens should be stopped to obtain reliable data. To achieve hydration stoppage and drying of the specimens, RILEM TC-238 SCM 'Recommendation on hydration stoppage by solvent exchange for the study of hydrate assemblages' [29] was applied.

4.4.2 Specimens for microscopy

From each specimen type, according to the first column of Table 4.4, four specimens were produced. One specimen per specimen type was exposed to one of four different simulated climatic conditions (see section 4.3 and Table 4.2) during the storage period between two consecutive microscopy tests.

Concrete specimens were cut from discs ø 50 mm x 10 mm thick taken from drilled core samples, as indicated in Figure 4.4. From the discs, columns of 10 x 10 x 50 mm^3 were cut.

Mortar specimens were cut from mortar beams (40 x 40 x 160 mm^3). A brief characterization of the mortar beams is given in Table 4.4. A more detailed description of the mortar beams is given in Appendix C. Slices of 10 mm thickness were cut from a mortar beam (10 x 40 x 40 mm^3). From the slices, columns of 10 x 10 x 40 mm^3 were cut (Figure 4.6).

ESEM specimens are mounted on a circular copper plate of ø 9,5 mm x 2.5 mm thick (see section 4.4.2.1). Therefore, the edges of the square columns were chamfered to create octagonal columns.

For each storage condition, one specimen was required. Since there were four different climatic conditions, 3 columns were cut from three slices of mortar beams or 3 discs from concrete core samples. From one column, two specimens can be prepared. The third column was used for spare specimens.

Table 4.4: Brief characterisation of the specimens, an extended characterisation is included in Appendices B and C

Specimen type	**Casting year**	**Age at 1st test [years]**	**Water-cement ratio [-]**	**Fly ash [kg/m^2]**
CEM I – concrete	1999	21	< 0.45	-
CEM III/B – concrete	1997-1998	22	0.47	-
CEM III/B + FA – concrete	1985	35	< 0.55	30
CEM III/C – concrete	2014-2015	5	0.37	-
CEM I – mortar	2020	0	0.5	-
CEM III/B – mortar	2020	0	0.5	-
CEM III/B + FA – mortar	2020	0	0.5	30
CEM III/C – mortar	2020	0	0.5	-

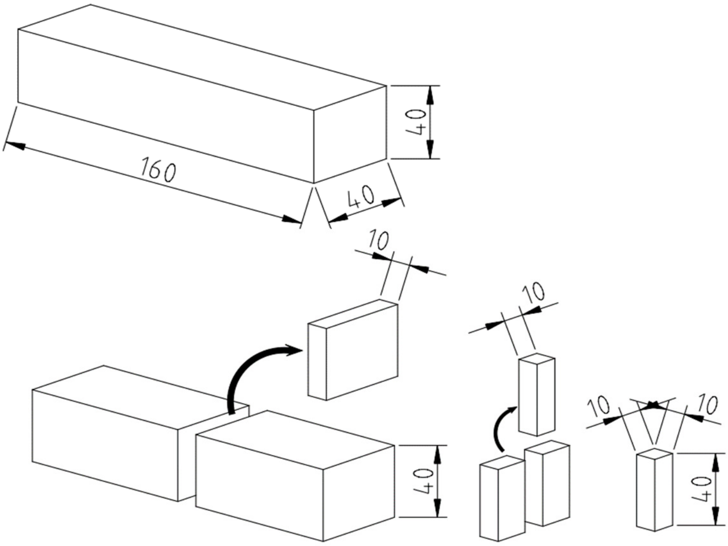

Figure 4.6: Cutting process for mortar specimens

After cutting the columns, the columns were cut in half (2 columns of 10 x 10 x 20 mm^3). The cut surfaces with cross-section of 10 x 10 mm^2 were wet ground with silicon carbide grinding paper of increasing fineness up to P4000 (a grain size of 5 µm). Between each grinding step, the specimens were cleaned in an ultrasound bath. After grinding, the specimens were cut with a precision diamond blade saw, as shown in Figure 4.7. The thickness of the specimen is 1 – 1.5 mm.

The core material, mortar beams and semi-finished specimens were constantly kept under water to avoid carbonation of the exposed surface during specimen preparation.

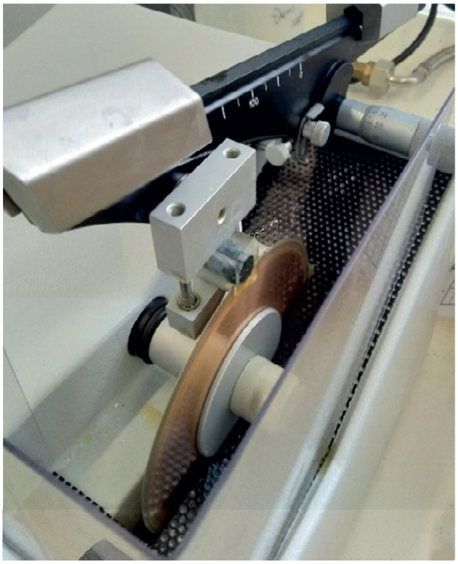

Figure 4.7: Cutting of the specimen to the required thickness with a precision diamond blade saw.

In spite of that, all specimens have carbonated surfaces. In all images, $CaCO_3$ crystals are visible in abundance. The $CaCO_3$ crystals, however, are attached to the cement paste, the movements of the crystals reflect the displacements within the cement paste. Therefore, the displacements are still representative for those occurring in the cement paste at microscopic scale.

4.4.2.1 Specimens for ESEM

ESEM specimens are glued to a circular copper plate (diameter 9.5 mm and 2.5 mm thick) with UV-hardening epoxy glue, to ensure good thermal conduction and to secure the specimen in place. Should the specimen not be fixed during an electron microscopy test, then it is very likely that due to depressurisation and degassing, the specimen may shift several millimetres or the specimen may even fall off the cooling stage. Other options for the fixation of the specimen were considered and tested. Use of thermal conductivity paste was considered but not tested because of the risk of contaminating the interior of the ESEM chamber or the vacuum pumps. Gluing the specimen at only 1 edge was tested in preliminary tests. It turned out, that the connection between the specimen and the copper disc was too vulnerable and an air gap would develop between the copper disc and the specimen. In that case the specimen temperature could no longer be controlled, hence the RH could not be controlled. The ESEM specimens were glued under ambient conditions in the Microlab of TU Delft. The temperature in the lab is generally about 20°C and the relative humidity generally varies between 50% RH and 70% RH.

Figure 4.8 shows a cross-section of the specimen assembly for ESEM tests. At a distance of about 1 mm from the edges of the specimen (restraint introductory zone), the bond between the specimen and the copper plate is complete. The circular copper plate forms a deformational restraint at the bottom of the specimen. The presence of an aggregate grain over the full thickness of the specimen will cause additional restraints in the specimen. The registered deformations at the analysed surface are biased by such a restraint, regardless if the restraint is inside or outside the field-of-view during the test.

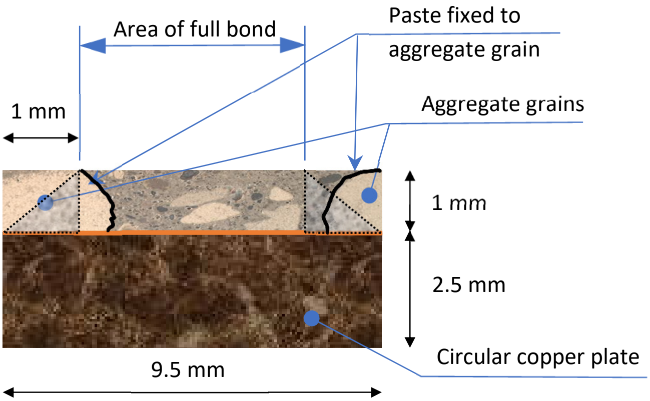

Figure 4.8: Cross-section of ESEM specimen glued to circular copper plate.

4.4.2.2 Specimens for optical microscopy

Optical microscopy specimens are not glued to a copper plate and can, therefore, move freely on the cooling stage. During the optical microscopy tests, the RH in the specimen is changed by a change of the specimen temperature. The specimens need not be fixed to the cooling stage because no degassing of the specimen occurs during the test. As a result, a deformation-restraining zone of full bond at the bottom - like in the ESEM specimens - is not present in the optical microscopy specimens. Unlike ESEM specimens, the temperature is changed in optical microscopy specimens in addition to the change of the RH. These temperature changes will bias the registered deformations at the surface of the specimen to some extent. In Appendix E, page E.6 the mean deformation resulting from the temperature change was estimated to be in the order of 0.1-0.2 ‰. Further theoretical background is given in section 4.7.2.

The difference between the deformations of ESEM and optical microscopy specimens as a result of RH change from 50% RH to 100% RH is schematically indicated in Figure 4.9. It shows, that the deformation at the top of the ESEM specimen is influenced by the restraint at the bottom. The cement paste structure is kept together firmly at the bottom of the specimen. Closer to the top, the degree of restraint (0 < ξ ≤ 1) decreases. As a result, the deformation (mean strain) at the top is smaller than in the optical microscopy specimen. The restraint at the bottom may, however, prevent debonding in the cement paste structure at high RH.

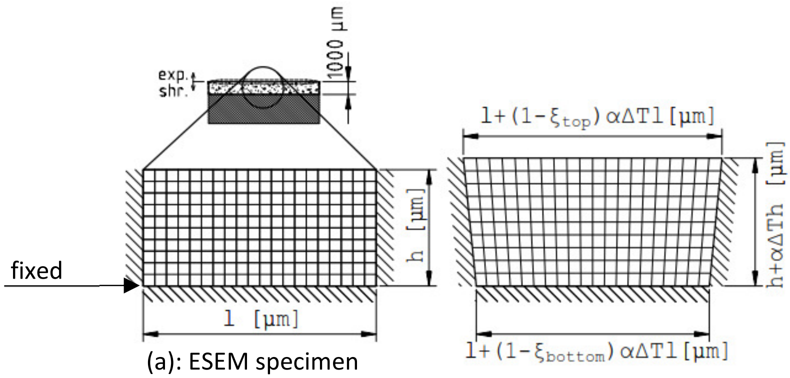

(a): ESEM specimen

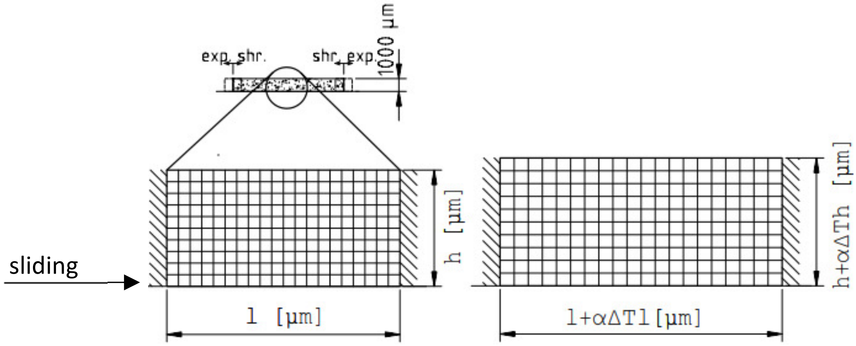

(b): optical microscopy specimen

Figure 4.9: Schematic deformations of ESEM specimen (a) and optical microscopy specimen (b). On the left, the initial dimensions of the enlarged sections are indicated. At the right, the deformed dimensions of the enlarged sections are indicated. ξ represents the degree of restraint, which is nearly 1 at the bottom of the ESEM specimen (a).

4.5 Test conditions – microscopic tests

4.5.1 Tests with environmental scanning electron microscope (ESEM)

Specimens are analysed in an environmental scanning electron microscope (ESEM). Goal is to analyse displacements in the microstructure of the cement paste in mortar and concrete specimens upon exposure to changing relative humidity. Measurements are performed with a FEI company Quanta FEG 650 electron microscope at the Microlab of TU Delft. The electron microscope is used in ESEM (wet) mode with a gaseous secondary electron detector (GSED). Observations are done at 1000x magnification. The size of the field-of-view (hereafter called area of interest, AOI) at that magnification is 400 x 300 μm^2. With this AOI and a resolution of 1536x1103 pixels, the different constituents in the cement paste can be distinguished.

4.5.1.1 Cooling the specimen

To control the relative humidity the specimen is exposed to, the specimen is cooled down to 5°C with a cooling stage, specifically built for use in an ESEM (Figure 4.10). The specimen temperature is kept constant while the pressure in the chamber of the ESEM is varied. The cooling stage consists of a specimen holder, a thermoelectric element and a heat exchanger body.

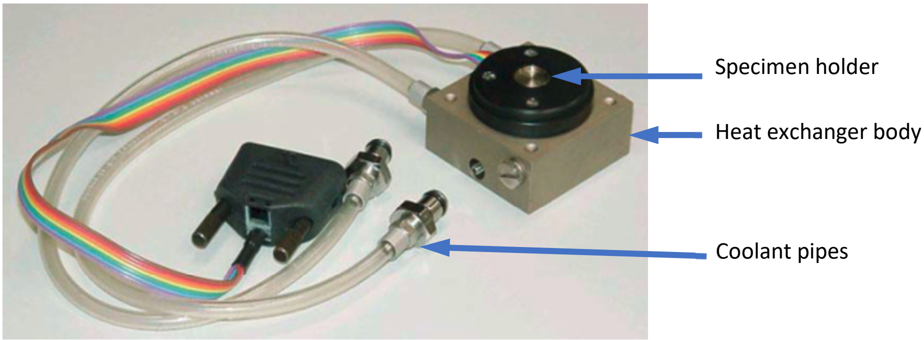

Figure 4.10: Cooling stage assembly for ESEM. Source: Quanta FEG user operation manual

The specimen holder has an inner diameter of 9.5 mm and a depth of 2.35 mm. A thermoelectric element is mounted on the bottom of the specimen holder, as indicated in Figure 4.11. The thermoelectric element can be used either as a cooler or as a heater, depending on the direction of the (DC) electric current. In this application, the cooling stage is primarily used for cooling of specimens. Because of the Peltier effect, heat is transferred from one side of the element (the cold side, in this case the bottom of the specimen holder) to the other side (the hot side). The hot side is fixed to a solid-to-liquid heat exchanger to dissipate the heat to an external liquid cooler. The temperature of the specimen holder is monitored by a PT100-type temperature sensor that is mounted to the specimen holder to create a feedback loop for the temperature controller. After the specimen is placed in the specimen holder, air is pumped out of the chamber. During pilot testing it turned out that the required time (about 5 minutes) to lower the pressure in the chamber of the ESEM until 4.4 mbar was long enough for the specimen to be cooled from ambient temperature (20°C) to 5°C.

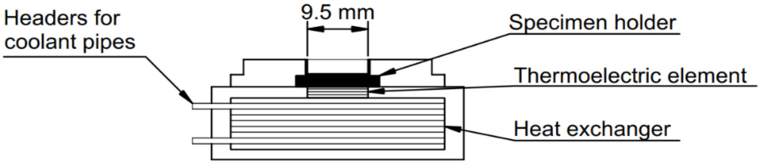

Figure 4.11: Cross-section of Peltier cooling stage

4.5.1.2 Changing the relative humidity (RH) the specimen is exposed to

Appendix E describes the theoretical background on changing the relative humidity in the chamber of the ESEM.

At each pressure step a short period of time is needed to form the image by changing the brightness and contrast. During this time the chamber pressure and the temperature of the specimen should stabilise as well. As soon as the desired values are reached and the image is of constant quality, the image is captured (the AOI is scanned) and the picture is stored.

After completion of the test cycle, the vacuum in the chamber is lowered to 0.25 mbar, to remove all moisture in the chamber before venting the chamber with nitrogen. A possible negative aspect of this step in the test procedure is that the RH at the surface of the specimen briefly drops to about 3% which causes drying of the specimen and potentially cracking due to shrinkage. Over the four test cycles, the temporary low RH in the chamber did not lead to damage in the specimen. The average time for one test cycle, incl. loading of the specimen, pumping to vacuum and venting of the chamber is 65 minutes.

4.5.2 Tests with optical microscope

A second series of microscopy tests is conducted with a DINO Lite USB optical microscope, model AM7515MT8A. This optical microscope has a magnification range between 750x - 950x. Observations are done at 950x magnification. The AOI at that magnification is 420 x 315 μm^2. Image resolution is 2592 x 1944 px. For these tests the specimens are not glued to a plate like the specimens for electron microscopy, but are placed with the polished side directly on the cooling stage. The relative humidity (RH) during these tests is regulated by changing the temperature of the specimen.

4.5.2.1 Cooling the specimen

The temperature of the specimen, and thus the RH the specimen was exposed to, were controlled with a cooling stage. In this stage, a thermo-electric cooler is used to cool or heat a stainless steel specimen carrier. In Figure 4.12 the optical microscopy setup is shown. A thermocouple is mounted ad the top of the specimen carrier to monitor the temperature of the specimen carrier. An infrared thermometer was used to monitor the temperature of the specimen. The opposite side of the thermoelectric cooler is fitted to a heat sink (air-to-air cooler).

4.5.2.2 Changing the relative humidity (RH) the specimen is exposed to

In the optical microscopy tests, the RH in the specimen is changed by changing the temperature of the specimen relative to the ambient temperature. The ambient RH and ambient temperature are monitored during the test. The change in RH with changing temperature is explained in Appendix E. Appendix E also describes the calculation of the required stage temperatures to achieve the steps of RH.

4.5.3 Consecutive test cycles and dataset

In the study of microscale displacements, the specimens are observed during four consecutive microscopic scale tests, each with approximately 15 weeks (ESEM specimens) of 10 weeks (optical microscopy specimens) in between. Between the test cycles, the specimens are stored in climate cabinets and exposed to one of four different environmental conditions (wet, dry, temperature cycles and alternating wet-dry). The first test cycle is carried out within five days after preparation of the specimens.

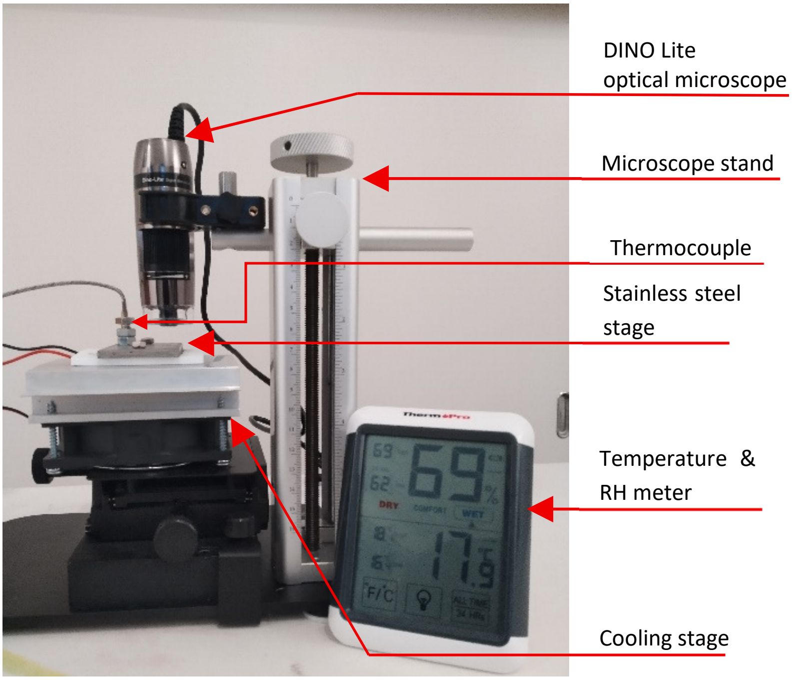

Figure 4.12: Test setup for microscopic scale tests with optical microscope

In both the electron microscopy tests and the optical microscopy tests, 32 specimens are analysed (4 binder types x 2 material types x 4 exposure conditions). On average, 12 images were captured during each test. In the graphical representation of the mean deformations (see chapters 7 and 8 and Appendices F and G), the RH steps in the wetting phase are preceded by a “W” (for wetting) and the RH steps in the drying phase are preceded by a “D” (for drying), thus W90, W100, D90, D80 etc.. On specimens that were stored in a wet environment, condensation tended to occur abruptly with increasing RH. This disrupted the image capturing process. Therefore, at 100% RH images are often missing from the image sets of wet specimens or wet-dry specimens. In some tests, multiple images were taken at one or more RH steps. This usually occurred when the temperature of the specimen or the pressure in the chamber were unstable during the image capturing process. Because these images are a surplus in the series of RH images (e.g. images at 2 x 60% RH, 70% RH, 2 x 80% RH, etc.), those additional images are designated in the graphs as 61% RH, 71% RH, 96% RH etc..

When a specimen is put in the ESEM and left to equilibrate to temperature and chamber pressure for about 5 minutes, the specimen is subject to drying, except for the specimens that had been exposed to dry conditions during interim storage. Because of the low pressure in the ESEM (4.4 mBar), the water in the specimen starts to evaporate. It depends, however, on the duration of exposure whether the specimen is fully equilibrated with the pressure and RH in the ESEM chamber. According to literature [30], vacuum drying is generally used at much lower pressure (< 0.1 Pa $\equiv 10^{-3}$ mBar) for much longer periods of time (24 hours to 1 week) to remove water from a specimen of similar size. It is assumed that the RH in the specimen is changed very rapidly at the observed (exposed) surface. Thus, the measured deformations are mainly the effects in the top layer of the specimens. This illustrates that large gradients occur over the thickness of the specimen.

On each test day, the specimens for that day were taken out of the climate cabinets and stored in a specimen container with designated locations for each specimen to avoid mix-ups during transport and testing. At the end of a day of testing, the specimens were placed back in the climate cabinets and stored. The duration of storage was about 15 weeks for the ESEM specimens and about 10 weeks for the optical microscopy specimens. Test dates are given in Appendix F.2 for ESEM tests and in Appendix G.2 for optical microscopy tests.

The captured images are saved as TIFF files, in order to store the images in an uncompressed state and without introducing noise[5] in the image due to image compression. For DIC analysis, noise in the images should be avoided.

4.6 Summary of specimen characteristics

In Table 4.5, an overview is given of test specimens that are used in this research and the conditions these specimens are exposed to.

XRD specimens

Two series of XRD tests were carried out. One series before exposure and one series after exposure to the environmental loads. The specimens in both series of XRD tests are given in Table 4.6. The specimens for XRD tests have dimensions of 10x10x10 mm^3.

ESEM and optical microscopy

Two series of microscopy tests are carried out. In each test series 32 specimens are analysed. In total 2 x 32 = 64 specimens were prepared.

---

[5] Noise obscures features in an image (speckles, deformities).

Table 4.5: List of different specimens for XRD tests on non-exposed specimens

#	Specimen details	Material
1	CEM I	Mortar
2	CEM I	Concrete
3	CEM III/B	Mortar
4	CEM III/B	Concrete
5	CEM III/B + FA	Mortar
6	CEM III/B + FA	Concrete
7	CEM III/C	Mortar
8	CEM III/C	Concrete

Table 4.6: List of specimens for microscopy tests and exposed XRD tests

#	Label	Binder	Material	Storage condition*
1	C1M1	CEM I	Mortar	Dry
2	C1M2			Wet
3	C1M3			Temp
4	C1M4			Wet-dry
5	C1C1	CEM I	Concrete	Dry
6	C1C2			Wet
7	C1C3			Temp
8	C1C4			Wet-dry
9	C2M1	CEM III/B	Mortar	Dry
10	C2M2			Wet
11	C2M3			Temp
12	C2M4			Wet-dry
13	C2C1	CEM III/B	Concrete	Dry
14	C2C2			Wet
15	C2C3			Temp
16	C2C4			Wet-dry
17	C3M1	CEM III/B + FA	Mortar	Dry
18	C3M2			Wet
19	C3M3			Temp
20	C3M4			Wet-dry
21	C3C1	CEM III/B + FA	Concrete	Dry
22	C3C2			Wet
23	C3C3			Temp
24	C3C4			Wet-dry
25	C4M1	CEM III/C	Mortar	Dry
26	C4M2			Wet
27	C4M3			Temp
28	C4M4			Wet-dry
29	C4C1	CEM III/C	Concrete	Dry
30	C4C2			Wet
31	C4C3			Temp
32	C4C4			Wet-dry

*: storage conditions are given in Table 4.2

4.7 Theoretical backgrounds – moisture in cementitious materials

Below, the physics behind volume changes as a result of humidity changes in the microstructure is described. This is useful for the interpretation of microscopic scale deformations in cement paste.

4.7.1 Kelvin & Young-Laplace equations

With the Kelvin equation and the Young-Laplace equation, the size of filled pores at a certain equilibrium RH and the pore pressure are calculated.

Kelvin equation: $ln\frac{p_v}{p_{sat}} = -\frac{2\cdot C\cdot\gamma\cdot V_l}{R\cdot T}$ (4.1)

in which p_v and p_{sat} are the actual vapour pressure and the saturation vapour pressure (p_v / p_{sat} is the relative humidity) respectively, C is the mean curvature of the liquid meniscus (the radius of the meniscus is 1/C), γ is the liquid/vapour surface tension (0.0728 N/m), V_l is the liquid molar volume (0.018 l/mol), R the ideal gas constant (8.314 J/K/mol) and T the absolute temperature (283 K during the test cycles).

Young-Laplace equation: $p_c = \frac{2\cdot\gamma\cdot cos\theta}{r_c}$ (4.2)

in which p_c is the capillary pressure, γ is the liquid/vapour surface tension (0.0728 N/m), Θ is the wetting angle of water to cementitious material (about 20° ≈ 0.35 rad) and r_c is the pore radius.

For a humidity range from 50% RH to 100% RH, pore pressures and pore radii calculated with Eq. 4.1 and 4.2 are given in Table 4.7. In this RH range, moisture changes occur mainly in capillary pores, as indicated in Figure 4.13 [31]. With the Kelvin and Young-Laplace equations a capillary pressure of about 91 MPa is calculated at 50% RH and a temperature of 283 K. As a reference, Wittmann calculated capillary pressures of a similar order of magnitude in [32], Zhou et al simulated capillary pore pressures of equal magnitude in [33]. The capillary pressure decreases rapidly with increasing RH. The difference between the magnitude of the pore pressure at 50% RH and 100% RH indicates that the microstructure of a material is subjected to great stresses upon drying. At 100% RH (saturation) and a temperature of 283 K, the capillary pressure is 0 (the pore pressure becomes hydrostatic). The radius of menisci in pores ranges from 1.6 nm to ∞ over the RH range of 50% RH to 100% RH.

Table 4.7: Relative humidity, pore pressure and pore radii, calculated with Kelvin (Eq. 2.1) and Young-Laplace (Eq. 2.2) equations (Temperature T = 283 K).

Relative humidity [%]	Pore pressure [MPa]	Pore radius [nm]	Radius of meniscus [nm]
50	90.6	1.5	1.6
70	46.6	2.9	3.1
80	29.2	4.7	5
90	13.8	9.9	10.6
95	6.7	20.4	21.7
99	1.3	104	111
99.99	0.01	10,446	111,138

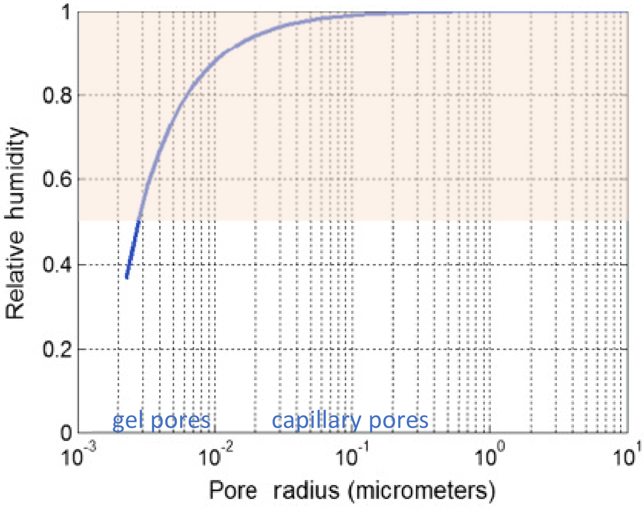

Figure 4.13: Relationship between pore diameter and equilibrium moisture content in pores (adapted from [31]). The coloured area indicates the RH range that was used in this study.

4.7.2 Effect of temperature changes on measurements

In the optical microscopy test cycles, RH in the direct vicinity of the specimen is controlled by changing the temperature of the specimen. For reaching high RH, the temperature of the specimen and its direct surroundings is lowered. To increase RH from 50% RH to 100% RH, a temperature decrease of 10-12°C is required. As a result of temperature changes, the volume of the solid cement paste changes with 0.01 ‰/°C (the coefficient of thermal expansion of cement paste) and the volume of the free water in the capillary pores changes with 0.069 ‰/°C. Thus, the volume change of the free water is about 7 times larger than the volume change of the solids. This leads to a redistribution of water in the specimens. These effects were shown by Wyrzykowski et al. [34] among other researchers [33,35-37]. The redistribution of gel and interlayer water leads to relatively large local deformations, as also found in [34].

In optical microscopy tests the temperature is changed throughout the specimen. Therefore, volume changes occur over the whole thickness of the specimen. Although the absolute volume change is small compared to the expected mean strains (and very small compared to local strains), RH changes affect the whole thickness of the optical microscopy specimens (especially at high RH) contrary to the ESEM specimens where the RH changes mainly affect the top layer.

5 Changes in the mineralogy caused by climatic conditions

Abstract

In this chapter, the performed experimental X-ray diffractometry (XRD) tests are described. The aim of the XRD tests is to qualitatively identify differences between the mineralogy of non-exposed concrete and mortar specimens and concrete and mortar specimens exposed to climatic conditions. In the XRD tests, the mineralogy of cement paste in mortar and concrete specimens is analysed. Exposed specimen cubes with dimensions of 10 x 10 x 10 mm³ are subjected to simulated climatic conditions as mentioned in section 4.3, Table 4.2. The mineralogy in the specimens is determined by means of qualitative XRD. The test specimens are retrieved from the same existing structures and laboratory specimens used in chapters 7 and 8.

It is anticipated that changes in the mineralogy of the cement paste can be found by comparing the mineralogy of exposed and non-exposed material. From the XRD measurements, the products from the hydration reaction of binder and water can be identified. During the time the specimens are exposed to climatic conditions, unhydrated binder particles will hydrate further. Ongoing hydration – a desirable process – can be compared to autonomous ageing and it can be enhanced by the exposure conditions with respect to available moisture among others. It is anticipated that the effect of ongoing hydration on the mineralogy of the cement paste can be determined from the XRD measurements. The climatic conditions to which the specimens are exposed are expected to cause carbonation in the specimens. Carbonation of cementitious material can be a degradation mechanism with respect to reinforcement corrosion. With regard to the density of the microstructure of cementitious material with CEM I binder, carbonation is not per se detrimental because the microstructure becomes denser. Carbonation occurs as a consequence of (prolonged) exposure to atmospheric carbon dioxide and the change of the material structure causes a change of performance. Other differences found between the mineralogy of non-exposed and exposed specimens, or between specimens exposed to different climatic conditions, are interpreted on the basis of the associated reactions.

In this chapter, first the test method is described. In the next section, the measurements and the results are discussed, which are evaluated and discussed in the consecutive section. In the last section, the concluding findings of the XRD tests are presented.

5.1 Methodology and techniques

X-ray diffractometry is used for the characterisation of the mineralogy in fine-grained specimens of (partly) crystalline materials. The principle of the method is based on the diffraction of X-rays by crystal structures. Reference diffraction patterns are stored in an international database, managed by the International Centre for Diffraction Data (ICDD). In the case of cementitious materials and other anorganic materials, the powder diffraction file (PDF) is generally used for the identification of the minerals present in the specimen.

A material specimen (usually less than 1 g of dry powder) is put into a specimen holder and scanned with the X-ray beam. During the measurement, the specimen holder rotates to increase the number of crystallites that contribute to the measured pattern.

From the measured diffraction pattern, the available phases in the material specimen are identified by comparing the peaks and intensities of the measurement with peaks and intensities from the PDF. This comparison is performed with appropriate software complemented by a manual analysis. The major peaks (i.e. peaks with high intensities) in the data should all be listed in the reference pattern, otherwise the identification is not valid.

The choice of qualitative rather than quantitative analysis stems from the search for the occurrence of different minerals in exposed and unexposed specimens. It was anticipated that additional constituents would be found compared to the reference. In general, the origin of those constituents can be deduced from the constituents already present in the reference, the constituents found and the conditions.

For the comparison of the mineralogy from exposed and non-exposed material, two test series are carried out: an analysis shortly after specimen preparation (at $t = 0$ weeks) and an analysis after prolonged exposure (at $t \geq 37$ weeks) to climatic conditions according to Table 4.2 in section 4.3.

5.2 Measurements and results

The following minerals were included in the comparison between the different XRD analyses.

Table 5.1: Characterization of minerals considered in the analysis

Mineral	Images		Description
	Macro	(E)SEM	
Quartz		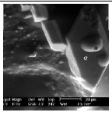	Silicate mineral, originates from (mainly fluvial) aggregates in concrete and mortar. Forms 6-sided prisms.
Portlandite		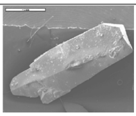	Calcium hydroxite. One of the reaction products of Portland cement clinker and water. Forms hexagonal plates.
Dolomite		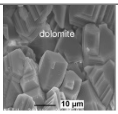	Calcium magnesium carbonate, originates from binder. Limited contribution to development of structural strength. Forms tabular crystals or prisms.
Ettringite		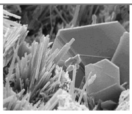	Calcium sulfo-aluminate that originates from Portland cement clinker. Forms needles or plates.
Calcite		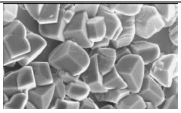	Calcium carbonate, product of reaction between Portlandite and CO_2. Rhombohedral structure.
Vaterite	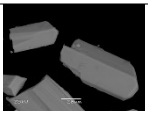	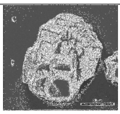	Metastable polymorph of calcium carbonate. Highly soluble in water. Forms fine fibers or complex rhombohedral structures.
Albite		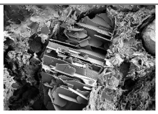	Feldspar mineral. Originates from aggregates. Tabular crystals, granular.
Montmorillonite-22A		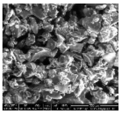	Clay mineral (phyllosilicate). Plate-shaped particles. Swells upon water adsorption. Originates from fines in aggregate.
Chlorite-serpentine (NR)		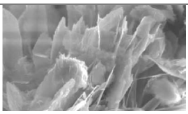	Phyllosilicate mineral. Originates from aggregates. Foliated masses or flakes.

5.2.1 Reference specimens

As mentioned in section 4.6, one specimen of each material-binder combination is used for XRD analysis[6] before exposure to climatic conditions. The specimens from mortar beams are analysed shortly after the beams had cured for 28 days. At that point in time, the specimens from existing concrete structures are analysed as well. The XRD analysis and identification of minerals of the first set of specimens is hereafter called the *reference analysis*. The other four sets of specimens are stored in the four different climate conditions.

The identified minerals in the reference analysis and their chemical composition are given in Table 5.2 and Table 5.3. The XRD measurement showed high intensities on the quartz peaks, illustrating the presence of inert aggregates (i.e. sand, gravel) in the specimens. These high peaks may hinder the detection of minor constituents.

Table 5.2: Identified minerals in reference analysis of specimens from existing concrete structures, shortly after gaining drilled cores.

Mineral	Chemical composition	CEM I (1999)	CEM III/B (1997-1998)	CEM III/B + FA (1985)	CEM III/C (2014-2015)
Quartz	SiO_2	🟩	🟩	🟩	🟩
Portlandite	$Ca(OH)_2$	🟩		🟩	
Dolomite	$CaMg(CO_3)_2$	🟩	🟩	🟩	🟩
Ettringite	$Ca_6Al_2(SO_4)_3(OH)_{12}(H_2O)_{24}$	🟩	🟩	🟩	🟩
Calcite	$CaCO_3$		🟩		🟩
Vaterite	$CaCO_3$				
Albite	$Na(AlSi_3O_8)$				
Montmorillonite-22A	$Na_{0.3}(Al,Mg)_2Si_4O_{10}(OH)_2 \cdot 8H_2O$				
Chlorite-serpentine (NR)	$(Mg,Al)_6(Si,Al)_4O_{10}(OH)_8$				

Except minerals that indicate the presence of aggregates, the reference specimens showed the presence of both Portlandite and ettringite, except for the specimens from existing concrete structures with CEM III/B and CEM III/C as binder. In those specimens

---

[6] For this research, the minerals in the powder specimens are qualitatively identified. The identification was performed by the Department of Materials Science and Engineering at Delft University of Technology. In Appendix F, the XRD measurements and the identifications of both the reference specimens and the specimens that were exposed to climatic conditions are given.

also calcite is found, which originates from carbonation of the cement paste. Carbonation in the reference specimen likely originates from carbonation of the drilled cores during storage prior to specimen preparation. In none of the specimens from mortar beams calcite was identified. In the specimen from the mortar beam with CEM III/C as binder, no Portlandite was identified, which can be explained by the high slag content in the binder. The dolomite in the mortar specimens originates from the binder and not from the aggregate because NEN-EN Standard sand was used for the aggregate in the mortar beams.

Table 5.3: Identified minerals in reference identification specimens from mortar beams, at an age of 28 days.

Mineral	Chemical composition	CEM I	CEM III/B	CEM III/B + FA	CEM III/C
Quartz	SiO_2	🟩	🟩	🟩	🟩
Portlandite	$Ca(OH)_2$	🟩	🟩	🟩	
Dolomite	$CaMg(CO_3)_2$	🟩	🟩	🟩	🟩
Ettringite	$Ca_6Al_2(SO_4)_3(OH)_{12}(H_2O)_{24}$	🟩	🟩	🟩	🟩
Calcite	$CaCO_3$				
Vaterite	$CaCO_3$				
Albite	$Na(AlSi_3O_8)$				
Montmorillonite-22A	$Na_{0.3}(Al,Mg)_2Si_4O_{10}(OH)_2 \cdot 8H_2O$				
Chlorite-serpentine (NR)	$(Mg,Al)_6(Si,Al)_4O_{10}(OH)_8$				

5.2.2 Exposed specimens compared to reference specimens

In the following section the mineralogy of the concrete and mortar specimens exposed to simulated climatic conditions will be compared with the mineralogy of the reference specimen. The observed differences are summarized in Table 5.4 **-** Table 5.10**.**

5.2.2.1 CEM I – Mineralogy of exposed concrete and mortar specimens compared to reference specimens (Table 5.4)

Specimens with CEM I as binder are exposed for 37 weeks to four simulated climate conditions. The identified minerals in the reference specimen and the specimens exposed to climatic conditions are summarized in Table 5.4. In all specimens that were exposed to climatic conditions (specimens from existing concrete and mortar beams), the same minerals are identified. Moreover, in all specimens exposed to climatic conditions calcite is identified, whereas this mineral is not found in the reference specimen. The presence of calcite in the exposed specimen indicates that in those specimens carbonation occurred. No further changes are identified between the reference specimens and the exposed specimens. Note that the specimen that was kept in wet conditions contained calcite as a result of carbonation despite being stored in 100% relative humidity.

Table 5.4: Comparison of identified minerals in reference analysis with identified minerals in specimens after 37 weeks of exposure to climatic conditions – specimens of existing concrete and specimens of mortar beams with CEM I, all four climatic conditions.

Mineral	Chemical composition	CEM I (Ref. - Table 5.2, Table 5.3)	CEM I Dry stored	CEM I Wet stored	CEM I Temperature cycles	CEM I Wet-dry stored
Quartz	SiO_2	🟩	🟦	🟦	🟦	🟦
Portlandite	$Ca(OH)_2$	🟩	🟦	🟦	🟦	🟦
Dolomite	$CaMg(CO_3)_2$	🟩	🟦	🟦	🟦	🟦
Ettringite	$Ca_6Al_2(SO_4)_3(OH)_{12}(H_2O)_{24}$	🟩	🟦	🟦	🟦	🟦
Calcite	$CaCO_3$		🟦	🟦	🟦	🟦
Vaterite	$CaCO_3$					
Albite	$Na(AlSi_3O_8)$					
Montmorillonite-22A	$Na_{0.3}(Al,Mg)_2Si_4O_{10}(OH)_2\cdot 8H_2O$					
Chlorite-serpentine (NR)	$(Mg,Al)_6(Si,Al)_4O_{10}(OH)_8$					

5.2.2.2 CEM III/B - Mineralogy of exposed concrete and mortar specimens compared to reference specimens

The following is a comparison between the reference analysis and the analysis of exposed specimens of *concrete* and *mortar* containing CEM III/B. Specimens exposed to climatic conditions were kept for 38 weeks in simulated climatic conditions. The minerals that were identified in specimens that were exposed to climatic conditions are shown in Table 5.5 (concrete) and Table 5.6 (mortar).

Specimens from existing concrete structures (Table 5.5)

The specimens from concrete with CEM III/B as binder were taken from drilled cores out of a separation wall inside a traffic tunnel. The cores were extracted from the tunnel in October 2019 and the cores were stored until specimen preparation in October 2020. The identification of calcite in the reference concrete specimen (Table 5.2) indicates that the concrete was carbonated before the XRD measurements were performed. The drilled cores for this investigation were taken at the same time as the drilled cores for a material investigation of the concrete in the tunnel [38]. This material investigation showed, that over a period of about 22 years, the carbonation front had penetrated to a depth of about 10-18 mm from the concrete surface. The evidence of carbonation found in the reference concrete specimen is therefore from carbonation of the drilled cores during storage prior to preparation of the specimen cubes. Because calcite was identified in the reference specimen, it was also found in all specimens exposed to simulated climatic conditions (as shown in Table 5.5).

Besides calcite, vaterite was identified in the specimen taken from the specimen that was kept in a dry environment. Vaterite is a metastable polymorph of $CaCO_3$ that is regularly formed in cement paste with binder having a high slag content [39]. When vaterite comes into contact with water, it dissolves and converts to calcite.

Portlandite was identified neither in the reference specimen nor in any of the specimens exposed to climatic conditions. It is highly unlikely that no Portlandite is present in the specimens at all. As mentioned earlier in section 5.1, in a qualitative XRD analysis, peaks emerge from the abundant constituents present. Therefore, Portlandite may still be present in the specimens, but only in very low amounts. The peaks for the identification of Portlandite coincide with peaks of other constituents, especially when only small amounts of Portlandite are present. However, Portlandite can either be consumed by carbonation of the cement paste or by ongoing slag hydration, which explains why it is less abundant.

In the analysis of the reference specimen, dolomite was present as a minor constituent. In the specimen that was exposed to temperature cycles, peak counts for dolomite were significantly higher than in the reference analysis. This may have occurred due to the presence of an accidental dolomite aggregate grain in the specimen.

Albite was not identified in the reference specimen. Albite is an inert feldspar mineral that originates from aggregates. In all specimens exposed to climatic conditions albite was identified. Although, contrary to the reference analysis, albite was present in the exposed specimens, the presence of albite is not discussed any further as it is not a reaction product of any change in the mineralogy of the cement paste.

Table 5.5: Identification of CEM III/B concrete specimens after 38 weeks of exposure to climatic condition.

Mineral	Chemical composition	CEM III/B (Reference - Table 5.2)	CEM III/B Dry stored	CEM III/B Wet stored	CEM III/B Temperature cycles	CEM III/B Wet-dry stored
Quartz	SiO_2	🟩	🟦	🟦	🟦	🟦
Portlandite	$Ca(OH)_2$					
Dolomite	$CaMg(CO_3)_2$	🟩			🟦	
Ettringite	$Ca_6Al_2(SO_4)_3(OH)_{12}(H_2O)_{24}$	🟩	🟦	🟦	🟦	🟦
Calcite	$CaCO_3$	🟩	🟦	🟦	🟦	🟦
Vaterite	$CaCO_3$		🟦			
Albite	$Na(AlSi_3O_8)$		🟦	🟦	🟦	🟦
Montmorillonite-22A	$Na_{0.3}(Al,Mg)_2Si_4O_{10}(OH)_2{\cdot}8H_2O$					
Chlorite-serpentine (NR)	$(Mg,Al)_6(Si,Al)_4O_{10}(OH)_8$					

Specimens from mortar beams (Table 5.6)

In all specimens from mortar beams with CEM III/B as binder that were exposed to climatic conditions, calcite was identified, whereas calcite was not identified in the reference specimen. This indicates that in all mortar specimens exposed to climatic conditions carbonation occurred. In every specimen that was exposed to climatic conditions vaterite was identified, except in the specimen that was stored in wet conditions. Because of the high solubility of vaterite, the mineral dissolves in water-filled pores and precipitates as calcite upon drying.

In the reference specimen, Portlandite was identified, while in none of the exposed specimens Portlandite was identified. In combination with the presence of calcite, this indicates carbonation and ongoing hydration. The strongest peaks that identify Portlandite were not found in the XRD diffractograms, therefore it can be concluded that Portlandite was depleted to a very small amount in the exposed specimens, as can be seen in Figure 5.1.

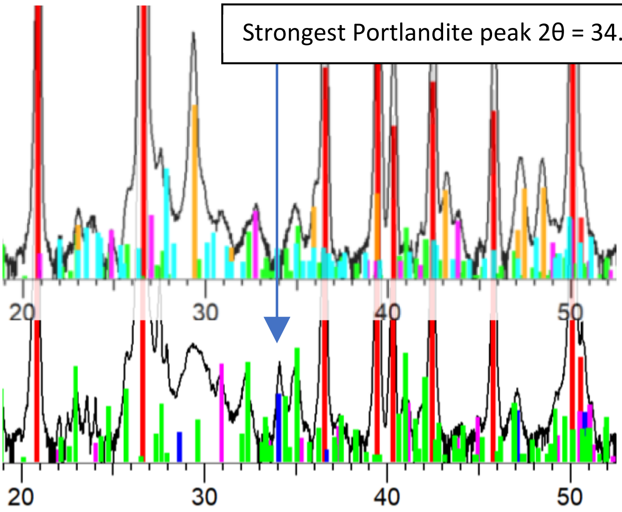

Strongest Portlandite peak 2θ = 34.09°

Diffractogram of exposed specimen

Diffractogram of reference analysis

Figure 5.1: Peaks in diffractograms of CEM III/B mortar specimens.

Table 5.6: Identification of CEM III/B ***mortar*** *specimens after 38 weeks of exposure to climatic conditions. Input marked with "m" is manually identified.*

Mineral	Chemical composition	CEM III/B (Reference Table 5.3)	CEM III/B Dry stored	CEM III/B Wet stored	CEM III/B Temperature cycles	CEM III/B Wet-dry stored
Quartz	SiO_2	🟩	🟦	🟦	🟦	🟦
Portlandite	$Ca(OH)_2$	🟩				
Dolomite	$CaMg(CO_3)_2$	🟩	m	m	m	m
Ettringite	$Ca_6Al_2(SO_4)_3(OH)_{12}(H_2O)_{24}$	🟩	🟦	🟦	🟦	🟦
Calcite	$CaCO_3$		🟦	🟦	🟦	🟦
Vaterite	$CaCO_3$		🟦		🟦	🟦
Albite	$Na(AlSi_3O_8)$		🟦	🟦	🟦	🟦
Montmorillonite-22A	$Na_{0.3}(Al,Mg)_2Si_4O_{10}(OH)_2{\cdot}8H_2O$					
Chlorite-serpentine (NR)	$(Mg,Al)_6(Si,Al)_4O_{10}(OH)_8$					

Dolomite was identified in the reference specimen, while in none of the specimens that were exposed to climatic conditions dolomite was identified. In the diffractograms of the exposed specimens, however, the strongest peaks that would identify brucite (one of the reaction products from the reaction of dolomite and Portlandite) were not found. With the help of the identification method according to the Hanawalt search manual [40] it was found, that the diffractograms *do* show the strongest peak of dolomite (at $2\theta = 30.96°$) as well as the second and third strongest peaks. Because dolomite was identified in this way, it is mentioned in the identification tables with “m”. Since only minor amounts of dolomite are present in the specimens the intensity peaks often coincide with other peaks.

Vaterite was found in all specimens that were exposed to climatic conditions, except in the specimen that was exposed to a wet environment. Albite was not identified in the reference analysis, but it was found in all exposed specimens. Albite is an inert feldspar mineral and therefore not further discussed.

5.2.2.3 CEM III/B + FA - Mineralogy of exposed specimens compared to reference specimens

The following is a comparison between the analysis of the reference specimen and of the exposed concrete and mortar specimens made from CEM III/B + FA. Specimens exposed to climatic conditions were kept for 39 weeks in simulated climatic conditions. The minerals that were identified in specimens that were exposed to climatic conditions are shown in Table 5.7 (concrete) and Table 5.8 (mortar).

Specimens from existing concrete structures (Table 5.7)

The drilled cores were extracted from the existing structure in October 2019 and the cores were stored until specimen preparation in October 2020.

In the analysis of the specimen that was exposed to a wet environment, the same minerals were identified as in the reference analysis. Calcite was identified in the analysis of all specimens that were exposed to climatic conditions, which indicates carbonation. Vaterite was found in all specimens that were exposed to climatic conditions, except in the specimen that was exposed to a wet environment.

Albite was identified in the analysis of all specimens that were exposed to climatic conditions.

In the analysis of the specimen that was kept in a dry environment, montmorillonite was identified. This is a clay mineral that originates from the fines in the aggregate. In the analysis of the specimens that were kept in alternately wet-dry environment chlorite-serpentine is identified, which is a phyllosilicate that also originates from aggregates. Both these minerals are considered as artefacts and, therefore, not further discussed.

In all analysis of specimens that were exposed to climatic conditions Portlandite was identified, except for the specimen that was kept in dry conditions. Upon closer consideration of the diffractograms, it turned out that with manual identification, Portlandite was identified in the specimen kept in dry conditions. It appears to have become less abundant as in the reference analysis, but the strongest peaks that identify Portlandite can be distinguished.

Calcite was identified in specimens that were exposed to climatic conditions. The presence of calcite indicates carbonation, however, the presence of Portlandite indicates that the pH in the pore solution is still relatively high.

In the reference specimen dolomite was identified, while in none of the specimens that were exposed to climatic conditions except for the specimen that was stored in 100% RH, dolomite was found. Upon closer examination of the diffractograms, it turned out that dolomite was present in the exposed specimens as well. Vaterite was present in all exposed specimens except for the wet stored specimen.

Table 5.7: Identification of CEM III/B + FA concrete specimens after 39 weeks of exposure to climatic conditions. Input marked with "m" is manually identified.

Mineral	Chemical composition	CEM III/B + FA (Reference Table 5.2)	CEM III/B + FA Dry stored	CEM III/B + FA Wet stored	CEM III/B + FA Temperature cycles	CEM III/B + FA Wet-dry stored
Quartz	SiO_2	🟩	🟦	🟦	🟦	🟦
Portlandite	$Ca(OH)_2$	🟩	🟦 m	🟦	🟦	🟦
Dolomite	$CaMg(CO_3)_2$	🟩	🟦 m	🟦	🟦 m	🟦 m
Ettringite	$Ca_6Al_2(SO_4)_3(OH)_{12}(H_2O)_{24}$	🟩		🟦	🟦	🟦
Calcite	$CaCO_3$		🟦	🟦	🟦	🟦
Vaterite	$CaCO_3$		🟦		🟦	🟦
Albite	$Na(AlSi_3O_8)$		🟦	🟦	🟦	🟦
Montmorillonite-22A	$Na_{0.3}(Al,Mg)_2Si_4O_{10}(OH)_2{\cdot}8H_2O$		🟦			
Chlorite-serpentine (NR)	$(Mg,Al)_6(Si,Al)_4O_{10}(OH)_8$					🟦

Specimens from mortar beams (Table 5.8)

In the specimens that were exposed to climatic conditions, the same minerals as in the reference specimen were identified. Additionally, calcite and vaterite were identified in all specimens that were exposed to climatic conditions. Vaterite was not present in the specimen that was kept in wet conditions. The presence of calcite in the specimens that were exposed to climatic conditions indicates carbonation. Albite is found in the exposed specimens but not in the reference analysis. Albite is an inert feldspar mineral, and thus not further discussed.

In the reference specimens dolomite is present. Therefore, the presence of dolomite is also expected in the specimens that were exposed to climatic conditions, which is the case. In the specimen that was kept in dry conditions, dolomite was identified manually, the peaks that identify dolomite coincide with other peaks.

In both the reference specimen and in the specimens that were exposed to climatic conditions, Portlandite was identified. In all specimens that were exposed to climatic conditions calcite is present. The presence of calcite indicates carbonation. However, the presence of Portlandite indicates that the specimens are not yet carbonated to an extent that all the Portlandite is consumed.

Table 5.8: Identification of CEM III/B + FA mortar specimens after 39 weeks of exposure to climatic conditions. Input marked with "m" is manually identified.

Mineral	Chemical composition	CEM III/B + FA (Reference Table 5.3)	CEM III/B + FA Dry stored	CEM III/B + FA Wet stored	CEM III/B + FA Temperature cycles	CEM III/B + FA Wet-dry stored
Quartz	SiO_2	🟩	🟦	🟦	🟦	🟦
Portlandite	$Ca(OH)_2$	🟩	🟦	🟦	🟦	🟦
Dolomite	$CaMg(CO_3)_2$	🟩	🟦 m	🟦	🟦	🟦
Ettringite	$Ca_6Al_2(SO_4)_3(OH)_{12}(H_2O)_{24}$	🟩	🟦	🟦	🟦	🟦
Calcite	$CaCO_3$		🟦	🟦	🟦	🟦
Vaterite	$CaCO_3$		🟦		🟦	🟦
Albite	$Na(AlSi_3O_8)$		🟦	🟦	🟦	🟦
Montmorillonite-22A	$Na_{0.3}(Al,Mg)_2Si_4O_{10}(OH)_2\cdot 8H_2O$					
Chlorite-serpentine (NR)	$(Mg,Al)_6(Si,Al)_4O_{10}(OH)_8$					

5.2.2.4 CEM III/C - Mineralogy of exposed specimens compared to reference specimens

The following is a comparison between the reference analysis and the analysis of exposed specimens of concrete and mortar containing CEM III/C. Specimens exposed to climatic conditions were kept for 40 weeks in simulated climatic conditions. The minerals that were identified in the analysis of the specimens that were exposed to climatic conditions are shown in Table 5.9 (concrete) and Table 5.10 (mortar).

Specimens from existing concrete structures (Table 5.9)

The cores were extracted from the existing structure in November 2019 and the cores were stored until specimen preparation in October 2020.

In the reference analysis of the specimen, calcite was identified which indicates that carbonation occurred before preparation of the specimen cubes. Portlandite was not present in abundance in the reference specimen, therefore it was not expected in abundance in specimens that were exposed to climatic conditions. From the diffractograms of both the reference analysis and the analysis of the exposed specimens, it appears that only very limited amounts of Portlandite are present in the specimens.

Dolomite was identified in the reference analysis. Therefore is it expected in the specimens that were exposed to climatic conditions dolomite, which is the case.

Table 5.9: Identification of CEM III/C concrete specimens after 40 weeks of exposure to climatic conditions.

Mineral	Chemical composition	CEM III/C (Reference Table 5.2)	CEM III/C Dry stored	CEM III/C Wet stored	CEM III/C Temperature cycles	CEM III/C Wet-dry stored
Quartz	SiO_2	🟩	🟦	🟦	🟦	🟦
Portlandite	$Ca(OH)_2$					
Dolomite	$CaMg(CO_3)_2$	🟩	🟦	🟦	🟦	🟦
Ettringite	$Ca_6Al_2(SO_4)_3(OH)_{12}(H_2O)_{24}$	🟩		🟦	🟦	🟦
Calcite	$CaCO_3$	🟩	🟦	🟦	🟦	🟦
Vaterite	$CaCO_3$		🟦		🟦	🟦
Albite	$Na(AlSi_3O_8)$		🟦	🟦	🟦	🟦
Montmorillonite-22A	$Na_{0.3}(Al,Mg)_2Si_4O_{10}(OH)_2{\cdot}8H_2O$					
Chlorite-serpentine (NR)	$(Mg,Al)_6(Si,Al)_4O_{10}(OH)_8$					

Quartz, calcite and ettringite were identified in the reference analysis and also in the analysis of the specimens that were kept in a wet environment, exposed to temperature cycles and exposed to wet-dry cycles. In the analysis of the specimen that was kept in a dry environment, ettringite was not identified although it is expected to be present. Ettringite is most probably present in specimen that was kept in a dry environment, but only in very limited amounts. In the analysis of the specimens that were kept in a dry environment, exposed to temperature cycles and exposed to wet-dry cycles, also Vaterite was identified. In all specimens that were exposed to climatic conditions, albite was identified.

Specimens from mortar beams (Table 5.10)

In the reference analysis dolomite was identified. Dolomite was therefore expected to be identified in all specimens exposed to climatic conditions, which turned out to be the case. In all analysis of specimens that were exposed to climatic conditions, except the specimen that was kept in a wet environment, calcite and Vaterite were identified. In the analysis of the specimen that was kept in a wet environment only calcite was identified. The presence of calcite indicates carbonation of the cement paste. Albite was identified in all specimens exposed to climatic conditions, although it was not found in the reference analysis. Because albite is inert, this is not discussed any further.

Table 5.10: Identification of CEM III/C mortar specimens after 40 weeks of exposure to climatic conditions

Mineral	Chemical composition	CEM III/C (Reference Table 5.3)	CEM III/C Dry stored	CEM III/C Wet stored	CEM III/C Temperature cycles	CEM III/C Wet-dry stored
Quartz	SiO_2	🟩	🟦	🟦	🟦	🟦
Portlandite	$Ca(OH)_2$					
Dolomite	$CaMg(CO_3)_2$	🟩	🟦	🟦	🟦	🟦
Ettringite	$Ca_6Al_2(SO_4)_3(OH)_{12}(H_2O)_{24}$	🟩	🟦	🟦	🟦	🟦
Calcite	$CaCO_3$		🟦	🟦	🟦	🟦
Vaterite	$CaCO_3$		🟦		🟦	🟦
Albite	$Na(AlSi_3O_8)$		🟦	🟦	🟦	🟦
Montmorillonite-22A	$Na_{0.3}(Al,Mg)_2Si_4O_{10}(OH)_2{\cdot}8H_2O$					
Chlorite-serpentine (NR)	$(Mg,Al)_6(Si,Al)_4O_{10}(OH)_8$					

5.3 Discussion

The XRD tests were carried out with the aim to check whether changes had occurred in the mineralogy of the cement paste of specimens from concrete and mortar, after exposure of the material to climatic conditions. With a qualitative analysis, the mineralogy of specimens from concrete and mortar with different binder types that were exposed to simulated climate conditions is compared with the mineralogy of a reference analysis of specimens taken from the same material.

Found differences between the composition of the reference specimens and the specimens that were exposed to climate conditions indicate that the mineralogy of the material changes upon prolonged exposure to climatic conditions. Some of the changes are due to carbonation of the material while others indicate ongoing formation of hydration products.

In the specimens with CEM I only carbonation occurred. This indicates that material with CEM I is only limitedly affected by exposure to climatic conditions.

Dolomite was identified in all specimens from mortar beams and existing concrete. Therefore, it was expected in the specimens exposed to climatic conditions as well. In most material-binder combinations this is the case, except for the concrete specimens with CEM III/B. Dolomite was identified in the reference analysis of the CEM III/C concrete specimen. Only in the specimen with CEM III/B that was exposed to temperature cycles, dolomite was identified. Although the drilled cores with CEM III/B were taken from the same structural element in the existing structure, cores were taken at different locations within the structure (as described in Appendix B). The structural element is cast with a concrete mixture with a different recipe and therefore, differences occurred.

In a number of exposed specimens with slag-containing binders, vaterite was identified. The fact that vaterite was not found in the CEM I specimens is consistent with several sources, that vaterite can only form in material with CEM I binder under specific circumstances [41,42]. In material with slag-containing binders, however, formation of vaterite is very common [43].

In both the reference specimens and the specimens exposed to climatic conditions of CEM III/B and CEM III/C concrete and CEM III/C mortar, Portlandite was not found. There are several reasons for the absence of Portlandite in the exposed CEM III/B and CEM III/C specimens. On the one hand, Portlandite may have been consumed by carbonation processes or by slag hydration. Leaching of Portlandite is a mechanism that is common in concrete cracks where water flows through. Leaching of Portlandite is then evident at the crack surface as calcite is formed at the surface. No traces of leaching were visible on the test specimens, although calcite was found in the exposed specimens. However, leaching may not occur in dry stored specimens and specimens exposed to temperature cycles, although no Portlandite was found in those specimens either. Therefore it is plausible that the majority of the Portlandite is consumed by carbonation (or further carbonation in the case of the already carbonated CEM III/B and CEM III/C concrete specimens) and by the hydration of slag.

In all specimens that were exposed to climatic conditions, calcite was found, hence, carbonation occurred. In the reference analysis, carbonation was found in the specimens of concrete from existing structures with CEM III/B and CEM III/C. Carbonation occurs in cementitious material upon exposure to air. Because none of the specimens were directly exposed to air before specimen preparation, carbonation must have occurred during the period of storage. Even in the specimens that were wet stored, carbonation was found. A possible explanation therefore is, that the specimens were not kept under water, but in an environment with an RH = 100%. In that environment, air was also present. As the specimen was continuously wetted with an atomizer, the OH^- leached out, causing the pH in the specimen to drop. The CO_2 in the air dissolved in the water mist and penetrated with the moisture into the specimen and formed calcite together with the Ca^{2+} -ions. Due to the dimensions of the specimen cubes, the complete specimen may have become carbonated in relatively short time.

Question is, to what extent the described changes in the material can be attributed to common degradation processes in the material or to ageing. It goes without doubt, that none of the changes in the material are uncommon. Carbonation is a process that is very common in cementitious materials. Ongoing hydration of binders in the material is also a regular process in cementitious materials.

Although the abovementioned changes are common in cementitious materials, all of them depend either on the availability of moisture in pores or on the absence of moisture in pores. In the case of carbonation, the pore structure should be dry to let air (with CO_2) into the pores. In the case of ongoing hydration, water is required for the dissolution of binder and the formation of reaction products. In any of the aforementioned cases, the climatic conditions provide the circumstances for the changes in the material to take place.

In the specimens with CEM I, few changes were observed apart from carbonation. This can mean that either few changes took place or that reactions took place but the reaction products were not depleted. If the reactions between dolomite and Portlandite in the specimens with CEM I did not take place, the material changed in structure only due to carbonation. When the dolomite also reacted, significant changes occurred in the structure of the material, especially considering the volume change associated with the conversions in the material. However, a comparison of the XRD diffractograms of the reference analysis with the specimens that were exposed to climatic conditions shows that actually only calcite had joined and no other peaks were found in the diffractograms.

5.4 Conclusions

From the XRD tests it appeared that one of the alterations in the concrete and mortar specimens can be ascribed to exposure of cementitious materials to climatic conditions, i.e. carbonation and the reaction of dolomite with Portlandite. The other alteration in the material is ongoing hydration, however changes in the degree of hydration can not be determined in a qualitative analysis. Found alterations are very common for cementitious materials. Mentioned reactions are not linked to regular ageing processes.

Based on the findings, specimens with CEM I are less susceptible to a change in the mineralogy of the material than specimens with CEM III.

6 Measuring microscopic displacements in mortar and concrete

Resulting from exposure to changing relative humidity

In this chapter the microscopic scale tests are described. The aim of the microscopic scale tests is to visualise displacements in hardened cement paste of concrete and mortar specimens upon exposure to changing relative humidity (RH). Deformations are measured by comparing images taken with an electron microscope and by comparing images taken with an optical microscope. Displacements in the specimens are induced by exposing the specimen to different RH (wetting and drying) during the test cycles.

6.1 Image capturing – the principle

To gather information about the displacements in cementitious materials, images were taken from the microstructure of cement paste in concrete and mortar specimens. Figure 6.1 shows an example of an electron microscopy image. Consecutive images are taken at different RH. In four consecutive test cycles images of the specimens were gathered. Between the test cycles, the specimens were stored in climate chambers and exposed to simulated climatic conditions to visualise the influence of the climatic conditions on the displacements in the microstructure as described in chapter 4.

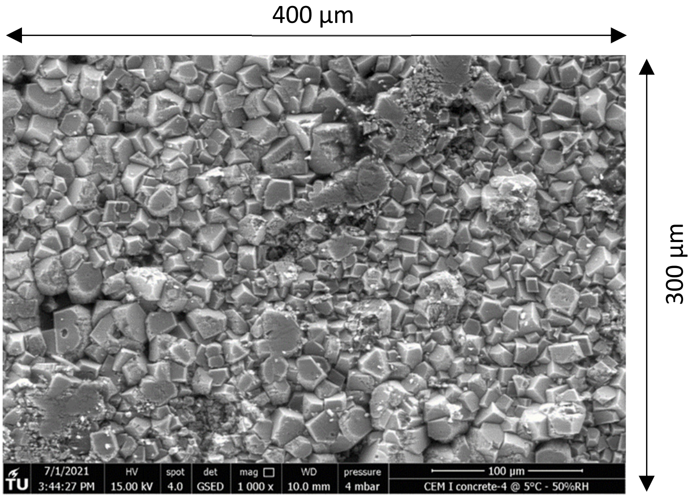

Figure 6.1: Example of an image of the cement paste in a concrete specimen, captured with an electron microscope.

The consecutive images from each test cycle were analysed with digital image correlation (DIC) software. In the DIC analysis, the deformations in the cement paste were calculated by comparing pixeled versions of consecutive images (Figure 6.2). In section 6.2.1 the principles of DIC analysis are described.

Image capturing in electron microscope compared to optical microscope

The optical microscopy images are not as sharp as the electron microscopy images. Firstly, because of the difference in depth-of-field between the ESEM and the optical microscope. Secondly because of the image capturing method. In the ESEM, the detector catches secondary electrons with the Gaseous Secondary Electron Detector (GSED). The electron beam is directed in a raster pattern over the specimen and each pixel of the image is detected separately. In the optical microscope the image (visible light) is captured with an ¼” image sensor of the complementary metal-oxide-semiconductor (CMOS) type.

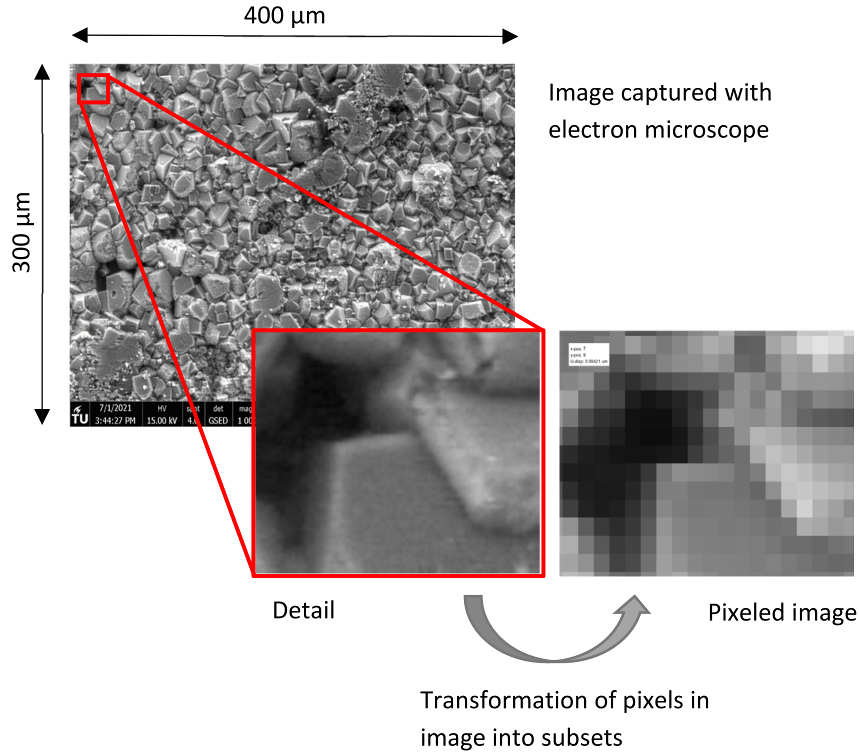

Figure 6.2: Example of pixeled image from image captured with electron microscope

Clarification with regard to figures in this chapter

For the interpretation of the results it should be noted here that the coordinate system as used in the analysis is not related to the orientation of the specimens in a structure or any kind of stratification in the material.

6.2 Data & data analysis

6.2.1 Digital Image Correlation

The displacements in the microstructure of the specimens are analysed with two-dimensional (2D) Digital Image Correlation (DIC) software. The principles behind DIC are described in-depth by LePage in [44].

With the help of DIC, differences between a series of images can be made visible. For DIC, the origin of differences is not relevant, as long as all the images in a series are taken from the same area, at the same magnification and all images are in focus. The images should be in grayscale, because the software uses the grayscale of a pixel in the image as an intensity parameter to identify groups of pixels in the image.

6.2.1.1 From digital image to subsets and displacements

The software uses characteristic points as markers in the image to track the displacements. These markers may be artificial (e.g.: a speckle pattern can be applied to the surface of the specimen) or, alternatively, the available characteristic points of the specimen are used. In this research, the surface of hardened cement paste is observed, in which ample characteristic points are available for tracking.

The images are divided into subsets as shown in Figure 6.3. The subsets consist of a user-defined number of pixels. In Figure 6.3, the subsets are chosen quite large for illustrative purposes.

The accuracy of the analysis depends on the size of the subsets and the step size, i.e. the distance between subset centres. These distances should be chosen small enough to ensure overlap between subsets, but not too small to avoid noisy output. Figure 6.4 and Figure 6.5 show the subset spacing and overlap. More on the accuracy of DIC is given in section 6.3.3.

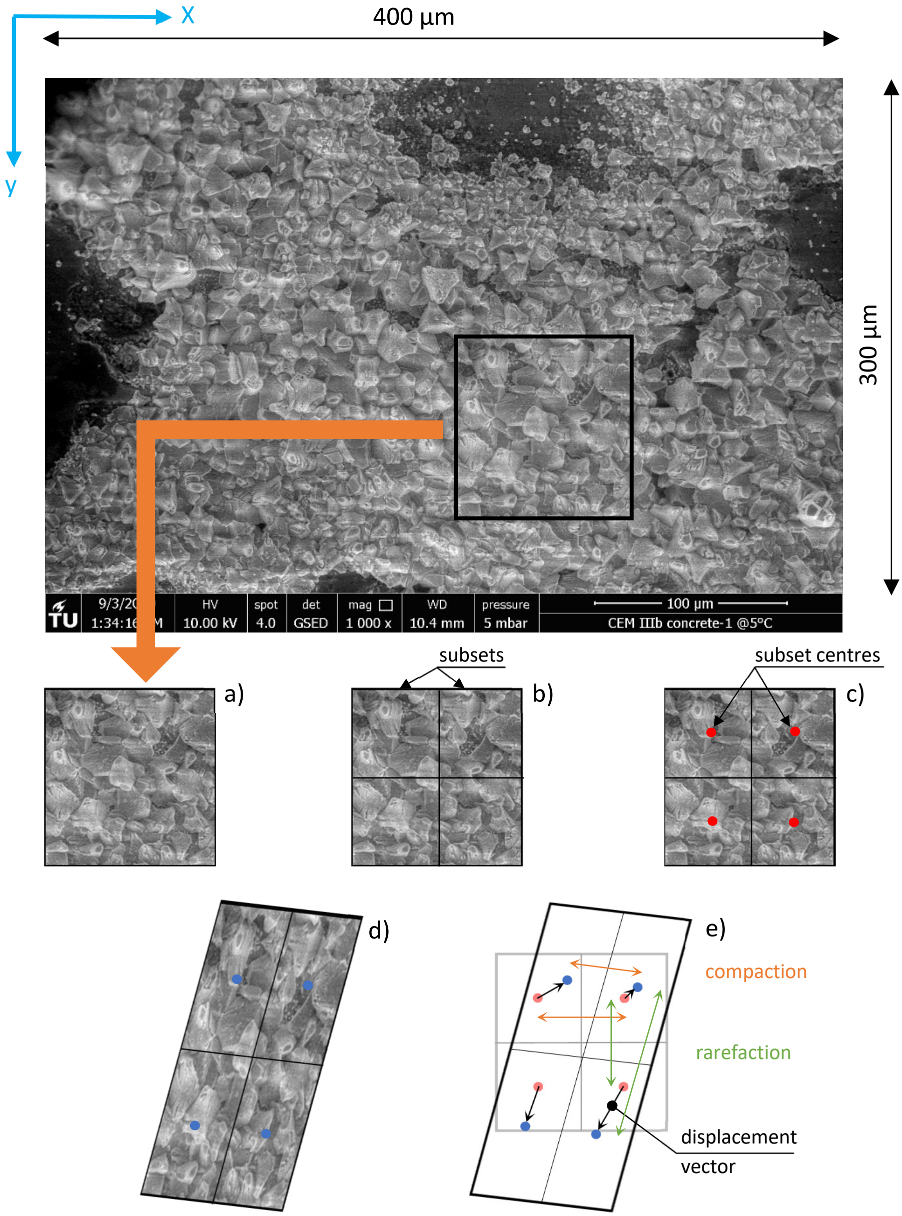

Figure 6.3: DIC analysis - principle of subsets, according to [2]: a) the morphology of the specimen is used as marker pattern, b) the image is subdivided into subsets, c) subset centre points (red dots) are defined, d) the deformed subsets are matched to the reference subsets, e) the displacements in X- and Y-direction are derived from the displacement vector of the subsets.

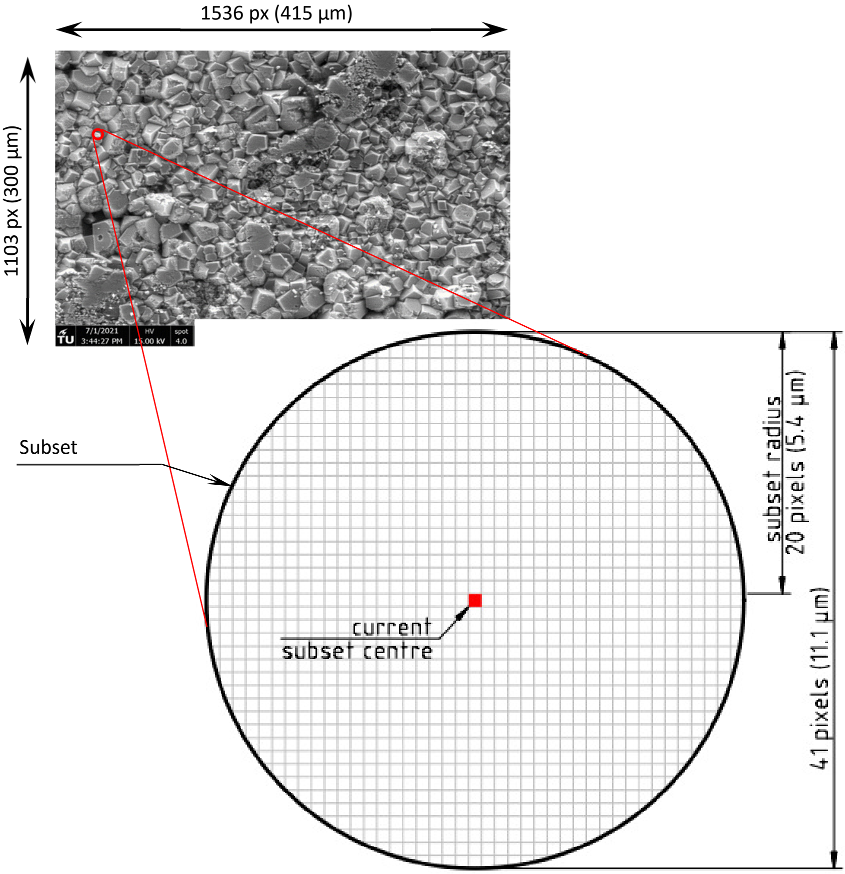

Figure 6.4: Subset radius. The red pixel represents the current subset centre.

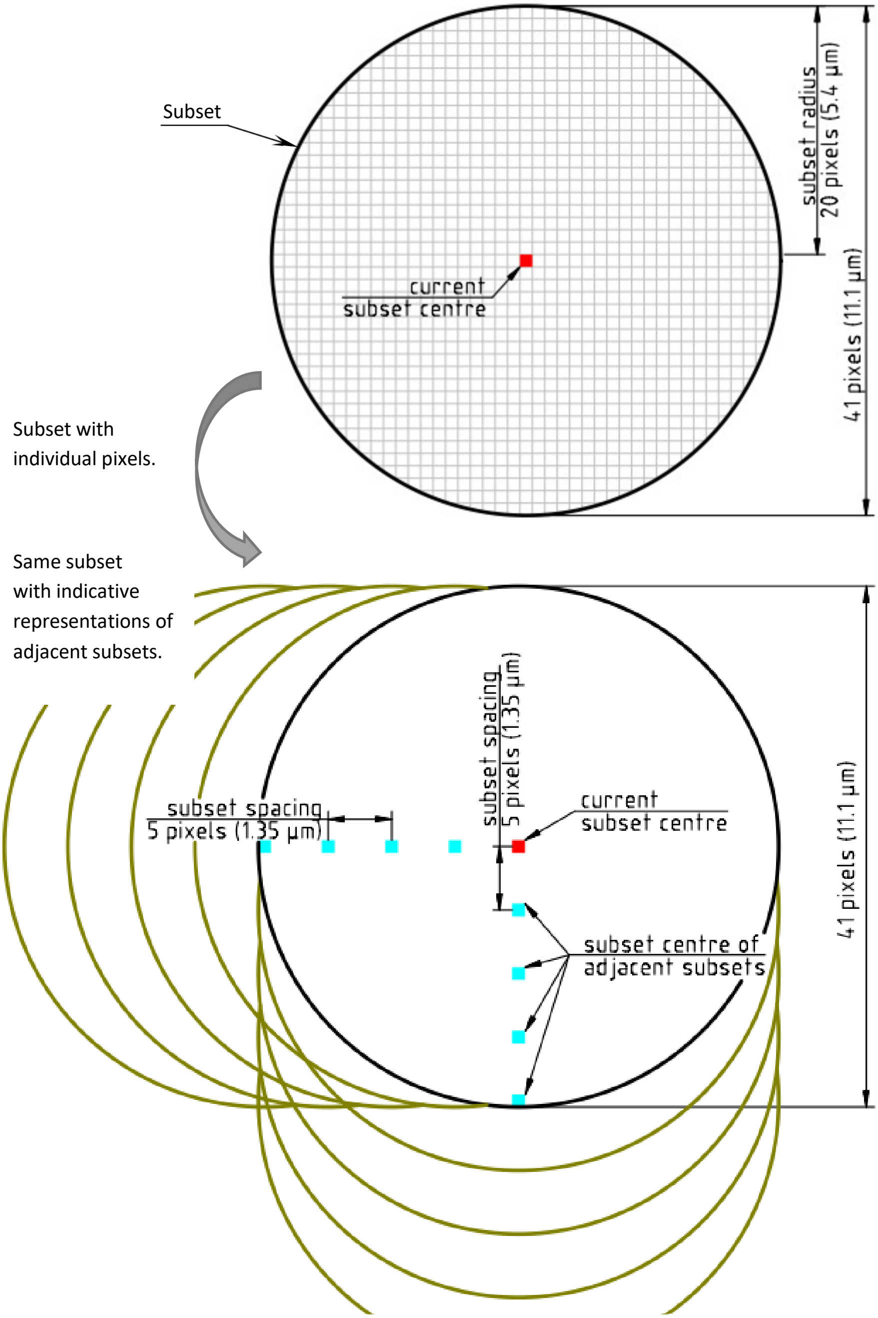

Subset with individual pixels.

Same subset with indicative representations of adjacent subsets.

Figure 6.5: Subset spacing and overlap of subsets. Every subset has an overlap of 4 subsets in X-direction and 4 in Y-direction. Red pixels indicates current subset centre, blue pixels indicate subset centres of adjacent subsets.

Before the displacements of subset centre points can be calculated, the displacements of the subset centres should be tracked first. DIC algorithms use combinations of linear transformations of the reference subset patterns to find a match between the reference subset pattern and the deformed subset pattern. The concept of linear transformations is shown in Figure 6.6. The combination of linear transformations of the reference subset pattern is called the warp function. Once a solution for a warp function *w* is found for a subset, it is used as starting variable for adjacent subsets to optimize calculation time.

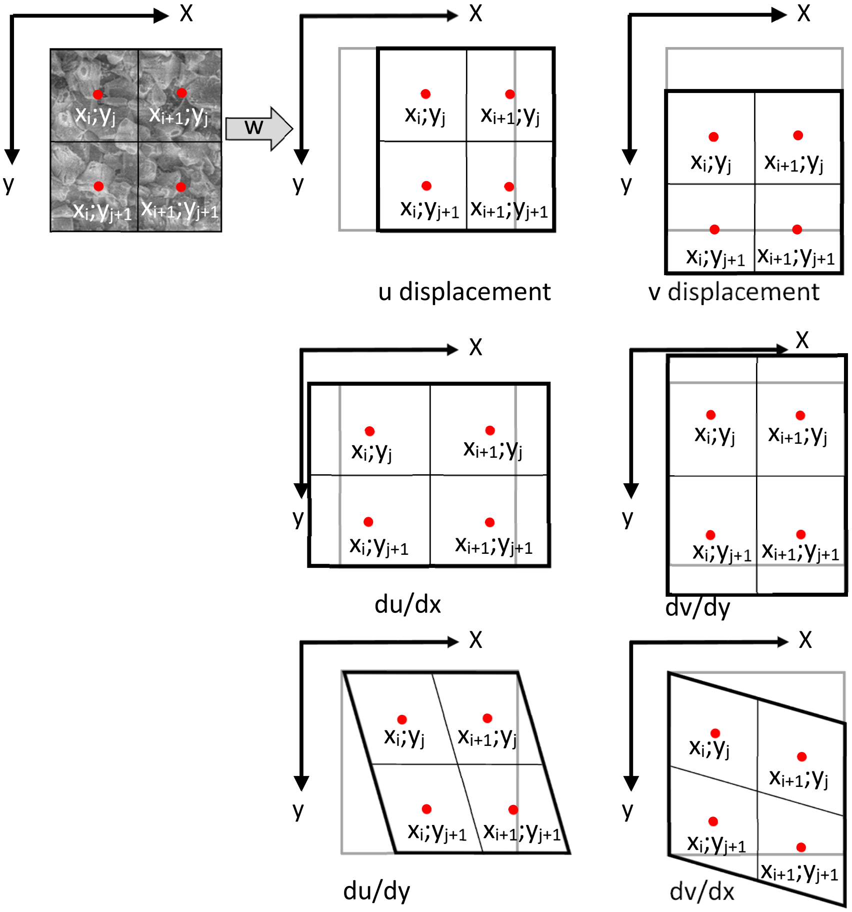

Figure 6.6: The displacements of the centre point of a subset (red dots) can be described by a linear combination of 6 linear transformations into a so-called warp function w.

The displacement of a subset centre point is calculated as a vector. Because a 2D analysis is used, the vector can be decomposed into X- and Y-directions in a Cartesian coordinate system. The displacements u and v in X- and Y-direction, respectively, with respect to their initial position, at each subset centre point in the area-of-interest (AOI) are stored in separate arrays for X- and Y-direction.

6.2.1.2 Determining compactions and rarefactions

The differences between the displacements of two adjacent points in the displacement matrix are called *compactions* in the case of a negative difference and *rarefactions* in the case of a positive difference. Analogous with engineering practice, compactions would indicate shrinkage and rarefactions would indicate elongation.

The physical meaning of compactions and rarefactions is explained in Figure 6.7. The dots in the figure represent the subset centres. With changing RH, the subset centres move, for example, towards each other in X-direction, while they move away from each other in Y-direction. The movement of the subsets relative to each other depends on the RH, the restraints in the microstructure and the stiffness of the phases in the material.

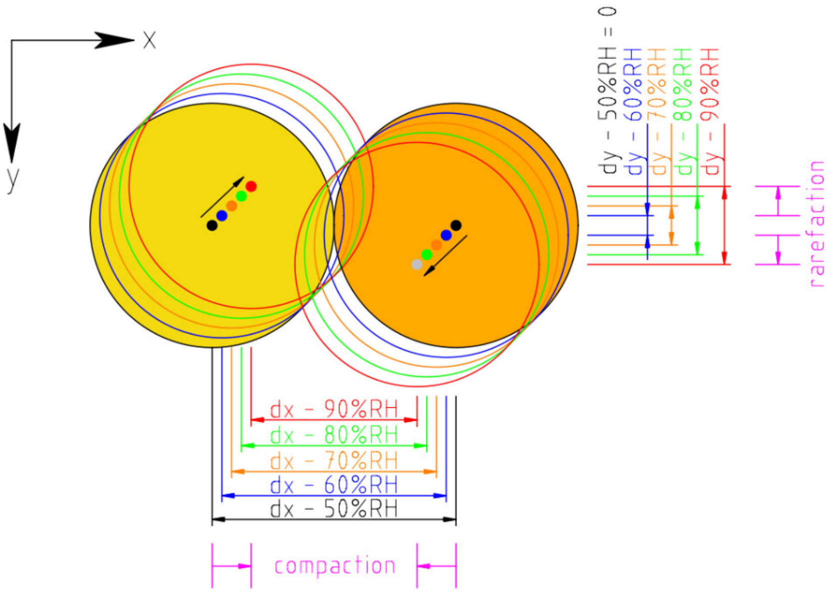

Figure 6.7: Illustrative example of compactions and rarefactions: displacement of two subsets as a result of increasing RH. In X-direction the subset centres move towards each other, in Y-direction the subset centres move apart.

6.2.1.3 Determination of fictitious strains from local displacements

The software that is used for the DIC analysis in this study is *Ncorr*, open source 2D DIC software based on MATLAB. A DIC analysis starts by loading the sequence of images. The first image in a series of images is used as the reference image. Next, the Area Of Interest (AOI) is defined and the subset size and subset spacing are chosen and the analysis is started. During the analysis, the image that is compared to the reference image is called the current image. The transformation from reference subset points to the current subset points is given by the following formulae:

$$x_{cur;i} = x_{ref;i} + u_{rc} + \frac{du}{dx_{rc}}(x_{ref;i} - x_{ref;c}) + \frac{du}{dy_{rc}}(y_{ref;j} - y_{ref;c}) \tag{6.1}$$

$$y_{cur;j} = y_{ref;j} + v_{rc} + \frac{dv}{dx_{rc}}(x_{ref;i} - x_{ref;c}) + \frac{dv}{dy_{rc}}(y_{ref;j} - y_{ref;c}) \tag{6.2}$$

In Eq. (6.1) and (6.2), index *cur* is for current image, *ref* is for reference image and *rc* is for the transformation of **r**eference to **c**urrent. The coordinates of the reference subset are represented by $x_{ref;c}$ and $y_{ref;c}$. After running the analysis, the subset displacements - which were until then calculated in pixel units - are converted from pixels to µm.

The DIC software calculates the displacements of subset points. The image size from the electron microscopy tests is 1536 x 1103 pixels (400 x 300 µm). A subset spacing of 4 pixels is applied for ESEM specimens (8 in case of optical microscopy). This means that every fifth pixel in the image is the centre of a subset (as shown in Figure 6.5).

The resulting array is (1536 px / (4 + 1)) = 307 columns wide and (1103 px / (4 + 1)) = 220 rows high. The subset radius is 20 pixels (as shown in Figure 6.4 and Figure 6.5), and each subset has an overlap with 4 subsets in X- and Y-direction, as shown in Figure 6.5. The AOI is slightly smaller than the total area of the image. This is caused by the title bar at the top or bottom of the images. Also, a frame must be present around the AOI so that subsets at the edge of the AOI remain within the edges of the image. Therefore, the arrays that contain the displacement results are slightly smaller than 307 x 220 pixels.

The displacements of the subset centre points that are calculated from the deformed reference patterns of subsequent images are stored in arrays. Per image two arrays are produced (one for X-direction and one for Y-direction).

To clarify how the displacement data are obtained, a small section of a captured image is shown in Figure 6.8 (top & middle image), together with the same section in which the subsets are shown (bottom image). The number of subsets in the small section of the image is 18 columns x 13 rows (bottom image). In this study, a common data array size is around 300 x 200 subsets (60,000 data points) per image. The grayscale of the subsets is averaged over all pixels in the subset. The DIC software uses the mean grayscale of the pixels in a subset for identification of the subset relative to its surroundings.

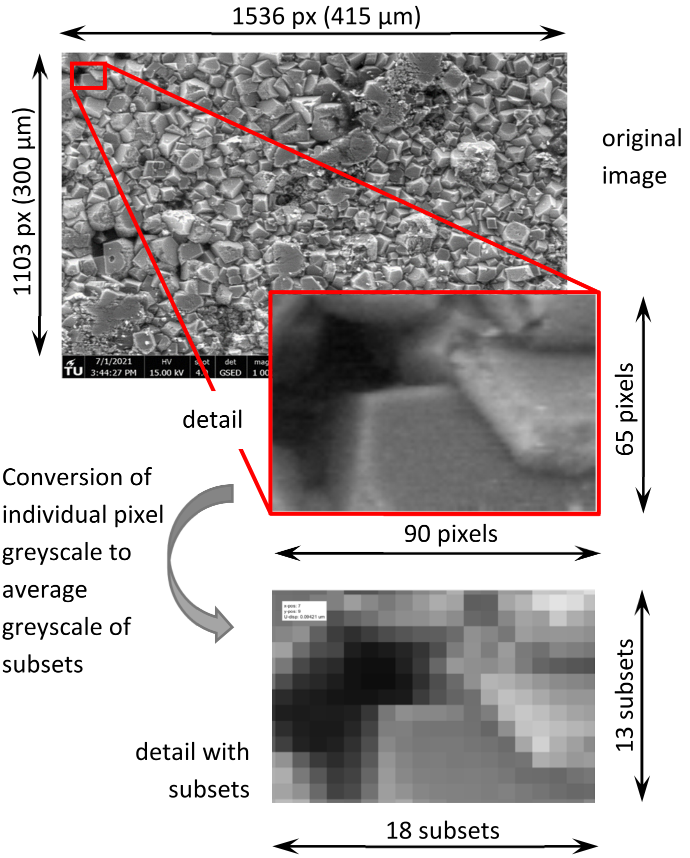

Figure 6.8: Detail of image from CEM I concrete specimen captured with electron microscope, stored for 45 weeks in wet-dry conditions. Middle: detail (90 x 65 pixels) of original image (top, 1536 x 1103 pixels), bottom: subsets in the same part of the image (18 x 13 subsets).

In Figure 6.9 the displacements of the same section as in Figure 6.8 are visualised in a colour plot. The colours indicate the intensity of the displacement. In Figure 6.10 the transformation of the subset displacement colour plot into a numerical data array is shown. The underlying numerical displacement data of the subset centres in the colour plots is used for further analysis. The data is exported to a spreadsheet program. In the exported data arrays, the displacements $x_{cur,I}$ and $y_{cur,j}$ (obtained by the DIC software according to Eq. (6.1) and (6.2)) of each subset centre relative to its reference location are collected.

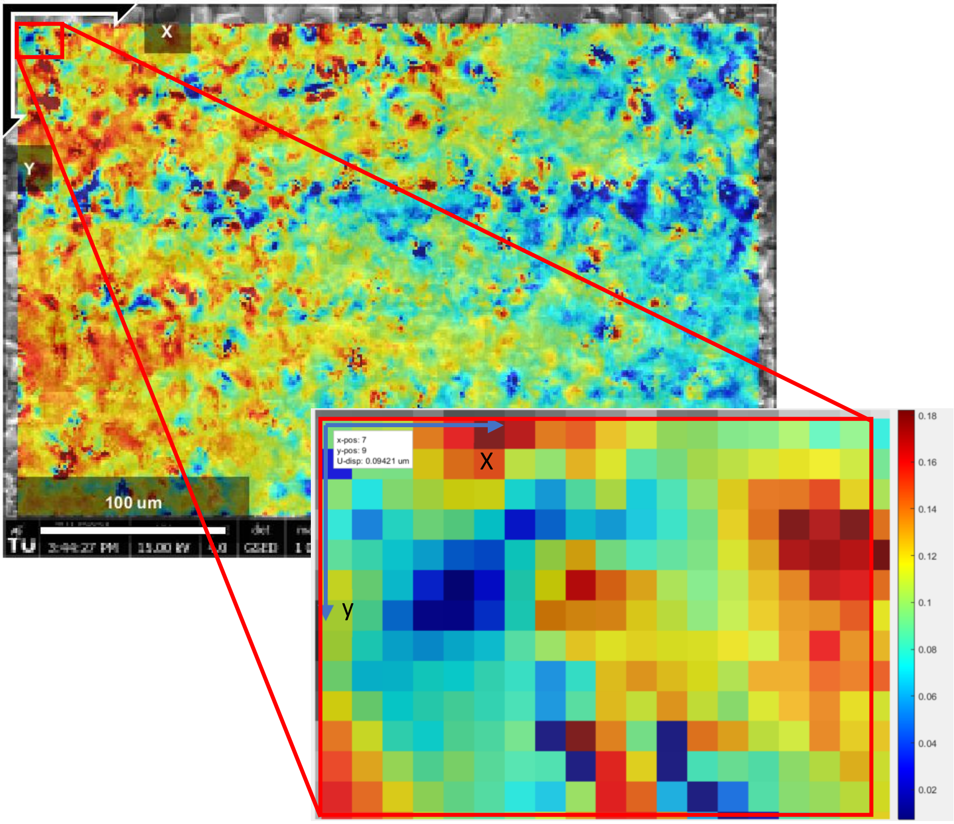

Figure 6.9: Displacements of subset centres in X-direction. CEM I concrete specimen after 45 weeks of exposure to wet-dry conditions. Shown are the displacements in the specimen during the first step: wetting 60% RH.

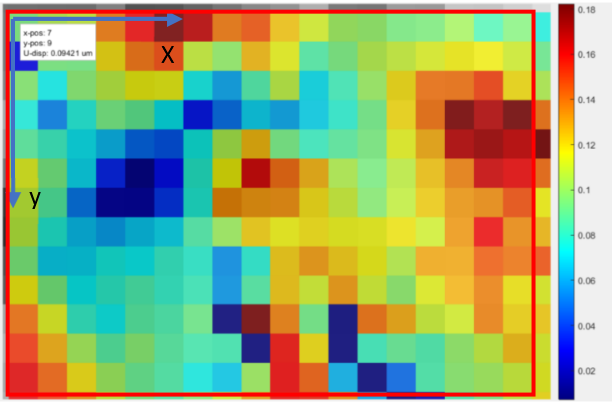

Visualisation of displacements in small section of colour plot in Ncorr.

(18 x 13 pixels)

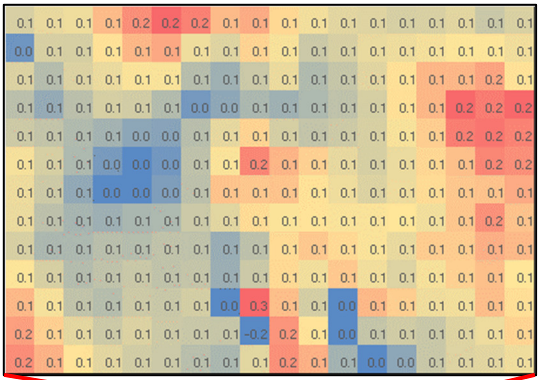

0.1	0.1	0.1	0.1	0.2	0.2	0.2	0.1	0.1	0.1	0.1	0.1	0.1	0.1	0.1	0.1	0.1	0.1
0.0	0.1	0.1	0.1	0.1	0.1	0.1	0.1	0.1	0.1	0.1	0.1	0.1	0.1	0.1	0.1	0.1	0.1
0.1	0.1	0.1	0.1	0.1	0.1	0.1	0.1	0.1	0.1	0.1	0.1	0.1	0.1	0.1	0.1	0.2	0.1
0.1	0.1	0.1	0.1	0.1	0.1	0.0	0.0	0.1	0.1	0.1	0.1	0.1	0.1	0.1	0.2	0.2	0.2
0.1	0.1	0.1	0.1	0.0	0.0	0.1	0.1	0.1	0.1	0.1	0.1	0.1	0.1	0.1	0.2	0.2	0.2
0.1	0.1	0.1	0.0	0.0	0.0	0.1	0.1	0.2	0.1	0.1	0.1	0.1	0.1	0.1	0.1	0.2	0.2
0.1	0.1	0.1	0.0	0.0	0.0	0.1	0.1	0.1	0.1	0.1	0.1	0.1	0.1	0.1	0.1	0.1	0.1
0.1	0.1	0.1	0.1	0.1	0.1	0.1	0.1	0.1	0.1	0.1	0.1	0.1	0.1	0.1	0.1	0.2	0.1
0.1	0.1	0.1	0.1	0.1	0.1	0.1	0.1	0.1	0.1	0.1	0.1	0.1	0.1	0.1	0.1	0.1	0.1
0.1	0.1	0.1	0.1	0.1	0.1	0.1	0.1	0.1	0.1	0.1	0.1	0.1	0.1	0.1	0.1	0.1	0.1
0.1	0.1	0.1	0.1	0.1	0.1	0.1	0.0	0.3	0.1	0.1	0.0	0.1	0.1	0.1	0.1	0.1	0.1
0.2	0.1	0.1	0.1	0.1	0.1	0.1	0.1	-0.2	0.2	0.1	0.0	0.1	0.1	0.1	0.1	0.1	0.1
0.2	0.1	0.1	0.1	0.1	0.1	0.1	0.1	0.1	0.2	0.1	0.1	0.0	0.0	0.1	0.1	0.1	0.1

Numerical representation of displacements in small section (colours added for clarification).

(18 x 13 pixels)

Numerical representation of displacements in area of interest (colours added for clarification).

(295 x 196 subsets, 1480 x 985 pixels)

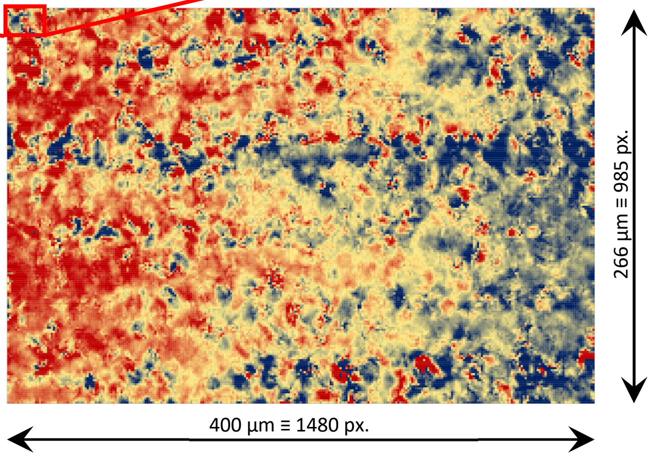

Figure 6.10: Transformation of the colour plots of the displacements in X-direction of the subset centres into numerical data.

6.2.2 Effects of restraints in the specimen

The bottom of ESEM specimens is fully bonded to a copper plate which causes a deformation restraint at the bottom. However, the specimens have a certain thickness (1-1.5 mm), which allows a certain amount of movement in the cement paste at the free surface of the specimen. The restraint at the bottom influences the displacements at the free surface.

Besides the restraint at the bottom of the specimen, displacements in the microstructure of a specimen can be influenced by a restraining particle outside of the area of interest. To illustrate this, Figure 6.11 shows an image of an old CEM I specimen. In the image, purple rectangles are placed. These rectangles represent the size of the AOI in microscopic scale tests (approximately 400 x 300 µm²). As this study focusses on the displacements in the cement paste, aggregate grains are generally not visible in the area of interest, but they will form a restraint for the cement paste in the observed area.

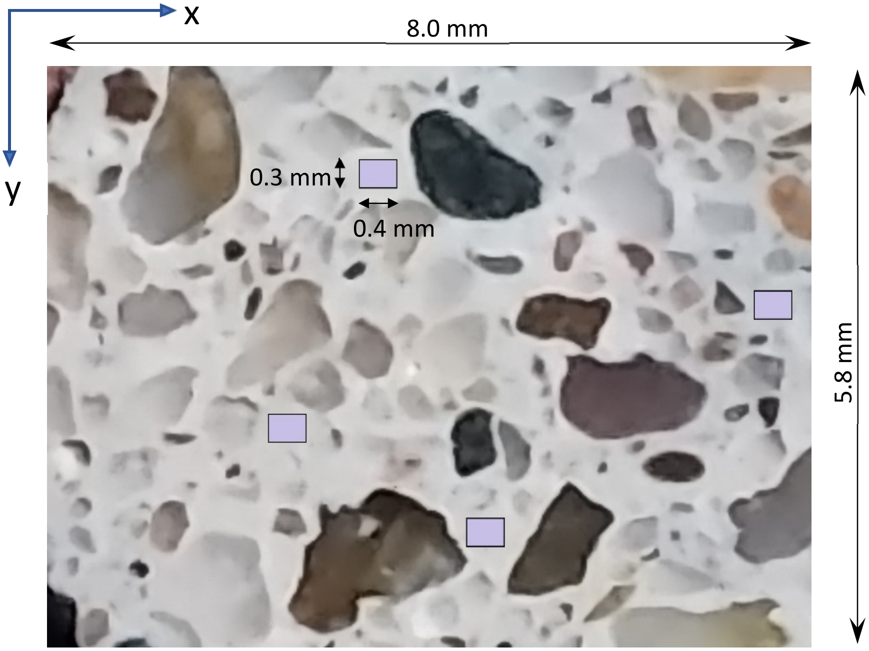

Figure 6.11: The purple-coloured frames represent the different areas of interest (AOI) of the microscopic scale test (0.4 x 0.3 mm²), projected on a mesoscale image of a concrete specimen with CEM I, stored in dry environment between microscopic scale tests.

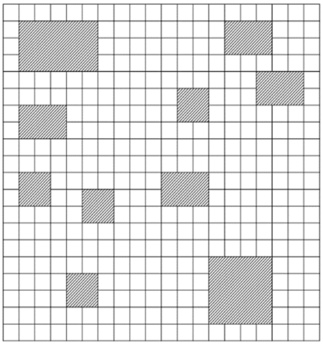

a) reference, non-deformed situation

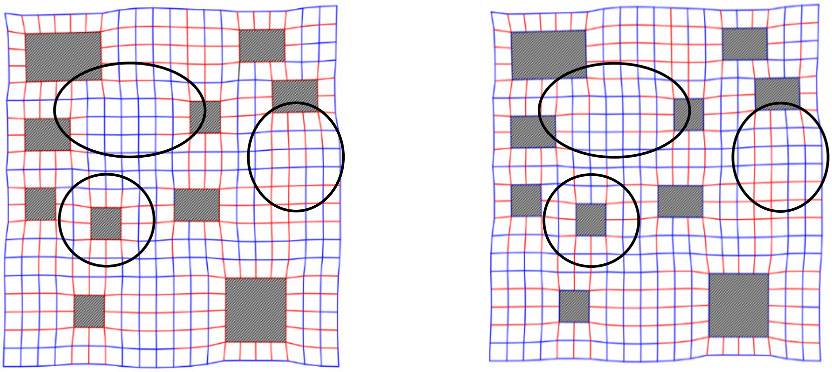

b) deformed situation, perfect bond between cement paste and aggregates

c) deformed situation, weak bond between cement paste and aggregates (50% stiffness)

Figure 6.12: Illustrative example of the effect of rigid inclusions on deformations and type of stress (compression of tension) of a specimen in case of imposed shrinkage of the cement paste . Scale: 1 square = 0.25 x 0.25 mm². Blue = compression, red = tension. Ovals indicate differences between b) and c).

In Figure 6.12, an example is given to illustrate simulated effects of restraints in the microstructure by rigid aggregate grains and the consequences of these restraints for deformations in the microstructure. The cement paste is represented as the quadrangles with dimensions of 0.25 x 0.25 mm². The paste is now supposed to shrink while being restrained by the aggregate particles. In Figure 6.12b, the deformations in the material are given assuming perfect bond between the aggregates and the shrinking cement paste. In Figure 6.12c, a lower stiffness (50%) of the material in the zone between the aggregate grain and the bulk cement paste is taken into account by lowering the stiffness of the connecting members between the aggregate and the surrounding paste. The differences between the deformations of b) and c) are small, but not negligible. The stiffness of the ITZ mainly affects the distribution of stresses directly around the aggregate grains. In the bulk paste, at some distance from the aggregate particles, the differences are marginal. In cement paste, the different particles also appear in different shapes and with different stiffnesses. Restraints may be present on every scale level, e.g. microscale restraints caused by sand grains and/or unhydrated cement grains, mesoscale restraints caused by aggregates and the ITZ, and macroscale restraints.

6.3 Gathering numerical data from DIC analysis

6.3.1 Determining mean strains in the cement paste over the AOI

From the DIC analysis the displacements at the surface of the specimen in X- and Y-direction are determined, relative to the reference image. The reference image is taken at 50% RH. The image that is compared with the reference is called current image.

The mean shrinkage and swelling in the cement paste over the AOI in X- and Y- direction represent the length change of the AOI in these two directions and is calculated with Eq. 6.3 and 6.4.

$$\overline{\varepsilon x} = \frac{\sum_{i=1}^{m} \sum_{j=1}^{n-1} (x_{cur;i;j+1} - x_{cur;i;j})}{m \cdot l_{init}} \tag{6.3}$$

$$\overline{\varepsilon y} = \frac{\sum_{j=1}^{n} \sum_{i=1}^{m-1} (y_{cur;i+1;j} - y_{cur;i;j})}{n \cdot l_{init}} \tag{6.4}$$

In Eq. (6.3) and (6.4), *i* and *j* are the indices for the rows and the columns respectively, $x_{cur,i}$ and $y_{cur,j}$ are the displacements of the current image in X- and Y-direction. Indices *m* and *n* represent the number of rows and columns, respectively. The subtractions $x_{cur;i;j+1} - x_{cur;i;j}$ and $y_{cur;i+1;j} - y_{cur;i;j}$ represent the local displacement between two adjacent subset points. l_{init} is the original centre-to-centre distance between two subsets.

6.3.2 Determining local strains

In the DIC analysis, the displacements of subsets in the AOI of the current image are determined relative to the position of those subsets in the reference image. Section 6.2.1 describes how the displacements of the subsets in the AOI are determined. From the displacements, local strains are calculated.

Local strains ε_x and ε_y are calculated from (global) displacements with Eq. (6.5) for X-direction and Eq. (6.6) for Y-direction:

$$\varepsilon_{x_{i,j}} = \frac{(x_{cur;i;j+1} - x_{cur;i;j})}{l_{init}} \tag{6.5}$$

$$\varepsilon_{y_{i,j}} = \frac{(y_{cur;i+1;j} - y_{cur;i;j})}{l_{init}} \tag{6.6}$$

Indices *i* and *j* are the row and column indices, respectively. Because of the definition of ε_x and ε_y in Eq. (6.5) and (6.6), the arrays in which the local strains are stored are one column (X-direction) or one row (Y-direction) smaller than the displacement arrays.

Because of the heterogeneity of the cement paste at this scale and magnification, the calculated strains are so-called fictitious strains because found displacements occur between subset points in the captured images which do not necessarily coincide with particles in the microstructure of the specimen. Local strains do not physically take place on one continuous particle, but may be distributed over several particles (with different properties).

In Figure 6.13, the same displacement data as shown in Figure 6.9 are shown including numerical data for clarification. The detail of the colour plot (top left) shows the displacements (Figure 6.13, top array). Below the displacements, the local strains in X-direction are given (Figure 6.13, bottom array).

6.3.3 Accuracy and errors in DIC analysis

Accuracy test

In [45], it was shown that global strains calculated with DIC software are very accurate but the local strains calculated by the software may be inaccurate.

In this study, only the displacements calculated by the DIC software are used for analysis. From the displacements, local strains are calculated. With the accuracy test method in [45], the accuracy of the source data is checked.

A random image from a microscopic scale test on an ESEM specimen is taken for this accuracy test (Figure 6.14). For the test, the image is copied and reduced in size by 1 %. The original image has 1536 x 1103 pixels and the resized image has 1521 x 1092 pixels. The number of pixels in the resized image is rounded off, therefore the size reduction in the longest direction (X-direction) is: $\frac{1536\,px - 1521\,px}{1536\,px} \cdot 100\,\% = 0.98\,\%$. In the short direction (Y-direction), the size reduction is: $\frac{1103\,px - 1092\,px}{1103\,px} \cdot 100\,\% = 1.00\,\%$. A DIC

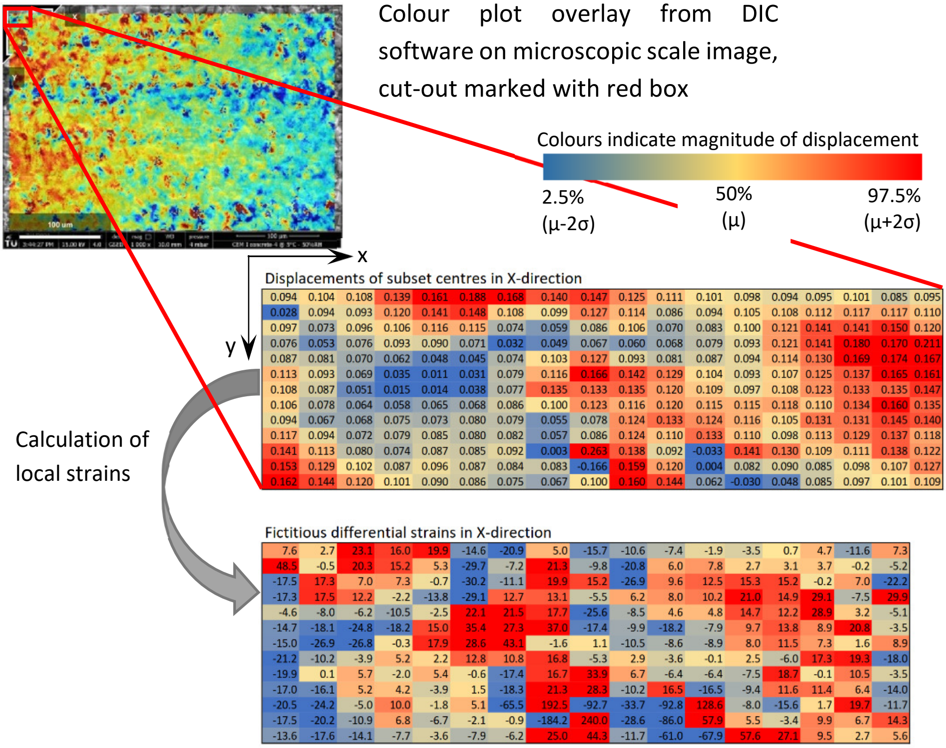

Colour plot overlay from DIC software on microscopic scale image, cut-out marked with red box

Colours indicate magnitude of displacement

2.5% (μ-2σ)

50% (μ)

97.5% (μ+2σ)

Calculation of local strains

Displacements of subset centres in X-direction

0.094	0.104	0.108	0.139	0.161	0.188	0.168	0.140	0.147	0.125	0.111	0.101	0.098	0.094	0.095	0.101	0.085	0.095
0.028	0.094	0.093	0.120	0.141	0.148	0.108	0.099	0.127	0.114	0.086	0.094	0.105	0.108	0.112	0.117	0.117	0.110
0.097	0.073	0.096	0.106	0.116	0.115	0.074	0.059	0.086	0.106	0.070	0.083	0.100	0.121	0.141	0.141	0.150	0.120
0.076	0.053	0.076	0.093	0.090	0.071	0.032	0.049	0.067	0.060	0.068	0.079	0.093	0.121	0.141	0.180	0.170	0.211
0.087	0.081	0.070	0.062	0.048	0.045	0.074	0.103	0.127	0.093	0.081	0.087	0.094	0.114	0.130	0.169	0.174	0.167
0.113	0.093	0.069	0.035	0.011	0.031	0.079	0.116	0.166	0.142	0.129	0.104	0.093	0.107	0.125	0.137	0.165	0.161
0.108	0.087	0.051	0.015	0.014	0.038	0.077	0.135	0.133	0.135	0.120	0.109	0.097	0.108	0.123	0.133	0.135	0.147
0.106	0.078	0.064	0.058	0.065	0.068	0.086	0.100	0.123	0.116	0.120	0.115	0.115	0.118	0.110	0.134	0.160	0.135
0.094	0.067	0.068	0.075	0.073	0.080	0.079	0.055	0.078	0.124	0.133	0.124	0.116	0.105	0.131	0.131	0.145	0.140
0.117	0.094	0.072	0.079	0.085	0.080	0.082	0.057	0.086	0.124	0.110	0.133	0.110	0.098	0.113	0.129	0.137	0.118
0.141	0.113	0.080	0.074	0.087	0.085	0.092	0.003	0.263	0.138	0.092	-0.033	0.141	0.130	0.109	0.111	0.138	0.122
0.153	0.129	0.102	0.087	0.096	0.087	0.084	0.083	-0.166	0.159	0.120	0.004	0.082	0.090	0.085	0.098	0.107	0.127
0.162	0.144	0.120	0.101	0.090	0.086	0.075	0.067	0.100	0.160	0.144	0.062	-0.030	0.048	0.085	0.097	0.101	0.109

Fictitious differential strains in X-direction

7.6	2.7	23.1	16.0	19.9	-14.6	-20.9	5.0	-15.7	-10.6	-7.4	-1.9	-3.5	0.7	4.7	-11.6	7.3
48.5	-0.5	20.3	15.2	5.3	-29.7	-7.2	21.3	-9.8	-20.8	6.0	7.8	2.7	3.1	3.7	-0.2	-5.2
-17.5	17.3	7.0	7.3	-0.7	-30.2	-11.1	19.9	15.2	-26.9	9.6	12.5	15.3	15.2	-0.2	7.0	-22.2
-17.3	17.5	12.2	-2.2	-13.8	-29.1	12.7	13.1	-5.5	6.2	8.0	10.2	21.0	14.9	29.1	-7.5	29.9
-4.6	-8.0	-6.2	-10.5	-2.5	22.1	21.5	17.7	-25.6	-8.5	4.6	4.8	14.7	12.2	28.9	3.2	-5.1
-14.7	-18.1	-24.8	-18.2	15.0	35.4	27.3	37.0	-17.4	-9.9	-18.2	-7.9	9.7	13.8	8.9	20.8	-3.5
-15.0	-26.9	-26.8	-0.3	17.9	28.6	43.1	-1.6	1.1	-10.5	-8.6	-8.9	8.0	11.5	7.3	1.6	8.9
-21.2	-10.2	-3.9	5.2	2.2	12.8	10.8	16.8	-5.3	2.9	-3.6	-0.1	2.5	-6.0	17.3	19.3	-18.0
-19.9	0.1	5.7	-2.0	5.4	-0.6	-17.4	16.7	33.9	6.7	-6.4	-6.4	-7.5	18.7	-0.1	10.5	-3.5
-17.0	-16.1	5.2	4.2	-3.9	1.5	-18.3	21.3	28.3	-10.2	16.5	-16.5	-9.4	11.6	11.4	6.4	-14.0
-20.5	-24.2	-5.0	10.0	-1.8	5.1	-65.5	192.5	-92.7	-33.7	-92.8	128.6	-8.0	-15.6	1.7	19.7	-11.7
-17.5	-20.2	-10.9	6.8	-6.7	-2.1	-0.9	-184.2	240.0	-28.6	-86.0	57.9	5.5	-3.4	9.9	6.7	14.3
-13.6	-17.6	-14.1	-7.7	-3.6	-7.9	-6.2	25.0	44.3	-11.7	-61.0	-67.9	57.6	27.1	9.5	2.7	5.6

Figure 6.13: Determining fictitious local strains, compactions and rarefactions from the displacement data.

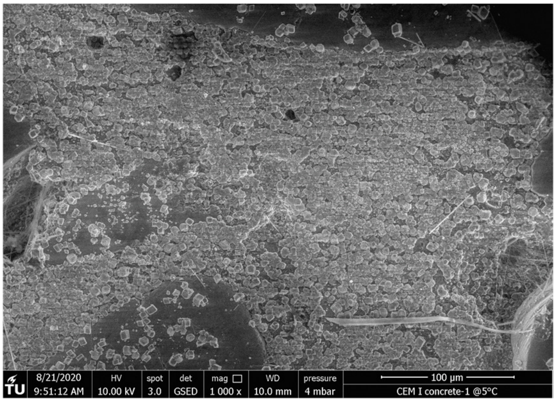

Figure 6.14: Image of a concrete specimen with CEM I, captured with electron microscope. Image resolution: 1536 x 1103 pixels

analysis is run with the original image as the reference and the resized image as the current image. From the analysis, the displacements of the individual subsets in the current image follow. It was expected that the displacements increase gradually from the origin [0;0] (top left) over the image in X- and Y-direction.

The mean strain in the AOI of the current image is calculated from the displacement data with Eq. (6.3) and (6.4) in section 6.3.1.

With Eq. (6.3) and (6.4), a mean shrinkage of the current image in X-direction of 0.98% and in Y-direction of 1.00 % is found, which exactly matches the calculated resize values.

It is expected that, when considering the displacements in X-direction, no differences occur between the displacements in adjacent rows. For the displacements in Y-direction, no differences between the displacements in adjacent columns are expected. The colour gradients in Figure 6.15 illustrate that the displacements indeed gradually increase over the length or width of the image. However, the (underlying) displacement data indicate that small deviations occur between the displacements of adjacent rows (X-direction) or columns (Y-direction). These deviations occur as a result of imperfections in the formation of subsets. The largest deviation is about 1.2% relative to the mean shrinkage, which is well acceptable.

This accuracy test is indeed a simple test that provides insight into the accuracy of the calculated displacements from DIC analyses performed on the images that were captured from the microscopic scale tests. With regard to the mean displacement, the findings are in line with the findings of [45]. In [45] it is shown that the fictive strain calculation in DIC software is, however, a lot less accurate. Strain analysis in DIC is generally used to determine ‘true’ engineering strains whereas in this study the fictitious local strains (compactions and rarefactions) are of interest. The fictitious local strains in this study are derived from the subset displacements (which are accurate).

Estimation of error

In [46], a method is described to estimate the uncertainty of DIC displacement field analysis. Different errors can be introduced during image gathering and during the analysis process, e.g.: Gaussian pixel noise, speckle pattern size and density, absolute displacement, intensity change amongst others. It was shown that, in spite of multiple error sources, the total uncertainty of displacements was small (< 10%).

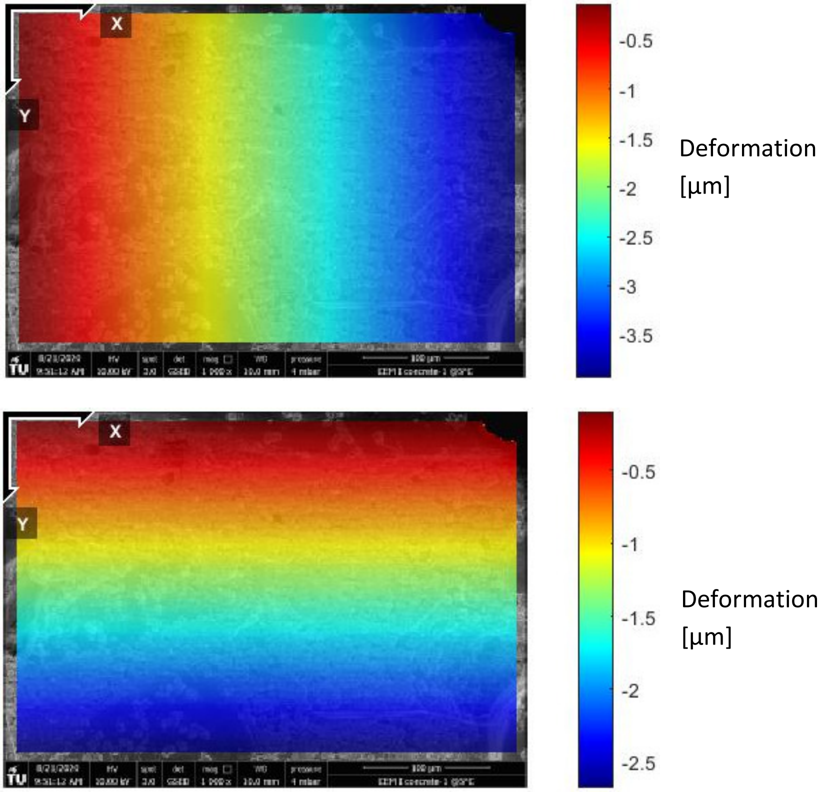

Figure 6.15: Displacement plots in X-direction (top) and Y-direction (bottom) from DIC analysis for accuracy test.

7 Results of the microscopic research – ESEM specimens

In this chapter the results of the microscopic scale tests on ESEM specimens, performed with an electron microscope, are presented and discussed. Microscopic scale tests reveal displacements in the cement paste of old (concrete) and young (mortar) specimens when exposed to changing relative humidity (RH). From the measured displacements, (fictitious) local strains are calculated.

In section 7.1 the microscopic scale tests on ESEM specimens are described briefly. In section 7.2 the strain data are presented and interpreted. In section 7.3, preliminary findings are discussed. In section 7.4 the preliminary findings of the microscopic scale tests on ESEM specimens are summarized and preliminary conclusions are presented.

A general discussion of the response of ESEM specimens follows in Chapter 9 in conjunction with the discussion on the response of optical microscopy specimens exposed to similar humidity cycles.

7.1 Description of specimens & microscopic scale tests

7.1.1 Test set-up of ESEM test cycles

A top view of an ESEM specimen is shown in Figure 7.1 (top left). The specimens, diameter about 10 mm and thickness of approximately 1 mm, are glued to a circular copper plate with a diameter of 9.5 mm and 2.5 mm thick. The specimens are placed in the ESEM, where they are exposed to wet/dry cycles (50% RH – 100% RH and back). One test cycle takes about 65 minutes. The deformational response of the cement paste at the top surface to humidity cycles is measured on microscopic scale in areas of approximately 400 x 300 μm² (the net area of interest (AOI) is only slightly smaller). Images were captured at a resolution of 1536 x 1025 px.

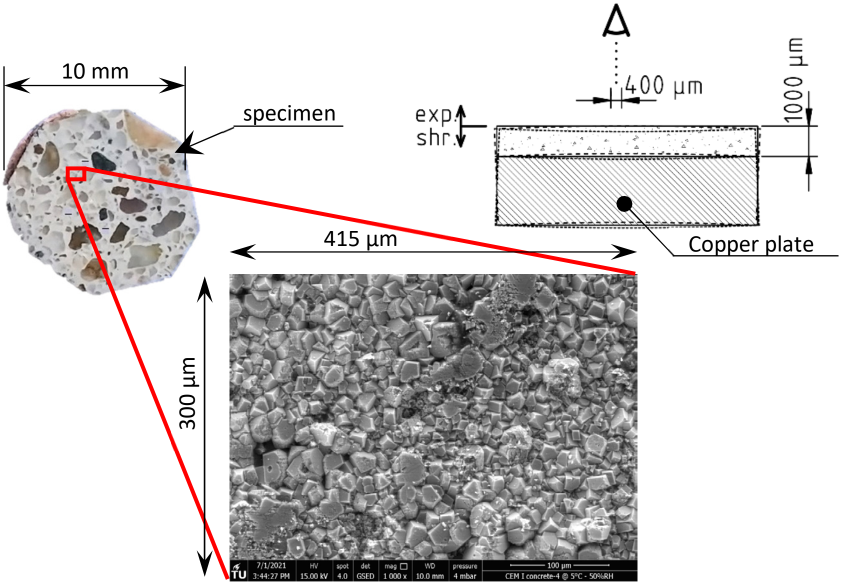

Figure 7.1: Illustration of microscopic scale images with regard to ESEM specimen. Top left: top view of specimen and of captured image of cement paste (bottom). Top right: cross-section of the specimen. ESEM specimens are glued to a circular copper plate. The bond between the specimen and the copper plate forms a restraint at the bottom of the specimen.

7.1.2 Exposure of specimens before, during and between test cycles

7.1.2.1 Storage conditions prior to testing

Prior to specimen preparation, the material samples were stored in 100% RH at 20°C. After specimen preparation and prior to the first test cycle, the specimens were kept under water at 20°C.

7.1.2.2 Exposure conditions between test cycles

Between the test cycles, during the interim storage, the specimens were stored in four different climatic conditions: dry, wet, temperature cycles and alternating wet-dry (as described in chapter 4 and indicated in Figure 7.4). Figure 7.2 indicates the imposed RH and temperature as function of time of specimens in different interim storage conditions. A period of 25 days is displayed; the wet storage prior to the first test cycle (about 5 days) up to 20 days after the first test cycle. The specimens exposed to dry and

Condition 1: dry interim storage

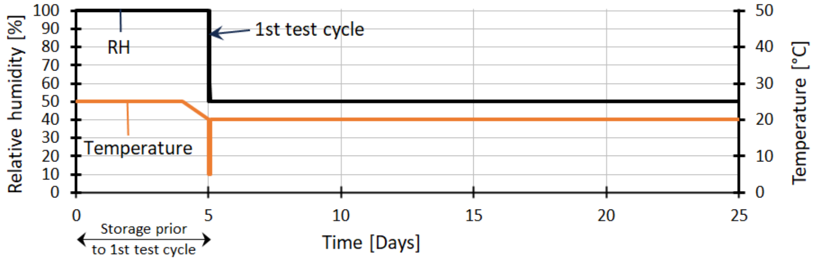

Condition 2: wet interim storage

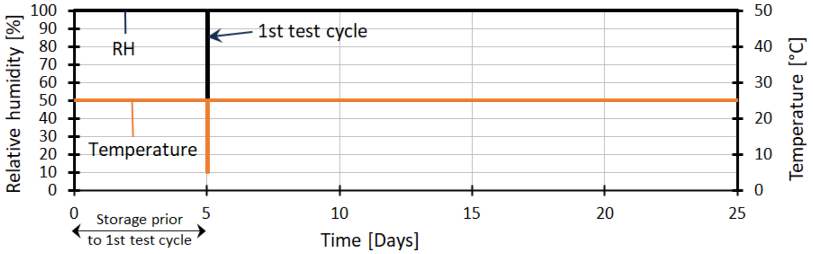

Condition 3: temperature cycles

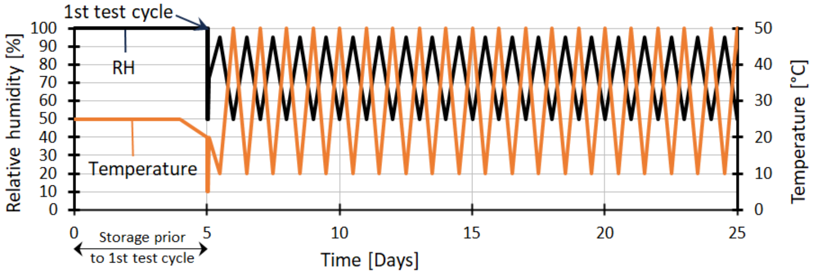

Condition 4: wet-dry interim storage

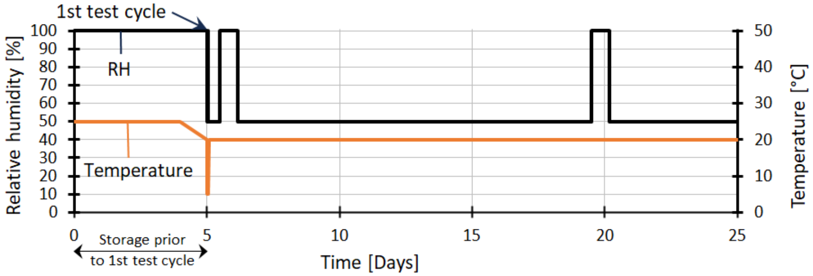

Figure 7.2: RH exposure (black curve) & temperature exposure (orange curve) over time of different specimens.

wet interim storage were subject to maximum 4 RH cycles (the ones during the microscopic scale tests).

Non-stationary interim storage – temperature cycles

The specimens that were exposed to temperature cycles during interim storage were also subject to humidity changes as a result of the temperature changes during storage. During the temperature cycles, the temperature varied from 10°C to 50°C and back, while the RH varied daily between 95% RH and 50% RH and back. The specimens exposed to temperature cycles during interim storage were subject to many humidity cycles (about 210 cycles) during the period between the first and the last (fourth) test cycle (executed about 45 weeks after the first test cycle). Should exposure to repeated humidity cycles lead to damage in the specimen, it is expected in the specimens exposed to temperature cycles.

Non-stationary interim storage – alternating wet-dry climate

The specimens that were exposed tot wet-dry conditions during interim storage were stored in wet climate for 8 hours followed by storage in dry climate for 328 hours (bi-weekly cycle). The specimens exposed to alternating wet-dry climate were subject to approximately 15 cycles during the period between the first and the last (fourth) test cycle (executed about 45 weeks after the first test cycle).

7.1.2.3 Exposure during testing

Before the test cycle is started, specimens are kept in the chamber of the ESEM at 50% RH until a stable image can be gathered. This can take up to 10 minutes. The RH-regime to which the specimens are exposed is shown in Figure 7.3. The cycle starts at RH = 50%, then increases stepwise to 100% and then down to 50% again. During the test cycle a series of images of the specimen is captured at different relative humidity (RH).

7.1.2.4 Test scheme

Microscopic scale tests were conducted at four different ages of the specimens (see Figure 7.4). Shortly after specimen preparation the first test cycle was conducted (week 1). Three test cycles followed in week 15, week 30 and week 45 (+/- 2 weeks).

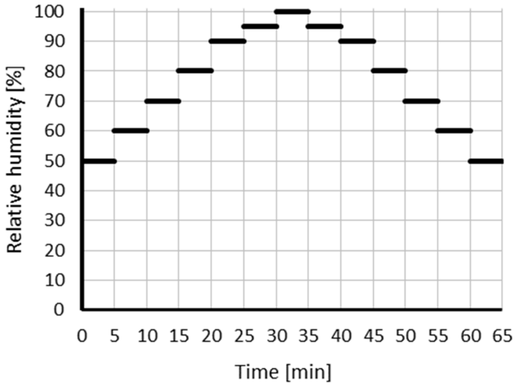

Figure 7.3: Schematic of RH-regime to which ESEM specimens are exposed during test cycles in week 1, 15, 30 and 45.

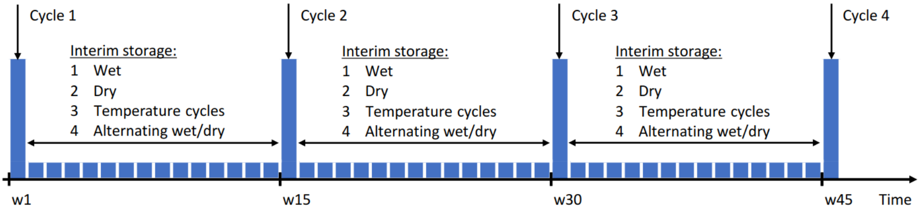

Figure 7.4: Test scheme of microscopic scale tests on ESEM specimens: 4 test cycles in week 1, 15, 30 and 45 with interim storage.

7.1.3 Mixture composition of test specimens

The mixture composition is given in Table 7.1 and Table 7.2 for old and young specimens, respectively:

Table 7.1: Mixture composition & properties of old (concrete) specimens.

Old specimens (concrete)				
Binder	CEM I	CEM III/B	CEM III/B+FA	CEM III/C
Strength class	B65	B35	B30	C30/37
w/b ratio [-]	<0.45	0.47	<0.55	0.37
Binder content [kg/m³]	>280	320	320+30	360
Age* [years]	21	22	35	6

*Age at test cycle 1

Table 7.2: Mixture composition & properties of young (mortar) specimens.

Young specimens (mortar)				
Binder	CEM I	CEM III/B	CEM III/B+FA	CEM III/C
Compressive strength [MPa]	36.1	44.2	42.0	31.0
w/b ratio [-]	0.5	0.5	0.5	0.5
Binder content [kg/m³]	510	510	510	510
Age* [years]	0.5	0.5	0.5	0.5

*Age at test cycle 1

7.2 Results: swelling, shrinkage and residual strains, local strains

7.2.1 Mean swelling and shrinkage over AOI

From the deformations measured at the surface of the specimens at varying RH, (fictitious) local strains were calculated (compactions and rarefactions). From these (fictitious) local strains, the mean strain $\bar{\varepsilon}(RH) = \Delta l/l$ over the AOI was calculated.

Figure 7.5 shows the mean strain $\bar{\varepsilon}(RH) = \Delta l/l$ over the AOI of a CEM I specimen as function of RH cycles. The mean strain curves show that, in spite of the deformation restraint at the bottom by the copper plate, and to some extent by aggregate particles close to the AOI, the cement paste in the AOI exhibits a mean swelling with increasing RH and a mean shrinkage with decreasing RH. At the end of the wet/dry cycle a residual strain remains. In Figure 7.6, the mean swelling $\bar{\varepsilon}_{50\%-100\%\,RH}$, the mean shrinkage $\bar{\varepsilon}_{100\%-50\%RH}$ and the residual strain $\bar{\varepsilon}_{res}$ are indicated for the test cycle in week 1.

General findings

Characteristic points of the calculated strains are:

1. Mean swelling;
2. Mean shrinkage.

In the following these characteristic points are summarized for all the tests on the four different interim storage conditions and the different specimen types. Individual measurements are summarized in Appendix F.3.

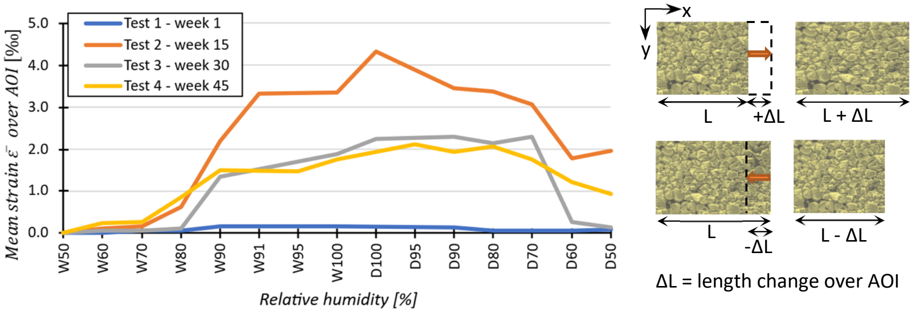

Mean strains (ΔL/L) over AOI in X-direction as function of RH – old specimen

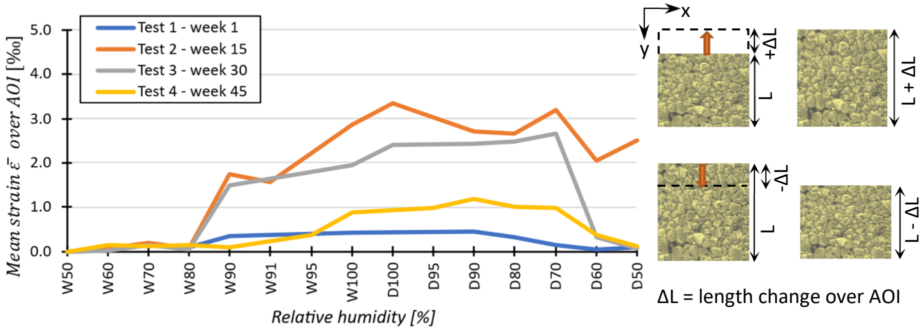

Mean strains (ΔL/L) over AOI in Y-direction as function of RH – old specimen

Figure 7.5: Mean strains $\bar{\varepsilon}(RH)$ over the area of interest (AOI) in the cement paste in X-direction (top) and Y-direction (bottom) in an old ESEM specimen with CEM I. Between microscopic scale tests, the specimen was stored in dry climate. The characters 'W' and 'D' preceding the RH values indicate the wetting and drying phase of the test cycle.

In Appendix F.3, the mean displacement $\bar{\varepsilon}$ over the AOI upon wetting from 50% RH to 100% RH and subsequently drying from 100% RH to 50% RH are given for all four test cycles on old and young specimens, respectively (in total 32 specimens). The strains shown in Appendix F.3 are summarized in box plots (mean swelling $\bar{\varepsilon}_{50\%-100\%\,RH}$ in Figure 7.7, mean shrinkage $\bar{\varepsilon}_{100\%-50\%\,RH}$ in Figure 7.8).

The measured mean swelling $\bar{\varepsilon}_{50\%-100\%\,RH}$ varies between 0.06 ‰ and 5.1 ‰ and the mean shrinkage $\bar{\varepsilon}_{100\%-50\%\,RH}$ varies between -0.01 ‰ and -4.3 ‰, much larger than what is considered as macroscale ultimate strains. However, no damage (cracking or otherwise) was observed on the surface of specimens. The small mean displacements are measured at locations on the specimen with a large restraint, either below the surface or in the direct vicinity of the AOI. Obviously, the large measured mean strains can not be directly compared with macroscale shrinkage or swelling strains for concrete

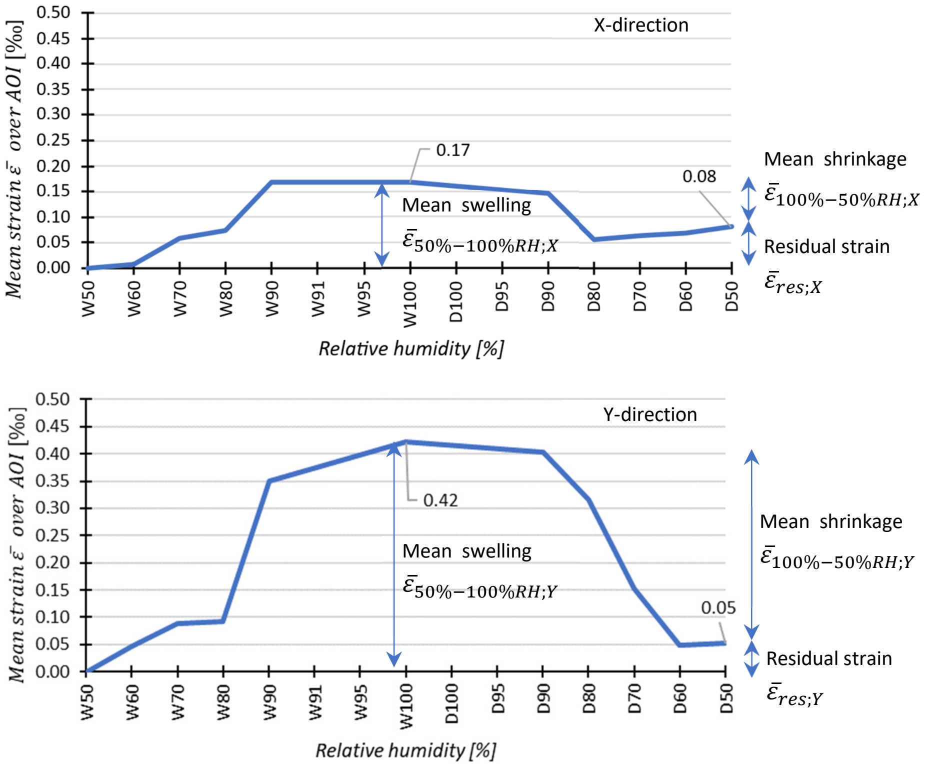

Figure 7.6: Mean strains $\bar{\varepsilon}(RH)$ over AOI in X-direction (top) and Y-direction (bottom) in the old specimen with CEM I during test cycle 1 in week 1, measured with electron microscope. During storage between microscopic scale test cycles, the specimen was exposed to dry climate.

and mortar found in literature. In this study microscopic scale displacements in the cement paste of a 1-1.5 mm thick piece of cementitious material are measured. Swelling and shrinkage strains reported in literature are measured on macroscale specimens. As indicated in Figure 3.1, section 3.2.1.4, the mean deformation at the surface of a specimen as a result of drying or wetting depends on the size of the specimen, due to internal restraints and diffusion of moisture from the specimen. It appears that, because the specimens are only 1-1.5 mm thick, both the degree of internal restraint is low and moisture exchange between the specimen and its environment occurs quickly.

Effect of interim storage condition on strain characteristics

The largest mean strains occur in specimens stored in dry interim storage as shown in the box plots in Figure 7.7a and Figure 7.8a. This may be expected, as the microstructure is conditioned dry and it can easily absorb moisture.

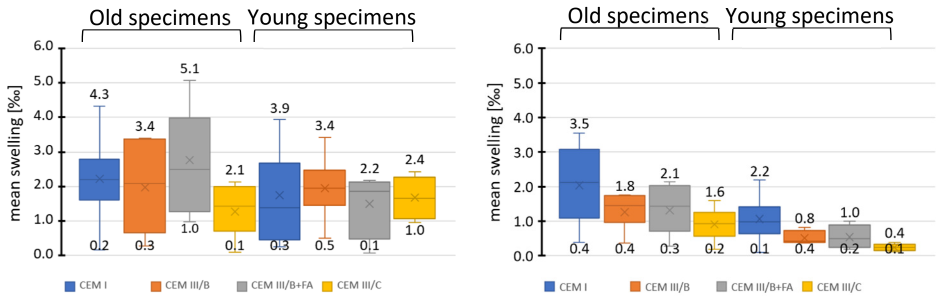

a) exposed to dry interim storage

b) exposed to wet interim storage

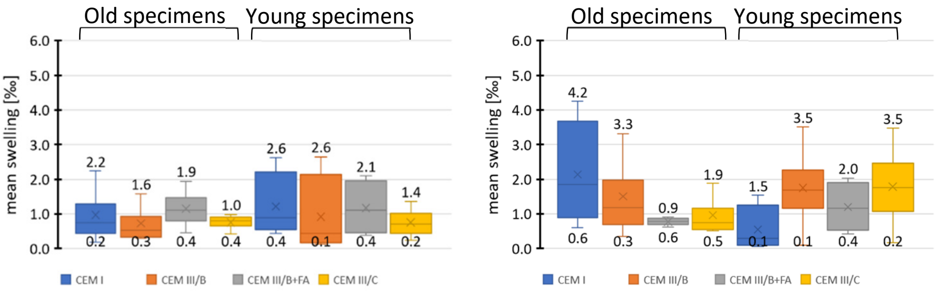

c) exposed to temperature cycles in interim storage

d) exposed to alternating wet-dry interim storage

Figure 7.7: Box plots of mean swelling $\bar{\varepsilon}_{50\%-100\%\,RH}$ in all four test cycles in old & young specimens for different interim storage conditions. Source data can be found in Appendix F.3

Effect of binder type on strain characteristics

The box plots in Figure 7.7b/d and Figure 7.8b/d show a significant difference between the mean strains over the AOI in the specimens exposed to wet or alternating wet-dry interim storage. In these two interim storage conditions, the mean swelling and shrinkage strains in specimens with CEM I were larger than the strains in specimens with CEM III (i.e.: CEM III/B, CEM III/B + FA, CEM III/C). The response of the specimens with

CEM I may be different from that of specimens with CEM III because of differences between the pore system of specimens with CEM I and CEM III. The pore system of specimens with CEM I obviously absorbs and releases water more easily than specimens with CEM III during the test cycle.

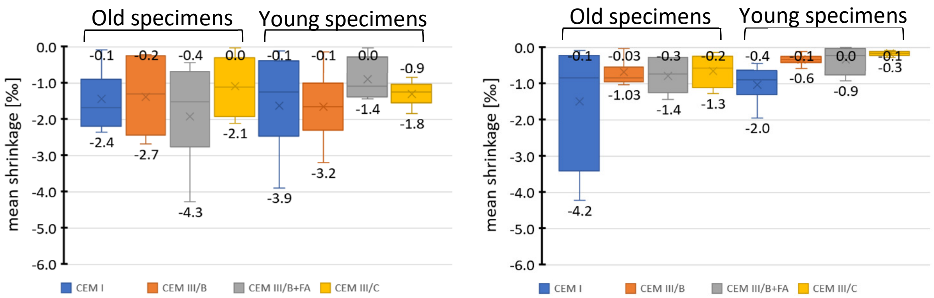

a) *exposed to dry interim storage*

b) *exposed to wet interim storage*

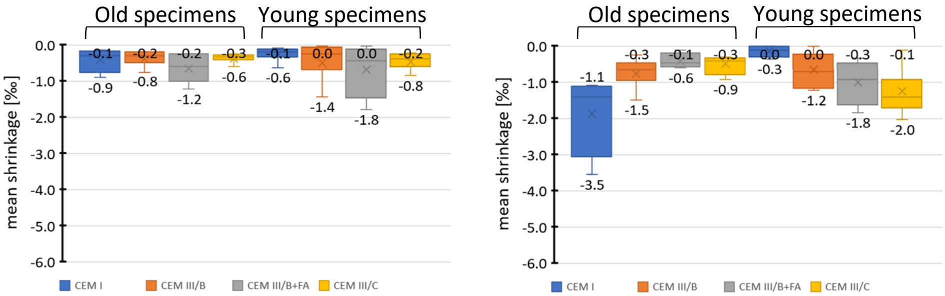

c) exposed to temperature cycles in interim storage

d) exposed to alternating wet-dry interim storage

Figure 7.8: Box plots of mean shrinkage $\bar{\varepsilon}_{100\%-50\%\,RH}$ *in all four test cycles in old & young specimens for different interim storage conditions. Source data can be found in Appendix F.3*

Effect of specimen age on strain characteristics

The box plots in Figure 7.8 show notable differences between the shrinkage strains in old and young specimens with CEM I binder. Between specimens with other binders than CEM I differences also occur, however, not as obviously as in the specimens with CEM I.

Differences between swelling strains (Figure 7.7) in old and young specimens with CEM I are less obvious, however, in the specimens exposed to wet and wet-dry interim storage the differences are significant.

Differences between the mean shrinkage and swelling strains in old and young specimens with the same nominal binder type are assumed to be caused by differences in pore size distribution and specimen type (concrete or mortar). The microstructure of cementitious materials develops over time. When it does so, the deformational response of the microstructure to changing humidity changes.

It appears that moisture uptake and release into the (carbonated) microstructure of old specimens with CEM I leads to a larger deformational response than in young (carbonated) specimens. After carbonation occurs in the specimens, as mentioned in section 4.4.2, the deformational response of cementitious specimens changes due to the pore size distribution in the microstructure. The microstructure of specimens with CEM I becomes denser after carbonation.

7.2.2 (Fictitious) local strains in the cement paste

This section zooms in on local strains (compactions and rarefactions) in the microstructure of cementitious material exposed to humidity cycles. Within a small area, large variations in local strains were measured; both positive local strains (rarefactions) and negative local strains (rarefactions) were found adjacently.

General findings

Fictitious local strains were calculated from the local displacements. The characteristics of local strains are:

1. Compactions and rarefactions;
2. Extreme fictitious local strains.

Figure 7.9 shows a 3D surface chart of the measured local displacements in a specimen. The majority of measured local displacements is in the range of +/- 100 ‰ (the mainly green & light blue area in the chart). Peaks in the chart indicate extreme strains (both compactions and rarefactions). The local strains in the green and light blue areas occur in the bulk cement paste. They are up to two orders of magnitude larger than the mean strains presented in section 7.2.1 (Figure 7.7 and Figure 7.8). No notable differences were found between the magnitude of local strains in specimens with different binder, interim storage conditions and specimen type.

Compactions and rarefactions

The occurrence of compactions and rarefactions under loading is caused by the heterogeneity of the microstructure. The 3D surface chart of the local strains in Figure 7.9 indicates the occurrence of large compactions and rarefactions near voids in the cement paste and along the edges of grains with a high stiffness (e.g. aggregate grains or unhydrated cement grains). Large local strains as shown in Figure 7.9 and Figure 7.10 were measured in all specimens and in all test cycles. Figure 7.10 shows part of the 3D surface chart which corresponds to the red square in the specimen image shown in Figure 7.9, which area includes a void. It appears that large local strains occur around the void. The indicated maximum and minimum strains occur adjacently.

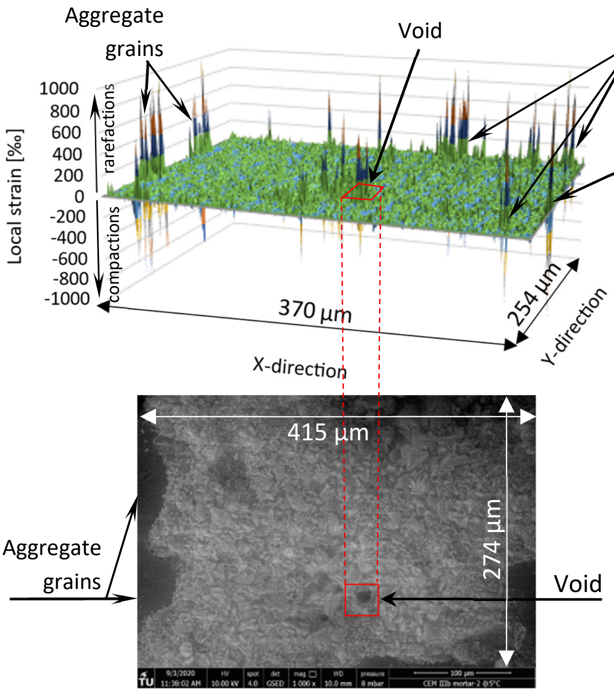

Figure 7.9: Local strains in X-direction at 100% RH in young specimen with CEM III/B during test cycle 1 (Top). Between test cycles, the specimen was kept in wet interim storage. The image at the bottom shows the morphology of the specimen, captured with ESEM. The red square indicates a void in the material.

Extreme fictitious local strains around stiff grains and voids

It is well known, that the (mesoscale!) interfacial transition zone between aggregate and cement paste is prone to microcracking due to the 'wall effect' which occurs around aggregates [47,48]. In the current study, however, no sign of damage or cracking in the (microscale) interface zone between aggregate grains and cement paste was found in any of the specimens, although very large local strains were measured in this zone. It is assumed that interfaces in the microstructure are capable of accommodating large deformations without taking damage. During the test cycles and during storage, pore water is always present in the specimen. The water interacts with the microstructure and may enable the large local strains in the material without permanent damage occurring in the microstructure.

Local strains in relation to mean strains

For the calculation of mean strains according to Eq. (6.3) and (6.4) in section 6.3.1, the sum of all local strains is divided by number of rows (for X-direction) or columns (for Y-direction). This implies that the influence of extreme compactions and rarefactions to the mean strain decreases when the area over which these extremes are spread increases. This is illustrated by the 3D surface chart of the part of the AOI indicated in Figure 7.10. The mean swelling strain over the area of the surface chart (19 x 19 μm^2) is 32 ‰, whereas the mean swelling strain in X-direction resulting from wetting from 50% RH to 100% RH over the whole AOI (400 x 300 μm^2) is not more than 0.66 ‰.

7.3 Discussion

Over the AOI (about 400 x 300 μm^2), deformations in the cement paste were measured with a resolution of 1.35 µm in X- and Y-direction. Local strains were calculated from the measured displacements in the cement paste. A wide distribution of fictitious local strains was found; the local strains can be subdivided in compactions (negative strains, points that move towards each other) and rarefactions (positive strains, points that move away from each other). Compactions and rarefactions are typically found when assessing deformations in heterogeneous material on a scale as used in the current study [21,22,49-51] .

Question is, how such large compactions and rarefactions can occur without apparently causing damage to the cement paste in the form of (micro)cracking? The key 'ingredient' for the large local strains may be found in the water that is present between the solid phase in the cement paste. During the test cycles as well as during interim storage, the specimens were always exposed to RH ≥ 50%. At such RH, gel pores remain saturated.

At RH ≥ 50%, capillary condensation occurs in pores and locally water accumulates [52]. The largest local strains were generally found at the highest RH, when all capillary pores

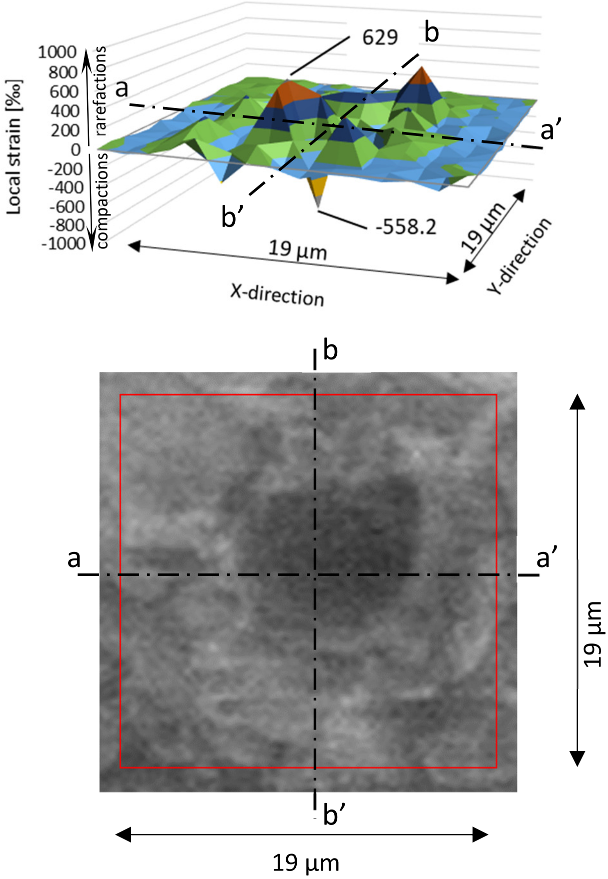

Figure 7.10: Local strains in X-direction at 100% RH in part of young specimen with CEM III/B during test cycle 1 (Top). Between test cycles, the specimen was kept in wet interim storage. The image at the bottom indicates the area considered in the 3D surface chart.

were filled with water (in many test cycles, water was seen bubbling out of pores during (macroscale) condensation conditions at 100% RH).

In section 6.2.2, Figure 6.19, an example was presented to illustrate that incompatibilities of deformation arise near voids and restraints as a result of heterogeneities. Similar incompatibilities were found in the measurements during the test cycles. It was found that extreme fictitious local displacements only occur in the vicinity of voids and around aggregate grains or unhydrated cement grains (restraints) in the cement paste. The effects of the restraints are, however, much larger than in the example of Figure 6.19, because the stiffness difference between cement paste and the stiff grains appears to be much larger than in the example.

The measured compactions and rarefactions in the cement paste were found to be up to three orders of magnitude larger than the mean swelling and shrinkage strains in bulk cement paste (mean strains up to 5 ‰, extreme fictitious local strains up to 1400 ‰ – these occurred sporadically). In spite of these large local displacements, no damage was found at microscale.

In section 6.3.3 the accuracy and magnitude of errors in DIC analysis was discussed. To put the extreme fictitious local strains into perspective, the 'mean' of all local strain measurements calculated from a displacement field (as indicated in Figure 6.13) is <|10 ‰| at a standard deviation σ ≈ 40 ‰. The displacements and the local strains are normally distributed, so that 99% of the calculated local strains are <|100 ‰| i.e.: (2.48 · σ). Should an error of 10% occur to the measurements, the mean would still be <|11 ‰| and 99% of the calculated local strains is expected to be <|110 ‰|; still one order of magnitude smaller than the extreme local strains. It is unlikely that the extreme fictitious local strains are the result of accuracy of the measurements and/or errors in the analysis.

In chapter 9 the extreme fictitious local strains are further discussed.

7.4 Conclusions

In this chapter, the results from the microscopic scale research on ESEM specimens were presented. The following conclusions are drawn:

- The mean swelling and shrinkage strains over the AOI in the cement paste of ESEM specimens as a result of RH changes from 50% RH to 100% RH and back are in the order of 0 - 5 ‰. These mean strains are larger than known shrinkage and swelling strains measured on macroscale because of the thin specimens that were used in this study. They are, however, within the same order of magnitude.
- Extreme compactions and rarefactions that were measured at the surface of the cement paste specimens appeared not associated with cracking or damage to the specimens. Found extremes are in the order of +/- 1400 ‰ in peaks. These large compactions and rarefactions were found around stiff grains and voids in the cement paste.
- The extreme fictitious local strains that were found after analysis and data-treatment were not caused by errors or inaccuracies in image capturing or DIC analysis.
- Extreme fictitious local strains appear very local whereas the mean strain over the AOI remains within a 'known' order of magnitude.

8 Results of the microscopic research – optical microscopy specimens

In this chapter the results of the microscopic scale tests on optical microscopy specimens, performed with an optical microscope, are presented and discussed.

In section 8.1 the microscopic scale tests on optical microscopy specimens are described briefly. In section 8.2, the strain data are presented and interpreted. In section 8.3, preliminary findings are discussed. In section 8.4, the preliminary findings of the microscopic scale tests on optical microscopy specimens are summarized and conclusions are presented.

8.1 Description of specimens & microscopic scale tests

8.1.1 Test set-up of test cycles on optical microscopy specimens

A top view of an optical microscopy specimen is shown in Figure 8.1 (top left). The specimens have dimensions of 10 x 10 mm² and thickness of approximately 1-1.5 mm. The specimens are placed on a temperature controlled stage, where they are exposed to wet/dry cycles by changing the temperature at the bottom of the specimen. The deformational response of cement paste at the top surface to moisture cycles is measured at microscopic scale in areas of approximately 400 x 300 µm² (the net area of interest (AOI) is only slightly smaller). Images were captured at a resolution of 2592 x 1944 pixels. Contrary to the ESEM specimens, the specimens are not glued to a supporting material and can, therefore, (macroscopically) deform without restraint.

8.1.2 Exposure of specimens before, during and between test cycles

Storage conditions prior to testing and in between test cycles were identical for ESEM specimens and optical microscopy specimens. These storage conditions are described in sections 7.1.2.1 and 7.1.2.2.

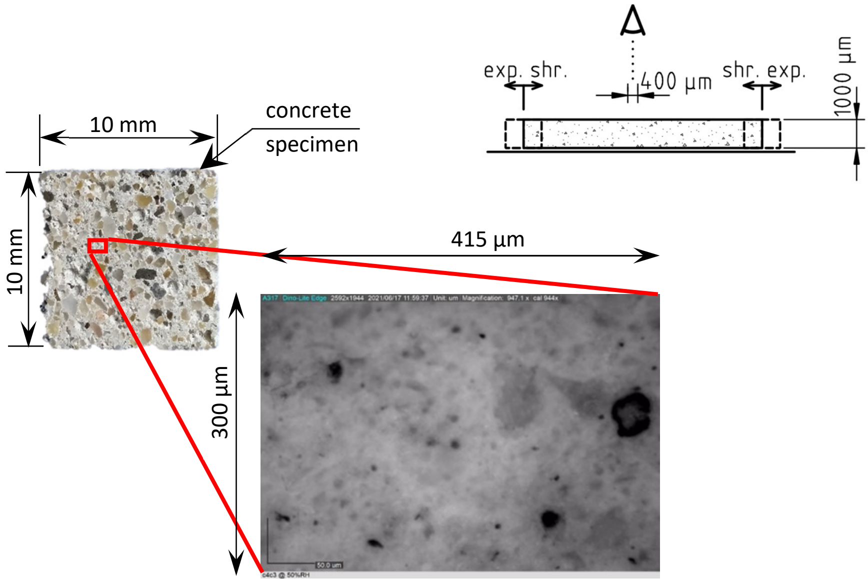

Figure 8.1: Illustration of microscopic scale images with regard to optical microscopy specimen Top left: top view of specimen and of captured image of cement paste (bottom). Top right: cross-section of the specimen.

8.1.2.1 Exposure during testing

To change the RH in direct proximity of the specimen, the temperature is changed by means of a temperature controlled stage (T >, RH < and vice versa). The temperature changes in the stage (ΔT = 2-5°C) between different RH steps generally took less than 10 seconds. The temperature change in the specimen occurred within a minute. During the test cycle, the stage temperature was continuously monitored and the specimen temperature was checked with an infrared thermometer. Images were taken when both the temperatures of the specimen and of the stage were stable. A minimum waiting time of 3 minutes was taken into account after stabilization of the temperatures. The RH steps are equal to those in the ESEM tests.

8.1.2.2 Test scheme

Microscopic scale tests were conducted at four moments in time (see Figure 8.2). Shortly after specimen preparation the first test cycle was conducted (week 1). Three consecutive test cycles followed at week 10, week 20 and week 30 (+/- 2 weeks). The RH-regime to which the specimens are exposed during the test cycles is equal to the tests on the ESEM specimens.

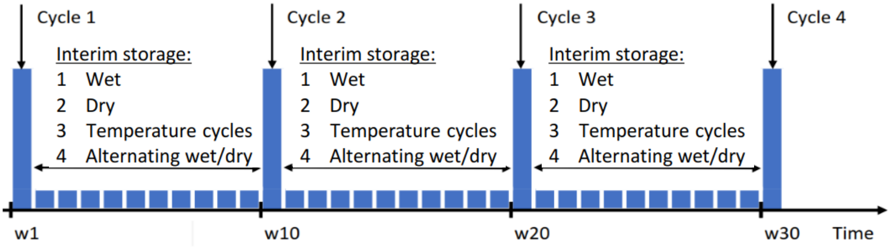

Figure 8.2: Test scheme of microscopic scale tests on optical microscopy specimens: 4 test cycles in week 1, 10, 20 and 30.

8.1.3 Mixture composition of test specimens

The mixture compositions of the old and young specimens are equal to those of the ESEM specimens, as mentioned in section 7.1.3.

8.2 Results: swelling and shrinkage, local strains

8.2.1 Mean swelling and shrinkage over AOI

General findings

Characteristic points of the measurements are:

1. Mean swelling;
2. Mean shrinkage.

In the following these characteristic points are summarized for all the tests on the four different interim storage conditions and the different specimen types. Individual measurements are summarized in Appendix G.3. In Appendix G.3, the mean deformation $\bar{\varepsilon}$ over the AOI upon wetting from 50% RH to 100% RH and subsequently drying from 100% RH to 50% RH are given for all four test cycles on old and young specimens, respectively. The strains shown in Appendix G.3 are summarized in box plots in Figure 8.3 and Figure 8.4 (mean swelling $\bar{\varepsilon}_{50\%-100\%\,RH}$ in Figure 8.3 and mean shrinkage $\bar{\varepsilon}_{100\%-50\%\,RH}$ in Figure 8.4). The measured mean swelling $\bar{\varepsilon}_{50\%-100\%\,RH}$ upon wetting from 50% RH to 100% RH varies between 0.05 ‰ and 8.2 ‰ and the mean shrinkage $\bar{\varepsilon}_{100\%-50\%\,RH}$ upon drying from 100% RH to 50% RH varies between -0.01 ‰ and -9.8 ‰. This is much larger than ultimate swelling and shrinkage strains observed at macroscale. The small mean displacements are measured at locations on the specimen with a large restraint, either below the surface or in the direct vicinity of the AOI.

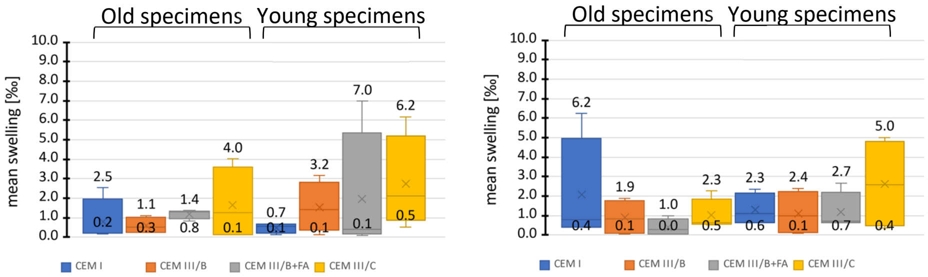

a) exposed to dry interim storage

b) exposed to wet interim storage

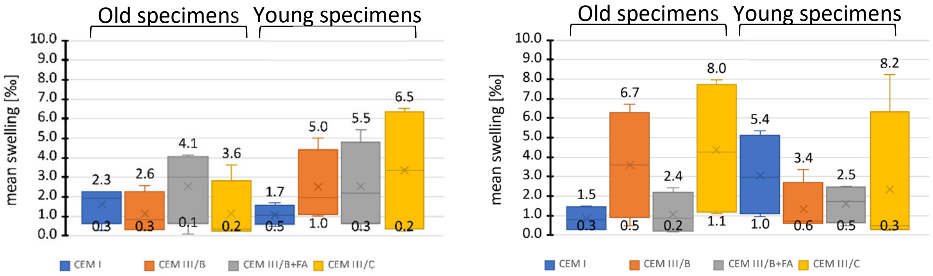

c) exposed to temperature cycles in interim storage

d) exposed to alternating wet-dry interim storage

Figure 8.3: Box plots of mean swelling $\bar{\varepsilon}_{50\%-100\%\,RH}$ in all four test cycles in old & young specimens for different interim storage conditions.

In spite of the large swelling and shrinkage, no damage was observed on the surface of the specimens. The mean strains were larger than the values found in the ESEM specimens. This was expected given the boundary conditions of the optical microscopy specimens. Because the optical microscopy specimens are only 1-1.5 mm thick, the degree of internal restraint is low and moisture exchange with the environment occurs quickly.

Effect of interim storage on strain characteristics

The box plots in Figure 8.3a/d and Figure 8.4a/d indicate that the largest mean strains in optical microscopy specimens did not occur in specimens that were exposed to dry interim storage but rather in specimens kept in alternating wet-dry interim storage. This is different from ESEM specimens where the largest mean strains were found in the specimens exposed to dry interim storage. This difference is assumed to be caused by the temperature changes that are used to control the RH in the direct vicinity of the optical microscopy specimens, as explained in section 4.7.2. In the ESEM tests, RH is controlled by changing the vapour pressure. Therefore, hygrothermal effects did not occur in ESEM tests.

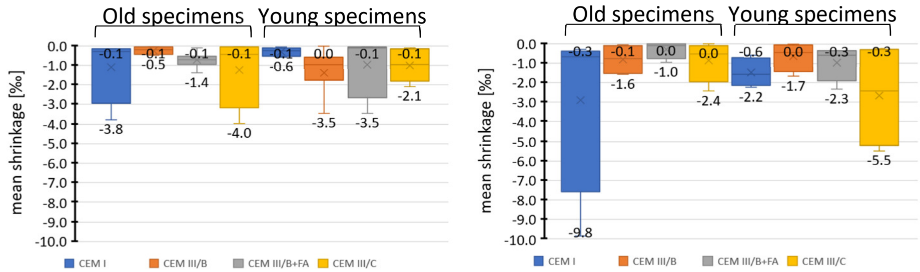

a) exposed to dry interim storage

b) exposed to wet interim storage

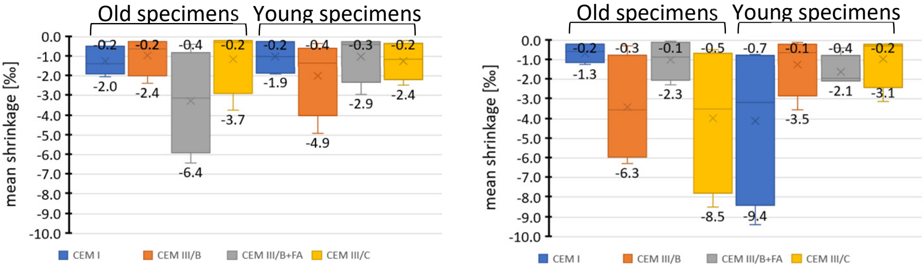

c) exposed to temperature cycles in interim storage

d) exposed to alternating wet-dry interim storage

Figure 8.4: Box plots of mean shrinkage $\bar{\varepsilon}_{100\%-50\%\ RH}$ in all four test cycles in old & young specimens for different interim storage conditions.

Effect of binder type on strain characteristics

From Figure 8.3 and Figure 8.4, no significant differences can be pointed out between specimens with different binders. However, it was found that the mean swelling in specimens with CEM III/C is often larger than in other specimens (Figure 8.3a-d, yellow boxes). It is assumed that this is caused by the difference between the pore system of specimens with CEM III/C and other specimens.

Effect of specimen age on strain characteristics

From the box plots in Figure 8.3 and Figure 8.4, no significant differences can be pointed out between specimens of different age.

8.2.2 (Fictitious) local strains in the cement paste

General findings

Fictitious local strains were calculated from the local displacements. The characteristics of local strains are:

1. compactions and rarefactions;
2. extreme fictitious local strains.

Figure 8.5 shows a 3D surface chart of the measured local strains in X-direction in a specimen. The majority of measured local strains is in the range of +/- 600 ‰ (the mainly green & light blue area in the chart). Peaks in the chart indicate extreme strains.

The strains in the optical microscopy specimens are about 5 times larger than in the ESEM specimens. This difference does not originate solely from the different boundary conditions of the specimen. As mentioned in section 4.7.2, the effect of warming up and cooling down of the specimens during the optical microscopy tests leads to significant redistributions of water in small pores, possibly explaining the large local strains.

Compactions and rarefactions

The 3D surface chart of the local strains, shown in Figure 8.5, indicates the occurrence of large compactions and rarefactions (in the order of 3000 – 4000 ‰) near voids in the cement paste and along the edges of grains with a high stiffness (e.g. aggregate grains or unhydrated cement grains).

Extreme fictitious local strains

Figure 8.6 shows a part of the 3D surface chart which corresponds to the red square in the specimen image shown in Figure 8.5. Extreme local strains of 4065 ‰ and -4527 ‰ were calculated along the edge of an aggregate grain.

Local strains in relation to mean strains

The mean strain over the area of the surface chart in Figure 8.6 (103 x 103 µm²) is 255 ‰, whereas the mean swelling over the whole AOI (about 400 x 300 µm²) is 1.1 ‰. The mean strains over respective areas of optical microscopy specimens are in the same order of magnitude as those of the ESEM specimens. However, the extreme local strains are much larger in measurements on optical microscopy specimens.

As in the ESEM specimens, no notable differences were found between the magnitude of local strains in specimens with different binder, between specimens exposed to different interim storage conditions and between specimens of different age.

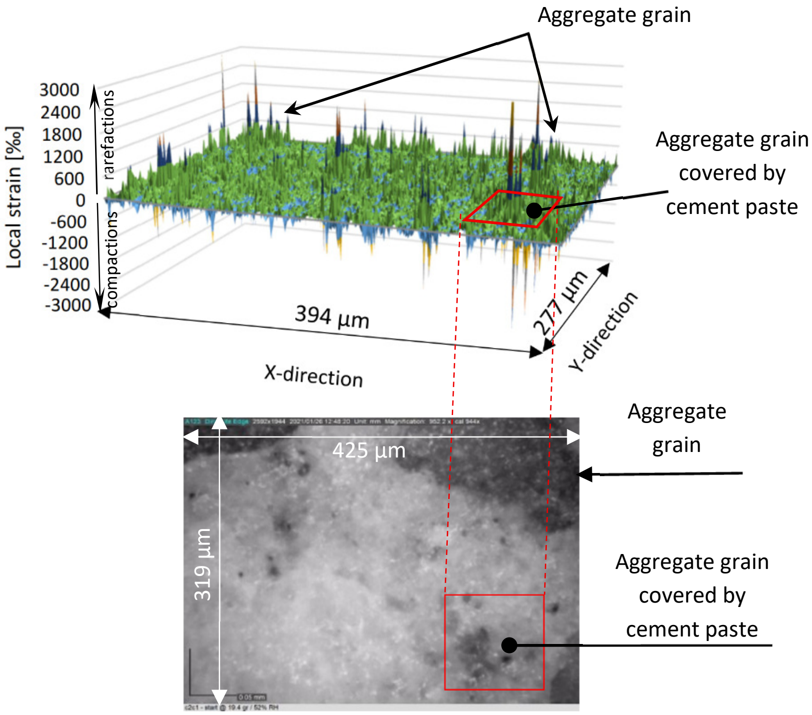

Figure 8.5: Local strains in X-direction at 100% RH in old specimen with CEM III/B during test cycle 2 (Top). Between test cycles, the specimen was kept in dry interim storage. The image at the bottom shows the morphology of the specimen, captured with optical microscope. The red square indicates an aggregate grain covered by cement paste.

8.3 Discussion

Differences were found between ESEM and optical microscopy specimens in the magnitude of the mean strains and of the local strains.

Mean strains

It was mentioned in section 8.2.1 that the mean strains in optical microscopy specimens are larger than in the ESEM specimens. This shows that the different boundary conditions of ESEM and optical microscopy specimens have an effect on the magnitude of mean swelling and shrinkage in the specimens. The small differences between the mean strains over the AOI measured on the surface of ESEM and optical microscopy specimens indicate that the restraint at the bottom of the ESEM specimen only slightly influences the mean strain at the top of the specimen, as explained in 4.4.2.2.

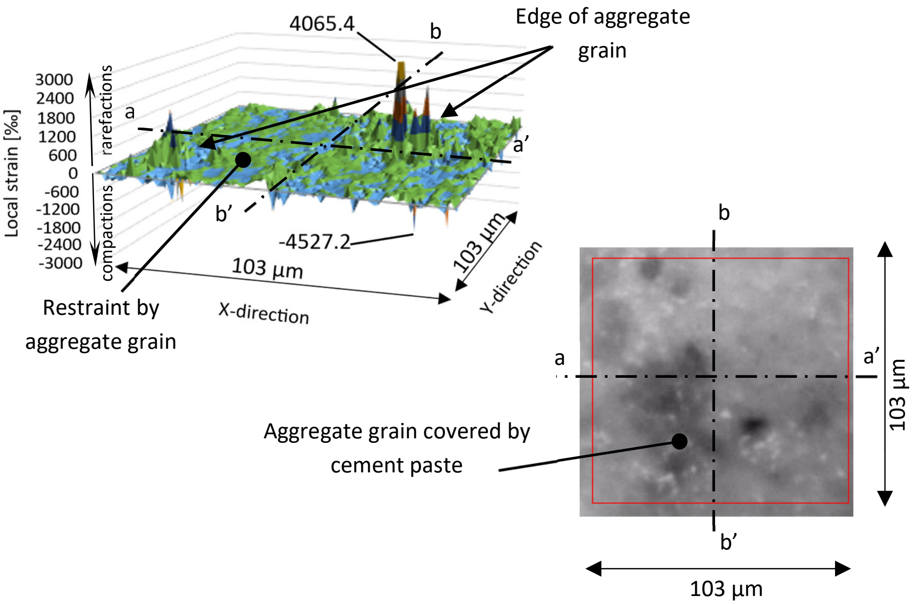

Figure 8.6: Local strains in X-direction at 100% RH in part of old specimen with CEM III/B during test cycle 2 (Top). Between test cycles, the specimen was kept in dry interim storage. The image at the bottom indicates the area considered in the 3D surface chart.

Local strains

The measured local strains were much larger in optical microscopy specimens than in ESEM specimens; the extreme local strains are approximately 5 times larger in optical microscopy specimens than in ESEM specimens. It may well be that the difference between the local strains in ESEM and optical microscopy specimens is caused by the temperature changes in the specimen during the test cycle, as was already mentioned in section 8.2.2. The behaviour of cementitious material under temperature changes on microscale is complex. Bazant [35] (amongst others) studied the coefficient of thermal expansion (CTE) of cement paste and concrete and split the response of cementitious material to temperature change up into three mechanisms: pure temperature dilatation, thermal expansion or swelling and hygrothermal dilatation. Pure temperature dilatation is the immediate dimensional response of the material to temperature change proportional to the CTE. Thermal expansion or swelling are the immediate and delayed effects of water exchange between gel pores and capillary pores as a result of energy equilibrium. Hygrothermal dilatation is the volume change as a result of a change in RH which comes with the temperature change. The hygrothermal dilatation is the response that was measured in the test cycles on ESEM specimens. The effects of pure temperature dilatation and (differential!) thermal expansion or swelling of different phases in the microstructure are specific for the optical microscopy specimens and may well be the reason why the local strains in optical microscopy specimens are much larger than in ESEM specimens.

Extreme fictitious local strains

In section 6.3.3, the accuracy and magnitude of errors in DIC analysis was discussed. The ‘mean’ of all local strain measurements in optical microscopy specimens calculated from a displacement field (as indicated in Figure 6.13) is $<|15\ ‰|$ at a standard deviation $\sigma \approx 260\ ‰$. The displacements and the local strains are normally distributed, so that 99% of the calculated local strains are $<|650\ ‰|$ i.e.: $(2.48 \cdot \sigma)$. Should an error of 10% occur to the measurements, the mean would still be $<|17\ ‰|$ and 99% of the calculated local strains is expected to be $<|700\ ‰|$; still about one order of magnitude smaller than the extreme local strains. It is unlikely that the extreme fictitious local strains are the result of accuracy of the measurements and/or errors in the analysis.

8.4 Conclusions

In this chapter, the results from the microscopic scale research on ESEM specimens were presented, interpreted and discussed. The following conclusions are drawn:

- The relatively small difference between the mean strains over the AOI in ESEM and optical microscopy specimens indicates that in a specimen with a thickness of 1-1.5 mm already representative mean strain values can be measured.
- Extreme compactions and rarefactions that were measured at the surface of the cement paste did not cause cracking or damage to the specimens. Found extreme local strains are in the order of +/- 5000 ‰. Such large compactions and rarefactions were concentrated around stiff grains and voids in the cement paste.
- Although the measured strains on optical microscopy specimens originate from a significantly different image gathering method, the measured mean strains over the AOI are comparable to the mean strains in the ESEM specimens. This indicates that no negative effects were introduced by the different way of image gathering.
- The extreme local strains in optical microscopy specimens are much larger than in ESEM specimens. This is probably the result of the temperature changes to which specimens were exposed during the test cycles.
- The calculated extreme fictitious local strains are not caused by measurement errors or inaccuracies during image capturing.
- The mean strains over the AOI were up to one order of magnitude larger than shrinkage and swelling strains measured on macroscale specimens. In actual structures deformations similar to those found in the optical microscopy specimens will not occur.

9 Evaluation, interpretation & conclusions

9.1 In search for traces of ageing in cementitious materials

Recap of the concept of ageing

Ageing is, by definition, a material-inherent change of the performance over time. Changes in performance are assumed to be caused by changes on atomic or molecular level (atoms shifting between vacancies or dislocations, basically diffusion of atoms or molecules through the material). The effects of changes at atomic level are expected preferably at grain boundaries between different crystals or between crystalline and amorphous material. Autonomous changes at atomic or molecular scale lead to changes in the micro- or sub-microstructure of the material. Such a development or change is denoted ageing. Autonomous ageing occurs without loading of the material. Internal gradients are considered to be the driving mechanisms behind ageing processes. These gradients lead to flow in the material and this flow may cause changes in the material that may affect its performance.

Aim of this study

In this study tests were conducted with the aim to explore signs of ageing phenomena in cementitious materials. Ageing processes occur at a slow rate. This complicates experimental testing of ageing phenomena. To identify ageing phenomena on microscopic scale, a research method was developed with the intention to accelerate ageing processes in the material by increasing the stress level. Strains were induced by exposing specimens to humidity cycles with or without temperature cycles. During these test cycles, images of the material were gathered with ESEM and optical microscopy. Deformations in the cement paste at the microscopic scale were measured by analysing differences between the images using suitable software. As a result of imposed higher stress levels, it was expected that ageing-related changes in the deformational behaviour would become measurable. Additionally, it was attempted to identify ageing phenomena from changes in the mineralogy with XRD tests.

9.2 Evaluation of findings

9.2.1 Findings from the XRD study

The goal of the XRD study was to investigate whether significant changes in the mineralogy of the cement paste occurred over time. Changes were investigated by comparing the mineralogic composition of cement paste samples before and after prolonged exposure (37-40 weeks) to four different exposure regimes.

The main changes in the mineralogy of the samples before and after exposure were carbonation and a reaction of dolomite with Portlandite. Observed changes are common in cementitious materials that are exposed to similar conditions. These changes are not related to or interpreted as ageing. They are the result of exposure to outdoor conditions, rather than what has been defined as autonomous ageing. It was found that cement paste specimens with CEM I are less susceptible to a change in the structure of the material than cement paste with CEM III.

9.2.2 Main findings from the microscopic scale study

The aim of the microscopic scale study was to find changes or decay in the cement paste of mortar and concrete specimens that might point to ageing. It was assumed that ageing changes the deformational behaviour at the microscopic scale. Changes in the deformational behaviour of the microstructure at the exposed surface of the specimen were investigated in four consecutive test cycles. In a test cycle, the specimens were exposed to humidity cycles with or without temperature cycles. The observed microscopic displacements developed within several minutes after exposure to changing humidity conditions. Because of the heterogeneity of the cement paste strain concentrations were expected when exposed to humidity changes. It is expected that at sites where local displacement concentrations occur, nano- or microcracking might occur during wetting and drying of the specimens.

Different test methods & boundary conditions of specimens

Two different test methods were used:

1. electron microscopy on 1-1.5 mm thick ESEM specimens that were glued to a copper base plate and
2. optical microscopy on 1-1.5 mm thick optical microscopy specimens.

Images from the top surface of the specimen (area of interest (AOI) 0.4 x 0.3 mm²) were captured during the test cycles at relative humidity between 50% and 100% RH. Deformations were measured at the top surface layer of the specimens. Image resolution is 1536 x 1025 pixels at a pixel size of 0.27 x 0.27 µm² for electron microscope images and 2592 x 1944 pixels at a pixel size of 0.164 x 0.164 µm² for optical microscope images. Similar experiments have been performed by Neubauer et al (2000) [21,22,53,54].

Analysis results - mean deformation and local deformation

From the measurements, two kinds of deformations were calculated:

1. The mean deformation over the AOI and
2. The local displacement of subsets[7] (so-called fictitious local strains).

1. Mean deformations – swelling and shrinkage

On wetting, mean swelling strains over the AOI up to 5.1 ‰ in ESEM specimens and up to 8.2 ‰ in optical microscopy specimens were measured. Mean shrinkage strains over the AOI up to -4.3 ‰ in ESEM specimens and up to -9.8 ‰ in optical microscopy specimens were measured. In the ESEM specimens the mean swelling strains are *smaller* than the mean shrinkage strain measured upon drying. In the optical microscopy specimens the mean swelling strains are *larger* than the mean shrinkage strains. A difference between the mean swelling and mean shrinkage indicates a residual deformation in the specimen. In ESEM specimens a residual mean swelling remains whereas in optical microscopy specimens a residual mean shrinkage remains. The difference between the residual mean strains in ESEM specimens and optical microscopy specimens is caused by the boundary conditions of the specimen, as explained in section 4.4.2.2. In the ESEM specimens moisture exchange takes place from the top of the specimen. When the specimen is still equilibrating at the end of the drying phase (moisture can only be desorbed from the top), the top of the specimen may not have been fully equilibrated to 50% RH and therefore a residual swelling remains. In the optical microscopy specimens moisture exchange takes place at both the top and the bottom of the specimen. During the drying phase the temperature of the specimen is increased to decrease the RH around the specimen. The ambient RH in the room where the optical microscopy tests were executed was >55 %. Therefore, the temperature at the last RH step (50% RH) needed to be elevated with respect to the ambient temperature. The hygrothermal response of the specimen may have led to a shrinkage strain in the specimen with respect to the initial situation.

---

[7] Subset: a group of pixels in an image, serves as 'landmark' for deformation analysis.

2. Local deformations – compactions and rarefactions

Fictitious local strains were calculated by subtracting the displacement of adjacent subsets. Positive fictitious local strains (subsets moving apart) are called rarefactions and negative fictitious local strains (subsets moving towards each other) are called compactions. Locally, fictitious local strains up to three orders of magnitude larger than the mean strains were measured, mainly at 90% < RH < 100%. Such large strains occurred mainly around solid particles with high stiffness, near voids but also on top of aggregate grains. Extreme local strains occur in couples; extreme compactions and extreme rarefactions were found in adjacent subsets with a spacing of about 1.3 - 5 µm.

Effect of interim storage conditions on mean deformation and local strains

Mean swelling and shrinkage strains were generally larger in specimens that were stored at a lower mean humidity (50% RH) prior to the test cycles than in specimens that were stored at higher mean humidity (>95% RH) prior to the test cycles.

No correlation could be found between the magnitude of *local* strains and the climatic conditions during interim storage of the specimens. In ESEM specimens fictitious local strains of up to 1400 ‰ were found in all four interim storage conditions. In optical microscopy specimens fictitious local strains of up to 5000 ‰ were found in all four interim storage conditions.

9.3 Interpretation and discussion on the microscopy study

9.3.1 Mean strains over AOI

Effect of different boundary conditions of specimens on swelling and shrinkage

In ESEM specimens the mean swelling strains over the AOI as a result of wetting from 50% RH to 100% RH were between 0.06 and 5.1 ‰. Mean shrinkage strains over the AOI upon drying from 100% RH to 50% RH were between -0.01 and -4.3 ‰.

In optical microscopy specimens, the mean swelling strains over the AOI as a result wetting from 50% RH to 100% RH were between 0.05 and 8.2 ‰ and mean shrinkage strains over the AOI upon drying from 100% RH to 50% RH were between -0.008 and -9.8 ‰.

Scatter in mean deformations is large between different test cycles and different specimens. The is caused by restraints in the specimen near the AOI or just below the surface of the specimen in the AOI. The optical microscopy specimens can deform without macroscale restraint and therefore any local restraint becomes more apparent in the measurements, compared to ESEM specimens. In Figure 9.1 an ESEM image is shown of an old specimen with CEM I with 3 aggregate grains surrounding the microstructure in the AOI. Mean swelling strain at 100% RH is 0.9 ‰ in X-direction and 0.05 ‰ in Y-direction (see Appendix F.3, page F.12, test 1). These small mean strains are assumed to be caused by stiff grains around the AOI or just below the surface of the specimen (either visible at the surface or just below) at the location of the AOI. In some cases the degree of restraint caused by stiff grains appeared to be up to 95% of the mean deformations that were found in other specimens. Due to the restraints in some of the specimens, only very small mean displacements could be measured at the top surface.

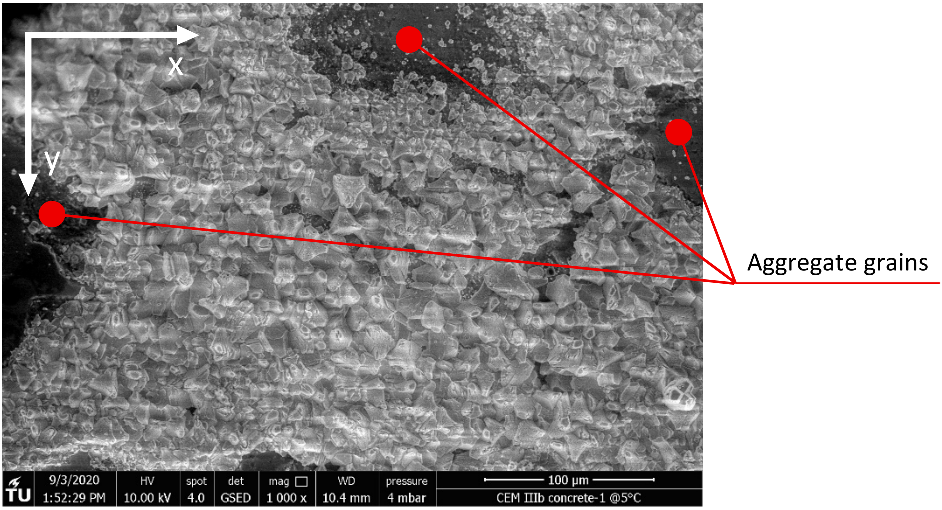

Figure 9.1: Stiff grains (in this case: aggregate grains) along edges of AOI. Old specimen with CEM I during test cycle 1. Between test cycles, the specimen was kept in dry interim storage.

The ESEM specimens were restrained at the bottom of the specimen (fully bonded to a circular copper plate). The swelling and shrinkage *patterns* measured at the top surface of restrained ESEM and free optical microscopy specimens were comparable, be it that the mean swelling and shrinkage strains at the top of ESEM specimens, measured over an area of about 300 x 400 µm², are roughly 50% smaller than in optical microscopy specimens.

The calculated mean strains over the AOI at the top surface of both optical microscopy and ESEM specimens (up to 9.8 ‰) are about one order of magnitude larger than shrinkage or swelling strains in macroscale cement paste specimens (up to about 1 ‰).

In section 3.2.1.4, the difference between the response of thin microscale and massive macroscale specimens to humidity changes was already clarified.

In section 9.2.2 it was mentioned that residual mean strains over the AOI occur. Given the test procedure in both ESEM tests and optical microscopy tests, these residual strains may be an artefact of the measurement. It is, therefore, not likely that these residual strains are a cause for damage. Possible stresses induced by the residual strains may have diminished as a result of creep and relaxation during interim storage.

Representativity of mean deformations – response time

The specimens were cut from bulk material, relatively far away from a zone where edge effects (e.g. due to exposure, sampling etc.) play a role. During the test cycles (50% RH to 100% RH) moisture exchange occurs mainly in capillary pores and the larger gel pores (as clarified in section 4.7.1). Because the specimens were thin (1-1.5 mm), moisture uptake and the resulting deformation occurred within a few minutes after being exposed. The quick response to humidity changes of the thin specimens used in this study is similar to the findings of Zhang et al. [55]. Zhang et al. performed water uptake tests in cracks of macroscale specimens. They showed that cementitious material on both sides of a crack becomes saturated within a minute after exposure to water up to a depth of about 2-3 mm. With that in mind, it is plausible that the deformations as a result of moisture changes in the specimens measured in this study occur quite quickly and the deformations are considered representative for microscopic scale deformations in thin specimens.

9.3.2 Fictitious local strains

9.3.2.1 Observations

From (subset) displacements, fictitious local strains are calculated, i.e. compactions and rarefactions. Compactions are negative strains, rarefactions are positive strains. In the majority of compactions and rarefactions the strain magnitude was <|200 ‰|. However, much larger local strains were also found, up to about |1000 ‰| and even larger (in optical microscopy specimens up to |5000 ‰|).

In Figure 9.2, fictitious local strains in the AOI of a restrained CEM III/C specimen after wetting from 50% RH to 95% RH are shown in an isometric surface map. The graph shows that, at microscopic scale, extreme fictitious local strains up to and beyond |1000 ‰| occur upon saturation of the specimen. Due to the heterogeneity of the microstructure a non-uniform deformation pattern is found.

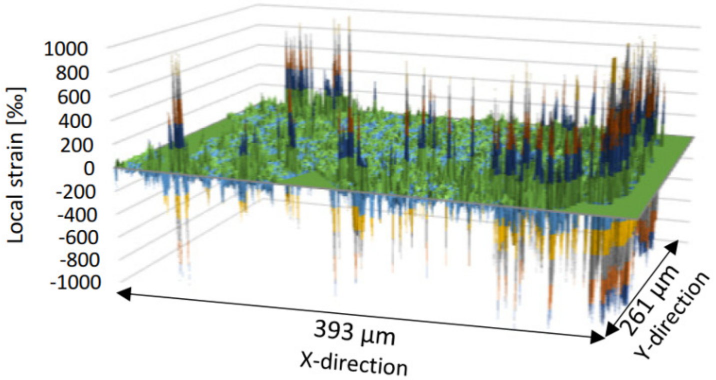

Figure 9.2: Isometric surface map of fictitious local strains calculated from deformations in X-direction after wetting from 50% RH to 95% RH in restrained CEM III/C mortar specimen during the second test cycle after 15 weeks. Between test cycles, the specimen was kept in alternating wet-dry interim storage.

Typically, fictitious local strains in the AOI appear to be normally distributed, although the tails of the distribution are very long as illustrated in Figure 9.3. About 90-95% of the strains are smaller than |100 ‰|. At high relative humidity, fictitious local strains of |1000 ‰| or more were calculated in 0.3% of the AOI. Local strains and the distribution of local strains in specimens with different binders were comparable. Over the four test cycles, no change in strain patterns was found, i.e. no propagation of sub-microscale damage could be found in the cement paste.

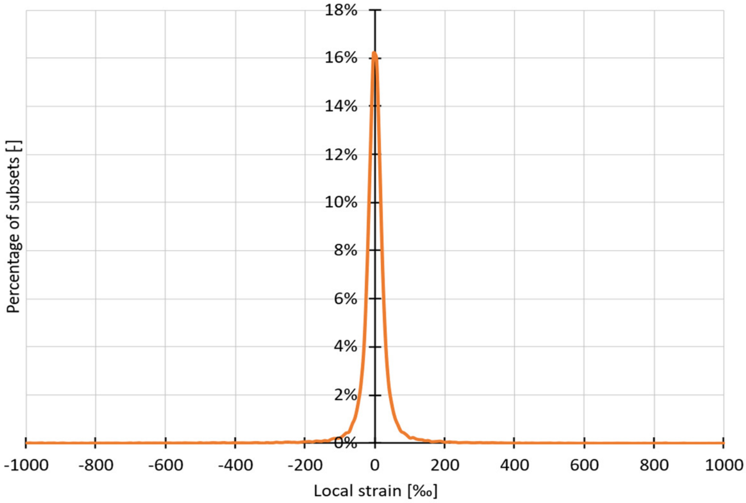

Figure 9.3: Typical distribution of fictitious local strains after wetting from 50% RH to 95% RH.

Development of extreme local strains during microscopy tests.

Figure 9.4 to Figure 9.7 show fictitious local strains in X-direction in the AOI of four specimens with different binders during a test cycle. The specimens are wetted (from 50% RH to 100% RH) and dried (from 100% RH to 50% RH). The maps show the strains with respect to the reference RH of 50% at the start of the test cycle. Upon wetting (increase in RH), the number of locations with extreme fictitious local strains increases and upon drying the number decreases.

The diagrams in Figure 9.4 to Figure 9.7 show that compactions and rarefactions with a magnitude <|200 ‰| increase and decrease with increasing and decreasing RH without significant residual strains. The majority of extreme fictitious strains occurred at high RH (> 90% RH) and at 50% RH at the end of the drying phase, almost all extreme local strains had disappeared.

9.3.2.2 Moisture and the microstructure at the surface of the specimens

For an interpretation and explanation of the local strains, the effects of moisture on both the microstructure and on microscopic imaging and image analysis are clarified.

During the test cycles the specimens were exposed to moisture changes. In section 4.7.1 the effects of moisture in the pore system of cement paste was described and quantified using the Kelvin and Young-Laplace equations. Based on that theory, moisture uptake and the effects on a cement paste is exemplified in Figure 9.8. The figure shows the location of a semi-loose particle (particle with red dot) at the top surface of cement paste near a void in subsequent RH stages. The water in capillary pores is shown at various RH. With increasing RH, at first small pores and gradually larger pores become filled with water. The diameter of the pores that become filled with water increased from 3 nm at 50% RH (Figure 9.8a) to 208 nm at 99% RH (Figure 9.8e). At RH > 99%, pores larger than about 100 nm (0.1 µm) become filled because condensation occurs at the surface. The capillary pressure decreases with increasing RH.

A particle next to a void may experience an asymmetrical pore pressure which may lead to relatively large deformations (at 90% RH and 99% RH in Figure 9.8d and e). The movement of small particles as indicated in Figure 9.8 appears plausible. It is, however, unsure whether it explains the extreme fictitious local strains in the cement paste that were calculated in this study. The imaging resolution in both the ESEM test cycles and the optical microscopy test cycles was too coarse (0.27 µm resp. 0.164 µm) to visualise such details.

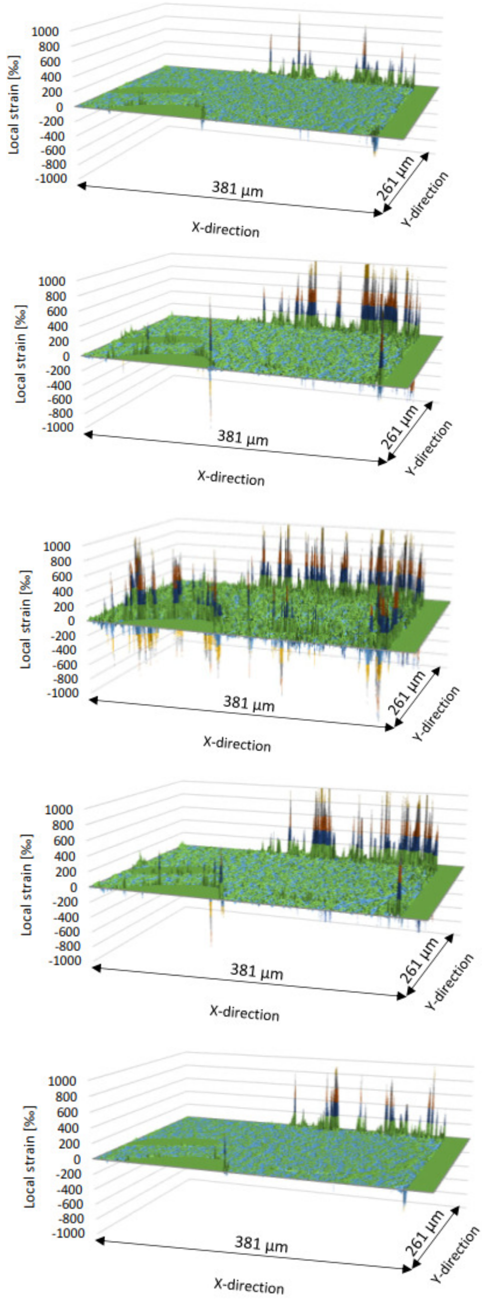

Wetting from 50% to 60% RH

Wetting from 50% to 80% RH

Wetting from 50% to 100% RH

Drying from 100% to 80% RH

Drying from 100% to 50% RH

Figure 9.4: Isometric fictitious local strain maps at different RH in an old specimen with CEM I during test cycle 1 (50% RH => 100% RH => 50% RH) (week 1). Between test cycles, the specimen was kept in dry interim storage.

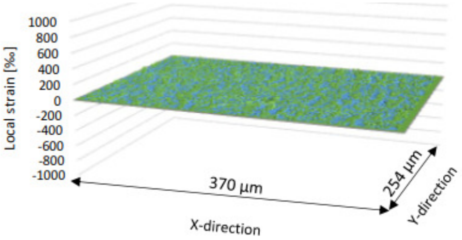

Wetting from 50% to 60% RH

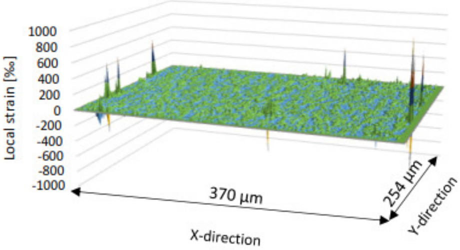

Wetting from 50% to 80% RH

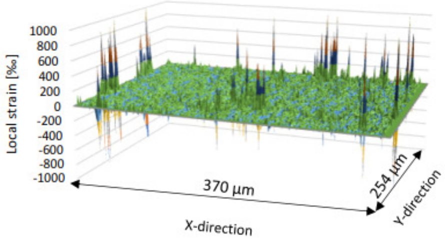

Wetting from 50% to 100% RH

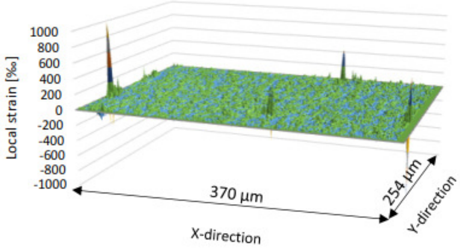

Drying from 100% to 80% RH

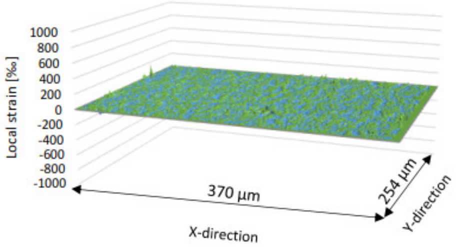

Drying from 100% to 50% RH

Figure 9.5: Isometric fictitious local strain maps at different RH in a young specimen with CEM III/B during test cycle 1 (50% RH => 100% RH => 50% RH) (week 1). Between test cycles, the specimen was kept in dry interim storage.

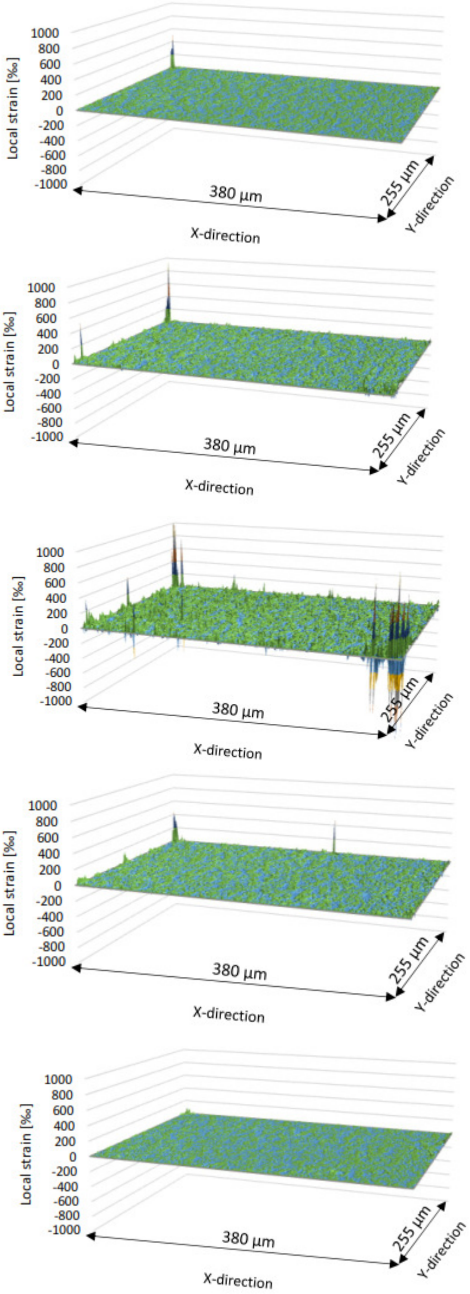

Wetting from 50% to 60% RH

Wetting from 50% to 80% RH

Wetting from 50% to 100% RH

Drying from 100% to 80% RH

Drying from 100% to 50% RH

Figure 9.6: Isometric fictitious local strain maps at different RH in an old specimen with CEM III/B+fly-ash during test cycle 1 (50% RH => 100% RH => 50% RH) (week 1). Between test cycles, the specimen was kept in alternating wet-dry interim storage.

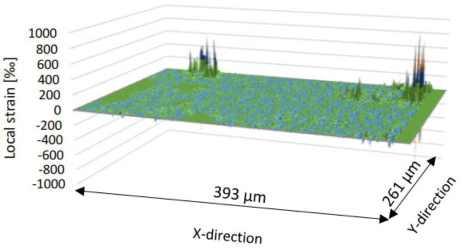

Wetting from 50% to 60% RH

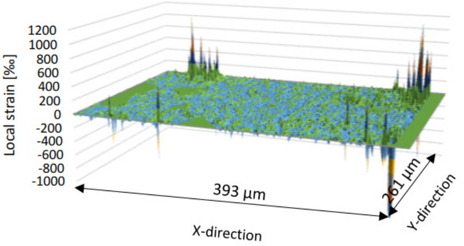

Wetting from 50% to 80% RH

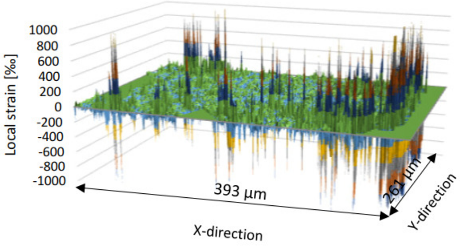

Wetting from 50% to 95% RH

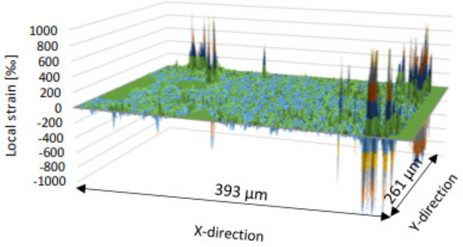

Drying from 95% to 80% RH

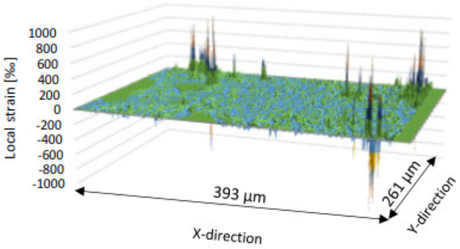

Drying from 95% to 50% RH

Figure 9.7: Isometric fictitious local strain maps at different RH in a young specimen with CEM III/C during test cycle 2 (50% RH => 100% RH => 50% RH) (15 weeks). Between test cycles, the specimen was kept in alternating wet-dry interim storage.

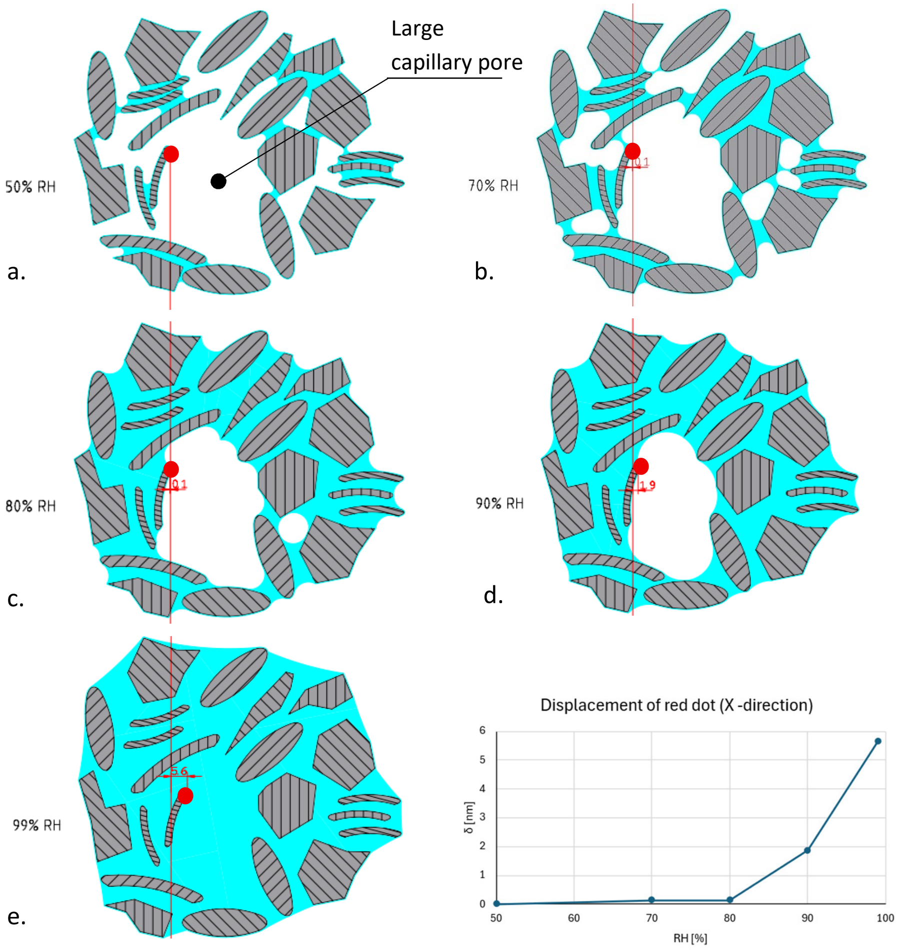

Figure 9.8: Pore water in microstructure during wetting and the movement of a semi-free particle near a void in the microstructure. At each RH, calculated radius (r_{pore}) of pores that become water-filled is given, the radius of the meniscus is given (R_{men}) and the pore pressure calculated with Young-Laplace is given.

The resolution issue could be solved by observing the specimens at a higher magnification. To match the appropriate scale (about 10 nm), the magnification would then have to be at least 25 x higher, decreasing the AOI to about 4 x 3 µm. This would make the DIC analysis much more difficult, as the topography of the specimen is no longer suitable for small subsets. On top of that, it becomes even more difficult to translate the observed effects to higher scales.

9.3.2.3 Interpretation of extreme fictitious local strains

Extreme local strains along edges of AOI at low (50% - 60% RH) humidity

What are the causes for extreme local strains at low RH? In test cycles that were conducted with ESEM, extreme fictitious local strains were found along the edges of the AOI at relative humidities much lower than 90% RH (as indicated in Figure 9.4 to Figure 9.7). It was observed that the edges of the AOI appeared dark grey or black (without visible details). This is caused by the diaphragm that regulates the width of the electron beam in the ESEM and the orientation of the GSED detector. Due to the topography of the specimens, dark grey or black areas appeared at low spots. In these dark areas the topography of the specimen is hard to distinguish. With increasing vapour pressure in the ESEM chamber more molecules are present. These molecules get hit by the electron beam and lead to an increased brightness of the images. Consequently the brightness and contrast need to be adjusted for each image. As a result, the darker spots become darker with increasing RH.

The analysis software requires contrasts between adjacent subsets to identify differences between an arbitrary image and the reference image. In most of the AOI, the topography of the specimen is sufficient for the software to identify differences between images with the selected subset size. However, when the intensity of multiple adjacent subsets is almost similar, the software struggles to identify ‘unique’ subset environments (subset + subset radius). A subset may then be recognised in a subsequent image at a location that is farther away from its actual location. When this happens, a mismatch occurs which results in extreme fictitious local strains along the edges of the AOI. In test cycles conducted with ESEM, these edge effects are considered a collateral effect of imaging in combination with the software analysis. In test cycles that were conducted with optical microscopy such edge effects were not observed (however, other difficulties occurred).

Extreme local strains at high (> 90% RH) humidity

Where do extreme local strains at high RH originate from? At high relative humidity, extreme compactions are generally found adjacent to extreme rarefactions of similar magnitude (as shown in chapters 7 & 8). The occurrence of such extreme local strains is illustrated in Figure 9.9. Extreme local strains appear when a subset makes a large shift relative to surrounding subsets. In the analysis the subsets are initially placed in an even pattern over the reference image (50% RH) as described in chapter 6. With increasing humidity a uniform swelling occurs (the perimeter subsets in the array of subsets appear to have moved gradually and show a uniform deformation). However, the middle subset has shifted out of the array; at one side a rarefaction occurred between subsets and at the other side a compaction occurred (fictitious local strains of 748 ‰ resp. -525 ‰).

At high RH capillary condensation occurs (see section 9.3.2.2 and Figure 9.8). The water in pores that become filled at high RH forms curved surfaces or menisci. In images menisci appear black with lighter edges. This leads to analysis issues in dark areas as mentioned before. Droplets on the surface appear as areas with various grey shades (from bright light grey to black) in the microscopic images due to reflection and/or refraction.

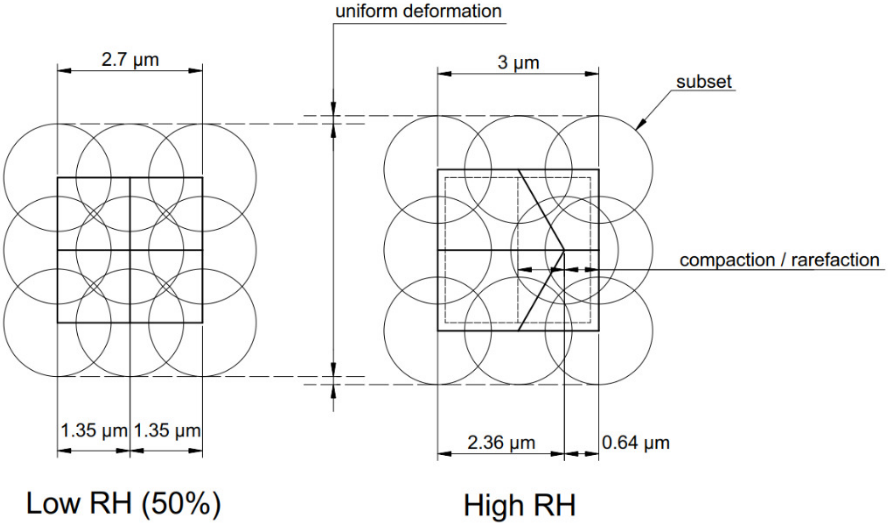

Figure 9.9: Shift of a subset leading to extreme fictitious local strain. The circles represent subsets and the lines represent the distances between the subsets. Left: undeformed group of subsets at low humidity. Right: deformed group of subsets at high humidity. One subset shifted to one side. Leading to an extreme fictitious local strain.

At high RH not only capillary condensation occurs, but also surface condensation at the top surface of the specimen. When condensation occurs, heat is released to the surroundings (heat of condensation). Because of this heat of condensation it may take a bit longer to reach a thermal equilibrium state when going to the next RH step in the test cycle. Larger grains (i.e. aggregate grains or unhydrated cement grains) form cold spots in the specimen due to their high density relative to the surrounding porous microstructure. These cold spots are points where surface condensation starts and where the first water droplets are formed. Figure 9.10 shows an example of droplet formation on an aggregate grain (cold spot). These droplets appear as areas with various grey shades. Consequently, details of the microstructure are lost and the analysis software struggles to recognise subsets in subsequent images.

Because of condensation of water at the top surface of the specimen (both the condensation originating from capillary pores and from ‘cold’ surface), tiny water droplets appear at high RH (> 90%). Due to these water droplets, the appearance of the specimen changes, which leads to previously mentioned analysis issues. Water droplet formation may well be a cause for the extreme fictitious local strains that were calculated during analysis.

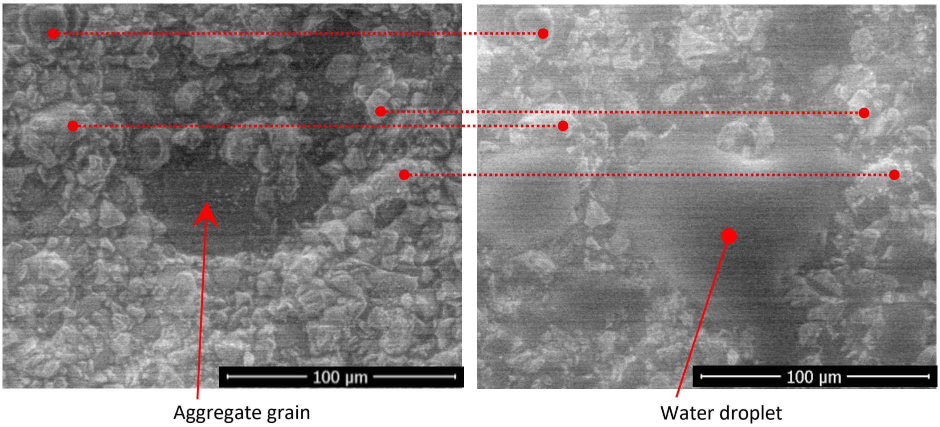

a. 80% RH b. 95% RH

Figure 9.10: Example of droplet formation on aggregate grain. Left image (a.) shows aggregate grain embedded in cement paste, right image (b.) shows water droplet on cold spot. Red dotted lines indicate similarities between both images. Young specimen with CEM III/B during test cycle 2 (15 weeks). Between test cycles, the specimen was kept in alternating wet-dry interim storage.

9.3.2.4 Visualisation of extreme fictitious local strains

This section attempts to visualise extreme local strains. A top view of the isometric surface map shown in Figure 9.2 is given in Figure 9.11a. The red square in Figure 9.11a indicates a location where an extreme compaction and rarefaction occur adjacently. In Figure 9.11b, the red square indicates the same location in the AOI on the specimen.

The area of the red square measures 23 x 23 µm². Figure 9.11c and Figure 9.11d show enlarged images of the area in Figure 9.11a and Figure 9.11b. The yellow arrow in Figure 9.11d indicates the location of the compactions and rarefactions.

Figure 9.11e and Figure 9.11f show an enlargement of Figure 9.11d. The microstructure observed at 50% RH (Figure 9.11e) and at 95% RH (Figure 9.11f) at the location of the extreme fictitious local strains is indicated by a red oval. The spacing in the orange grid indicates the subset spacing that was used in the deformation analysis and indicates the scale of the figures and the deformations. The images in Figure 9.11e and Figure 9.11f indicate that the specimen underwent a mean deformation when the RH increased from 50% to 95% (the microstructure indicated in the red oval shifted horizontally from columns 7-10 to 8-11 and vertically from rows 7-8 to 6-7).

Within the indicated red oval in Figure 9.11e and Figure 9.11f (row 7 - columns 8 & 9), extreme fictitious local strains (rarefaction of 750 ‰ and compaction of -660 ‰) were calculated. These deformations did not appear when images Figure 9.11e and Figure 9.11f are compared visually. If such large deformations are calculated, these should become visible in a comparison between images. If these deformations can not be visualised at this magnification and at the resolution used in the analysis, it is plausible that they did not actually occur. In that case, they are the result of an anomaly in the calculation due to noise[8] in the image, which is the case here. The extreme compactions and rarefactions are an analysis artefact and do not exist at all. They are most probably caused by noise in the images.

9.3.2.5 Are extreme local strains a sign for damage?

Can these extreme compactions and rarefactions be considered as damage? Whether or not extreme local strains are a sign of decay could possibly be determined using fracture mechanics. Fracture mechanics, however, presumes that damage occurs, or has occurred, and just that is still to be found out. In the work of Wittmann [56], Griffiths theory for brittle fracture (1921) [57] was used to describe crack formation in cementitious materials. It is based on the atomic distances model with the premise of linear elasticity and unlimited stress at the crack tip. A crack is considered a discontinuity in the material and the material is considered homogeneous and brittle. Cementitious materials are obviously not homogeneous at the considered scale. Because no microcracking was found in the specimens and the basic premises for Griffith's theory are, strictly speaking, not fulfilled, fracture mechanics can not play a role in the interpretation of the extreme fictitious local strains. Additionally, more recent studies [58-60] show, that this theory is less suitable for the study of fractures in cementitious materials at the scale considered in this study.

---

[8] Noise obscures features in an image; artefacts appear to be features but they are not.

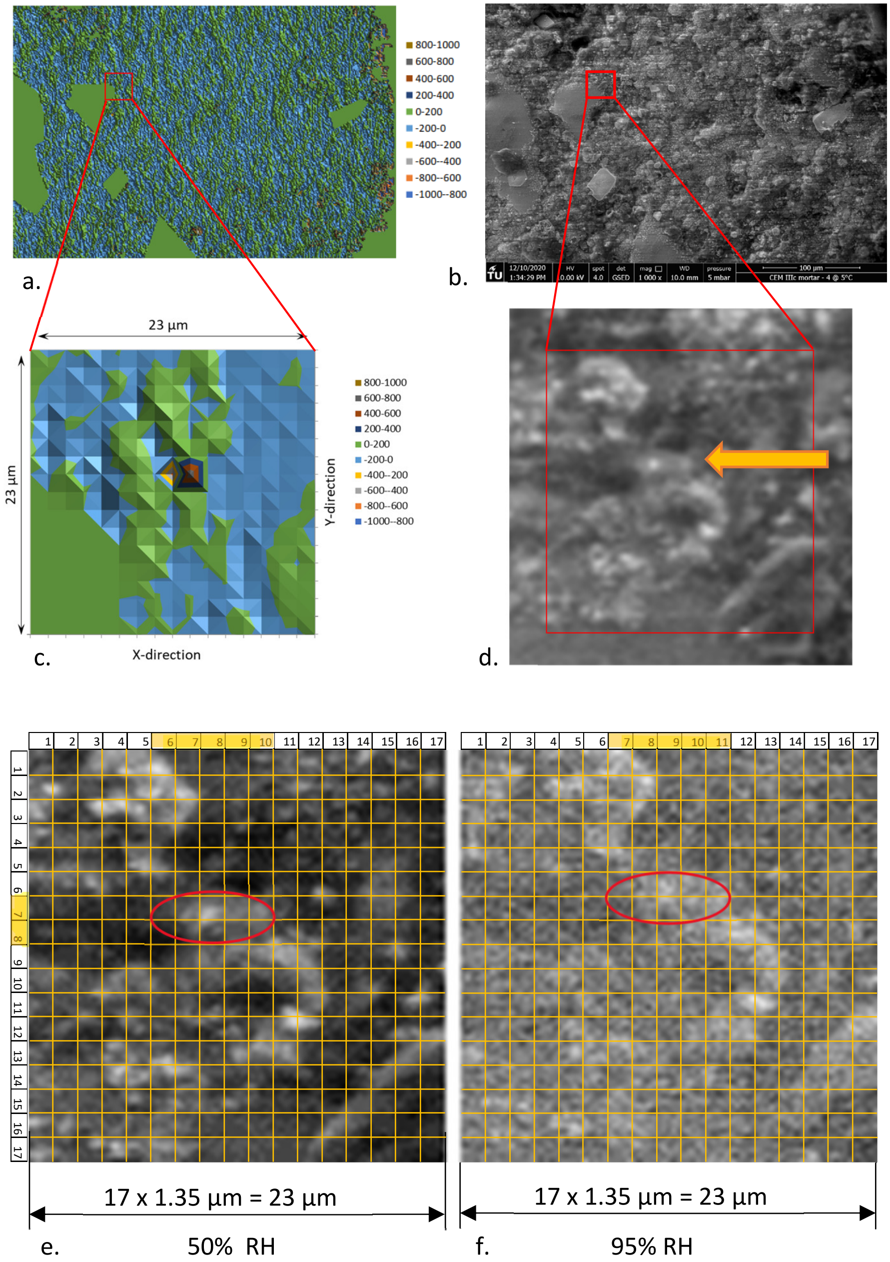

Figure 9.11: Plane map of fictitious local strains in X-direction (a) after wetting from 50% to 95% RH. Detail of local strains map (c) and microscopy images of detail section (e: at50% RH, f: at95% RH). Young specimen with CEM III/C during test cycle 2 (15 weeks). Between test cycles, the specimen was kept in alternating wet-dry interim storage. The red ovals in e and f indicate the location of calculated extreme compactions and rarefactions.

9.3.2.6 Comparison of local strains with literature

In this section, local strains published by other researchers are compared to the local strains in this study.

In the study of Neubauer and Jennings [21,22,53,54], compactions and rarefactions with a magnitude of |500 ‰| were calculated from deformation fields. Calculated deformations are about the same order of magnitude found in this study. Figure 9.12 shows the local strain distribution of a specimen that was dried from 90% RH to 55% RH (red line) from Neubauer et al.. This is roughly the same RH range as used in this study (green line, drying from 95% to 50% RH). Neubauer et al. found that the sum of compactions and rarefactions with a magnitude >|6%| was near zero, in spite of the different shapes of the left side (compactions) and the right side (rarefactions) of the graph. This is also the case with the deformations in this study, although the shape of the histograms is much more symmetric. Neubauer et al. stated that "almost all" deformations were <|6%| and that the few percent of deformations larger than 15% might be noise. This indicates that the jagged course of their graphs is partly caused by noise. In this study 90% of local strains were <|6%| and 95% of local strains were <|15%|. The extreme local strains (>200 ‰) calculated in this study are also considered as noise (see also sections 9.3.2.3 and 9.3.2.4).

A reason for the different course of the deformation graphs of Neubauer et al. and the one in this study could be that Neubauer et al. used 1 mm thick cast cement paste specimens, whereas in this study about 1 mm thick specimens were used that were cut from mortar or concrete samples. Aggregate particles form restraints, which hinder free deformation of the cement paste. The stiff grains do not deform upon changing RH. As a result, the mean strains become smaller, even though large local strains may occur because of the restraints.

In both the study of Neubauer et al. and in the experiments in this study no damage was found in the material (in the work of Neubauer et al. at least not in the drying tests up to 55% RH). In both studies large local strains up to |200 ‰|, or in the case of the study of Neubauer et al. up to |500 ‰|, could be accommodated by the cement paste without damage. The difference between the width of the range of strains between both studies is attributed to differences in the materials that were used, cement paste compared to mortar or concrete specimens. The fine aggregate particles in mortar or concrete specimens are inert. Under changing humidity, no deformational changes occur in these particles. Around aggregate particles, concentrations of compactions and rarefactions occur (with local strains up to |200 ‰|). Neubauer et al. stated that their measurements probably contained noise at local strains >|15%|, this may explain the difference between the deformation curves of Neubauer et al. and this study.

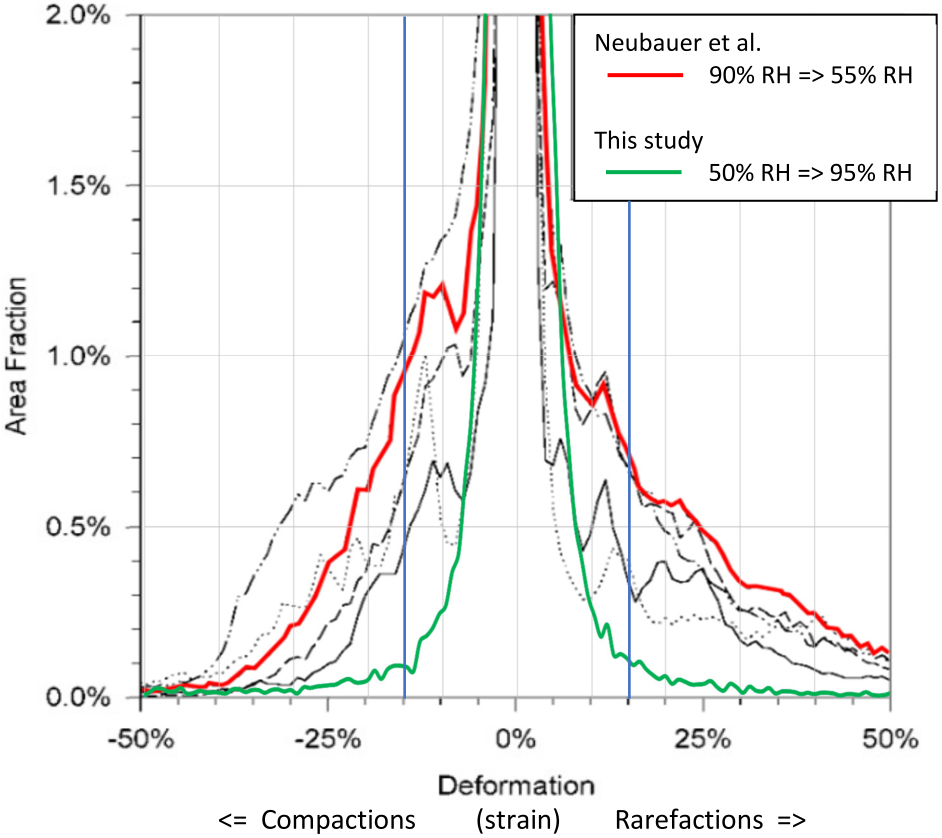

Figure 9.12: Deformation (local strain) distributions > |6%| of 7 day old cement paste sample (w/c ratio = 0.5) with an overlay of Figure 9.3 from this study (green line). Blue vertical lines indicate |150 ‰|range. Adapted from Neubauer et al.[21]. AOI in [21] = 100 x 100 µm², resolution 512 x 512 px. AOI in this study = 400 x 300 µm², resolution 1536 x 1025 px.

The work of Neubauer et al. focussed on visualising microscopic scale deformations in cement paste with the aim to visualise different shrinkage mechanisms in pastes when exposed to a humidity range of 90% to 5% RH. The current study focusses on visualising microscopic scale deformations upon exposure to humidity changes from 50% RH to 100% RH and back and searching for changes in the deformational response between subsequent test cycles. The humidity range of 50% RH to 100% RH during the test cycles was chosen to mimic exposure to outdoor environments. Although in the study of Neubauer et al. different specimens were used and other objectives were pursued than in this study, microscale deformations of similar magnitude were found.

9.3.2.7 Considerations and conclusions on local strains

The measurements in this study involve 2D images taken from the top surface of cementitious specimens. The specimens with a surface area of about 100 mm² and 1 mm thickness were cut from bulk material (mortar and concrete).

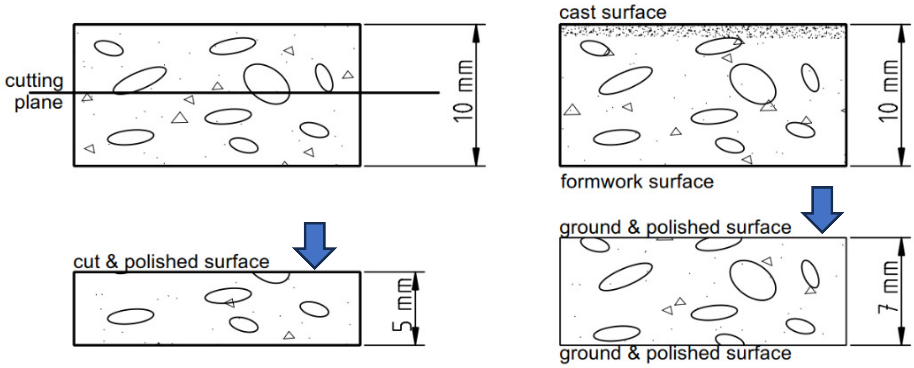

A: Specimen from cut surface

B: Specimen from cast surface

Figure 9.13: Cut surface compared to cast surface or formwork surface. Blue arrow indicates the observed surface.

The specimens were ground and polished during specimen preparation. Specimens that are taken from a cast surface or a formwork surface, as indicated in Figure 9.13, are usually ground flush and polished to avoid effects of the cement skin. The cement skin at the formwork surface and the cement skin at the cast surface (with effects of casting, compacting and (possibly) bleeding) are usually very porous and do not represent bulk material properties.

Neubauer et al. [21,22,53,54] used (unpolished) cement paste flakes with a thickness of 1 mm for similar tests. They calculated local strains of |500 ‰| in the RH range of 50% - 90% RH, about half the magnitude of the calculated extreme local strains in ESEM specimens and one order of magnitude smaller than extreme local strains in optical microscopy specimens. The different magnitude of the extreme local strains is assumed to be caused by the different specimen surface preparation of Neubauer et al. compared to the specimens in this study.

As indicated in Figure 9.4 to Figure 9.7, the bulk of extreme fictitious local strains occurred at high RH (95-100% RH). Extreme fictitious local strains were calculated near voids in the cement paste, around stiff grains or in the middle of a grain (as indicated in

Figure 9.11). The deformation analysis indicated large relative subset displacements that could not be visualised (as indicated in Figure 9.11e and Figure 9.11f). Extreme fictitious local strains were not only calculated at high RH (> 90% RH) but also at low RH (50%-60% RH).

In section 9.3.2.3 and Figure 9.8, the role of moisture during microscopic scale imaging and deformation analysis was explained. Although it is plausible that the mechanism as indicated in Figure 9.8 occurs, it may not be dominant with regard to local strains at the observed scale. The extreme local strains that were found in the deformation analysis are considered to be analysis artefacts as these could not be visualised nor reconstructed. Compactions and rarefactions up to about |200 ‰| are considered 'real' microscopic scale local strains, i.e. strains of this magnitude could be reconstructed from the microscopy images. This indicates that the adopted test method needs further sophistication as validation of strains >|200 ‰| is not possible.

9.3.3 Absence of damage

The objective in this study was to find changes or indications of decay in the microstructure of cementitious material that might be a sign of ageing. To find these changes, the material was exposed to humidity cycles (50% RH – 100% RH and back) with or without temperature changes. A study closest to this one is the work of Neubauer et al. [21,22,53,54]. The objective of their work was to perform microscale shrinkage measurements in cement paste due to drying from 90% RH to 55% RH and down to 5% RH .

In this study no changes in performance (response) of the material were found over the course of four test cycles. Test cycles were performed at 10-15 week intervals. No visible damage, no change in deformational behaviour and no change in mineralogy. Even specimens that were exposed to simulated daily temperature and humidity cycles during interim storage (supposedly the most severe of the four interim storage conditions), showed no progressive damage or change of the material (as indicated in chapters 5, 7 and 8). This is in agreement with the work of Neubauer et al. in test cycles with a similar RH range. The question remains how the material can cope with compactions and rarefactions of about |200 ‰| without taking visible or otherwise measurable decay at the adopted scale.

It is assumed that moisture in capillary pores contributes to the material's ability to accommodate the observed local deformations. The microstructure of cement paste is a composite of different constituents. Some are amorphous, other crystalline and all come in different shapes. The constituents appear as platens, long needles, hair-like webs, balls or orthorhombic crystals. They form a composite in which they are mainly connected via molecular bonds and, mostly, van der Waals bonds. A relatively small amount of bonds between constituents are (strong) chemical bonds [56]. The large deformations measured in this study require a certain malleability of the composite to accommodate the compactions and rarefactions that were shown in the isometric mappings. The porosity of the composite on the microscale determines its malleability, whereas strain concentrations (large local deformations) are the result of the heterogeneity of the composite. These large strains may be a precursor for damage, however, in this study no signs of damage were observed.

Water layers in the microstructure

In the chosen RH range the specimens were exposed to, moisture is always present in the smallest capillary pores (with a diameter of about 3 nm). At high RH (when the largest local strains were measured), the majority of the pores in the pore system is filled. The water adhered on the pore walls, combined with pore water (as illustrated in Figure 9.8), creates a layer that can accommodate large shear deformations. According to Hagymassy [61] the thickness of the adhered water layer in the RH range from 50% to 100% RH varies between 1.5 to 5.5 monomolecular layers (about 0.45 to 1.65 nm). A water layer of such thickness (at RH > 70%) enables large shear deformations. Adhesion forces between solids and water and hydrogen bonds between water molecules are generally much stronger than Van der Waals forces between molecules. Because of that, the water layers act as a 'lubricant' that enables large local displacements [62].

9.3.4 Ageing phenomena? – A discussion

The aim of this study was to find traces of change or decay in the microstructure of cementitious material that could indicate autonomous ageing. The emphasis was on changes in the deformational behaviour of cementitious material. Over the course of four test cycles (about 9 months) on small cement paste specimens, no traces of change or decay were found.

Ageing phenomena are slow and take a long time to develop. In this study it was tried to accelerate ageing processes in cement paste by exposing paste samples to humidity cycles, causing large strains and, if restrained, also stresses. A wide range of strains was measured, i.e. calculated, from observed displacements in the microstructure. The calculated strains are large <|200‰|, certainly larger than strains generally considered at macroscale (e.g. in engineering). Calculated strains are larger because of the small thickness of the specimens, as illustrated in section 3.2.1.4. These rather large local strains did, however, not lead to changes or decay in the material. Hence, at the microscale no changes of the microstructure were observed that could be referred to ageing.

Stress and strain

Large mean strains were calculated in the microscopy study. Strain only leads to stresses when restrained to any degree. The optical microscopy specimens were not restrained and the mean strains did not lead to stresses. The ESEM specimens are restrained at the bottom. This should lead to stress in the specimen, however, no damage was found during the test cycles.

With regard to fictitious local strains, the macroscale stiffness properties of cement paste are not representative at the observed scale; calculating stresses from such large strains would lead to the conclusion that specimens should be severely damaged which was, obviously, not the case. This was already explained in section 3.2.1.

What to expect with regard to ageing in cementitious material?

Ageing refers to a change in material behaviour over time. It is hard to imagine that solely time can cause such a change. The extreme local strains in the cement paste upon changing RH are caused by the heterogeneity of the paste. In a material with multiple interfaces per unit of volume some form of autonomous change is expected. This study focusses on the deformational behaviour of the cement paste under induced strain to find changes after subsequent test cycles. The premise was that, as a result of damage or decay, the deformational response of the cement paste would change. This would result in differences between local strain patterns over consecutive test cycles (exposure to humidity cycles with or without temperature cycles). Such changes were not found in this study. The question remains what to expect from ageing in cementitious material.

Effects of environmental loads on chemical activity

Gradients in the microstructure of cement paste are a precursor for “flow” or “change” in the material and they are considered the driving force behind ageing. In concrete structures that are exposed to outdoor environments, daily or seasonal temperature changes in the material lead to temperature gradients in the material. The strain in the material as a result of thermo-mechanical effects, combined with temperature changes, leads to diffusion of pore solution in the material (as explained in 4.7.2). The diffusion rate affects the rate of reaction between ions in the pore solution and minerals in the solid. As a result, a chain of events may be triggered leading to an increased probability for chemical reactions.

In this study, the effects of different exposure conditions on the occurrence of changes in the material were factored by the different interim storage conditions in which the specimens were kept between the test cycles. It was found that the effects of storage conditions on materials performance were only noticeable in the mean strains over the area of interest (AOI). Swelling was much larger in specimens that were kept in dry storage between test cycles than in the specimens that were kept in one of the other three interim storage conditions[9]. The interim storage conditions were not distinctive for local strains, let alone for changes in the microstructure or decay.

Answering the research question

In section 3.1 the following research hypothesis was posed: “Understanding ageing phenomena is a prerequisite for estimating the long-term performance of cementitious materials.”. The research question was formulated as follows: “Which changes in cementitious materials can be visualised and quantified and can be referred to as ageing?”. In this study no signs of ageing were found. Neither autonomous nor induced ageing that satisfy the definitions of ageing as formulated in section 2.6. Given the exposure time and the exposure conditions during interim storage (which were intended to mimic Dutch outdoor exposure conditions), no signs of damage or decay were found.

It was hypothesized that a change in the deformational behaviour of cement paste over time could be quantified by observing cement paste at microscopic scale. The microscopic scale studies of Neubauer et al. (2000) [21,22] were used as inspiration for the research programme. Changes in the deformational behaviour and/or decay of cementitious material as a result of ageing appears to occur at an even lower rate than anticipated beforehand. This is a reassuring finding.

In search for accelerated ageing, some interesting and relevant information was found (e.g.: magnitude of local strains, similar deformational behaviour of different binders). It can be concluded that cement paste is a robust material that can accommodate large (calculated) local strains without taking damage at microstructural scale. It is assumed that ageing may occur but its effects could not be traced in this study from only a small number of exposure situations.

---

[9] Interim storage conditions: see section 4.3

9.4 Conclusions

In search for signs of ageing phenomena in cementitious material, microscopic scale deformations in cement paste were measured. The following conclusions can be drawn:

- The experimental studies performed in this study showed that cement paste has the ability to accommodate large local strains without exhibiting signs of decay. Cementitious material can be qualified as a robust material.
- In this study, no signs of ageing phenomena were found. This indicates that the suitability of the test method is limited with regard to finding signs of ageing phenomena.
- In the microscopic scale tests no differences were found between the deformational behaviour of specimens with different binder types.
- Alterations in the material that were found in the XRD study on cement paste samples can not be referred to ageing. Changes that occurred are common in cementitious materials (i.e.: carbonation, ongoing hydration). It was found, however, that samples with CEM I are less susceptible to changes in mineralogy than specimens with CEM III under similar exposure conditions.
- In the XRD study, as well as in the microscopic scale study, the different exposure conditions during interim storage were not distinctive with regard to ageing.

9.5 Recommendations for further study

In this study, it was attempted to find changes or decay in the microstructure of cementitious material that might indicate signs of ageing. Although no signs of ageing were found, the adopted test method revealed interesting features of cementitious materials. Some suggestions and recommendations that may lead to more insight in ageing phenomena are:

- When using DIC on microscopy images without an artificial speckle pattern on the specimens (as in this study), the magnification and the image resolution should be chosen carefully. A high resolution requires a fine (artificial) speckle pattern and provides many details, however, requires long calculation times. A lower resolution leads to shorter calculation times and possibly avoids using an artificial speckle pattern but provides less details.
- The role of self-healing with regard to ageing was not mentioned yet. It may be the case, that when microcracks close, the original strength of the material is

recuperated. Would it be possible that damage in the microstructure caused by ageing almost immediately becomes repaired by self-healing?

- The occurrence of self-healing depends on the potential for self-healing of the material. To determine whether self-healing plays a role in the repair of ageing damage, the potential for self-healing should be quantified. Up to now, no such method has been developed yet.
- It may be of interest to investigate the similarities between fatigue and ageing in cementitious materials. When damage occurs in the microstructure which is repaired by self-healing, there may be a point in time when self-healing can no longer occur. If specimens are exposed to cyclic loads (multiple humidity cycles), the material may take damage due to fatigue. As the material self-heals and consumes its self-healing potential, changes or decay may be detected. Such tests will provide insight in the microscopic scale decay in cementitious material due to cyclic loading with humidity cycles.

References

[1] K. Van Breugel, D. Koleva, and T. Beek, *The Ageing of Materials and structures - towards scientific solutions for the ageing of our assets*. 2018.

[2] K. van Breugel, "Urgency and challenges of ageing in science and engineering," in *The Ageing of Materials and Structures*, 2018, ch. 1, pp. 3–13.

[3] J. R. White, "Polymer ageing : physics , chemistry or engineering ? Time to reflect," *C.R. Chimie*, vol. 9, pp. 1396–1408, 2006, doi: 10.1016/j.crci.2006.07.008.

[4] L. Struik, "Physical aging in amorphous polymers and other materials," 1977. doi: 10.1016/0040-6031(82)85085-5.

[5] AZoM, "Aging Metallurgical Processes Benefits of Aging," pp. 1–3, 2013, [Online]. Available: https://www.azom.com/article.aspx?ArticleID=9547 P

[6] Ibtisam Abbasi, "New Aging Test Method for Semiconductor Devices," AZO Materials. Accessed: Jun. 03, 2025. [Online]. Available: https://www.azom.com/article.aspx?ArticleID=22564#:~:text=Effects%20of%20Semiconductor%20Aging&text=One%20of%20the%20impacts%20of,on%20and%20turn%2Doff%20timings.

[7] Bryon Moyer, "What Causes Semiconductor Aging?," Semiconductor Engineering. Accessed: Jun. 03, 2025. [Online]. Available: https://semiengineering.com/what-causes-semiconductor-aging/

[8] W. J. Quist and A. J. van Bommel, "The Noble Patina of Age BT - The Ageing of Materials and Structures: Towards Scientific Solutions for the Ageing of Our Assets," K. van Breugel, D. Koleva, and T. van Beek, Eds., Cham: Springer International Publishing, 2018, pp. 153–165. doi: 10.1007/978-3-319-70194-3_12.

[9] Corrosionpedia, "Age-hardening," corrosionpedia.com. Accessed: Sep. 18, 2022. [Online]. Available: https://www.corrosionpedia.com/definition/58/age-hardening

[10] A. K. Van Der Vegt and L. E. Govaert, *Polymeren van keten tot kunststof*, 5th ed. Delft: VSSD, 2005.

[11] M. Kassir *et al.*, "Aging Mechanisms for Concrete Components of High-Level Waste Storage Tanks," *Concrete*.

[12] E. G. Phillipose K.E., Gregor, “Ageing Management of Candu TM Concrete Containment Buildings,” *RILEM Workshop NUCPERF 2009*, no. 1, pp. 275–285, 2009.

[13] Z. Yu, G. Ye, K. van Breugel, and W. Chen, “Ageing of Portland cement concrete cured under moist condition,” in *AMS’14 proceedings of the international conference on ageing of materials & structures*, Delft, 2014.

[14] T. Dolen, “Materials properties model of aging concrete,” 2005 doi: 10.1007/s002340050578.

[15] B. Kucharczyková, L. Topolář, P. Daněk, D. Kocáb, and P. Misák, “Comprehensive Testing Techniques for the Measurement of Shrinkage and Structural Changes of Fine-Grained Cement-Based Composites during Ageing,” *Advances in Materials Science and Engineering*, vol. 2017, 2017, doi: 10.1155/2017/3832072.

[16] K. van Breugel and T. Van Beek, “Ageing of old and modern concrete structures – Observations and research,” *Revista Alconpat*, vol. 7, no. 1, pp. 57–72, 2017.

[17] F. L. Lambert, “Chemical Kinetics: As Important As The Second Law Of Thermodynamics?,” *The Chemical Educator*, vol. 3, no. 2, pp. 1–6, 1998, doi: 10.1007/s00897980189a.

[18] F. L. Lambert, “A student’s approach to the Second Law and Entropy,” Entropy sites - a guide. Accessed: Sep. 17, 2022. [Online]. Available: https://web.archive.org/web/20090718205856/http://entropysite.oxy.edu/students_approach.html

[19] J. Hutchinson, *Equilibrium and the Second Law of Thermodynamics*. Houston: LibreTexts, 2025.

[20] NNI, “NEN-EN 1990/a1/c2 Eurocode - Grondslagen van het constructief ontwerp Eurocode,” 2010.

[21] C. M. Neubauer, E. J. Garboczi, and H. M. Jennings, “The use of digital images to determine deformation throughout a microstructure Part II Application to cement paste,” *J Mater Sci*, vol. 35, pp. 5751–5765, 2000, doi: 10.1023/A:1004835830352.

[22] C. M. Neubauer, E. J. Garboczi, and H. M. Jennings, “The use of digital images to determine deformation throughout a microstructure Part I Deformation mapping technique,” *Journal of material science*, vol. 5, pp. 5751–5765, 2000.

[23] Betoniek, “Betoniek vakblad 17/06 - Uitdrogingskrimp,” 2021.

[24] G. C. Bouquet and R. C. Braam, “Numerical analysis of long term effects on eigenstresses and micro-cracking in concrete,” in *High Tech Concrete: Where technology and engineering meet*, 2018, pp. 56–64. doi: 10.1007/978-3-319-59471-2.

[25] Guus Bouquet, *Effect of relaxation on eigenstresses and microcracking in concrete under imposed deformation*. 2019. doi: 10.4233/uuid.

[26] NNI, “NEN-EN 196-1 Beproevingsmethoden voor cement - Deel 1: Bepaling van de sterkte,” 2016.

[27] A. (KNMI) Huiskamp, “Jaaroverzicht van het weer in Nederland - 2018,” De Bilt, 2018.

[28] CUR, “CUR report 90-3 carbonation, corrosion en humidity,” 1990.

[29] R. Snellings *et al.*, “RILEM TC-238 SCM recommendation on hydration stoppage by solvent exchange for the study of hydrate assemblages,” *Materials and Structures/Materiaux et Constructions*, vol. 51, no. 6, pp. 1–4, 2018, doi: 10.1617/s11527-018-1298-5.

[30] K. Scrivener, R. Snellings, and B. Lothenbach, *A practical guide to microstructural analysis of cementitious materials*. CRC Press / Taylor & Francis, 2016.

[31] F. Gong, D. Zhang, E. Sicat, and T. Ueda, “Empirical Estimation of Pore Size Distribution in Cement, Mortar, and Concrete,” *Journal of Materials in Civil Engineering*, vol. 26, no. 7, Jul. 2014, doi: 10.1061/(asce)mt.1943-5533.0000945.

[32] F. Wittmann, “Surface tension shrinkage and strength of hardened cement paste,” vol. 1, no. 6, pp. 547–552, 1947.

[33] T. Zhou, K. Ioannidou, F. J. Ulm, M. Z. Bazant, and R. J. M. Pellenq, “Multiscale poromechanics of wet cement paste,” *Proc Natl Acad Sci U S A*, vol. 166, no. 22, pp. 10652–10657, 2019, doi: 10.1073/pnas.1901160116.

[34] M. Wyrzykowski, P. J. McDonald, K. L. Scrivener, and P. Lura, “Water Redistribution within the Microstructure of Cementitious Materials due to Temperature Changes Studied with 1H NMR,” *Journal of Physical Chemistry C*, vol. 121, no. 50, pp. 27950–27962, Dec. 2017, doi: 10.1021/acs.jpcc.7b08141.

[35] Z. Bazant, “Delayed thermal dilatations of cement paste and concrete due to mass transport,” *Nuclear Engineering and Design*, vol. 14, pp. 308–318, 1970.

[36] Z. P. Bažant and M. Jirásek, “Solid Mechanics and Its Applications Creep and Hygrothermal Effects in Concrete Structures.” [Online]. Available: http://www.springer.com/series/6557

[37] M. B. Pinson *et al.*, “Hysteresis from multiscale porosity: Modeling water sorption and shrinkage in cement paste,” *Phys Rev Appl*, vol. 3, no. 6, 2015, doi: 10.1103/PhysRevApplied.3.064009.

[38] P. (TNO) Pipilikaki and T. G. (TNO) Nijland, “Betononderzoek tunnels : achtergrondrapport bij TNO-2019-R11918,” 2020.

[39] O. Copuroglu and K. Sisomphon, “Stabilization of vaterite and aragonite in carbonated GGBFS cement paste by Na-MFP,” in *Thirty-Second International Conference on Cement Microscopy New Orleans, Louisiana USA*, 2010.

[40] J. D. Hanawalt, “Manual Search/Match Methods For Powder Diffraction in 1986,” *Powder Diffr*, vol. 1, no. 1, pp. 7–13, 1986, doi: 10.1017/S0885715600011209.

[41] E. T. Stepkowska, J. L. Pérez-Rodríguez, M. J. Sayagués, and J. M. Martínez-Blanes, “Calcite, vaterite and aragonite forming on cement hydration from liquid and gaseous phase,” 2003. doi: 10.1023/A:1025158213560.

[42] T. Saito, E. Sakai, M. Morioka, and N. Otsuki, “Carbonation of γ-Ca2SiO4 and the mechanism of vaterite formation,” *Journal of Advanced Concrete Technology*, vol. 8, no. 3, pp. 273–280, 2010, doi: 10.3151/jact.8.273.

[43] A. Leemann, H. Pahlke, R. Loser, and F. Winnefeld, “Carbonation resistance of mortar produced with alternative cements,” *Materials and Structures/Materiaux et Constructions*, vol. 51, no. 5, pp. 1–12, 2018, doi: 10.1617/s11527-018-1239-3.

[44] W. LePage, “digitalimagecorrelation.org.” Accessed: Dec. 23, 2021. [Online]. Available: www.digitalimagecorrelation.org

[45] O. Glushko, “A simple and effective way to evaluate the accuracy of digital image correlation combined with scanning electron microscopy (SEM-DIC),” *Results in Materials*, vol. 14, no. February, p. 100276, 2022, doi: 10.1016/j.rinma.2022.100276.

[46] B. Wieneke and R. Prevost, “DIC uncertainty estimation from statistical analysis of correlation values,” in *Conference Proceedings of the Society for Experimental Mechanics Series*, H. Jin, C. Sciammarella, S. Yoshida, and L. Lamberti, Eds., Springer, 2014, pp. 125–136. doi: 10.1007/978-3-319-00768-7_15.

[47] H. S. Wong, M. Zobel, N. R. Buenfeld, and R. W. Zimmerman, "Influence of the interfacial transition zone and microcracking on the diffusivity, permeability and sorptivity of cement-based materials after drying," *Magazine of Concrete Research*, vol. 61, no. 8, pp. 571–589, 2009, doi: 10.1680/macr.2008.61.8.571.

[48] K. L. Scrivener, A. K. Crumbie, and P. Laugesen, "The interfacial transition zone (ITZ) between cement paste and aggregate in concrete," *Interface Science*, vol. 12, no. 4, pp. 411–421, 2004, doi: 10.1023/B:INTS.0000042339.92990.4c.

[49] Y. Chen, J. Wei, H. Huang, W. Jin, and Q. Yu, "Application of 3D-DIC to characterize the effect of aggregate size and volume on non-uniform shrinkage strain distribution in concrete," *Cem Concr Compos*, vol. 86, pp. 178–189, 2018, doi: 10.1016/j.cemconcomp.2017.11.005.

[50] E. D. Dzaye, E. Tsangouri, K. Spiessens, G. De Schutter, and D. G. Aggelis, "Digital image correlation (DIC) on fresh cement mortar to quantify settlement and shrinkage," *Archives of Civil and Mechanical Engineering*, vol. 19, no. 1, pp. 205–214, 2019, doi: 10.1016/j.acme.2018.10.003.

[51] Z. Li *et al.*, "Study of the Failure Mechanism of Mortar Rubble Using Digital Image Correlation, Acoustic Emission and Scanning Electron Microscopy," *Buildings*, vol. 12, no. 1313, 2022.

[52] POWERS and T. C., "Mechanism of Shrinkage and Reversible Creep of hardened cement Paste," *Proc. Int. Symp. Concr., London, 1965*, pp. 319–344, 1965, [Online]. Available: http://ci.nii.ac.jp/naid/10014912385/en/

[53] C. M. Neubauer, H. M. Jennings, and E. J. Garboczi, "Mapping drying shrinkage deformations in cement-based materials," *Cem Concr Res*, vol. 27, no. 10, pp. 1603–1612, 1997.

[54] C. M. Neubauer, T. B. Bergstrom, K. Sujata, Y. Xi, E. J. Garboczi, and H. M. Jennings, "Drying shrinkage of cement paste as measured in an environmental scanning electron microscope and comparison with microstructural models," *J Mater Sci*, vol. 32, no. 24, pp. 6415–6427, 1997, doi: 10.1023/A:1018682404655.

[55] P. Zhang, F. H. Wittmann, T. Zhao, and E. H. Lehmann, "Neutron imaging of water penetration into cracked steel reinforced concrete," *Physica B Condens Matter*, vol. 405, no. 7, pp. 1866–1871, 2010, doi: 10.1016/j.physb.2010.01.065.

[56] F. Wittmann, "Grundlagen eines Modells zur Beschreibung charakteristischer Eigenschaften des Betons," *Deutscher Ausschuss für Stahlbeton*, vol. 290, 1977.

[57] Mechanical, “Griffith Theory of Brittle Fracture,” 2011, [Online]. Available: http://mechanical-materialstechnology.blogspot.co.id/

[58] F. H. Wittmann, Z. Sun, and T. Zhao, “Surface energy and fracture energy,” *FraMCos-7*, pp. 13–20, 2010.

[59] J. Wang, X. Ye, X. Yang, M. Liu, and X. Li, “The applicability and the low limit of the classical fracture theory at nanoscale: The fracture of graphene,” *Eng Fract Mech*, vol. 284, no. December 2022, p. 109282, 2023, doi: 10.1016/j.engfracmech.2023.109282.

[60] S. Jiménez-Alfaro and D. Leguillon, “Finite fracture Mechanics at the micro-scale. Application to bending tests of micro cantilever beams,” *Eng Fract Mech*, vol. 258, no. September 2021, 2021, doi: 10.1016/j.engfracmech.2021.108012.

[61] J. Hagymassy, S. Brunauer, and R. S. Mikhail, “Pore structure analysis by water vapor adsorption. I. t-Curves for water vapor,” *J Colloid Interface Sci*, vol. 29, no. 3, pp. 485–491, 1969, doi: 10.1016/0021-9797(69)90132-5.

[62] P. Acker, V. Baroghel-Bouny, and S. Garcia, “Can water be the glue?,” in *Why does cement set? - An interdisciplinary approach’, 2 "d RILEM Workshop on “Hydration and setting”,* 1997, pp. 23–36.

[63] Tracy Smith, “5 stages of asset management,” SwainSmith Maintenance Repair & Operations. Accessed: Apr. 29, 2025. [Online]. Available: https://swainsmith.com/5-stages-asset-management-excellence/

[64] Anand Paul, “CO2 emissions from cement production,” https://civildigital.com/co2-emissions-from-cement-production/. Accessed: May 06, 2025. [Online]. Available: https://civildigital.com/co2-emissions-from-cement-production/

[65] Zeke Hausfather and Pierre Friedlingstein, “Analysis of global CO2 emissions will reach new high in 2024 despite slower growth,” https://www.carbonbrief.org/analysis-global-co2-emissions-will-reach-new-high-in-2024-despite-slower-growth/. Accessed: May 06, 2025. [Online].

[66] Statistica, “Carbon dioxide (CO_2) emissions from cement worldwide from 2010 to 2023, with projections to 2050, by scenario,” Statistica.com. Accessed: May 06, 2025. [Online]. Available: https://www.statista.com/statistics/1557020/cement-co2-emissions-by-scenario/

Publications

Hendrix, Bart - Searching for ageing phenomena in cementitious material (2025)

Hendrix, Bart – Considerations regarding ageing in cementitious material (2025)

Acknowledgements

At the end of my PhD journey, I can look back at a vast number of people that supported, encouraged, triggered and helped me along the way. As a 'buitenpromovendus' (an external doctoral candidate), it became quite a lengthy journey as I divided my available time between my job at Rijkswaterstaat and my PhD study. Exactly 8 years and 1 month after the official start of my PhD study (17th of November 2017), the last formalities were completed. Time to reflect and to express my gratitude.

In the first place, I'd like to express my utmost gratitude to Professor van Breugel, my promotor and supervisor, who inspired me to start up my long-cherished dream of diving into my own research topic. Although it was quite a challenging journey from time to time (both technically as motivational), you got me 'back on track' when needed. My gratitude also goes to Professor Schlangen, my second promotor, thank you! You evaluated my work during our yearly progress meetings and half-yearly 'catch-up' meetings. Your honest and constructive feedback offered me perspective when I was about to lose track. It was, and is, a great pleasure to find someone speaking my mother tongue at the coffee machine.

Furthermore, I'd like to thank the committee members for their critical review of my thesis. My gratitude goes to Professor Cwirzen from Luleå University of Technology, Dr. Boutz from SGS and Professor Sluijs, Professor van der Horst, Dr. Šavija and Professor Jonkers from Delft University of Technology.

To make sure that this work meets practical application, a supervisory committee guided me during the first five years of this study. I'd like to thank Professor Simon Wijte from Eindhoven Technical University, Dr. Gert van der Wegen† from SGS Intron and my colleagues Hans de Vries and Joost Gulikers at Rijkswaterstaat for their valuable input during our meetings.

In this study, material from existing concrete structures was used. Thank you for your co-operation: Jaco Kreber from BAM, Henk Voogt and Martin Minnaard from Port of Rotterdam, Ewald van der Waals and Ben Hooglugt from Gemeente Den Haag, Rob Wensink from Holcon and Adri Vervuurt, Herdis Heinemann and Huibert Borsje from TNO.

For several interesting discussions outside of my direct network, I'd like to thank Timo Nijland and also Werner Krohm from KroBet in Dortmund for their time and sharing their knowledge.

During the phase of my experimental work, the crew of technicians from the Microlab were always prepared to help and guide me. I'd like to express special thanks to Maiko van Leeuwen, my roommate from the beginning until the end of my journey. Thank you Maiko for numerous occasions when we laughed until we cried (or just cried). Thank you for your friendship, it is heart-warming to see how you make every PhD student feel welcome in the Microlab family. Our sessions in the concrete lab involved mixing fresh concrete and pouring concrete beams, crushing test cubes and mortar beams and cutting samples. It was always a delight. Your insights, experience and training in the Microlab enabled me to prepare specimens that were suitable for use in the ESEM. This brings me to Arjan Thijssen. Arjan and I spent numerous hours at the ESEM. Thank you for your trust, leaving me alone to work with such a powerful and precious instrument. Thank you as well, John van den Berg and Ton Blom for assistance where needed and you trusting me to work in your labs. And Ruud Hendrikx at the Department of Materials Science and Engineering is acknowledged for the X-ray analysis. For daily support with room reservations, issues with key cards etcetera, I could rely on the secretary team: Claire, Jacqueline, Sandra and Iris. Thank you for your help.

This study would not have been possible without the support of my employer Rijkswaterstaat. Not only was Rijkswaterstaat the sponsor of this study, Rijkswaterstaat enabled me in spending time on my study. A special word of gratitude goes to my heads of department: Albert Manenschijn, Mieke van Leeuwen, Veda Lončarić, Larissa Bakker and Annemieke Sietses. I wasn't always the best version of me and still I got your support. Thank you! My colleagues at Rijkswaterstaat were faced with a colleague that was only partly available for quite some time. I believe that your reflections and support helped me a lot when I was going through a rough time. Thank you for your patience with me and your encouragement during my journey.

My family and friends, who had to put up with me, always distracted in some way and always with something on my mind. Thank you for giving me space and always checking in on my progress!

Last but not least, I would like to thank my wife and children. A sheer endless period ends with finishing this book. It was only possible thanks to you, enabling me on this journey (e.g.: no holidays without my laptop!). It is due to your endless support and patience that my dream became reality. Your unconditional support is a sign of true love and that is the greatest gift we can share. Thank you, I love you.

Curriculum Vitae

Hubertus Maria (Bart) Hendrix

26 December 1978	**Born in Geleen, the Netherlands**

Education

September 1997 – June 2001	Bachelor's degree Civil Engineering Zuyd Polytechnic, Heerlen, the Netherlands
September 2006 – July 2008	Master programme Concrete design & engineering Betonvereniging, Gouda, the Netherlands
October 2008 – October 2009	Master's degree Master of Structural Engineering Delft University of Technology, the Netherlands
November 2017 – present	PhD researcher Faculty of Civil Engineering and Geosciences Delft University of Technology, the Netherlands
Email	barthmhendrix@gmail.com

Occupation

2010 – present	Senior technical advisor civil engineering Rijkswaterstaat Major Projects & Maintenance Utrecht, the Netherlands

Appendix A

Durability in Dutch standards for structural concrete – an overview

A.1 State-of-the-art in Standards and regulations

In this Appendix, an overview is given on the historic development of Dutch standards regarding concrete structures. The available binder types as well as mix design and requirements regarding durability are described and commented.

A.1.1 Historic overview of Dutch concrete construction standards

The first Dutch building standard regarding reinforced concrete was released in 1912 by the KIVI (the Royal Dutch Engineers Society): the GBV 1912 (Gewapend Beton Voorschriften - Reinforced concrete regulations) [1]. During the century that followed after this GBV 1912, the construction standards regarding reinforced concrete evolved and expanded into a network of more-or-less cohesive regulations covering the entire field of use of concrete construction.

In the work of Heinemann [2], an overview is given from the first concrete standards (GBV 1912) until the re-construction period after the second world war, up to and including the GBV 1962. In the following, that overview is completed with the regulations from GBV 1962 up to the present day (2021). First, the cement types that are accepted for use in the different standards are presented and discussed, followed by an overview of the different design approaches regarding the function of concrete. Following that, several conformity criteria in the standards are analysed. Changes in the chemical composition of cements over time, the setting time, time dependent effects, the minimum cement content and water-to-cement or water-to-binder ratio and finally the concrete cover thickness are presented and discussed. The elucidation of the conformity criteria shows the development of different requirements which the cement and/or concrete needs to fulfil, in the light of the development of concrete standards in time. From this discussion, the knowledge gaps of today are stated.

A.1.2 Cement types allowed according to building standards

During the first decade of the 20th century, not only Portland cement was used; cements were imported from Germany, where a tradition of trass addition to cements was quite common. The first Dutch concrete standards GBV 1912 [1] were taken into effect in 1912 and with the introduction of the GBV 1912, these trass cements – as well as iron slag cements – were considered inferior and were therefore not allowed to be used.

However, the use of blast furnace slag (BFS) cement has become quite common in the Netherlands – mainly because of the steel industry located near IJmuiden in which slag is a by-product. Also, the good performance (compared to Portland cement) of BFS cement in marine environments and for watertight structures became apparent. An overview in time of the allowed cement types in the building standards is given in Table A1.1.

Over time, in the Netherlands the ratio of the use of BFS cement compared to Portland cement increased from 21% in 1921 to around 60% in 1971 [3]. Nowadays, between 50 and 60% of the total amount of cement used in the Netherlands (2018: ca. 5 million tons) is BFS cement, about 35% is Portland cement and the remaining 5-15% are composite cements.

According to Table A1.1, the number of accepted cement types can be related to increasing experience with different cement types and production methods. The requirements for concrete construction contributed to the development of different cement types (e.g.: construction pace, reduction of hydration heat, watertightness, etc.) as well as the developments in the precast concrete products industry during the last century. Many of the cement types that are accepted for use in the current standards are mixtures of cements or binders and are usually niche products for a dedicated use.

The choice of a specific binder type for a specific application is usually based on experience. Many design rules in the standards and regulations are based on empirical data rather than on an exact knowledge of all influencing parameters and mechanisms. Extrapolating from these empirical design rules is therefore considered to be questionable and should always be accompanied by suitability testing during the design

Table A1.1: Overview of the cement types allowed in the different versions of the G.B.V.

		GBV 1912	GBV 1918	GBV 1930	GBV 1940	GBV 1950	GBV 1962	VB 1974	VB 1984	VBT 1986	VBT 1995	NEN-EN 206 / NEN 8005 / NEN-EN 197-1
cement type allowed	Portlandcement	Y	Y	Y	Y	Y	Y	Y	Y	Y	Y	Y
	IJzerportlandcement (Portland-slag cement)	-	-	(Y)	(Y)	(Y)	Y	Y	Y	Y	Y	Y
	Hoogovencement (Blast furnace slag cement)	-	-	(Y)	(Y)	(Y)	Y	Y	Y	Y	Y	Y
	Aluminiumcement (High aluminium cement)			(Y)	(Y)	(Y)	(Y)	(Y)	(Y)	(Y)	(Y)	Y
	Tras-Portland cement (Trass cement)	-	-	-	-	-	(Y)	(Y)	(Y)	Y	Y	Y
	Gesulfateerd cement (Supersulphated cement)			-	-	-	(Y)	(Y)	(Y)	(Y)	(Y)	Y
	Slakkencement (Slag-lime cement)	N	-	-	-	-	-	-	-	-	-	-
	Portlandvliegascement (Portland-fly ash cement)										Y	Y
	Portlandleisteencement (Portland - slate cement)										-	Y
	Composietcement (Portland-slag composite cement)										(Y)	Y
	Portlandsilicacement (Portland-silica cement)											Y
	Portlandpuzzolaancement (Portland-pozzolana cement)											Y
	Portlandkalksteencement (Portland-limestone cement)											Y
	Portlandcomposietcement (Portland-composite cement)											Y

Legend: Y = allowed; (Y) = restricted use allowed; N = not allowed; - = not mentioned;   = not yet available.

phase and be monitored after application to ensure safety and durability of the structure. The current standards offer a wide range of cement types which are allowed for use in (structural) concrete. Many of the widely available cement types can be used without suitability testing, provided the cement meets the requirements in the standards.

For applications with non-standard binder types, the standards have always offered only limited possibilities for experimenting in actual structures. Current EN standards, combined with national guidelines (like the CUR 48 guideline [4]) actually offer most possibilities for innovation after the concrete construction standards have become in use.

A.1.3 Basic requirements & design approach for concrete in standards

The design approach in the GBV 1912 [1] and GBV 1918 [5] standards is about the (average) compressive strength only ("able to resist the forces working on it"). In the GBV 1918, some remarks are introduced regarding the compaction of concrete and avoiding cavities and voids in the concrete (and thus, implicitly mentioning durability aspects).

In the GBV 1930 [6] and GBV 1940 [7], the emphasis remains on the quality of the concrete in relation to limiting the water content for workability and avoiding voids and cavities. This remains largely the same in the GBV 1950 [8]. Until the GBV 1950, the regulations followed the developments in the concrete construction industry. Due to the scale of the post-second world war reconstruction works, the concrete construction industry (in all sectors: domestic buildings, office buildings, factories, industrial buildings and infrastructural works) developed rapidly and all these experiences were incorporated in the next concrete construction standard: the GBV 1962 [9].

The GBV 1962 marks a turning point in the standards. Because of the European cooperation in the Comité Européen du Beton (CEB) a more fundamental approach was chosen. The standards should not only summarize the experiences in the sector, but provide regulations for a wide variety of applications. Experience with concrete works was now widespread across the construction industry making a new approach of standardization necessary. Durability of concrete was considered only by mentioning a minimum concrete cover thickness and by setting a maximum allowed crack width. Focus in design still was mainly on structural safety rather than durability.

In the years up to the VB 1974 [10]–[16], many study and working groups (CUR, CEB, FIB etc.) and commercial organisations worked together on improvement of the concrete standards. All these working groups were coordinated by a commission which uniformed the individual initiatives. This led to the VB 1974, an extensive standard work divided in seven parts for different subjects. This division evolved due to the different working groups in which different parties of the concrete construction industry were represented. In this standard, notes and clarifications were no longer presented at the bottom of each page, but on the opposite page for a better overview and better readability. This remained the same until the NEN regulations were replaced by the Eurocodes in 2010. The clarifications offered background information on clauses in the standard. These clarifications could be used for a more theoretical approach and a better interpretation of the standard. With the VB 1974, a more rational approach of the standards was introduced (i.e. by incorporation of knowledge gained in more fundamental laboratory research) but still the basic framework was offered to be on the safe side. Material properties are described in much more detail compared to the GBV 1962 for both concrete and steel, offering more degrees of freedom in the design of concrete structures. The design approach was, however, still similar to the GBV 1962: structural integrity as the main subject for concrete structures. A lot of effort is put into optimising the concrete quality for easy casting and compacting. This forms the basis for a new point of view in the next version of the standard.

A new approach to durability is introduced in the VB 1974/1984 [17] (Voorschriften Beton; Regulations for Concrete structures). For the first time, the structural integrity is mentioned in one article together with the environmental exposure. Together with a more statistical approach on structural parameters from the previous standard (VB 1974), the basis for a more integral approach of structural and durability design is developed. From the VB 1984 [18] onwards, different topics regarding concrete construction are dealt with in different standards. Up to the VB 1984, almost all aspects regarding concrete construction were covered in one standard. After the VB 1984, structural aspects, concrete mix design and execution of concrete works are dealt with in different standards. With the introduction of the new VBT 1986 [19] (Voorschriften Beton Technologie; Regulations for Concrete Technology) (NEN 5950 series), the VB 1974 is replaced completely and the integral design approach is even further expanded. The introduction of the VBT 1986 is also an important step in the detachment of the different aspects of concrete construction.

The development of the integral design approach continues when the VBT 1995 [20] is introduced. A new set of standards (VBC 1995 [21] , Voorschriften Beton Constructieve regelgeving; Regulations for Structural Concrete) is introduced, based on the latest scientific insights and experiences in the concrete construction industry.

Parallel to the introduction of the VBC 1995, the Eurocode system was developed. The Eurocodes offer much more degrees of freedom for the design of concrete structures, but require more insight in the matter. Regarding integral structural and durability design however, no fundamental changes are made compared to the VBT 1995 standard. The Eurocode systematic offers more freedom for the designer but requires more knowledge from the designer than in the VBC 1995 which had more of a guiding character.

Conclusions on design approach

The design approach has changed quite a lot in just over 100 years of concrete standards, mostly because of the increase in experience and knowledge. Also, the widespread use of concrete in the construction industry (both in the Netherlands as well as worldwide) demanded the concrete standards to become more explicit and extensive. Coming from mainly offering a guide to structural safety to an integral design approach which provides different interpretations of the standard and where a thorough knowledge of structural design and material technology is required.

However, the standards and regulations are focussed on the performance at an early age of the structure: providing a mix design which can be compacted well and which is deemed to protect the reinforcement against corrosion for a long time. The application of detailing rules is still used to comply verifiably with long-term performance criteria.

A.1.4 Conformity criteria in standards

The conformity criteria for cements have changed over the years; an overview is given in the following subparagraphs. In the different paragraphs, a comparison is made for the development of different cement properties in concrete. In the discussion at the end, the developments are evaluated and possible blind spots are highlighted.

A.1.4.1 Chemical composition of cements

In the standards only general requirements are mentioned regarding the chemical composition of cement. The requirements mentioned are about the composition of Portland cement (GBV 1918 [5] and onwards) or about the slag composition of iron Portland cement (GBV 1930 through GBV 1940 (N483) [22], up to the VBT 1986 (NEN 3550) [23]).

The first appearance of fly ash in Dutch standards is in 1986. Fly ash contains mainly reactive SiO_2 and Al_2O_3 and some Fe_2O_3 and other oxides, CaO content is usually lower than 5% and thus considered negligible. The required SiO_2 content of fly ash for use in Portland fly ash cement is 35%.

Chemical compositions of cements are available from literature. In more recent years these can be found on the internet although not all cement producers are keen on broadly presenting the chemical composition of their products. Heinemann [3] presented an historic overview on chemical compositions of cements, which is extended with more recent data and shown in Table A1.3. In Table A1.2 an overview on the chemical composition of Blast furnace slag (BFS) cement is given.

A.1.4.2 Setting time

In Table A1.4 the start of setting time is listed as mentioned in several standards. Both the GBV 1912 and the GBV 1918 require the start of the setting of concrete to be not earlier than 2 hours after adding water to the cement. From the GBV 1930 up to the VBT 1986 the required start of setting of concrete should not be earlier than 1 hour after the addition of water to the cement. The background behind these requirements lies mainly in practical application. In the governing years of the GBV 1912 and the GBV 1918, concrete was mixed at the work site by hand or it was mixed in a concrete mixing plant and transported to the work site by lorry. Mixing plants were not as common as nowadays and transport (both on the road as at the work site) was not as efficient as it is nowadays. Therefore, a late setting time was required in the early standards. When transport and handling times became more controllable, the requirements for the setting time became less stringent. From the VBT 1995 and onwards, the setting times are more variable, depending on the cement type. In the VBT 1995, cements are classified according to their strength and strength evolution in time.

A.1.4.3 Time dependent effects

In the VB 1974, time dependent material effects (shrinkage, creep and relaxation) were first introduced as material related parameters in the standards, however only to be regarded in the static calculations – as macroscale effects. This approach has not been changed ever since. Since the VBC 1995 standards series, these time dependent material parameters are mentioned in the NEN 6720, the standard for static calculations on concrete structures which are superseded by the (NEN-)EN 1992-1-1. The standards mention different values for shrinkage, creep and relaxation for different environmental conditions, for different cement types and for different dimensional and structural parameters.

What is not mentioned in any Dutch cement or concrete standard however, is a test method for the determination of the creep/shrinkage/relaxation of a specific concrete mixture. It is, therefore, unknown to what extent these time-dependent effects are influenced by small deviations in the chemical composition of the binder or by the usage of chemical additives, because the determination of time dependent effects is not required in the standards unless it is required by the client. Unfortunately, this lack of

Table A1.2: chemical composition of Portland cement BFS cement

Comparison Portland cement and blast furnace slag cement	Portland cement (Anon., 1931)	Granulated blast furnace slags (Anon., 1931)	CEM III/B 42,5 LH HS (ENCI 1998)	CEM III/B 42,5 LH HS plus (ENCI 1998)	Granulated blast furnace slags (Neville, 2008)	CEM III/B 42,5 N LH (Moerdijk, HCM, mei 2009)	CEM III/B 42,5 N-LH/SR (Maastricht, ENCI, apr. 2014)	CEM III/B 42,5 N-LH/SR (Maastricht, ENCI, mrt. 2015)	CEM III/B 42,5 N-LH/SR (Maastricht, ENCI, feb. 2016)	CEM III/B 42,5 N-LH/SR (IJmuiden, ENCI, feb. 2019)	CEM III/A 42,5 N (HCM, 2019)	**trend**
Calcium oxide (CaO)	65	33	46	44	40 - 50	48	45	45	45	46	48	↑
Silicon dioxide (SiO_2)	21	33	30	28	30 - 40	29	30	29	28	29	28	↑
Aluminium oxide (Al_2O_3)	6	14	10	12	8 - 18	9,7	11	11	11	10,65	9,6	↑↓
Iron oxide (Fe_2O_3)	3	-				1,48	1	1	1	1	2	
(FeO)	-	1	1,5	1		-	-	-	-	-	-	
Magnesium oxide (MgO)	1	2	8	9	0 - 8	5,2	-	-	-	-	4,9	↑
Gypsum ($CaSO_4$)	2	-	3	3	-		6,5	6,2	6,2	4,95	4,7	

↑ increasing; ↓ decreasing; ↑↓ fluctuations

Blaine [m^2/kg]			490	470								
Slag content [%]			70	76								

Table A1.3: chemical composition of Portland cements

	Delfzijl cement, 1870's (Heerding, 1971)	Germany, 1883 (Scharroo, 1910)	Germany, 1907 (van der Kloes, 1908)	unknown origin (Bergsma & Homan van der Heide, 1910)	Germany (Scharroo 1916)	Germany, 1919 (van der Kloes et al., 1924)	unknown, possible Dutch (Bergsma, 1934)	High quality Portland cement (Bergsma, 1934)	Dutch ENCI (van Dijk & van der Baan, 1952)	CEM I 52,5 N (Seibel, 2009)	CEM I 42,5 N (ENCI, apr. 2014)	CEM I 52,5 R (ENCI, mrt. 2015)	**tendency**
Calcium oxide (CaO)	54,1	58,22 - 65,59	57,72 - 67,60	59 - 65	60,84	54,42 - 67,47	61 - 65	61 - 65	66,5	63	64	64	↑↓
Silicon dioxide (SiO_2)	28,2	19,8 - 26,45	17,23 - 24,04	20 - 26	23,16	17,76 - 24,18	22	21	21,7	21	20	19	↓, =
Aluminium oxide (Al_2O_3)	15,1	4,16 - 9,45	2,96 - 9,08	7 - 14	4,94	4,95 - 8,74	7	7	3,8	4,8	5	5	↑↓
Iron oxide (Fe_2O_3)	2,6	2,19 - 4,47	1,23 - 4,62	7 - 14	2,61	1,27 - 4,08	3	3	3,8	3,2	3	3	↑, =
Magnesium oxide (MgO)	-	1 - 2,89	0,51 - 3,57	1 - 3	2,61	0,66 - 5,11	1,5	1,5	1,4	1	-	-	↓
Sulphates (SO_3)	-	0,19 - 2,19	0,88 - 3,30	<2	2,38	0,81 - 3,89	1,9	1,7	1,7	3,1	2,9	3,1	↓
Alkalis: sodium oxide (Na_2O) and potassium (K_2)	-	0,19 - 2,19	0,23 - 2,01	<3	1	-	-	-	-	0,65	0,63	0,63	↑↓
Gypsum ($CaSO_4$)	Not mentioned												

↑ increasing; ↓ decreasing; ↑↓ fluctuations

Table A1.4: cement content in Dutch concrete standards, adapted from [2]

	minimum cement content	proportions sand and coarse aggregates [vol.]	exposure class		concrete type	water content	start binding [mins]
GBV 1912	360 kg/m^3 (135 kg/2 hl sand)	1:1 - 1:2	n/a	①	n/a	n/a	> 120
GBV 1918	360 kg/m^3 (125 kg/2 hl sand)	1:1 - 1:1,5	n/a		n/a	n/a	> 120
	360 kg/m^3 (250 kg/3 hl sand)	max. 1:2	n/a	①	n/a	n/a	
GBV 1930	360 kg/m^3 (125 kg/2 hl sand)	1:1 - 1:1,5			n/a	n/a	> 60
	360 kg/m^3 (250 kg/3 hl sand)	max. 1:2	②	①	n/a	n/a	
GBV 1940	360 kg/m^3 (125 kg/2 hl sand)	1:1 - 1:1,5			n/a	③	> 60
	360 kg/m^3 (250 kg/3 hl sand)	max. 1:2	②	①	n/a		
GBV 1950	360 kg/m^3 (125 kg/2 hl sand)	1:1 - 1:1,5			n/a	③	> 60
	360 kg/m^3 (250 kg/3 hl sand)	max. 1:2	②	①	n/a		
GBV 1962	300 kg/m^3				Plain concrete		> 60
	325 kg/m^3	1:1 - 1:1,5			K160		
	350 kg/m^3 (1:1.2:2,4)	1:2			K160		
	min. 325 kg/m^3	replaced by fineness			K225	max 0.60	
	Increase possible	modulus	②		K300	max 0.55	
VB 1974	280 - 340 kg/m^3				B12,5		> 60
	280 - 360 kg/m^3	replaced by fineness		Class I	B17,5	④	
	300 - 360 kg/m^3	modulus			B22,5		
	280 kg/m^3			Class II	B30 - B60		
VB 1984	280 - 340 kg/m^3				B12,5		> 60
	280 - 360 kg/m^3	replaced by fineness		Class I	B17,5	< 0.60	
	300 - 360 kg/m^3	modulus			B22,5		
	280 kg/m^3			Class II	B30 - B60	< 0.60 ⑤	
VBT 1986	280 - 300 kg/m^3	Grading influences the cement content; gap grading requires higher content	Environmental classes 1-5 influence water/cement ratio		B5-B55	< 0.60 (environmental class 1) < 0.55 (environmental class 2-5) AND < 0.45 when no air entraining agent is present	> 60
VBT 1995	150 - 300 kg/m^3	Grading influences the cement content; gap grading requires higher content	Environmental classes 1-5 influence cement content		plain concrete	0.45 - 0.70 depends on exposure class	> 60 > 45 for 52,5 strength class cement
	260 - 300 kg/m^3				reinforced concrete	0.45 - 0.65 depends on exposure class	
NEN-EN 206-1	200- 340 kg/m^3	Grading influences the cement content; gap grading requires higher content	Environmental classes influence cement content and water/cement ratio		structural concrete	0.45 - 0.70 depends on exposure class	> 75 for strength class 32,5 > 60 for strength class 42,5 > 45 for strength class 52,5
	> 300 kg/m^3				mass concrete	< 0.50	

Legend: ① average cement content is given; cement content varies on water content; ② sea water or other aggressive waters; ③ none specified but consistent plasticity of concrete paste required; ④ none specified but limited by grading and consistency class; ⑤ for watertight concrete, water-cement ratio < 0.55

knowledge led to several cases of damage because imposed loads were not foreseen and caused cracking of the concrete. Furthermore, the ongoing hydration in the concrete should be quantified for different cement types. This also gives an impression of the potential for autogenous self-healing.

A.1.4.4 Cement content and water/cement ratio

In Table A1.4, the required minimum cement content is listed for the different concrete standards over time. In Figure A1.1, the cement content is presented graphically. Below, the table is discussed.

In the first sets of standards for structural concrete, the requirements for mix design were given in volume units. Hence the term 1-2-3 concrete (1 volumetric part of cement, 2 volumetric parts of sand and 3 volumetric parts of coarse aggregate). Between the GBV 1912 and GBV 1918, the required minimum cement content decreased from 135 kg per 200 litres of sand to 125 kg per 200 litres of sand, which translates in an average cement content of 250 kg/m³. The water-cement ratio (wcr, the ratio between the mass of the added water and the mass of the added cement) was however not a parameter in the mix design; workability of the fresh concrete was regulated by changing the water content.

Up to the GBV 1962, the so-called 1-2-3 concrete remained in use. A maximum water/cement ratio was first mentioned in the GBV 1962, when the fineness modulus was introduced to control the cement paste amount in the concrete mix for a better control of workability. Until then, workability was regulated by changing the water content (which influenced the concrete strength). (Super)plasticizers were not used in concrete construction until the GBV 1962. After 1962, these chemical additives became more common, which made lower water/cement ratios possible without loss of workability. In the VB 1974 and VB 1984, no maximum water/cement ratio is given but a minimum cement content is given. Together with an optimization of the grading, the amount of cement paste is controlled, providing good workability and compaction. Only three exposure classes are used: dry, moist and aggressive.

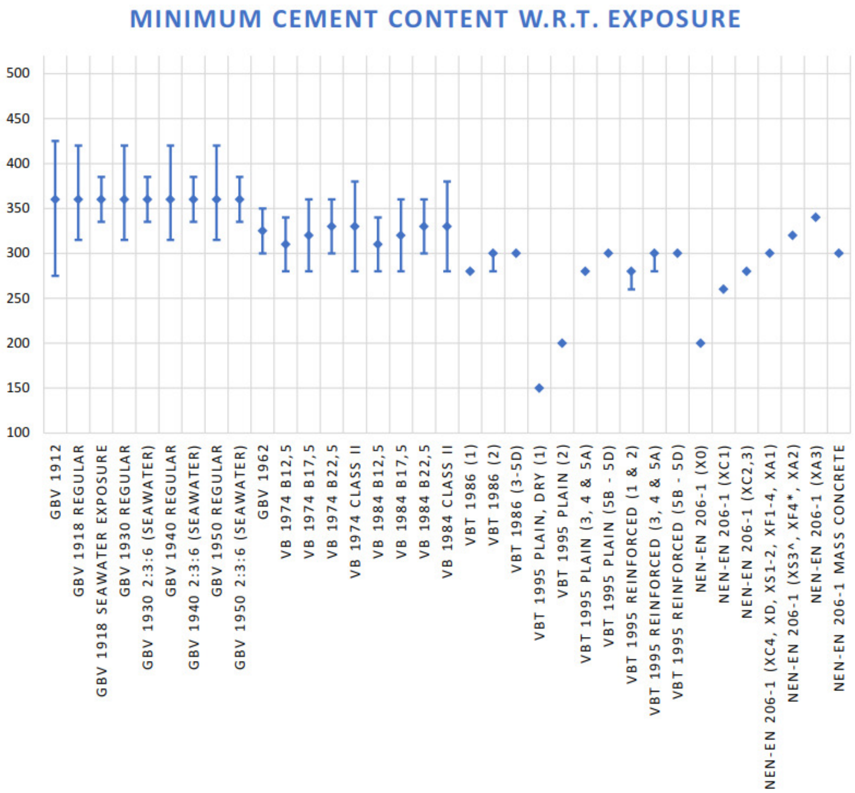

* lower wbr when no requirements for air content; ^ 300 kg/m^3 for mass concrete

Figure A1.1: cement content as function of exposure class in superseding standards

In the VB 1984, the minimum cement content was not directly related to the exposure class. Minimum cement content was connected to the grading of the aggregates (i.e.: in case a more optimal grading was obtained, the cement content (fine material) could be reduced). It was considered a way of creating a mixture that required little water with optimal flowability around the reinforcement.

Around the introduction of the VB1974, the concrete construction industry changed from using plain bars to ribbed bar reinforcement. Reinforcement steel changed from plain bars Fe 220 to ribbed bars FeB 400 and ribbed bars FeB 500 with tensile strengths of respectively 220 MPa, 400 MPa and 500 MPa. The relation between bond strength and structural performance was emphasized as higher steel qualities were becoming more common. The advances in concrete technology provided the base for reliable bond strengths between steel and concrete, leading to reliable structural performance of concrete structures.

From the VBT 1986 onwards, the minimum cement content and the maximum water/cement ratio is given. Also, new exposure classes were introduced (see Table A1.5), depending on the environment the structure is placed in. Both the minimum cement content and the maximum water/cement ratio are directed by the exposure class. These exposure classes remained in use until they were replaced by those in the Eurocode system in [24].

Table A1.5: environmental classes since the TGB 1990

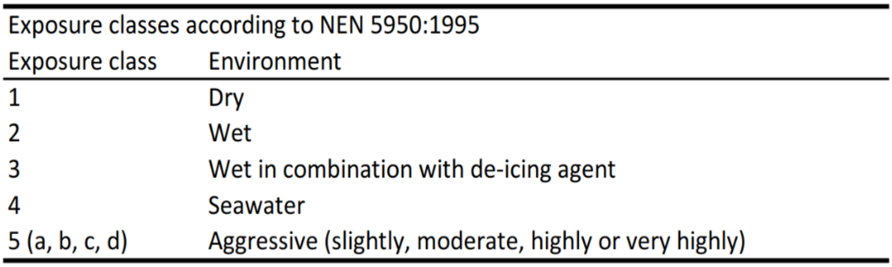

Exposure classes according to NEN 5950:1995	
Exposure class	Environment
1	Dry
2	Wet
3	Wet in combination with de-icing agent
4	Seawater
5 (a, b, c, d)	Aggressive (slightly, moderate, highly or very highly)

Since 2010, the Eurocode system is valid for all member nations of the EU. In Eurocode 2, the regulations for concrete structures are given. During a relatively long period of time, the VBC 1995 and the pre-EC codes coexisted (since the early 2000’s) until the VBC system was eventually abandoned. The Eurocode approach to cement content and water/cement ratio is for the greater part the same as in the VBC period, including the exposure class dependence. In the Eurocode however, there are some more exposure classes, 18 in total (see Table A1.6).

Table A1.6: exposure classes in the Eurocode system

Exposure classes according to NEN-EN 1992-1-1: 2004 Class designation		
1 No risk of corrosion		
	X0	Concrete without reinforcement or embedded metal [..] very dry environment
2 Corrosion induced by carbonation		
	XC1	Dry or permanently wet
	XC2	Wet, rarely dry
	XC3	Moderate humidity
	XC4	Cyclic wet and dry
3 Corrosion induced by chlorides other than by seawater		
	XD1	Moderate humidity
	XD2	Wet, rarely dry
	XD3	Cyclic wet and dry
4 Corrosion induced by chlorides from seawater		
	XS1	Exposed to airborne salt but not in direct contact with the seawater
	XS2	Permanently submerged
	XS3	Tidal, splash and spray zones
5 Freeze-Thaw attack		
	XF1	Moderate water saturation without de-icing agent
	XF2	Moderate water saturation with de-icing agent
	XF3	High water saturation without de-icing agent
	XF4	High water saturation with de-icing agent
6 Chemical attack		
	XA1	Slightly aggressive, chemical environment according to EN 206-1, Table 2
	XA2	Moderate aggressive, chemical environment according to EN 206-1, Table 2
	XA3	Highly aggressive, chemical environment according to EN 206-1, Table 2

A.1.4.5 Water content and water-cement ratio

The necessary water content in fresh concrete depends on the grading of the aggregates, the required consistency class, the shape of the aggregate grains and the usage of water-reducing additives like (super)plasticizers. For full hydration of 1 kg of cement, 0.3 – 0.33 kg of water is required. However, for a workable concrete mixture more water is required, unless chemical additives are used (e.g. (super)plasticizers). The water-cement ratio is defined as follows:

$$\text{Water-cement ratio (wcr)} = \frac{m_{effective\ water}}{m_{binder}} \quad [-]$$

That is the mass of the effective water (i.e. the available water at the time of setting of the concrete) divided by the mass of the cement (or binder in the case of water-binder ratio). The effective water content is defined as the difference between the total water present in the concrete and the water absorbed by and adhered to the aggregates. The absorbed and adhered water become available at a later point in time when the relative humidity of the system drops.

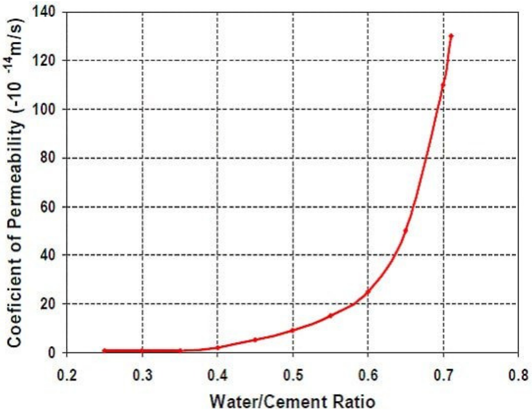

Figure A1.2: Correlation between wcr and permeability according to Powers [25], Fig. 6

The permeability of concrete depends strongly on the water-cement ratio of the concrete mixture. This has already been mentioned by Powers [25], as shown in Figure A1.2. In this figure, a relationship is depicted (based on curve-fitting of permeability measurements on cement paste samples). In the VBT 1986, the absorbed water of the coarse aggregate (around 0.7% in Dutch fluvial aggregates) is allowed to be subtracted from the effective water content. In the EN 206-1, both the absorbed water in the coarse aggregate (around 1.7% because of a different determination method) *and* in the fine aggregate (about 0.6%) are allowed to be subtracted from the total water content [26]. The effective water content will therefore be reduced, compared to the VBT 1986. Reducing the effective water content will reduce the cement content (which is calculated based on the necessary water and the chosen water-cement ratio). The total water content in the concrete is, however, still present (although absorbed in the aggregate) and available for the formation of hydration products in the paste. With the reduced cement content, the apparent water-cement ratio will then increase, causing a higher permeability of the cement paste and hence, the concrete.

A.1.4.6 Concrete cover layer

The durability of a structure depends mainly on the quality of the cover concrete and the thickness of the concrete cover. The quality of the cover concrete depends mainly on the execution of the work (i.e. casting, compacting and curing of the concrete). The specified thickness of the concrete cover has developed significantly since it was first mentioned in design standards, mainly due to new insights in concrete technology and empirical research on concrete structures. In Table A1.7 an overview is given on the development of the concrete cover in time. Figure A1.3 shows a graphical representation of the values given in Table A1.7. The data shows that the difference between slabs and beams/columns is present in all standards. Due to the lack of redistribution of forces, columns and beams are considered more vulnerable than slabs and thus the requirements are slightly higher for columns and beams.

In the first standards for structural concrete (GBV 1912 - 1930), no additional cover was required for casting against uneven or unstable surfaces or structures in an aggressive environment, which became common in the GBV 1940. This is also the reason for the 'whiskers' in the graph; it shows the additional concrete cover thickness (when required) in case of casting against uneven or unstable surfaces (noted "no control" in Figure A1.3) or aggressive environment. In the Eurocodes (EN 1992-1-1), the additional cover thickness is also a function of the construction class (see also Table A1.7). This causes a much bigger scatter on the cover thickness than before. Most prominent is however, that the scatter in one exposure class can be up to 25 mm depending on the structural class of the structural element, whereas the scatter in earlier regulations used to be less than 10 mm. The origin of this different approach has a statistical background.

Abroad, additional requirements are included in the standards with regard to the concrete cover thickness. In the UK and Denmark, for instance, the binder type is included in the requirements for the concrete cover thickness. Durability assessment of structures is embodied in the Eurocode standards via structural classes; the acceptable chance of failure for a structural member depends on the function of the member in the superstructure and the exposure class. Every member nation may, however, add or adapt certain design methods according to the common practice in that nation.

A.1.5 Discussion on Dutch standards for concrete construction

More than 100 years of experience with concrete construction have been incorporated in Dutch concrete standards. Regulations have changed from mainly practical rules to performance criteria for materials and structures. Also international collaboration between standardisation committees as well as the incorporation of findings from scientific research have contributed to a set of standards which is sufficient for the design and construction of most concrete structures.

Table A1.7: development of concrete cover from GBV 1912 until Eurocodes, adapted from [1]

	Reference point	slabs: No special exposure class	slabs: Exposed to wind and water	slabs: No control of surface after casting possible	slabs: Agressive environments[a]	beams: No special exposure class	beams: Exposed to wind and water	beams: No control of surface after casting possible	beams: Agressive environments[a]	columns: No special exposure class	columns: Exposed to wind and water	columns: No control of surface after casting possible	columns: Agressive environments[a]	additional cover: Surface treatment which damages cement film	additional cover: Prestressing	additional cover: Lightweight concrete
concept Betonijzer art. 15	◊	10				15										
GBV 1912 art. 15	◊	10[b]				15				15						
GBV 1918 art. 17	✦	10[b]			20[c]	25			35[c]	35			50[c]			
GBV 1930 art. 13	✦	10		20	20	25		35	35	35		50	50			
GBV 1940 art. 13	✦	10		20	+10	25		35	+10	35		45	+10	+10		
GBV 1950 art. 13	○	d ≤ 12 cm: 10[d] d > 12 cm: 15	15[d]	20	+10	20	25	40	+10	30	35	40	+10	+10		
GBV 1962 art. 28	○	10	15	20[e]	+10	20	25[e]	30	+10	25	30	35	+10	+10		
VB 1974 art. B-707.	○	10[f]	15[f]	+5	25[f]	20	25	+5	35	25	30	+5	40	+10	+10	
VB 1984 art. A-707.1 < B17,5	○	15	25	+5	35	25	35	+5	40	30	40	+5	45	+5	n/a	+5
> B22,5	○	15	25	+5	30	25	30	+5	35	30	35	+5	40	+5	+10	+5
		slabs, walls				beams, foundation blocks, console				columns						
TGB 1990 art. 9.2		exposure classes according to NEN 5950:1995, see below														
		1 | 2		3, 4, 5		1	2	3, 4, 5		1	2	3, 4, 5				
	○	15 | 25		30		25	30	35		30	35	40		+5		

NEN-EN 1992-1-1 art. 4.4.1.2

Reference point	construction class	XC0	XC1	XC2/XC3	XC4	XD1/XS1	XD2/XS2	XD3/XS3	
		exposure classes according to NEN-EN 1992-1-1:2004, see below							
○	S1	10	10	10	15	20	25	30	prestressing: XC1 +5 mm for S1 & S2, +10 mm for others;
	S2	10	10	15	20	25	30	35	>XC1 +10 mm all classes
	S3	10	10	20	25	30	35	40	execution tolerance: +10 mm
	S4	10	15	25	30	35	40	45	slabs: -1 class
	S5	15	20	30	35	40	45	50	100 years service life: +2 classes
	S6	20	25	35	40	45	50	55	quality control: -1 class
		≥C30/37 -1 class	≥C30/37 -1 class	≥C35/45 -1 class	≥C40/50 -1 class	≥C40/50 -1 class	≥C40/50 -1 class	≥C45/55 -1 class	← concrete type

◊ None defined; ✦ Main reinforcement; ○ Outer reinforcement

a) High temperatures due to fire, sea water, aggressive water or gases. b) Valid for all other elements which are neither beams nor columns. c) Only for possible exposure to fire. d) Valid for walls and slabs. e) Includes also contact to soil and ground water. f) Walls: + 5 mm

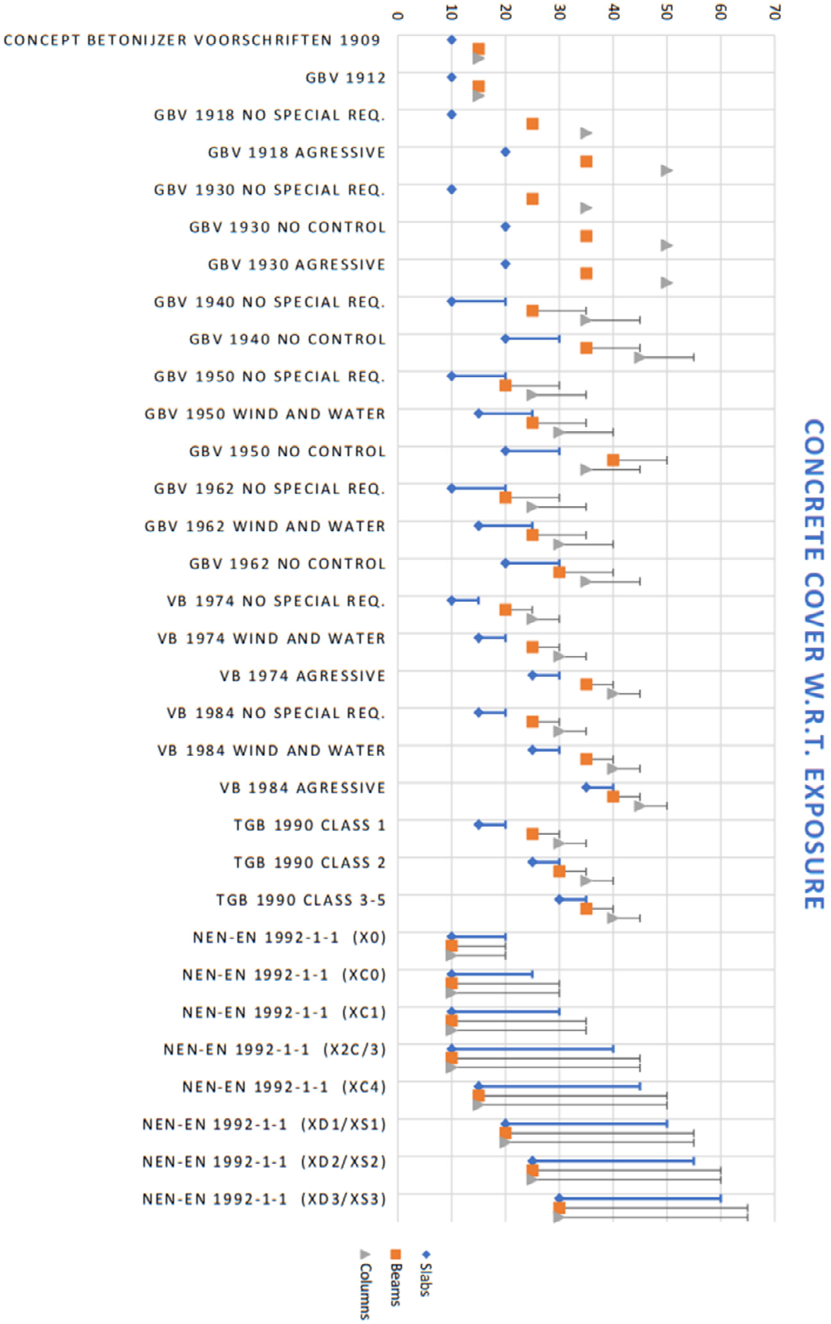

Figure A1.3: graphical presentation of concrete cover in relation to exposure

There remain, however, some gaps which are not covered by the standards. One of these gaps is the time-dependent degradation behaviour of concrete. Time-dependent deformations are covered in the standards, however, the Dutch standards do not offer test methods nor do they offer a proper design approach regarding time-dependent degradation behaviour. Also, a test method for quantification of the effects of differences in the chemical composition of cement is not available. Now that the construction industry is facing a transition with regard to a more sustainable use of raw materials and a reduction of carbon dioxide emissions, changes in the composition of binder materials are inevitable (as well as the use of alternative materials) and the effects on the time-dependent degradation behaviour of the binder and the concrete should be known to be able to predict the long-term behaviour of the performance of both the material and the structure.

A.1.6 References

[1] KIVI, "GBV 1912 Gewapend beton voorschriften." 1912.

[2] H. Heinemann, "Historic Concrete - From Concrete Repair to Concrete Conservation," Delft University, 2013.

[3] A. Heerding, *Cement in Nederland*. The Hague: Cemij, 1971.

[4] CUR, "CUR Aanbeveling 48: Geschiktheidsonderzoek van nieuwe cementen voor toepassing in beton," 2010.

[5] KIVI, "GBV 1918 Gewapend betonvoorschriften 1918." 1918.

[6] KIVI, "GBV 1930 Gewapend-beton-voorschriften." 1931.

[7] KIVI, "GBV 1940 Gewapend-beton-voorschriften N 1009." 1940.

[8] KIVI, "GBV 1950 Gewapend-beton-voorschriften N 1009." 1950.

[9] KIVI, "GBV 1962 Gewapend-betonvoorschriften NEN 1009." 1962.

[10] NNI, "NEN 3861 VB 1974 Voorschriften beton - deel A - Gemeenschappelijk gedeelte." 1977.

[11] NNI, "NEN 3862 VB 1974 Voorschriften Beton - deel B - In het werk gestort beton - aanvullende bepalingen." 1974.

[12] NNI, "NEN 3863 VB 1974 Voorschriften Beton - deel C - vooraf vervaardigd beton - aanvullende bepalingen." 1976.

[13] NNI, "NEN 3864 VB 1974 Voorschriften beton - deel D - Ongewapend beton aanvullende bepalingen." 1975.

[14] NNI, "NEN 3865 VB 1974 Voorschriften Beton - deel E - Gewapend beton aanvullende bepalingen." 1977.

[15] NNI, "NEN 3866 VB 1974 Voorschriften beton - deel F - Voorgespannen beton aanvullende bepalingen." 1976.

[16] NNI, "NEN 3867 VB 1974 Voorschriften beton - deel G - Lichtbeton - aanvullende bepalingen." 1978.

[17] VNC, "Betoniek 6/19 Voorschriften Beton VB 1974/1984 (NEN 3880)." 1984.

[18] NNI, "NEN 3880 VB 1974/1984 Voorschriften Beton." 1984.

[19] NNI, "NEN 5950 Voorschriften beton technologie (VBT 1986) - Eisen, vervaardiging en keuring." 1986.

[20] NNI, "NEN 5950 Voorschriften Beton, technologie (VBT 1995) - Eisen, vervaardiging en keuring." 1995.

[21] NNI, “NEN 6720 TGB 1990 VBC 1995 Voorschriften beton - constructieve eisen en rekenmethoden.” 1995.

[22] KIVI, “N 483 IJzerportlandcement - definitie en keuringseisen.” 1953.

[23] NNI, “NEN 3550 aanvulling Cement - definities, eisen en keuring.” 1986.

[24] NNI, “NEN-EN 1992-1-1+C2 Eurocode 2: Ontwerp en berekening van betonconstructies - Deel 1-1: Algemene regels en regels voor gebouwen.” 2011.

[25] T. C. Powers, L. E. Copeland, J. C. Hayes, and H. M. Mann, “Porosity of portland cement paste,” *J. Am. Concr. Inst.*, vol. 51, no. 11, pp. 285–298, 1954.

[26] P. de Vries, “We halen er steeds meer uit.” Mebin, VC12, IJmuiden, 2003.

Appendix B

Samples from existing structures

B.1 CEM I samples

Figure B2.1: 'Grollegat' viaduct in connecting road between A65 and A58 motorways near Tilburg, the Netherlands. The orange arrow points at the location where the core are drilled. Source: Google Streetview

Concrete samples with CEM I binder were taken in 2018 from a precast concrete beam of the viaduct "Grollegat" in the connecting road between the A65 and A58 motorways in the "De Baars" junction.

Figure B2.2: Viaduct 'Grollegat' in the 'De Baars' junction. The orange arrow points at the location where the cores are drilled. Source: Google Streetview

The Rijkswaterstaat topographical code for this structure is 50F-120. The precast beams of the main span are made of prestressed and reinforced concrete in strength class B65 with CEM I 52.5 R binder and a water-to-cement ratio of 0.45. The exact mix design is

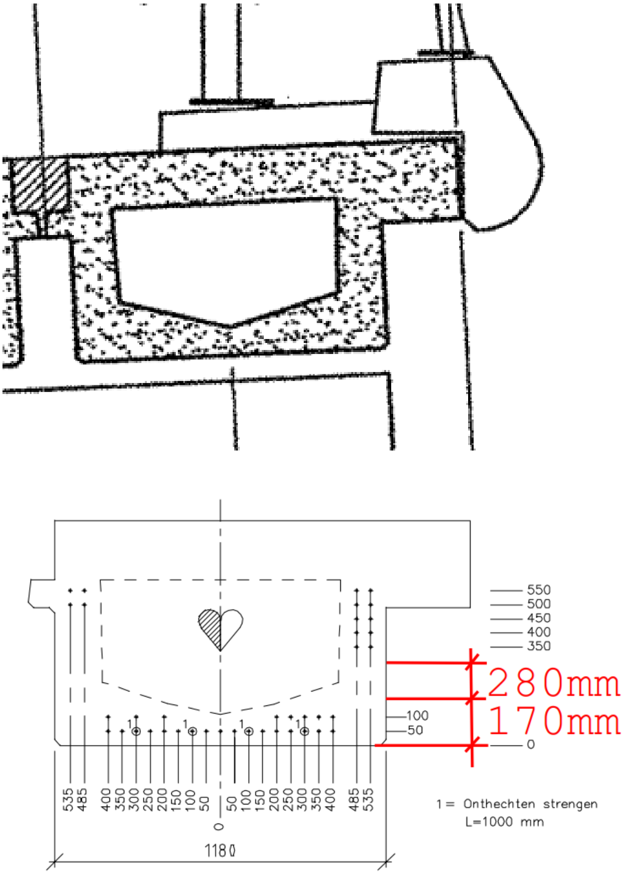

Figure B2.3: Cross-section of beam K1 with side element (top) and cross-section of beam K1 with vertical location of cores in beam (bottom).

no longer traceable. Concrete cover thickness according to element drawings: 35 mm. The beams are cast in 1999, the bridge is erected and put into service in 1999.

Two core samples with a diameter of 95 mm and a length of 190-205 mm were taken from the K1 precast concrete beam which is located on the high side of the span (the outermost, below the side element) as shown in Figure B2.1 and Figure B2.2. Chloride exposure on this side is minimal. The sample is taken from the south-west side of the viaduct and partly below the side element, so there will also be rather minimal precipitation exposure and only limited exposure to direct sunlight (see also Figure B2.3).

B.2 CEM III/B

Concrete samples with CEM III/B binder were taken in 2019 from an intermediate wall in the 2nd Beneluxtunnel in the A4 motorway between Pernis and Vlaardingen, near Rotterdam, the Netherlands.

Figure B2.4: Entrance of the A4 motorway at the 2nd Beneluxtunnel. Source: Wegenwiki.nl

The 2nd Beneluxtunnel is an immersed tunnel and the tunnel elements were constructed in the building dock near Barendrecht, the Netherlands between 1997 and 1998. The Rijkswaterstaat topographical code for the 2nd Beneluxtunnel is 37G-302-02.

The cast-in-situ tunnel structure was built with concrete in strength class B35 with 320 kg/m³ CEM III/B 42.5 LH HS binder and a water-to-binder ratio of 0.47. The thickness of the concrete cover layer is: 45-50 mm (according to core drillings).

Four core samples with a diameter of 50 mm and lengths between 50 and 95 mm were taken from the evacuation tunnel wall adjacent to tunnel tube ‘D’. Two cores were taken from tunnel element 3, segment A (see Figure B2.6) and two cores were taken from tunnel element 4 (see Figure B2.5), segment B. Although the concrete type was nominally the same in both segments, different mixtures w.r.t. aggregates were used in segment A of element 3 (mainly because of the higher reinforcement ratio around the escape door). The concrete in the evacuation tunnel is not exposed to any sunlight, de-icing salt or precipitation. The thickness of the walls is 500 mm.

In the past, Rijkswaterstaat carried out long-term monitoring on the climatic conditions in tunnels. This showed that climatic conditions in tunnels with an enclosed length of up to 1.5 km are similar to the climatic conditions outside of the tunnel.

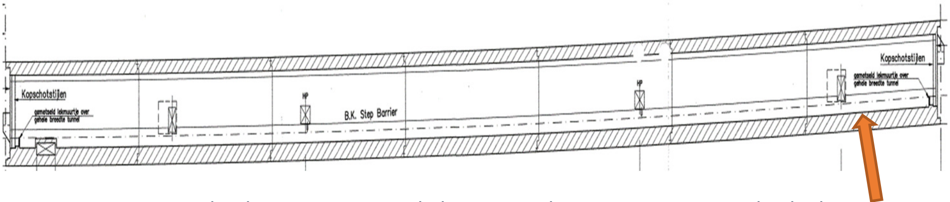

Figure B2.6: Longitudinal section on tunnel element 3. The orange arrow marks the location where the cores are taken.

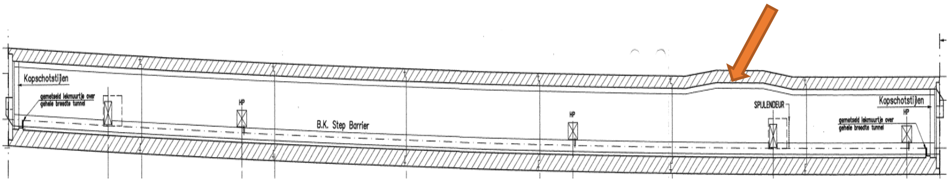

Figure B2.5: Longitudinal section on tunnel element 4. The orange arrow marks the location where the cores are taken.

B.3 CEM III/B + fly ash

Concrete samples with CEM III/B + fly ash binder were taken in 2019 from a panel of a wind deflecting structure along the Caland channel next to the Caland bridge near Rozenburg in the Rotterdam harbour area.

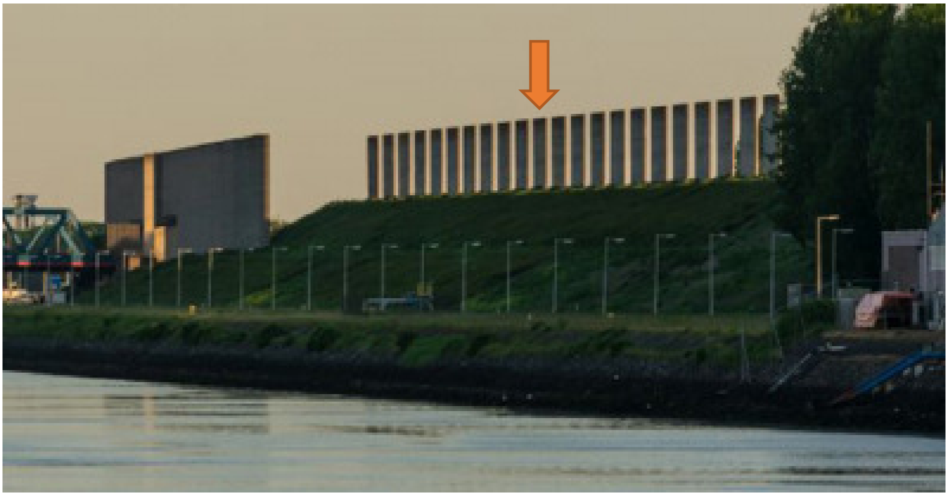

Figure B2.7: Picture of the wind deflector elements and the location of the wind deflector in relation to the Caland canal. The orange arrow points at the element where the cores were taken. Source: www.bkor.nl/beelden/windscherm-calandkanaal/

Until the early 1980's, CEM III/B + fly ash was not commonly used in the Netherlands. It was used in 1985 for the wind deflecting structure as a pilot application, mostly because the structure was considered as non-critical; should the concrete deteriorate more rapidly than can be expected of a regular used concrete type, this wouldn't cause a threat for critical infrastructure or people safety with regards to replacement or repair. The structure is built with concrete of strength class B30. The thickness of the concrete cover layer is 40 mm. Because of the pilot application status, the concrete mixture is well documented. In CUR 2000-2, [1] the test results from practical durability tests are described.

The wind deflector consists of 3 separate sections; a section in which straight walls are built on top of an embankment (see Figure B2.7) and two sections with semi-circular shaped sections (in two different radii). The curved parts are constructed with sliding formwork and because of that, they have a quite rough surface. The section with the straight walls is constructed in a traditional way and these panels have a smoot, uniform cover zone with regard to formwork influences.

The straight walls are 9.75 m high and 10 m wide and the wall thickness above the foundation is 300 mm. Samples were taken from wind deflector element number N39, the 11th straight wall element when counting from the south. Samples were taken from the east side of the wall, which is the least exposed to sea winds. The element is exposed to sunlight for at least 12 hours per day and exposed to all weather conditions. No de-icing salts are used anywhere near the straight wall elements and because of its orientation off the prevailing wind direction (see Figure B2.8), salt intrusion from seawater is reduced to a minimum.

Four cores with a diameter of 50 mm and a length of 100 mm were retrieved from the wall element.

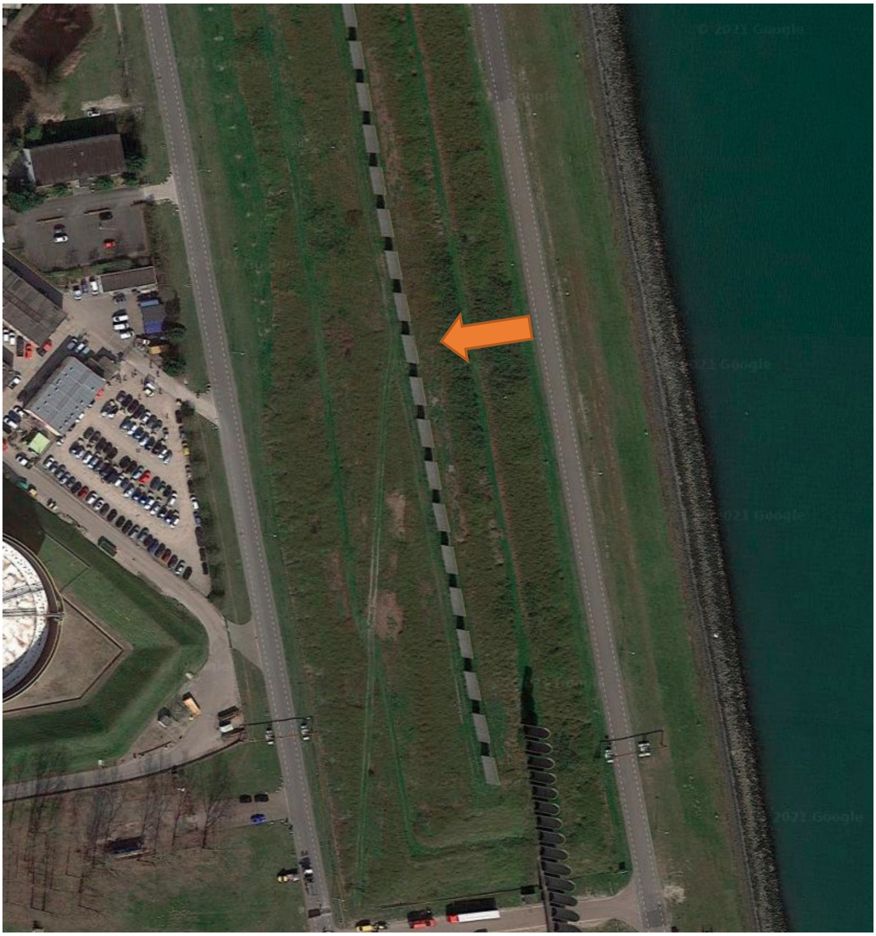

Figure B2.8: Location and orientation of the wind deflector. Source: Google Maps

B.4 CEM III/C

Concrete samples with CEM III/C binder were taken in 2019 from the underpass at the Neherkade, The Hague (see Figure B2.9). This underpass was built in 2014-2015 with concrete in strength class C30/37 with 360 kg/m³ binder CEM III/C 32.5 N/LH/HSR/LA and a water-to-binder ratio of 0.37. The thickness of the concrete cover layer is 55 mm.

Figure B2.9: Location and orientation of underpass Neherkade, The Hague. Source: Google Maps

The underpass has a closed section with a length of 130 m. The location where the cores were drilled is located in the wall directly adjacent to the road and near to the exit of the closed section (see also Figure B2.9 and Figure B2.10). The structure is soil retaining and groundwater retaining.

Four cores with a diameter of 50 mm and a length of 100 mm were retrieved from the wall element.

Figure B2.10: Location of core drillings (marked with the orange arrows). Source: Google Street view

B.5 References

[1] CUR, “CUR 2000-2 Duurzaamheid van beton met poederkoolvliegas in de praktijk,” Gouda, 2000.

Appendix C

Composition and structural properties of laboratory samples

CEM I

Casting date: 19 February 2020 (6 mortar beams)

Demoulded: 20 February 2020 & stored in mist room

Mortar beams:

Mix according to NEN-EN 196-1:2016

450 gr. cement, 1350 gr. CEN standard sand (0-2 mm), 225 gr. water per 3 beams

Table B.1: Flexural and compressive strength of mortar beams with CEM I

Casting date: 19 February 2020			**Test date: 18 March 2020**			
Beam nr.	Flexural strength		Compressive strength 1		Compressive strength 2	
	[kN]	[MPa]	[kN]	[Mpa]	[kN]	[Mpa]
1	3.489	8.177	56.762	35.476	59.047	36.904
2	3.448	8.081	58.801	36.751	57.691	36.057
3	3.812	8.934	51.936	32.460	62.065	38.791
Mean:		**8.4 Mpa**		**36.1 Mpa**		

CEM III/B

Casting date: 4 March 2020 (6 mortar beams)

Demoulded: 5 March 2020 & stored in mist room

Mortar beams:

Mix according to NEN-EN 196-1:2016

450 gr. cement, 1350 gr. CEN standard sand (0-2 mm), 225 gr. water per 3 beams

Table B.2: Flexural and compressive strength of mortar beams with CEM III/B

Casting date: 4 March 2020			**Test date: 1 April 2020**			
Beam nr.	Flexural strength		Compressive strength 1		Compressive strength 2	
	[kN]	[Mpa]	[kN]	[Mpa]	[kN]	[Mpa]
1	4.713	11.046	69.761	43.601	75.271	47.044
2	4.301	10.078	69.863	43.664	69.493	43.433
3	4.072	9.543	69.385	43.366	70.442	44.026
Mean:		**10.2 Mpa**		**44.2 Mpa**		

CEM III/B + FA

Casting date: 28 April 2020 (6 mortar beams)

Demoulded: 30 April 2020 & stored in mist room

Mortar beams:

Mix according to NEN-EN 196-1:2016

450 gr. cement, 1350 gr. CEN standard sand (0-2 mm), 23 gr. fly ash & 225 gr. water per 3 beams

Table B.3: Flexural and compressive strength of mortar beams with CEM III/B + FA

Casting date: 11 May 2020			**Test date: 11 June 2020**			
Beam	Flexural strength		Compressive strength 1		Compressive strength 2	
nr.	[kN]	[Mpa]	[kN]	[Mpa]	[kN]	[Mpa]
1	3.874	9.080	69.949	43.718	65.105	40.690
2	4.189	9.817	71.273	44.546	63.742	39.839
3	3.492	8.184	67.154	41.972	70.923	44.327
4	4.534	10.627	67.225	42.015	70.185	43.865
Mean:		**9.0 Mpa** (3 lowest values)		**42.0 Mpa** (6 lowest values)		

CEM III/C

Casting date: 28 April 2020 (6 mortar beams)

Demoulded: 30 April 2020 & stored in mist room

Mortar beams:

Mix according to NEN-EN 196-1:2016

450 gr. cement, 1350 gr. CEN standard sand (0-2 mm), 225 gr. water per 3 beams

Table B.4: Flexural and compressive strength of mortar beams with CEM III/C

Casting date: 11 May 2020			**Test date: 11 June 2020**			
Beam	Flexural strength		Compressive strength 1		Compressive strength 2	
nr.	[kN]	[MPa]	[kN]	[MPa]	[kN]	[MPa]
1	4.059	9.514	51.761	32.351	49.411	30.882
2	3.979	9.326	51.258	32.036	47.234	29.521
3	4.072	9.543	51.214	32.008	53.073	33.170
4	3.874	9.080	50.188	31.368	47.833	29.896
Mean:		**9.3 MPa**		**31.0 MPa**		
		(3 lowest values)		(6 lowest values)		

Appendix D

XRD results

X-RAY FACILITIES GROUP

Dr. Amarante Böttger *A.J.Bottger@tudelft.nl*
phone +31(0)1527·82243
Dhr. Ruud Hendrikx *R.W.A.Hendrikx@tudelft.nl*
Drs. Richard Huizenga *R.M.Huizenga@tudelft.nl*

Delft University of Technology, Faculty of 3mE
Department of Materials Science and Engineering
Mekelweg 2, NL-2628 CD Delft, the Netherlands, phone +31(0)1527·82255/89459

XRD identification of cement powders

Author : Ruud Hendrikx
Date : 01 oct 2020
Researcher : Bart Hendrix, CITG
Research question : Phase identification

Sample

Cement powder samples, labeled: "C1b" to "C4b" and "C1m" to "C4m"

Specimen

About 0.7 g of sample powder was deposited in PMMA holder L25.

Experimental

Instrument: Bruker D8 Advance diffractometer Bragg-Brentano geometry and Lynxeye position sensitive detector. Cu Kα radiation. Divergence slit V12, scatter screen height 5 mm, 45 kV 40 mA. Sample spinning. Detector settings LL 0.11 W 0.14.

Measurements

Coupled θ -2θ scan 10° - 110°, step size 0.021 ° 2θ, counting time per step 1 s.

Data evaluation

Bruker software DiffracSuite.EVA vs 5.2.

Results

Figures 1 - 8 show the measured XRD patterns in black, after background subtraction and small displacement correction. For better display of the small peaks, the intensity scales are square root.
The colored sticks give the peak positions and intensities of the possibly present phases, using the ICDD pdf4 database, see table 1. Some small peaks could not be identified.

If the analysis is a significant part of a publication, a co-authorship is preferred.

In any case, it is useful to involve us in the preparation of any presentation to ensure optimum and correct use of the analysis results!

Whenever used in a publication, an acknowledgement will be appreciated, e.g.:
"personX at the Department of Materials Science and Engineering of the Delft University of Technology is acknowledged for the X-ray analysis".

sample	*compound*	
C1b	Quartz	SiO_2
	Portlandite	$Ca(OH)_2$
	Dolomite	$CaMg(CO_3)_2$
	Ettringite	$Ca_6Al_2(SO_4)_3(OH)_{12}(H_2O)_{24}$
C2b	Quartz	SiO_2
	Portlandite	$Ca(OH)_2$
	Calcite	$CaCO_3$
	Ettringite	$Ca_6Al_2(SO_4)_3(OH)_{12}(H_2O)_{24}$
C3b	Quartz	SiO_2
	Portlandite	$Ca(OH)_2$
	Dolomite	$CaMg(CO_3)_2$
	Ettringite	$Ca_6Al_2(SO_4)_3(OH)_{12}(H_2O)_{24}$
C4b	Quartz	SiO_2
	Portlandite	$Ca(OH)_2$
	Calcite	$CaCO_3$
	Ettringite	$Ca_6Al_2(SO_4)_3(OH)_{12}(H_2O)_{24}$
C1m	Quartz	SiO_2
	Portlandite	$Ca(OH)_2$
	Dolomite	$CaMg(CO_3)_2$
	Ettringite	$Ca_6Al_2(SO_4)_3(OH)_{12}(H_2O)_{24}$
C2m	Quartz	SiO_2
	Portlandite	$Ca(OH)_2$
	Dolomite	$CaMg(CO_3)_2$
	Ettringite	$Ca_6Al_2(SO_4)_3(OH)_{12}(H_2O)_{24}$
C3m	Quartz	SiO_2
	Portlandite	$Ca(OH)_2$
	Dolomite	$CaMg(CO_3)_2$
	Ettringite	$Ca_6Al_2(SO_4)_3(OH)_{12}(H_2O)_{24}$
C4m	Quartz	SiO_2
	Dolomite	$CaMg(CO_3)_2$
	Ettringite	$Ca_6Al_2(SO_4)_3(OH)_{12}(H_2O)_{24}$

Table 1.

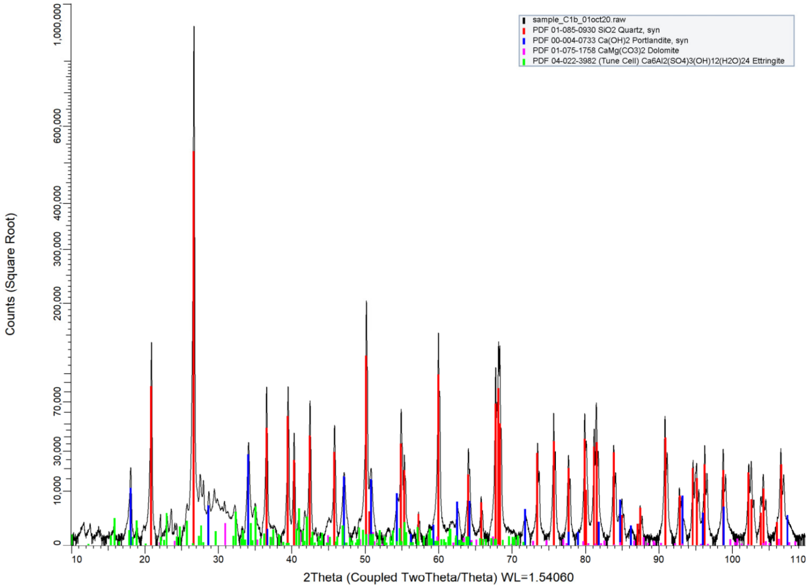

Figure 1 XRD pattern sample "C1b "

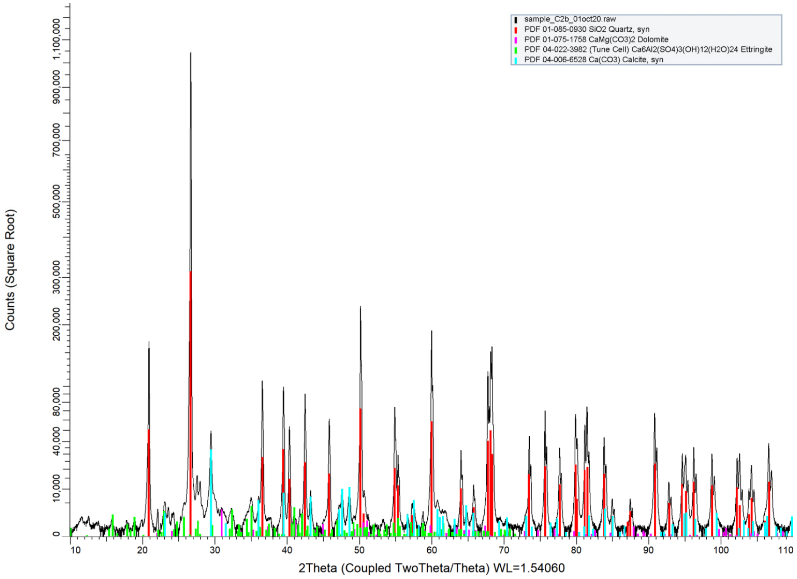

Figure 2 XRD pattern sample "C2b "

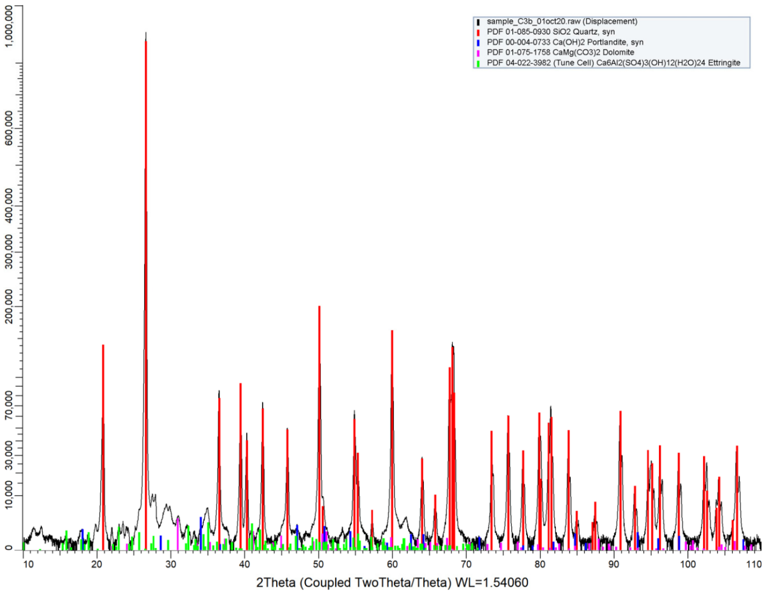

Figure 3 XRD pattern sample "C3b "

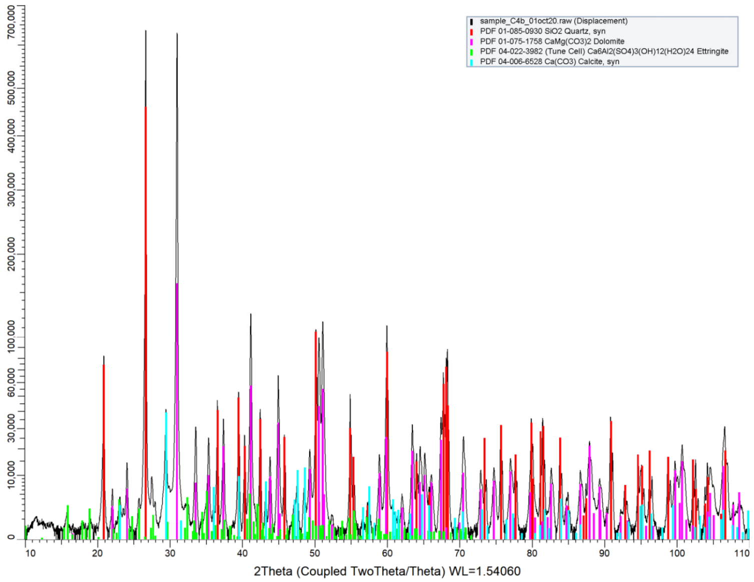

Figure 4 XRD pattern sample " C4b"

Figure 5 XRD pattern sample " C1m"

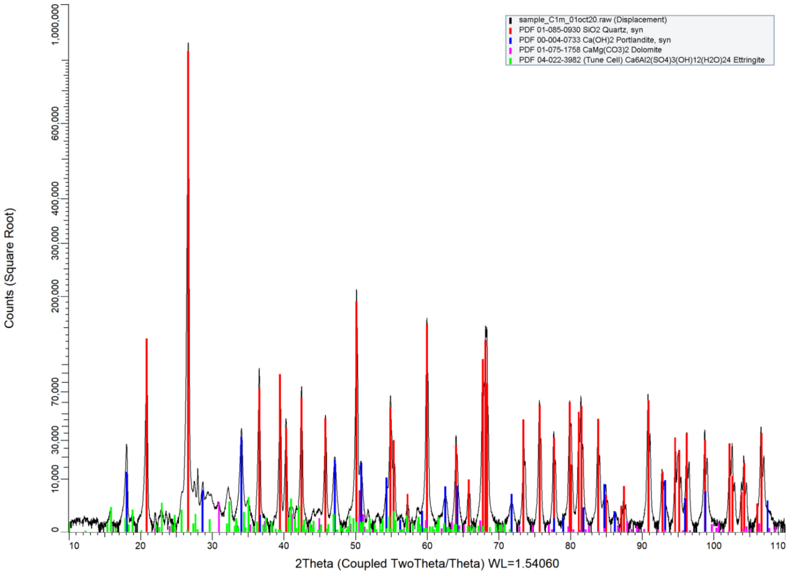

Figure 6 XRD pattern sample "C2m "

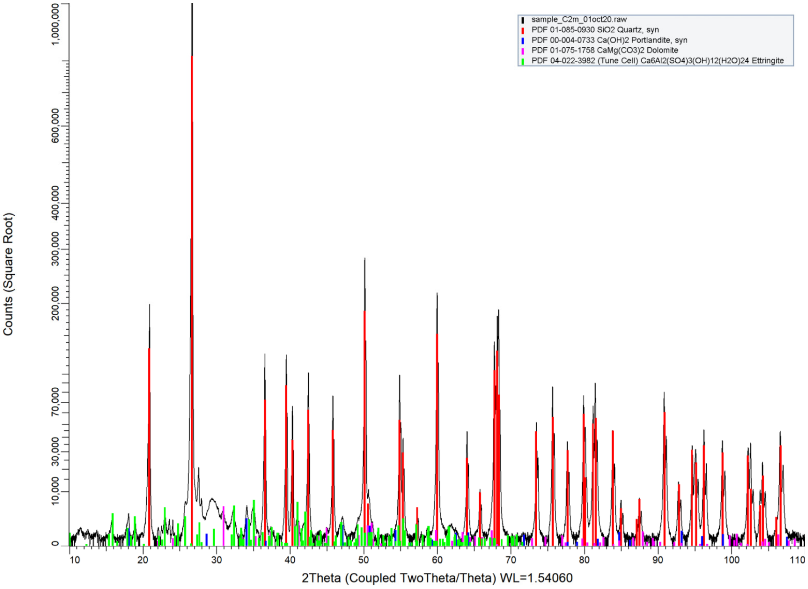

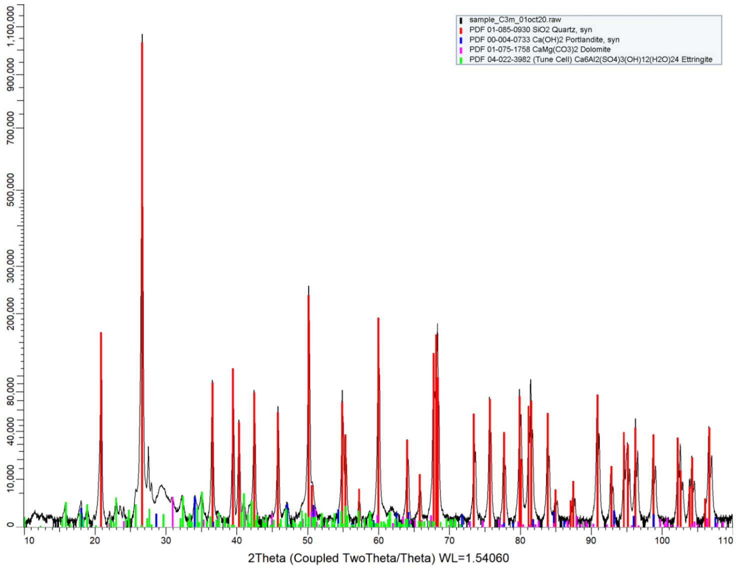

Figure 7 XRD pattern sample "C3m "

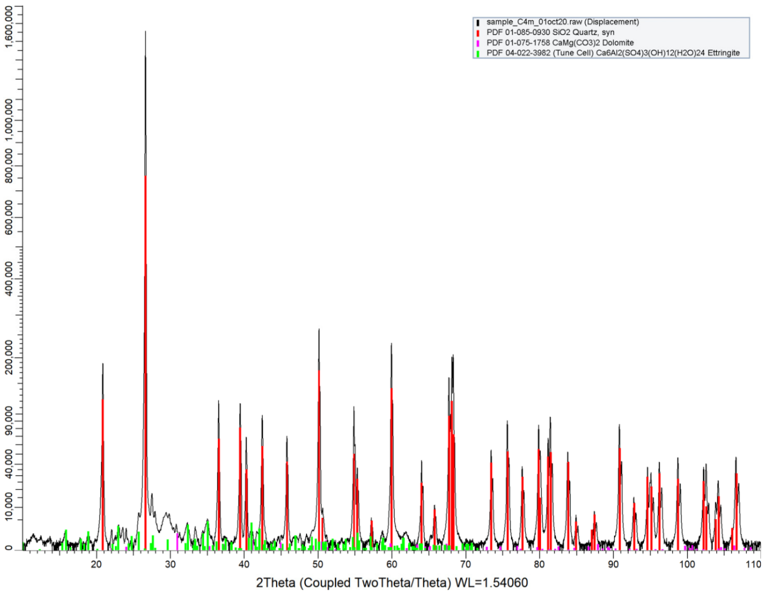

Figure 8 XRD pattern sample "C4m "

X-RAY FACILITIES GROUP

Dr. Amarante Böttger *A.J.Bottger@tudelft.nl*
phone +31(0)1527·82243
Dhr. Ruud Hendrikx *R.W.A.Hendrikx@tudelft.nl*
Drs. Richard Huizenga *R.M.Huizenga@tudelft.nl*

Delft University of Technology, Faculty of 3mE
Department of Materials Science and Engineering
Mekelweg 2, NL-2628 CD Delft, the Netherlands, phone +31(0)1527·82255/89459

XRD identification of cement powders

Author : Ruud Hendrikx
Date : 16 jun 2021
Researcher : Bart Hendrix, CITG
Research question : Phase identification

Sample

Cement powder samples, labeled: "C1C1" to "C1C4" and "C1M1" to "C1M4"

Specimen

About 0.7 g of sample powder was deposited in PMMA holder L25.

Experimental

Instrument: Bruker D8 Advance diffractometer Bragg-Brentano geometry and Lynxeye position sensitive detector. Cu Kα radiation. Divergence slit V12, scatter screen height 5 mm, 45 kV 40 mA. Sample spinning. Detector settings LL 0.11 W 0.14.

Measurements

Coupled θ -2θ scan 10° - 110°, step size 0.021 ° 2θ, counting time per step 1 s.

Data evaluation

Bruker software DiffracSuite.EVA vs 5.2.

Results

Figures 1 - 8 show the measured XRD patterns in black, after background subtraction and small displacement correction. For better display of the small peaks, the intensity scales are square root.
The colored sticks give the peak positions and intensities of the possibly present phases, using the ICDD pdf4 database, see table 1. Some small peaks could not be identified.

sample	*compound*	
C1C1	Quartz	SiO2
	Portlandite	Ca(OH)2
	Dolomite	CaMg(CO3)2
	Ettringite	Ca6Al2(SO4)3(OH)12(H2O)24
	Calcite	CaCO3
C1C2	Quartz	SiO2
	Portlandite	Ca(OH)2
	Dolomite	CaMg(CO3)2
	Ettringite	Ca6Al2(SO4)3(OH)12(H2O)24
	Calcite	CaCO3
C1C3	Quartz	SiO2
	Portlandite	Ca(OH)2
	Dolomite	CaMg(CO3)2
	Ettringite	Ca6Al2(SO4)3(OH)12(H2O)24
	Calcite	CaCO3
C1C4	Quartz	SiO2
	Portlandite	Ca(OH)2
	Dolomite	CaMg(CO3)2
	Ettringite	Ca6Al2(SO4)3(OH)12(H2O)24
	Calcite	CaCO3
C1M1	Quartz	SiO2
	Portlandite	Ca(OH)2
	Dolomite	CaMg(CO3)2
	Ettringite	Ca6Al2(SO4)3(OH)12(H2O)24
	Calcite	CaCO3
C1M2	Quartz	SiO2
	Portlandite	Ca(OH)2
	Dolomite	CaMg(CO3)2
	Ettringite	Ca6Al2(SO4)3(OH)12(H2O)24
	Calcite	CaCO3
C1M3	Quartz	SiO2
	Portlandite	Ca(OH)2
	Dolomite	CaMg(CO3)2
	Ettringite	Ca6Al2(SO4)3(OH)12(H2O)24
	Calcite	CaCO3
C1M4	Quartz	SiO2
	Portlandite	Ca(OH)2
	Dolomite	CaMg(CO3)2
	Ettringite	Ca6Al2(SO4)3(OH)12(H2O)24
	Calcite	CaCO3

Table 1.

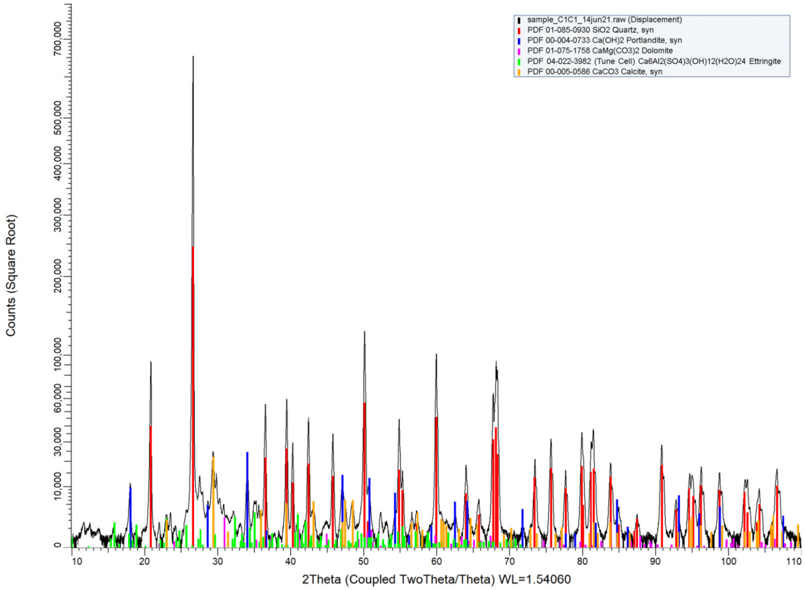

Figure 1 XRD pattern sample "C1C1 ", intensity scale is square root

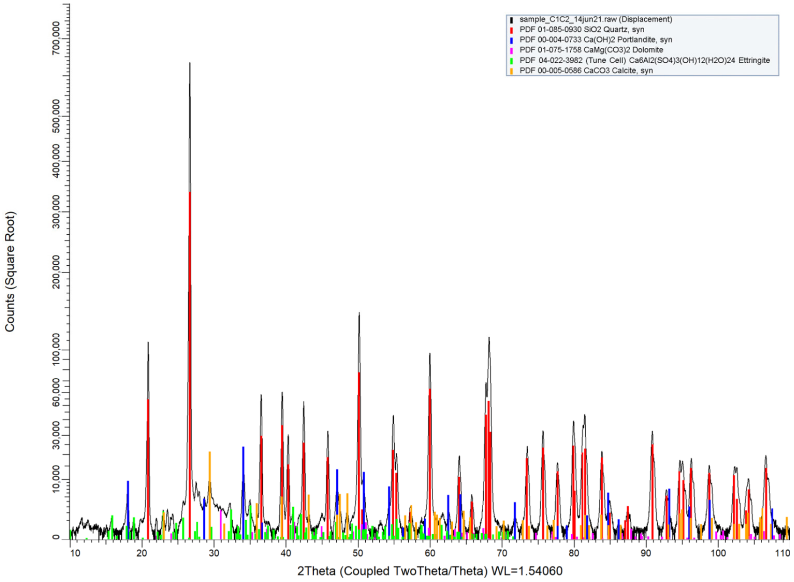

Figure 2 XRD pattern sample "C1C2 ", intensity scale is square root

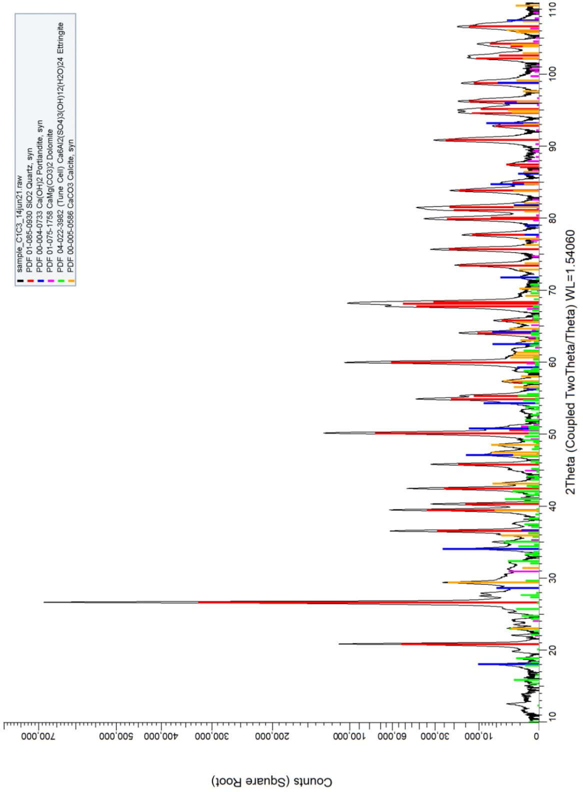

Figure 3 XRD pattern sample "C1C3 ", intensity scale is square root

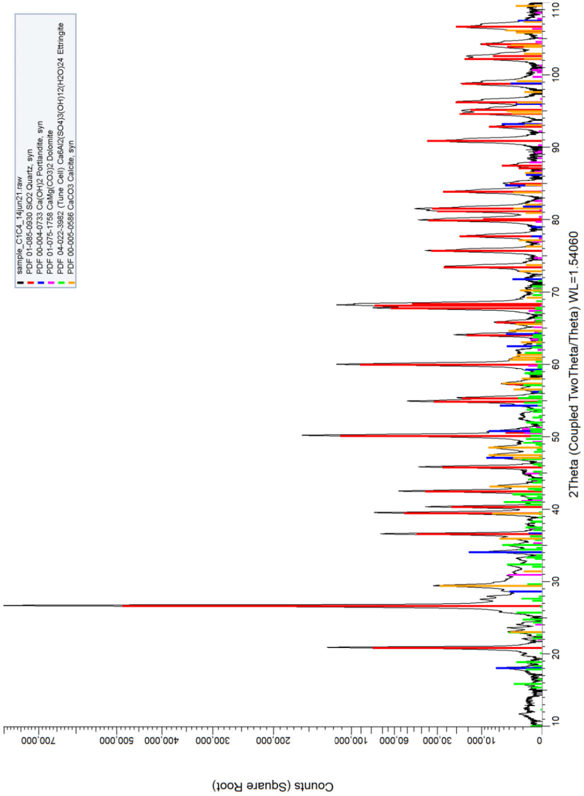

Figure 4 XRD pattern sample " C1C4 ", intensity scale is square root

Figure 5 XRD pattern sample " C1M1, intensity scale is square root

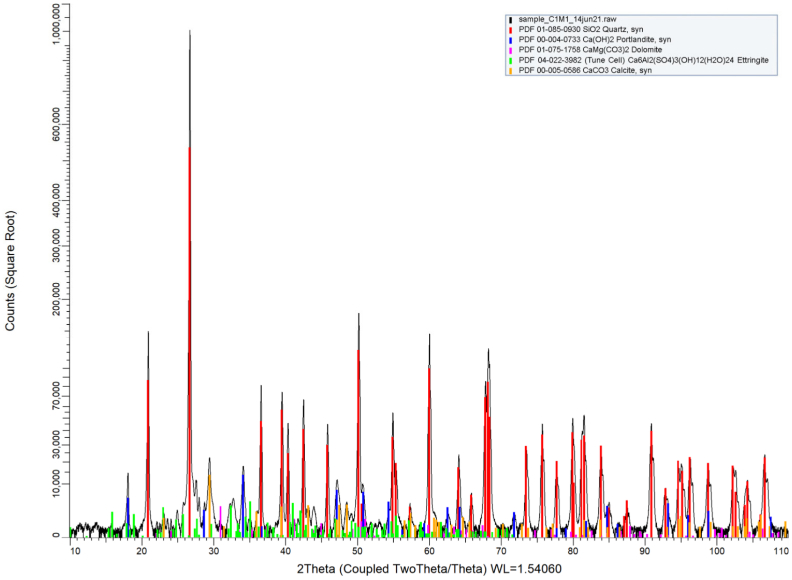

Figure 6 XRD pattern sample "C1M2 ", intensity scale is square root

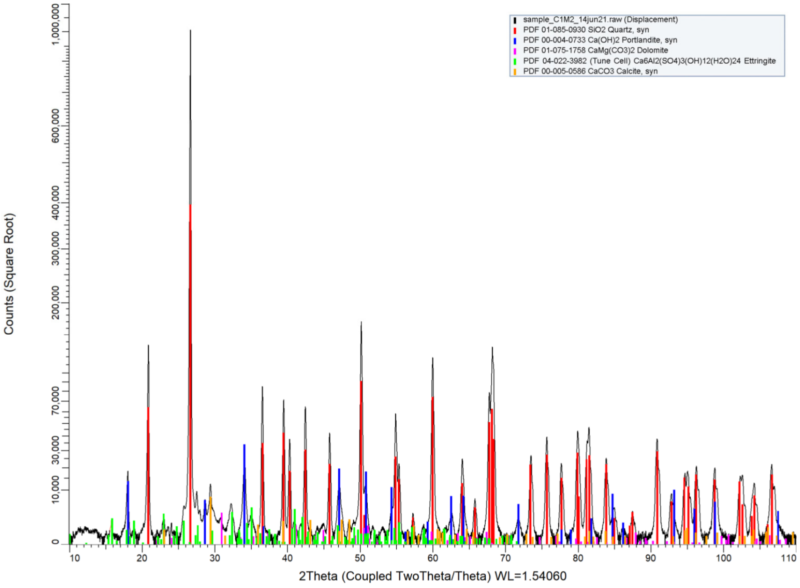

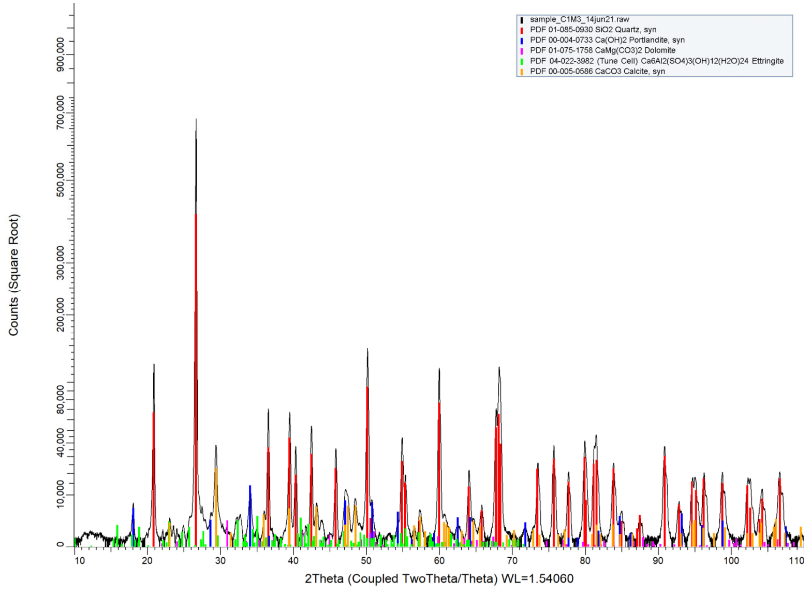

Figure 7 XRD pattern sample "C1M3"

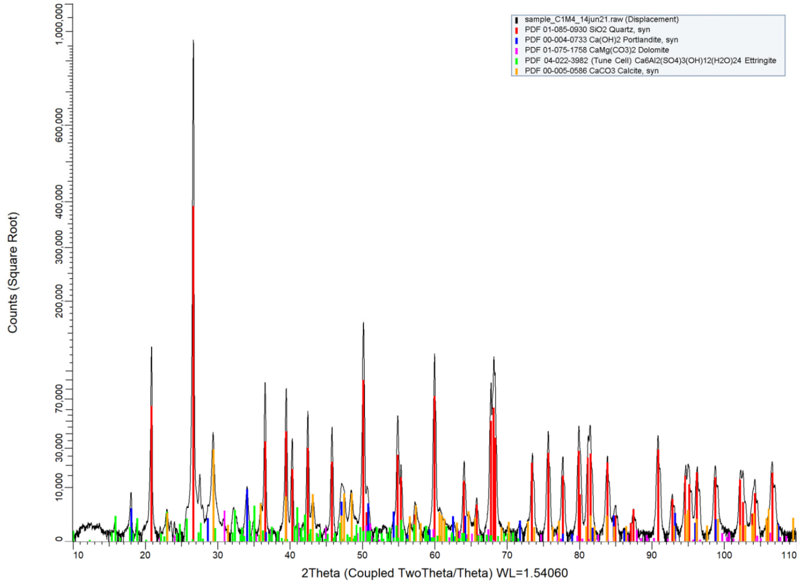

Figure 8 XRD pattern sample "C1M4 "

X-RAY FACILITIES GROUP

Dr. Amarante Böttger *A.J.Bottger@tudelft.nl*
phone +31(0)1527·82243
Dhr. Ruud Hendrikx *R.W.A.Hendrikx@tudelft.nl*
Drs. Richard Huizenga *R.M.Huizenga@tudelft.nl*

Delft University of Technology, Faculty of 3mE
Department of Materials Science and Engineering
Mekelweg 2, NL-2628 CD Delft, the Netherlands, phone +31(0)1527·82255/89459

XRD identification of cement powders

Author : Ruud Hendrikx
Date : 23 jun 2021
Researcher : Bart Hendrix, CITG
Research question : Phase identification

Sample

Cement powder samples, labeled: "C2C1" to "C2C4" and "C2M1" to "C2M4"

Specimen

About 0.7 g of sample powder was deposited in PMMA holder L25.

Experimental

Instrument: Bruker D8 Advance diffractometer Bragg-Brentano geometry and Lynxeye position sensitive detector. Cu Kα radiation. Divergence slit V12, scatter screen height 5 mm, 45 kV 40 mA. Sample spinning. Detector settings LL 0.11 W 0.14.

Measurements

Coupled θ -2θ scan 10° - 110°, step size 0.021 ° 2θ, counting time per step 1 s.

Data evaluation

Bruker software DiffracSuite.EVA vs 5.2.

Results

Figures 1 - 8 show the measured XRD patterns in black, after background subtraction and small displacement correction. For better display of the small peaks, the intensity scales are square root.
The colored sticks give the peak positions and intensities of the possibly present phases, using the ICDD pdf4 database, see table 1. Some small peaks could not be identified.

If the analysis is a significant part of a publication, a co-authorship is preferred.

In any case, it is useful to involve us in the preparation of any presentation to ensure optimum and correct use of the analysis results!

Whenever used in a publication, an acknowledgement will be appreciated, e.g.:
"personX at the Department of Materials Science and Engineering of the Delft University of Technology is acknowledged for the X-ray analysis".

sample	*compound*	
C2C1	Quartz	SiO_2
	Ettringite	$Ca_6Al_2(SO_4)_3(OH)_{12}(H_2O)_{24}$
	Calcite	$CaCO_3$
	Vaterite	$CaCO_3$
	Albite	$Na(AlSi_3O_8)$
C2C2	Quartz	SiO_2
	Ettringite	$Ca_6Al_2(SO_4)_3(OH)_{12}(H_2O)_{24}$
	Calcite	$CaCO_3$
	Albite	$Na(AlSi_3O_8)$
C2C3	Quartz	SiO_2
	Ettringite	$Ca_6Al_2(SO_4)_3(OH)_{12}(H_2O)_{24}$
	Calcite	$CaCO_3$
	Dolomite	$CaMg(CO_3)_2$
	Albite	$Na(AlSi_3O_8)$
C2C4	Quartz	SiO_2
	Ettringite	$Ca_6Al_2(SO_4)_3(OH)_{12}(H_2O)_{24}$
	Calcite	$CaCO_3$
	Dolomite	$CaMg(CO_3)_2$
	Albite	$Na(AlSi_3O_8)$
C2M1	Quartz	SiO_2
	Ettringite	$Ca_6Al_2(SO_4)_3(OH)_{12}(H_2O)_{24}$
	Calcite	$CaCO_3$
	Vaterite	$CaCO_3$
	Albite	$Na(AlSi_3O_8)$
C2M2	Quartz	SiO_2
	Ettringite	$Ca_6Al_2(SO_4)_3(OH)_{12}(H_2O)_{24}$
	Calcite	$CaCO_3$
	Albite	$Na(AlSi_3O_8)$
C2M3	Quartz	SiO_2
	Ettringite	$Ca_6Al_2(SO_4)_3(OH)_{12}(H_2O)_{24}$
	Calcite	$CaCO_3$
	Vaterite	$CaCO_3$
	Albite	$Na(AlSi_3O_8)$
C2M4	Quartz	SiO_2
	Ettringite	$Ca_6Al_2(SO_4)_3(OH)_{12}(H_2O)_{24}$
	Calcite	$CaCO_3$
	Vaterite	$CaCO_3$
	Albite	$Na(AlSi_3O_8)$

Table 1.

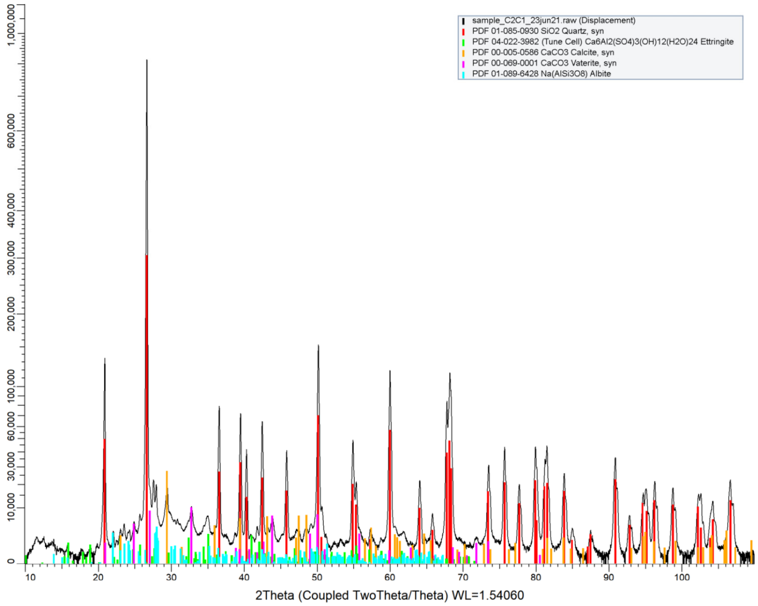

Figure 1 XRD pattern sample "C2C1 ", intensity scale is square root

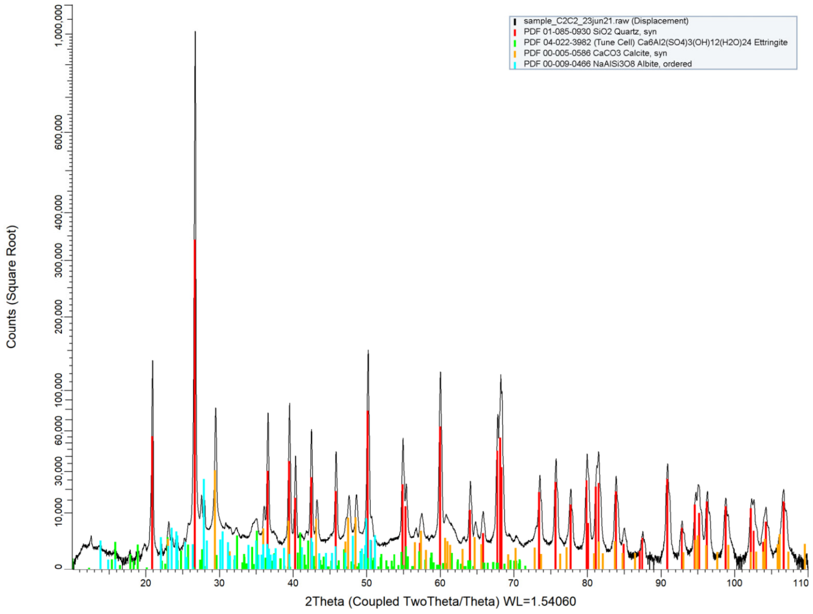

Figure 2 XRD pattern sample "C2C2 ", intensity scale is square root

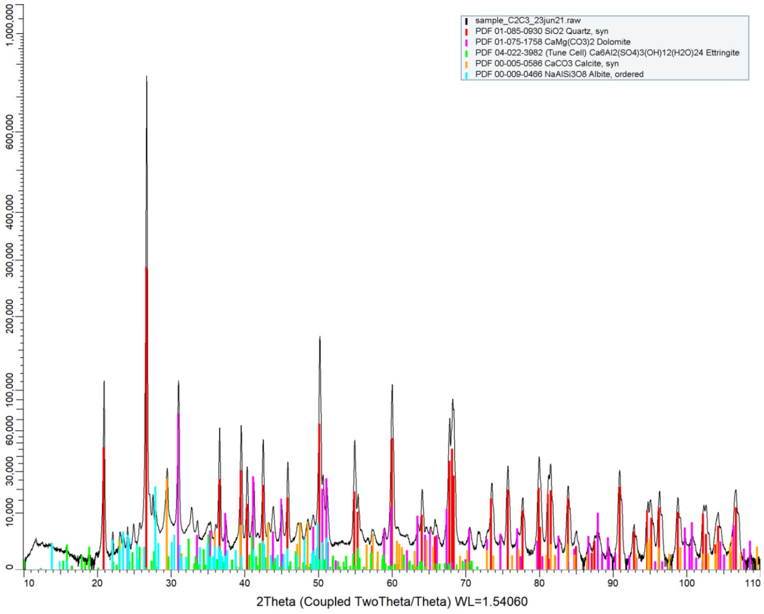

Figure 3 XRD pattern sample "C2C3 ", intensity scale is square root

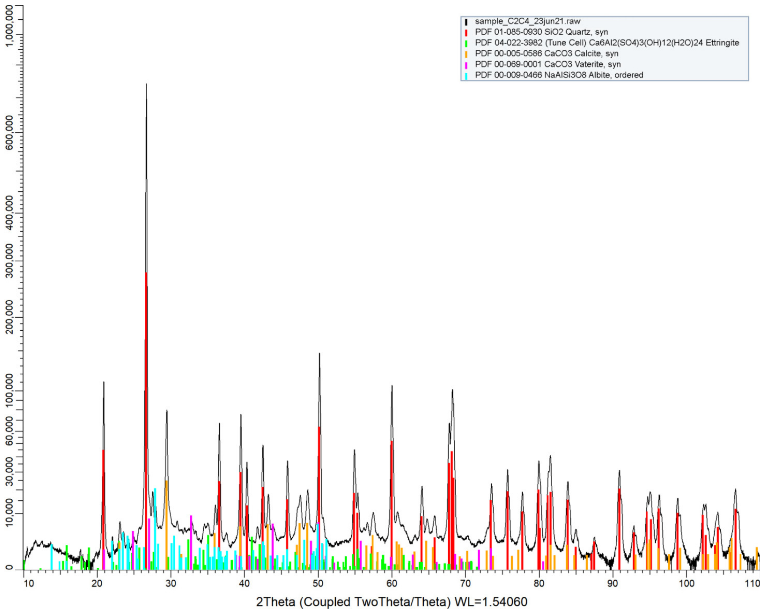

Figure 4 XRD pattern sample " C2C4 ", intensity scale is square root

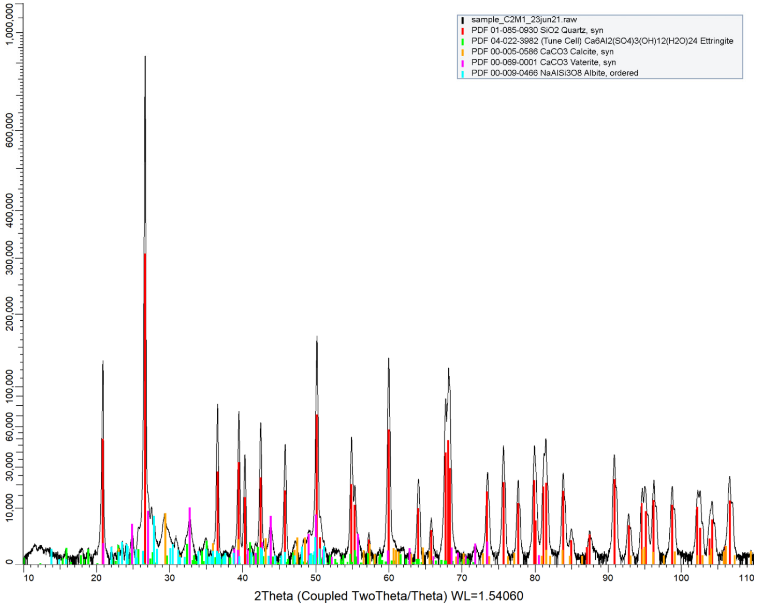

Figure 5 XRD pattern sample " C2M1, intensity scale is square root

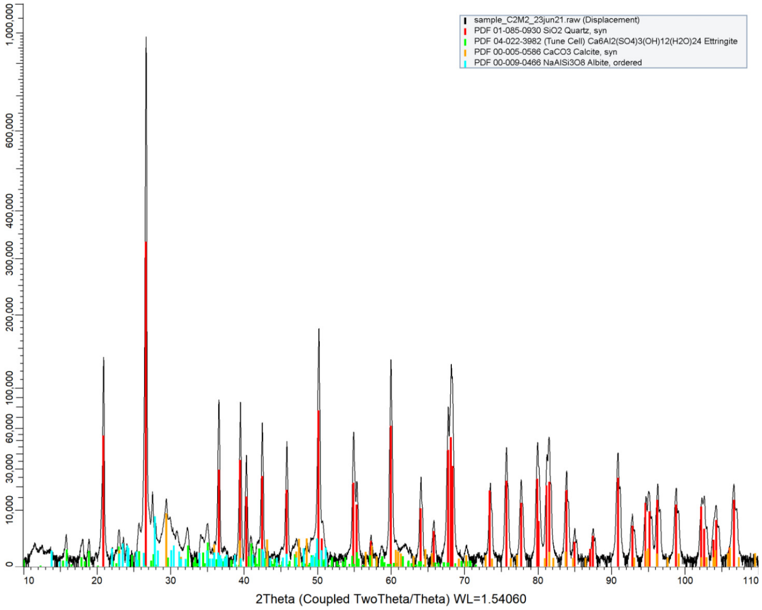

Figure 6 XRD pattern sample "C2M2 ", intensity scale is square root

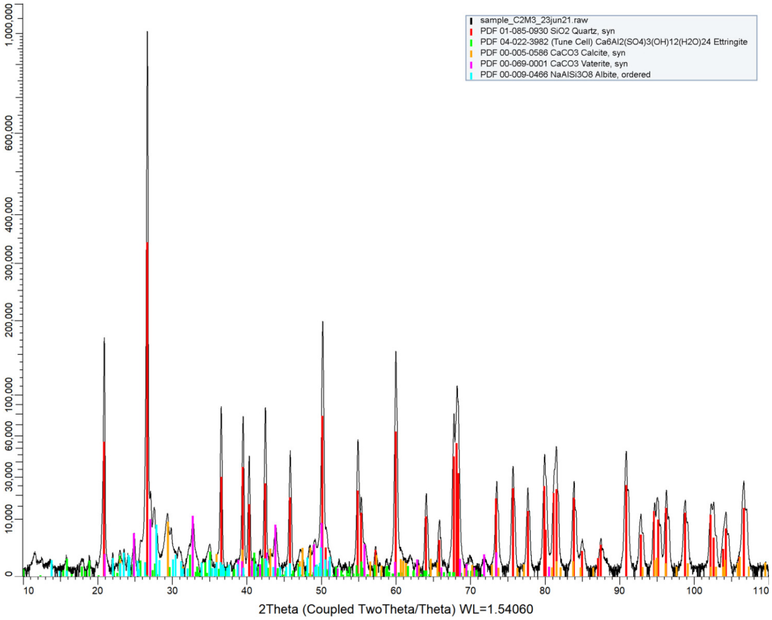

Figure 7 XRD pattern sample "C2M3 ", intensity scale is square root

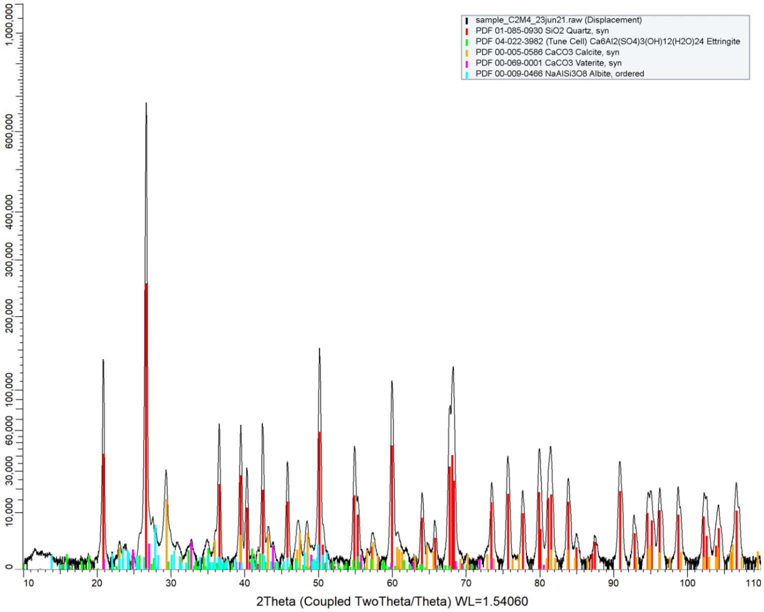

Figure 8 XRD pattern sample "C2M4 ", intensity scale is square root

X-RAY FACILITIES GROUP

Dr. Amarante Böttger *A.J.Bottger@tudelft.nl*
phone +31(0)1527·82243
Dhr. Ruud Hendrikx *R.W.A.Hendrikx@tudelft.nl*
Drs. Richard Huizenga *R.M.Huizenga@tudelft.nl*

Delft University of Technology, Faculty of 3mE
Department of Materials Science and Engineering
Mekelweg 2, NL-2628 CD Delft, the Netherlands, phone +31(0)1527·82255/89459

XRD identification of cement powders

Author : Ruud Hendrikx
Date : 30 jun 2021
Researcher : Bart Hendrix, CITG
Research question : Phase identification

Sample

Cement powder samples, labeled: "C3C1" to "C3C4" and "C3M1" to "C3M4"

Specimen

About 0.7 g of sample powder was deposited in PMMA holder L25.

Experimental

Instrument: Bruker D8 Advance diffractometer Bragg-Brentano geometry and Lynxeye position sensitive detector. Cu Kα radiation. Divergence slit V12, scatter screen height 5 mm, 45 kV 40 mA. Sample spinning. Detector settings LL 0.11 W 0.14.

Measurements

Coupled θ -2θ scan 10° - 110°, step size 0.021 ° 2θ, counting time per step 1 s.

Data evaluation

Bruker software DiffracSuite.EVA vs 5.2.

Results

Figures 1 - 8 show the measured XRD patterns in black, after background subtraction and small displacement correction. For better display of the small peaks, the intensity scales are square root.
The colored sticks give the peak positions and intensities of the possibly present phases, using the ICDD pdf4 database, see table 1. Some small peaks could not be identified.

If the analysis is a significant part of a publication, a co-authorship is preferred.

In any case, it is useful to involve us in the preparation of any presentation to ensure optimum and correct use of the analysis results!

Whenever used in a publication, an acknowledgement will be appreciated, e.g.:
"personX at the Department of Materials Science and Engineering of the Delft University of Technology is acknowledged for the X-ray analysis".

sample	*compound*	
C3C1	Quartz	SiO2
	Calcite	CaCO3
	Vaterite	CaCO3
	Albite, ordered	NaAlSi3O8
	Montmorillonite-22A	Na0.3(Al,Mg)2Si4O10(OH)2·8H2O
C3C2	Quartz	SiO2
	Portlandite	Ca(OH)2
	Dolomite	CaMg(CO3)2
	Ettringite	Ca6Al2(SO4)3(OH)12(H2O)24
	Calcite	CaCO3
	Albite, ordered	NaAlSi3O8
C3C3	Quartz	SiO2
	Portlandite	Ca(OH)2
	Vaterite	CaCO3
	Ettringite	Ca6Al2(SO4)3(OH)12(H2O)24
	Calcite	CaCO3
	Albite, ordered	NaAlSi3O8
C3C4	Quartz	SiO2
	Portlandite	Ca(OH)2
	Ettringite	Ca6Al2(SO4)3(OH)12(H2O)24
	Calcite	CaCO3
	Vaterite	CaCO3
	Chlorite-serpentine (NR)	(Mg,Al)6(Si,Al)4O10(OH)8
	Albite, ordered	NaAlSi3O8
C3M1	Quartz	SiO2
	Portlandite	Ca(OH)2
	Ettringite	Ca6Al2(SO4)3(OH)12(H2O)24
	Calcite	CaCO3
	Vaterite	CaCO3
	Albite, ordered	NaAlSi3O8
C3M2	Quartz	SiO2
	Portlandite	Ca(OH)2
	Dolomite	CaMg(CO3)2
	Ettringite	Ca6Al2(SO4)3(OH)12(H2O)24
	Calcite	CaCO3
	Albite, ordered	NaAlSi3O8
C3M3	Quartz	SiO2
	Portlandite	Ca(OH)2
	Dolomite	CaMg(CO3)2
	Ettringite	Ca6Al2(SO4)3(OH)12(H2O)24
	Calcite	CaCO3
	Vaterite	CaCO3
	Albite, ordered	NaAlSi3O8

Table 1.

C3M4	Quartz	SiO2
	Portlandite	Ca(OH)2
	Dolomite	CaMg(CO3)2
	Ettringite	Ca6Al2(SO4)3(OH)12(H2O)24
	Calcite	CaCO3
	Vaterite	CaCO3
	Albite, ordered	NaAlSi3O8

Table 1 contimued.

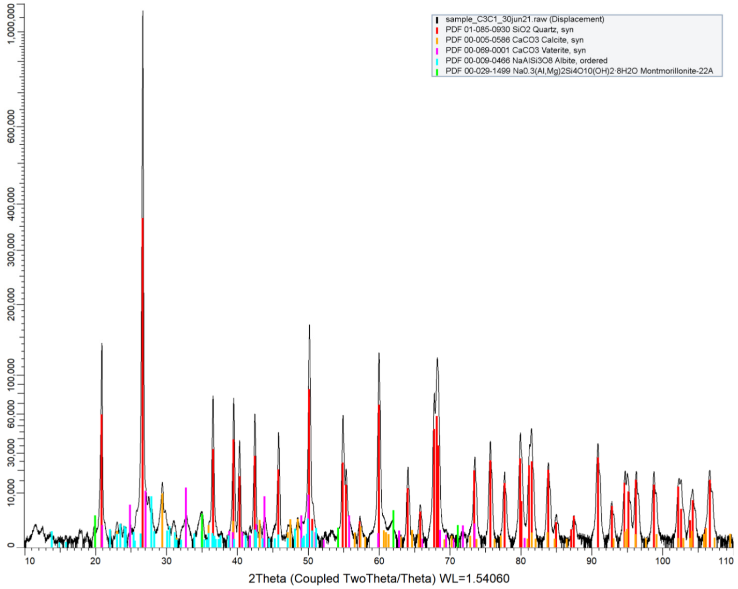

Figure 1 XRD pattern sample "C3C1 ", intensity scale is square root

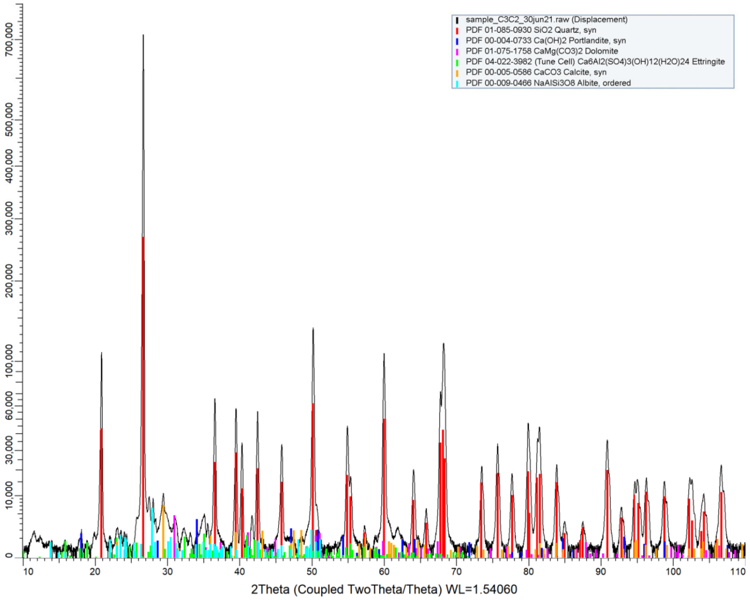

Figure 2 XRD pattern sample "C3C2 ", intensity scale is square root

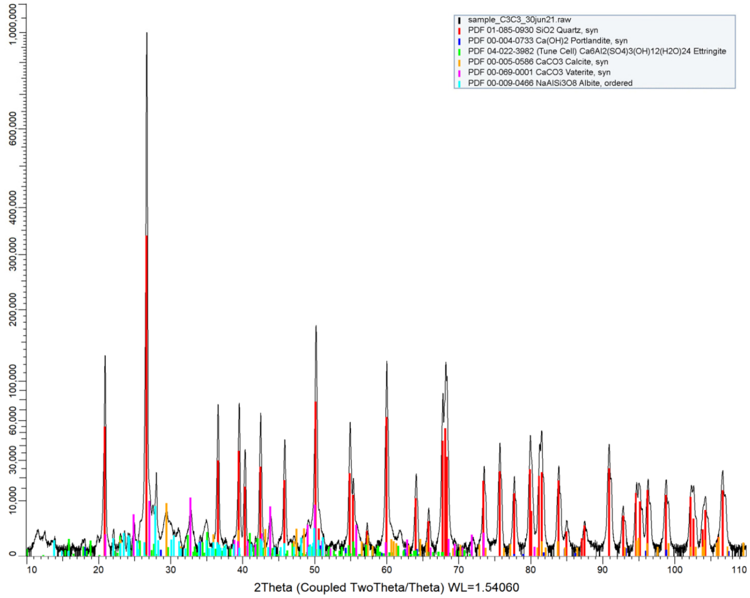

Figure 3 XRD pattern sample "C3C3 ", intensity scale is square root

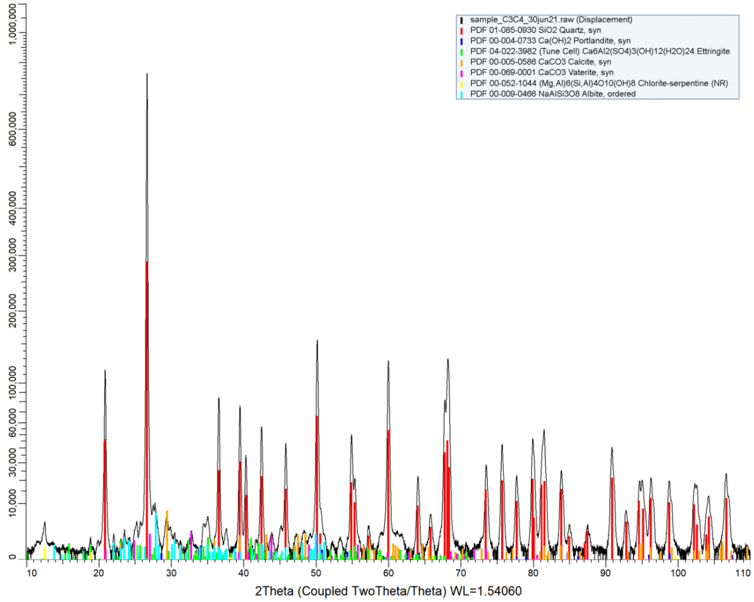

Figure 4 XRD pattern sample " C3C4 " , intensity scale is square root

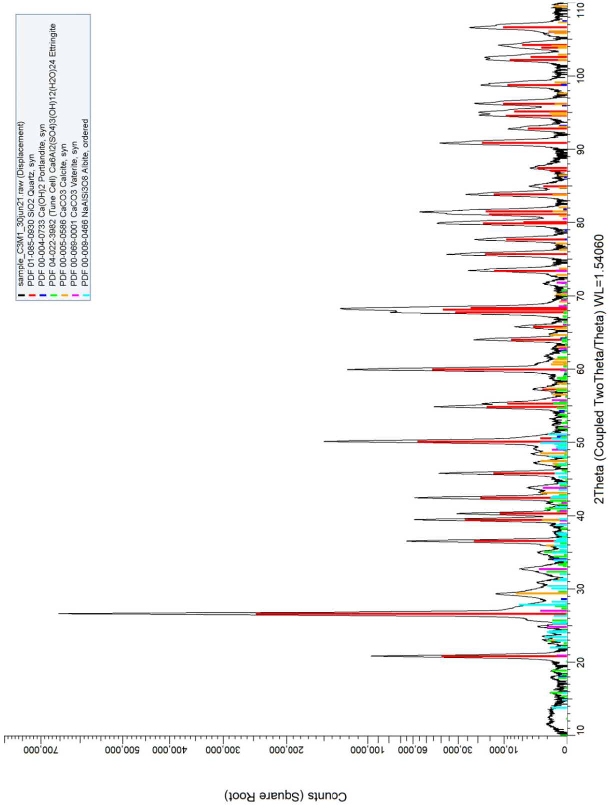

Figure 5 XRD pattern sample " C3M1, intensity scale is square root

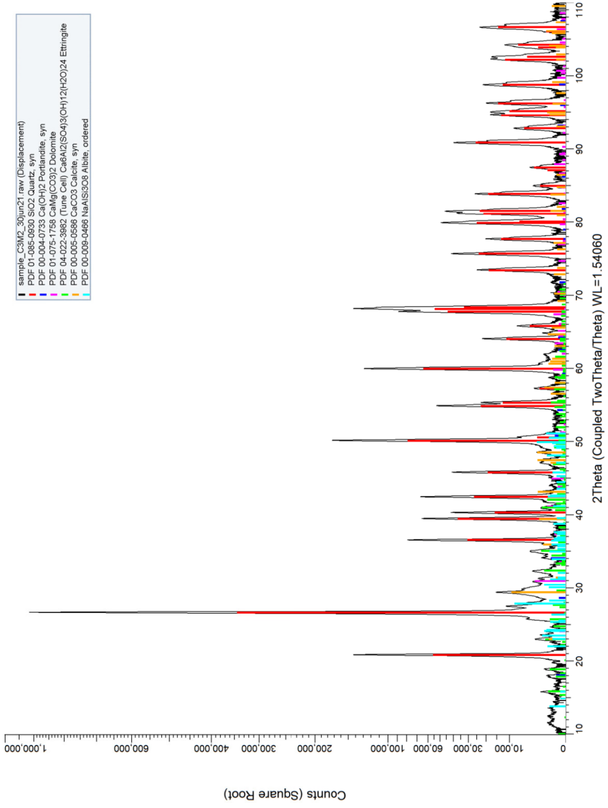

Figure 6 XRD pattern sample "C3M2 ", intensity scale is square root

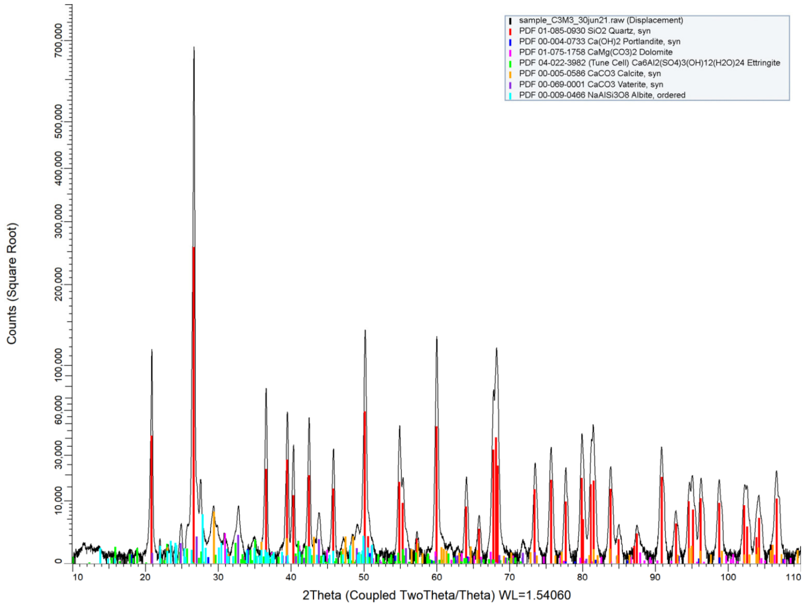

Figure 7 XRD pattern sample "C3M3 ", intensity scale is square root

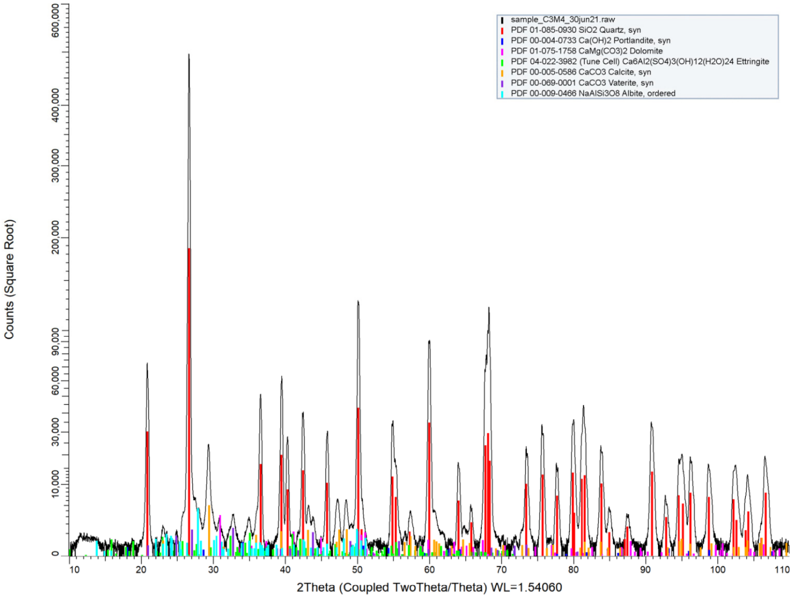

Figure 8 XRD pattern sample "C3M4 ", intensity scale is square root

X-RAY FACILITIES GROUP

Dr. Amarante Böttger *A.J.Bottger@tudelft.nl*
phone +31(0)1527·82243
Dhr. Ruud Hendrikx *R.W.A.Hendrikx@tudelft.nl*
Drs. Richard Huizenga *R.M.Huizenga@tudelft.nl*

Delft University of Technology, Faculty of 3mE
Department of Materials Science and Engineering
Mekelweg 2, NL-2628 CD Delft, the Netherlands, phone +31(0)1527·82255/89459

XRD identification of cement powders

Author : Ruud Hendrikx
Date : 02 jul 2021
Researcher : Bart Hendrix, CITG
Research question : Phase identification

Sample

Cement powder samples, labeled: “C4C1” to “C4C4” and “C4M1” to “C4M4”

Specimen

About 0.7 g of sample powder was deposited in PMMA holder L25.

Experimental

Instrument: Bruker D8 Advance diffractometer Bragg-Brentano geometry and Lynxeye position sensitive detector. Cu Kα radiation. Divergence slit V12, scatter screen height 5 mm, 45 kV 40 mA. Sample spinning. Detector settings LL 0.11 W 0.14.

Measurements

Coupled θ -2θ scan 10° - 110°, step size 0.021 ° 2θ, counting time per step 1 s.

Data evaluation

Bruker software DiffracSuite.EVA vs 5.2.

Results

Figures 1 - 8 show the measured XRD patterns in black, after background subtraction and small displacement correction. For better display of the small peaks, the intensity scales are square root.
The colored sticks give the peak positions and intensities of the possibly present phases, using the ICDD pdf4 database, see table 1. Some small peaks could not be identified.

If the analysis is a significant part of a publication, a co-authorship is preferred.

In any case, it is useful to involve us in the preparation of any presentation to ensure optimum and correct use of the analysis results!

Whenever used in a publication, an acknowledgement will be appreciated, e.g.:
"personX at the Department of Materials Science and Engineering of the Delft University of Technology is acknowledged for the X-ray analysis”.

sample	*compound*	
C4C1	Quartz	SiO2
	Dolomite	CaMg(CO3)2
	Vaterite	CaCO3
	Calcite	CaCO3
	Albite, ordered	NaAlSi3O8
C4C2	Quartz	SiO2
	Dolomite	CaMg(CO3)2
	Calcite	CaCO3
	Albite, ordered	NaAlSi3O8
	Ettringite	Ca6Al2(SO4)3(OH)12(H2O)24
C4C3	Quartz	SiO2
	Dolomite	CaMg(CO3)2
	Calcite	CaCO3
	Vaterite	CaCO3
	Albite, ordered	NaAlSi3O8
	Ettringite	Ca6Al2(SO4)3(OH)12(H2O)24
C4C4	Quartz	SiO2
	Dolomite	CaMg(CO3)2
	Calcite	CaCO3
	Vaterite	CaCO3
	Albite, ordered	NaAlSi3O8
	Ettringite	Ca6Al2(SO4)3(OH)12(H2O)24
C4M1	Quartz	SiO2
	Dolomite	CaMg(CO3)2
	Calcite	CaCO3
	Vaterite	CaCO3
	Albite, ordered	NaAlSi3O8
	Ettringite	Ca6Al2(SO4)3(OH)12(H2O)24
C4M2	Quartz	SiO2
	Dolomite	CaMg(CO3)2
	Calcite	CaCO3
	Albite, ordered	NaAlSi3O8
	Ettringite	Ca6Al2(SO4)3(OH)12(H2O)24
C4M3	Quartz	SiO2
	Dolomite	CaMg(CO3)2
	Calcite	CaCO3
	Vaterite	CaCO3
	Albite, ordered	NaAlSi3O8
	Ettringite	Ca6Al2(SO4)3(OH)12(H2O)24
C4M4	Quartz	SiO2
	Dolomite	CaMg(CO3)2
	Calcite	CaCO3
	Vaterite	CaCO3
	Albite, ordered	NaAlSi3O8
	Ettringite	Ca6Al2(SO4)3(OH)12(H2O)24

Table 1.

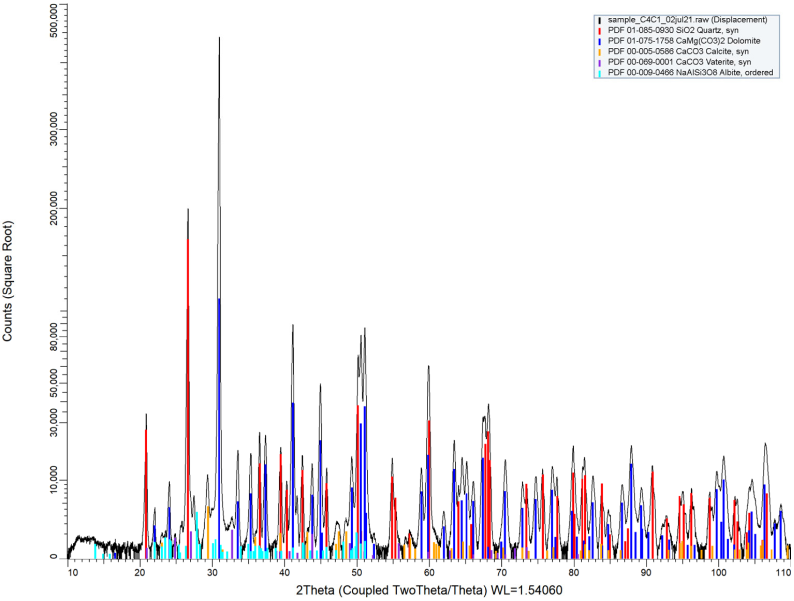

Figure 1 XRD pattern sample "C4C1 ", intensity scale is square root

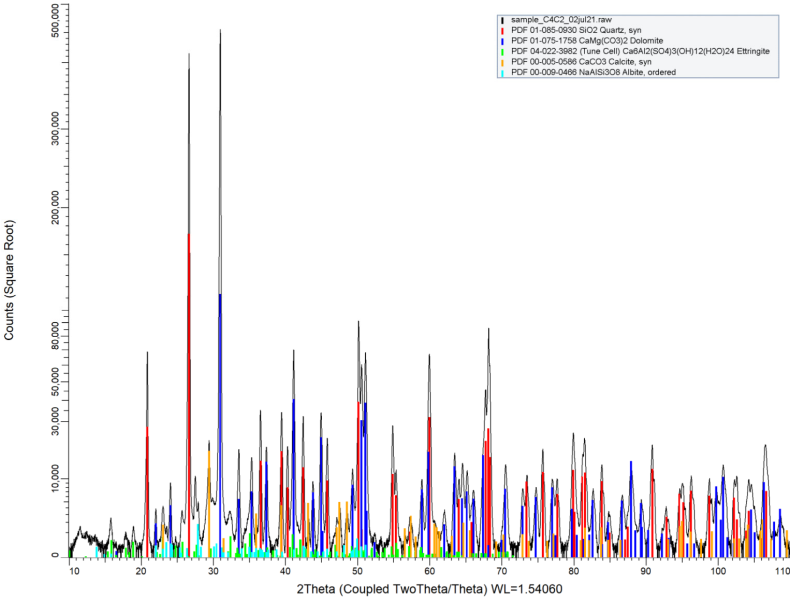

Figure 2 XRD pattern sample "C4C2 ", intensity scale is square root

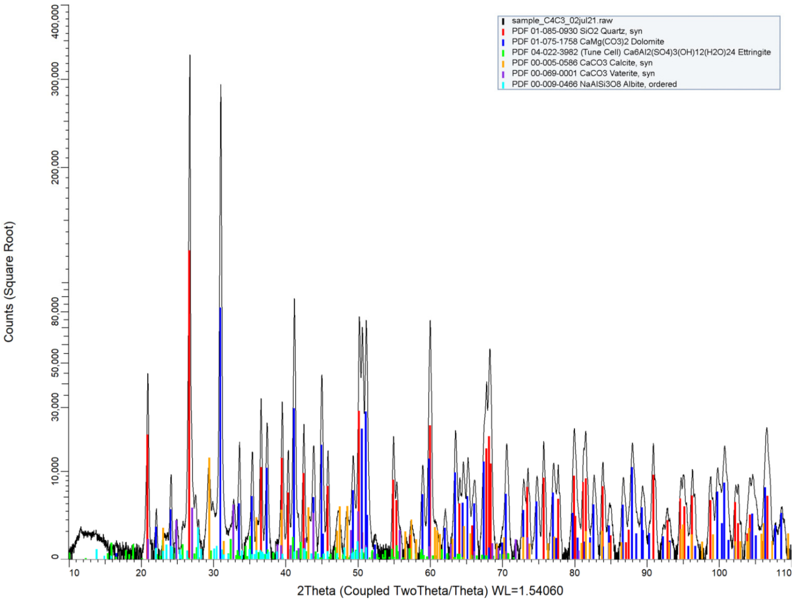

Figure 3 XRD pattern sample "C4C3 ", intensity scale is square root

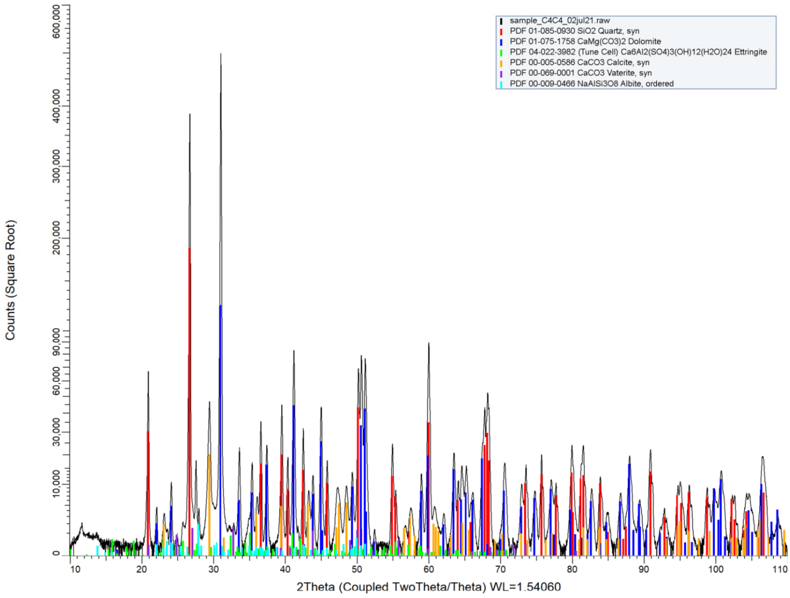

Figure 4 XRD pattern sample " C4C4 ", intensity scale is square root

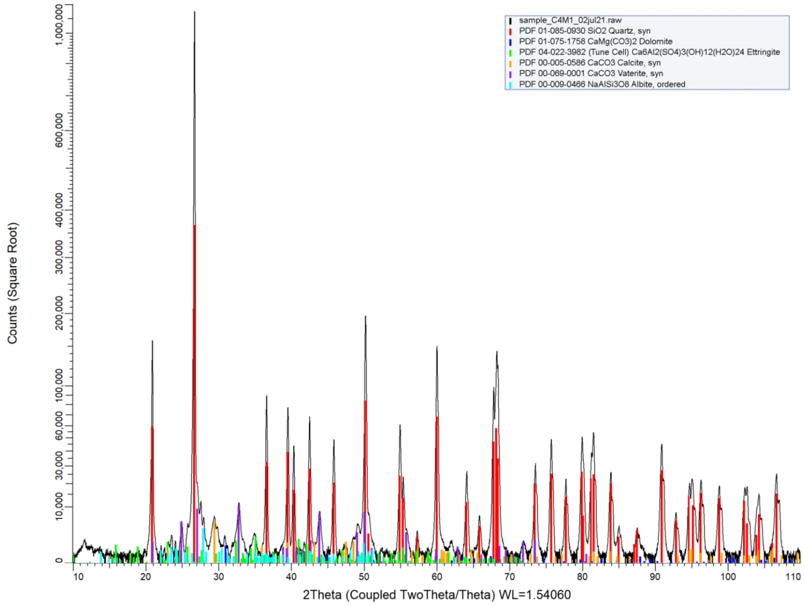

Figure 5 XRD pattern sample "C4M1, intensity scale is square root

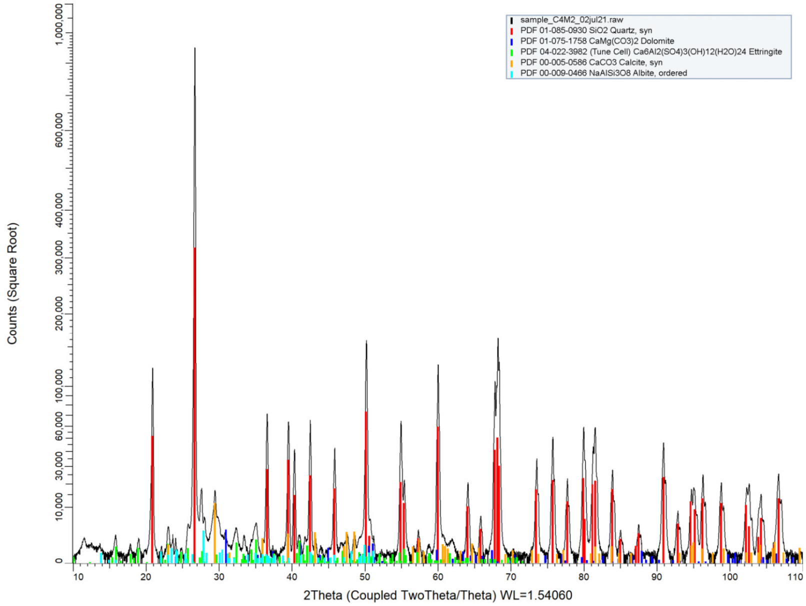

Figure 6 XRD pattern sample "C4M2 ", intensity scale is square root

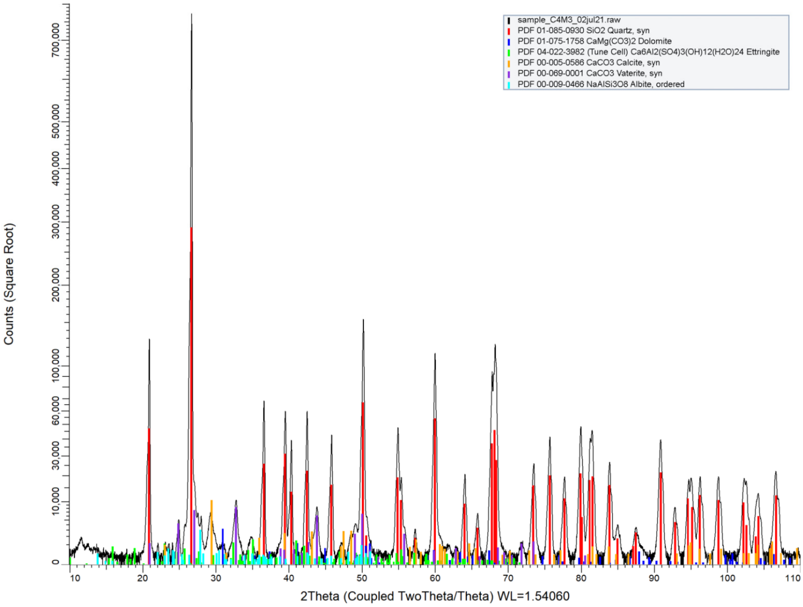

Figure 7 XRD pattern sample "C4M3 ", intensity scale is square root

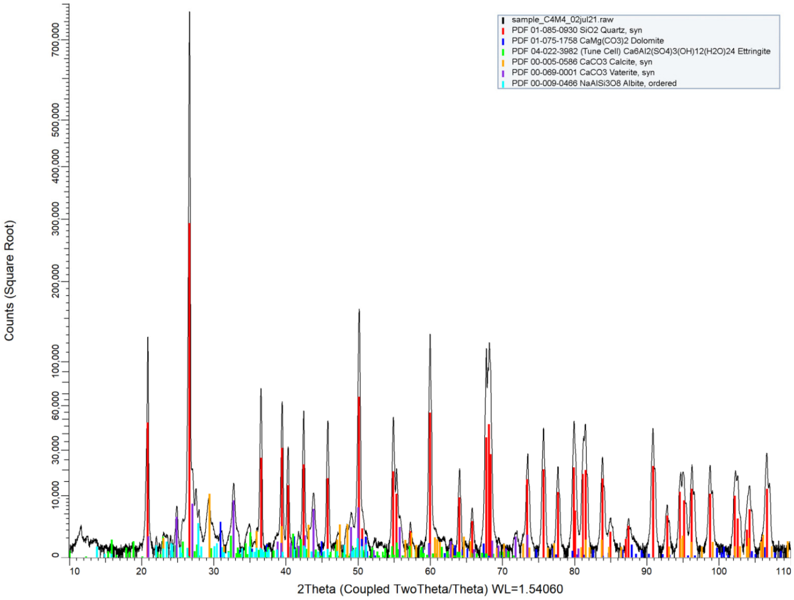

Figure 8 XRD pattern sample "C4M4 ", intensity scale is square root

Appendix E

Theoretical backgrounds chapter 6

Changing the relative humidity (RH) the specimen is exposed to - ESEM

In Figure E.1, a part of the phase diagram for water is shown. A phase diagram is used to indicate the conditions under which thermodynamically different phases of a material occur at any pressure and temperature. In Figure E.1 the (upper) dark blue line represents the phase boundary between water in the liquid phase and the gaseous phase. In terms of relative humidity (RH), the upper line represents 100% RH, the maximum amount of water that can be held in air at the given pressure and temperature.

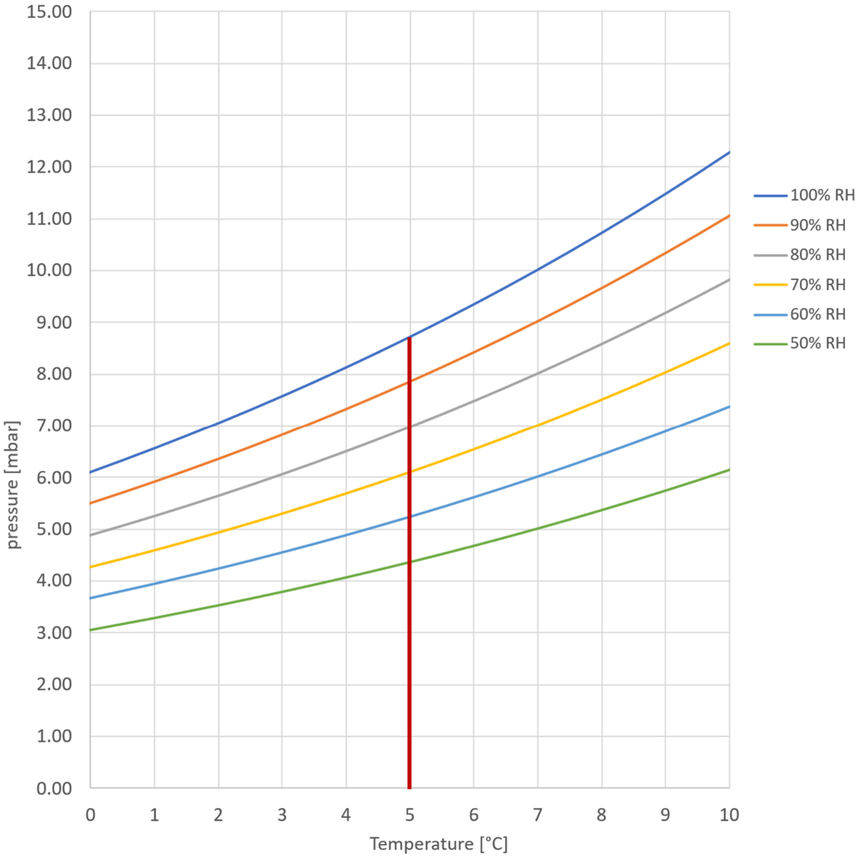

Figure E.1: Phase diagram for water at low pressures. The red line indicates the pressure range that was applied in the electron microscopy tests.

The pressure steps during a test cycle are listed in Table E.1. During one test cycle, the humidity is changed in steps from 50% RH to 100% RH and back to 50% RH (i.e.: 50% RH, 60% RH, 70% RH, 80% RH, 90% RH, (95% RH), 100% RH, (95% RH), 90% RH, 80% RH, 70% RH, 60% RH, 50% RH).

Table E.1: Pressure and relative humidity for humidity cycles in electron microscopy tests

Pressure [mbar]	**Relative humidity [%]**
4.4	50
5.2	60
6.1	70
7.0	80
7.9	90
8.3	95
8.7	100

The values in Table E.1 are calculated with Tetens' formula [1]:

$$P_s = 0.61078 \cdot e^{\left(\frac{17.27 \cdot T}{T+237.3}\right)} \; [kPa] \tag{E.1}$$

in which P_s is the saturation vapor pressure of water in air in kPa (0.1 kPa = 1 mbar) and T is the temperature in °C. The saturation vapor pressure is the partial pressure of water in air at the saturation point.

Changing the relative humidity (RH) the specimen is exposed to – optical microscopy

Changing the temperature of the specimen results in a change of RH in the specimen, which can be calculated with Tetens' formula in (E.1) and the ideal gas law equation:

$$P \cdot V = n \cdot R \cdot T \tag{E.2}$$

Based on the temperature and the absolute air pressure (in Pa), the actual amount of water vapor in the air can be calculated with the molar weight of water at 18 g/mol, temperature T in Kelvin and the universal gas constant R = 8.31 J/mol/m^3.

The ambient RH and ambient temperature are monitored during the test. The required stage temperature to achieve the steps of RH (according to Table E.1) are calculated using Eq. (E.1) and (E.2). The change in RH with changing temperature is explained in

Figure E.2. The red line in the graph shows the required temperature in order to reach the desired RH the specimen is exposed to.

For example: the ambient temperature is 19.6°C and the ambient RH is 52% (this point is marked in Figure E.2 with the intersection of the horizontal red line with the dotted vertical blue line). The partial water vapour pressure P_w at given RH and temperature in the air is calculated from the saturation vapour pressure P_s:

$$P_s = 0.61078 \cdot e^{(\frac{17.27 \cdot 19.6}{19.6+237.3})} = 2.280 \text{ kPa} \tag{E.3}$$

$$P_w = 0.52 \cdot 2.280 \text{ kPa} = 1.186 \text{ kPa} \tag{E.4}$$

The amount of water vapour W_s in the air at the saturation point can be calculated with the general gas law (Eq. E.2): $n = P \cdot V / R \cdot T$ (E.5)

With $n = W_s$ *[kg] / 18 [g/mol]*, $V = 1$ *[m*^{3}*]*, $R = 8.31$ *[J/mol/m*^{3} *]*, 0°C = 273.16 K

Equation (E.5) becomes:

$$W_s = \frac{18}{8.31} \cdot \frac{P}{T+273.16} \equiv 2.166 \cdot \frac{P}{T+273.16} \left[\frac{g}{m^3}\right] \tag{E.6}$$

$$W_s = 2.166 \cdot \frac{2280\ Pa}{19.6+273.16} \left[\frac{g}{m^3}\right] = 16.87\ g/m^3 \tag{E.7}$$

The amount of water at ambient RH = 52% and temperature T = 19.6°C:

$$W_w = 0.52 \cdot 16.87\ g/m^3 = 8.77\ g/m^3 \tag{E.8}$$

The amount of water vapour in ambient air can not be changed. However, the RH the specimen is exposed to can be changed by changing the temperature of the specimen. For each step of RH, the required specimen temperature can be calculated. First the vapour pressure P_w in the ambient air is calculated with (E.1) and the ambient temperature and RH as input parameters. With a transformation of (E.1) into (E.9), the required temperature is calculated.

$$\frac{P_w}{0.61078} = e^{\left(\frac{17.27 \cdot T}{T+237.3}\right)} \equiv \ln\left(\frac{P_w}{0.61078}\right) = \frac{17.27 \cdot T}{T+237.3} \quad => \quad T = \frac{237.3 \cdot \ln\left(\frac{P_w}{0.61078}\right)}{17.27 - \ln\left(\frac{P_w}{0.61078}\right)} \tag{E.9}$$

For the combination of temperature and ambient RH in the example, the temperatures for the humidity cycles in the test are given in Table E.1.

Table E.1: Stage temperatures and relative humidity for humidity cycles in optical microscopy tests. Ambient conditions: temperature 19.6 °C, RH 52%.

Temperature [°C]	Relative humidity [%]
20.2	50
19.6 (ambient)	52 (ambient)
17.3	60
14.9	70
12.8	80
11.1	90
10.2	95
9.5	100

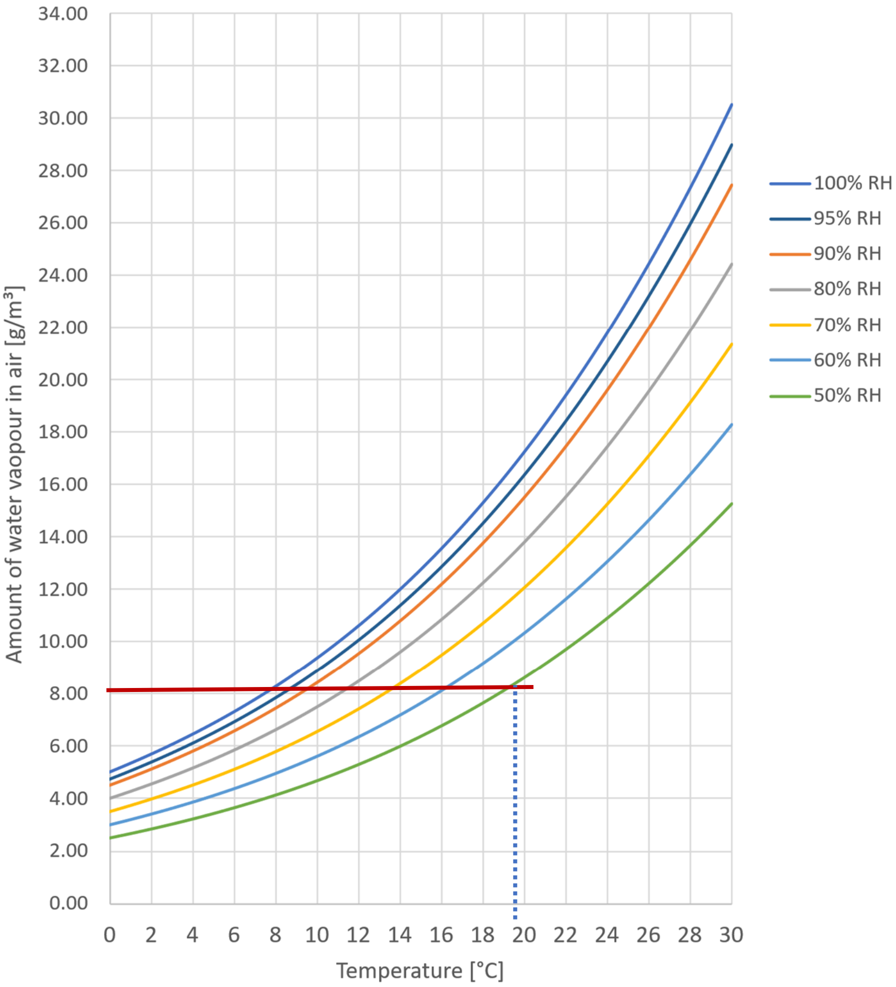

Figure E.2: Amount of water vapour in air. The red line indicates how the RH changes with changing temperature.

With the ambient conditions as given in Table E.1, the specimen temperature of the specimen is changed between 9.5°C an 20.2°C in order to reach the required RH. The mean strain due to the changing temperature of the specimen is estimated on the basis of the average value for the coefficient of thermal expansion of cement paste which varies with changing RH. According to [2], the coefficient of thermal expansion of cement paste α_c varies between 10 and 22 µm/mK for cement paste with CEM I and between 9.5 and 21.5 µm/mK for cement paste with CEM III. With the temperature difference (20.2° - 9.5° =) 10.7°C, the mean strain resulting from the imposed temperature load varies between 0.107 ‰ and 0.235 ‰ for cement paste with CEM I and between 0.102 ‰ and 0.230 ‰ for cement paste with CEM III.

References

[1] AMSO, “Tetens’s formula,” American Meteorological Society. Accessed: Feb. 04, 2022. [Online]. Available: https://glossary.ametsoc.org/wiki/Tetens%27s_formula

[2] K. van Breugel, “Artificial Cooling of hardening concrete,” 1980.

Appendix F

ESEM tests

F.1 Parameters for Ncorr analysis

An average sequence of 12 images is captured per specimen during a test cycle. These images are analysed with Ncorr, the parameters that were used in the analysis are given in Table F.1.

Table F.1: Ncorr - parameters for DIC analysis – electron microscopy analysis

DIC parameters	
Subset radius	20
Subset spacing	4
Nr. of iterations	100
Nr. of threads	4
Format displacements	1536 x 1025 pixels 414 x 276 µm²
- **Units/pixel**	0.2702
- **Units**	µm
Set strain parameters	
- **Strain radius**	1-10 depending on data match

F.2 Summary of test dates per specimen

Test cycle 1		
CEM I	20 & 21 August 2020	week 34 2020
CEM III/B	3 & 4 September 2020	week 36 2020
CEM III/B + FA	4 & 14 September 2020	weeks 36 & 38 2020
CEM III/C	14 & 15 September 2020	week 38 2020

Test cycle 2		
CEM I	3 & 4 December 2020	week 49 2020
CEM III/B	25 November & 4 December 2020	weeks 48 & 49 2020
CEM III/B + FA	9 December 2020	week 49 2020
CEM III/C	9 & 10 December 2020	week 49 2020

Test cycle 3		
CEM I	16 & 17 March2021	week 11 2021
CEM III/B	22 April 2021	week 12 2021
CEM III/B + FA	23 April 2021	week 12 2021
CEM III/C	23 & 26 April 2021	week 12 2021

Test cycle 4		
CEM I	1 July 2021	week 26 2021
CEM III/B	1 & 2 July 2021	week 26 2021
CEM III/B + FA	2 & 15 July 2021	weeks 26 & 28 2021
CEM III/C	15 & 16 July 2021	week 28 2021

F.3 Mean strains over AOI

Mean strains over AOI as function of RH in old (existing concrete) specimen with CEM I. Between test cycles the specimen was stored in dry climate (W = wetting (increasing RH), D = drying (decreasing RH)).

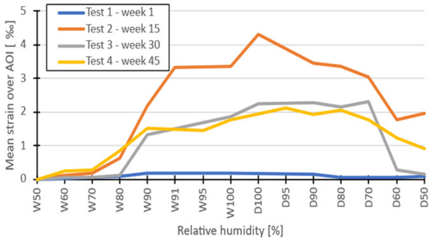

Figure F.1: Mean strain over AOI in X-direction

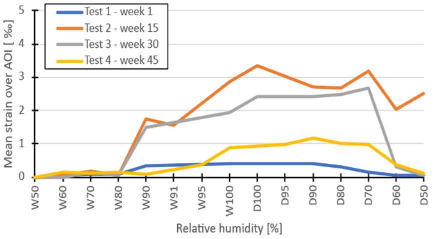

Figure F.2: Mean strain over AOI in Y-direction

Mean strains over AOI as function of RH in old (existing concrete) specimen with CEM I. Between test cycles the specimen was stored in wet climate (W = wetting (increasing RH), D = drying (decreasing RH)).

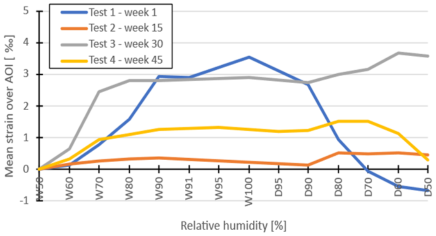

Figure F.3: Mean strain over AOI in X-direction

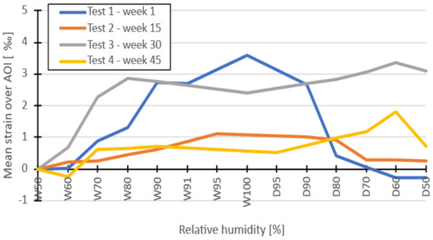

Figure F.4: Mean strain over AOI in Y-direction

Mean strains over AOI as function of RH in old (existing concrete) specimen with CEM I. Between test cycles the specimen was stored in temperature cycles (W = wetting (increasing RH), D = drying (decreasing RH)).

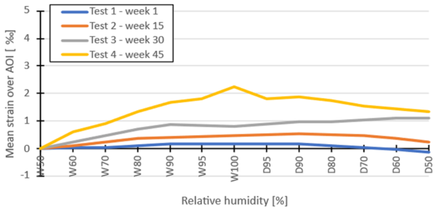

Figure F.5: Mean strain over AOI in X-direction

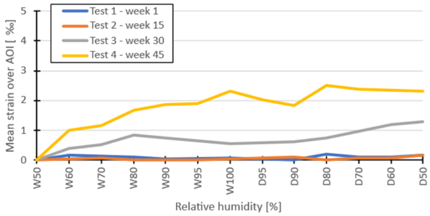

Figure F.6: Mean strain over AOI in Y-direction

Mean strains over AOI as function of RH in old (existing concrete) specimen with CEM I. Between test cycles the specimen was stored in alternating wet-dry climate (W = wetting (increasing RH), D = drying (decreasing RH)).

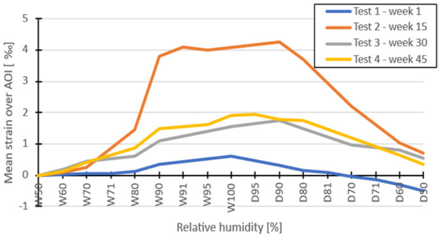

Figure F.7: Mean strain over AOI in X-direction

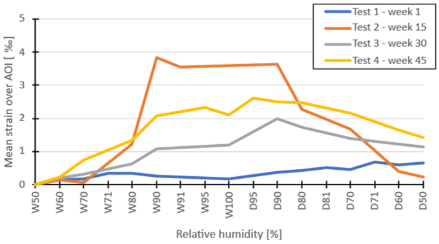

Figure F.8: Mean strain over AOI in Y-direction

Mean strains over AOI as function of RH in young (laboratory mortar) specimen with CEM I. Between test cycles the specimen was stored in dry climate (W = wetting (increasing RH), D = drying (decreasing RH)).

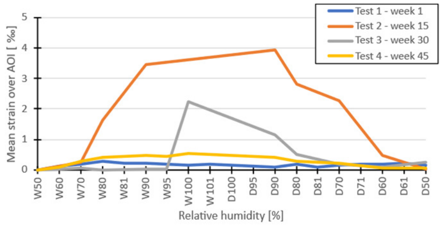

Figure F.9: Mean strain over AOI in X-direction

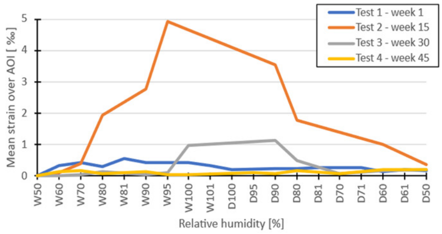

Figure F.10: Mean strain over AOI in Y-direction

Mean strains over AOI as function of RH in young (laboratory mortar) specimen with CEM I. Between test cycles the specimen was stored in wet climate (W = wetting (increasing RH), D = drying (decreasing RH)).

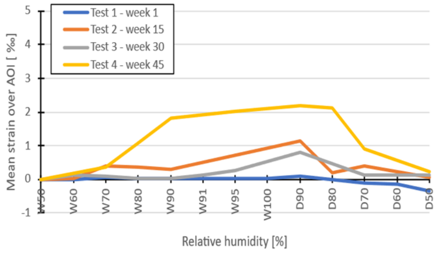

Figure F.11: Mean strain over AOI in X-direction

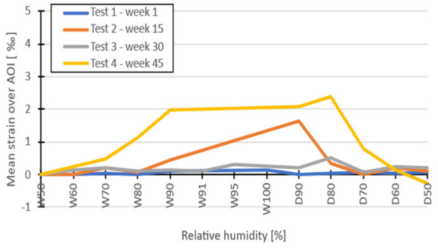

Figure F.12: Mean strain over AOI in Y-direction

Mean strains over AOI as function of RH in young (laboratory mortar) specimen with CEM I. Between test cycles the specimen was stored in temperature cycles (W = wetting (increasing RH), D = drying (decreasing RH)).

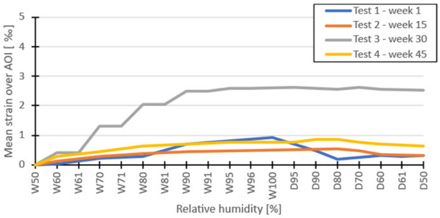

Figure F.13: Mean strain over AOI in X-direction

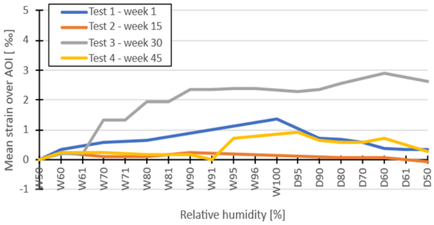

Figure F.14: Mean strain over AOI in Y-direction

Mean strains over AOI as function of RH in young (laboratory mortar) specimen with CEM I. Between test cycles the specimen was stored in alternating wet-dry climate (W = wetting (increasing RH), D = drying (decreasing RH)).

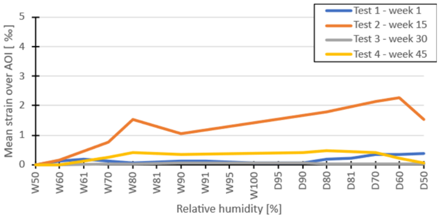

Figure F.15: Mean strain over AOI in X-direction

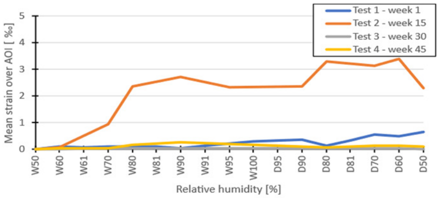

Figure F.16: Mean strain over AOI in Y-direction

Mean strains over AOI as function of RH in old (existing concrete) specimen with CEM III/B. Between test cycles the specimen was stored in dry climate (W = wetting (increasing RH), D = drying (decreasing RH)).

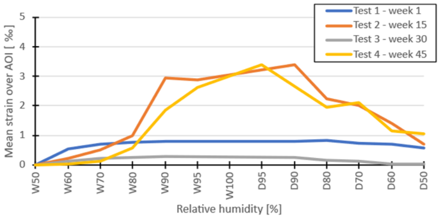

Figure F.17: Mean strain over AOI in X-direction

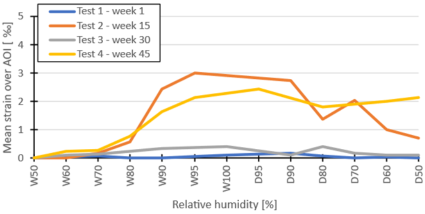

Figure F.18: Mean strain over AOI in Y-direction

Mean strains over AOI as function of RH in old (existing concrete) specimen with CEM III/B. Between test cycles the specimen was stored in wet climate (W = wetting (increasing RH), D = drying (decreasing RH)).

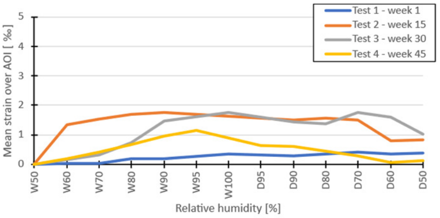

Figure F.19: Mean strain over AOI in X-direction

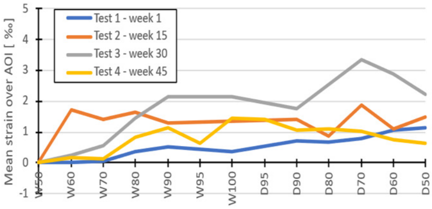

Figure F.20: Mean strain over AOI in Y-direction

Mean strains over AOI as function of RH in old (existing concrete) specimen with CEM III/B. Between test cycles the specimen was stored in temperature cycles (W = wetting (increasing RH), D = drying (decreasing RH)).

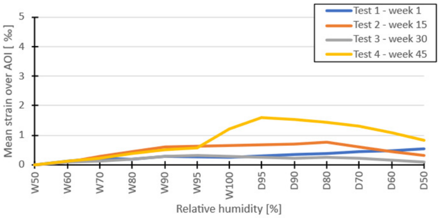

Figure F.21: Mean strain over AOI in X-direction

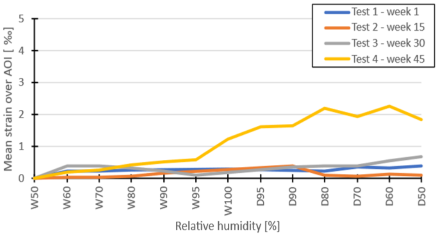

Figure F.22: Mean strain over AOI in Y-direction

Mean strains over AOI as function of RH in old (existing concrete) specimen with CEM III/B. Between test cycles the specimen was stored in alternating wet-dry climate (W = wetting (increasing RH), D = drying (decreasing RH)).

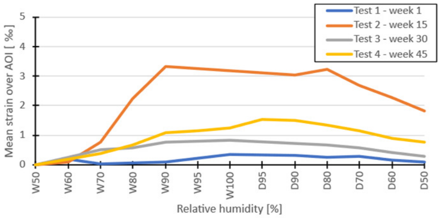

Figure F.23: Mean strain over AOI in X-direction

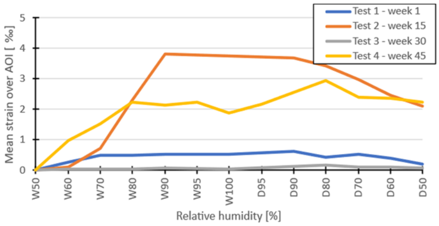

Figure F.24: Mean strain over AOI in Y-direction

Mean strains over AOI as function of RH in young (laboratory mortar) specimen with CEM III/B. Between test cycles the specimen was stored in dry climate (W = wetting (increasing RH), D = drying (decreasing RH)).

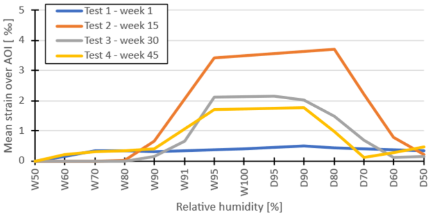

Figure F.25: Mean strain over AOI in X-direction

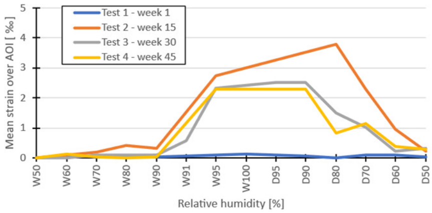

Figure F.26: Mean strain over AOI in Y-direction

Mean strains over AOI as function of RH in young (laboratory mortar) specimen with CEM III/B. Between test cycles the specimen was stored in wet climate (W = wetting (increasing RH), D = drying (decreasing RH)).

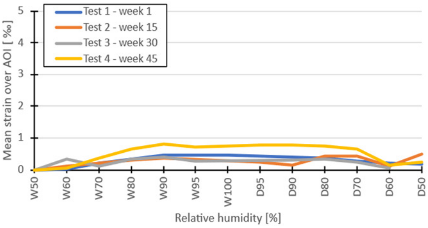

Figure F.27: Mean strain over AOI in X-direction

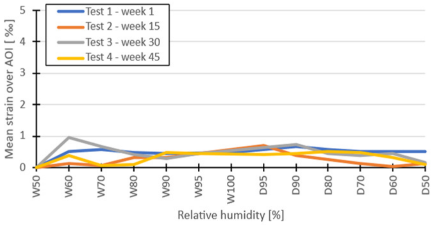

Figure F.28: Mean strain over AOI in Y-direction

Mean strains over AOI as function of RH in young (laboratory mortar) specimen with CEM III/B. Between test cycles the specimen was stored in temperature cycles (W = wetting (increasing RH), D = drying (decreasing RH)).

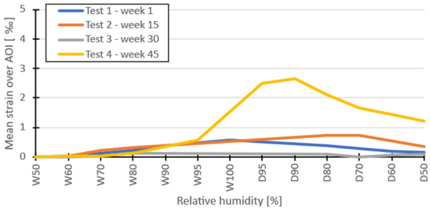

Figure F.29: Mean strain over AOI in X-direction

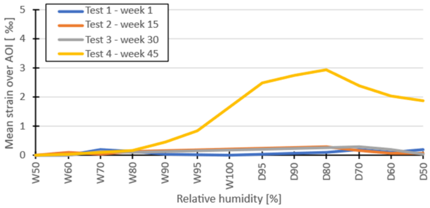

Figure F.30: Mean strain over AOI in Y-direction

Mean strains over AOI as function of RH in young (laboratory mortar) specimen with CEM III/B. Between test cycles the specimen was stored in alternating wet-dry climate (W = wetting (increasing RH), D = drying (decreasing RH)).

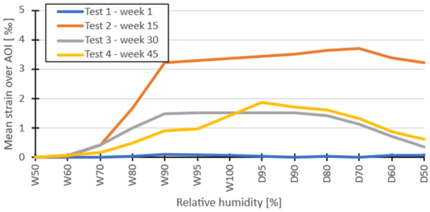

Figure F.31: Mean strain over AOI in X-direction

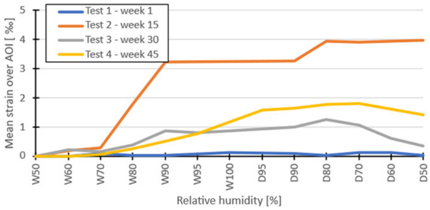

Figure F.32: Mean strain over AOI in Y-direction

Mean strains over AOI as function of RH in old (existing concrete) specimen with CEM III/B + FA. Between test cycles the specimen was stored in dry climate (W = wetting (increasing RH), D = drying (decreasing RH)).

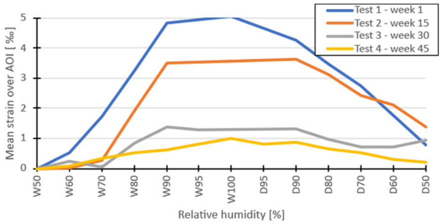

Figure F.33: Mean strain over AOI in X-direction

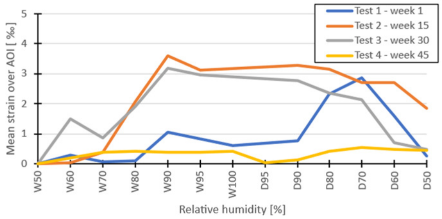

Figure F.34: Mean strain over AOI in Y-direction

Mean strains over AOI as function of RH in old (existing concrete) specimen with CEM III/B + FA. Between test cycles the specimen was stored in wet climate (W = wetting (increasing RH), D = drying (decreasing RH)).

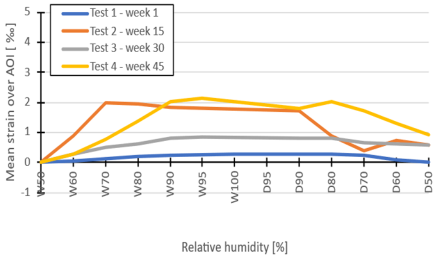

Figure F.35: Mean strain over AOI in X-direction

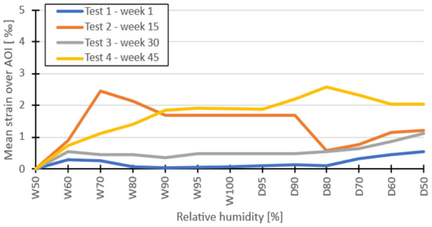

Figure F.36: Mean strain over AOI in Y-direction

Mean strains over AOI as function of RH in old (existing concrete) specimen with CEM III/B + FA. Between test cycles the specimen was stored in temperature cycles (W = wetting (increasing RH), D = drying (decreasing RH)).

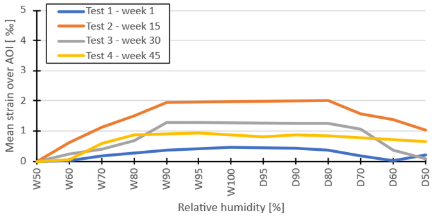

Figure F.37: Mean strain over AOI in X-direction

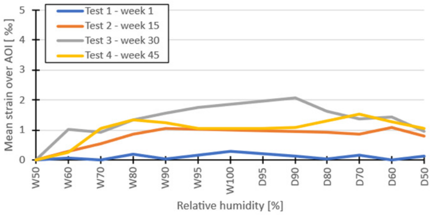

Figure F.38: Mean strain over AOI in Y-direction.

Mean strains over AOI as function of RH in old (existing concrete) specimen with CEM III/B + FA. Between test cycles the specimen was stored in alternating wet-dry climate (W = wetting (increasing RH), D = drying (decreasing RH)).

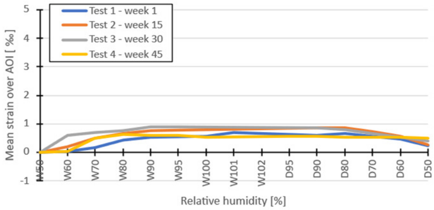

Figure F.39: Mean strain over AOI in X-direction

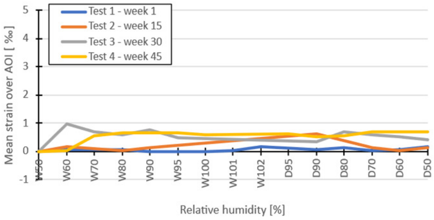

Figure F.40: Mean strain over AOI in Y-direction

Mean strains over AOI as function of RH in young (laboratory mortar) specimen with CEM III/B + FA. Between test cycles the specimen was stored in dry climate (W = wetting (increasing RH), D = drying (decreasing RH)).

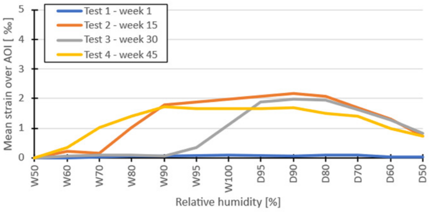

Figure F.41: Mean strain over AOI in X-direction

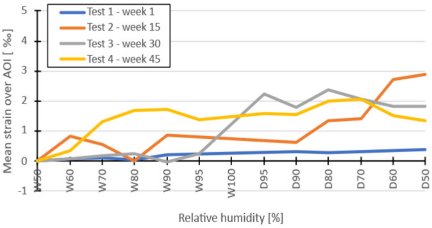

Figure F.42: Mean strain over AOI in Y-direction

Mean strains over AOI as function of RH in young (laboratory mortar) specimen with CEM III/B + FA. Between test cycles the specimen was stored in wet climate (W = wetting (increasing RH), D = drying (decreasing RH)).

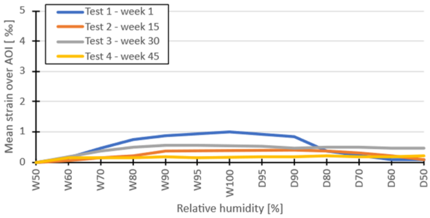

Figure F.43: Mean strain over AOI in X-direction

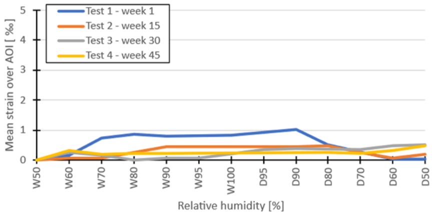

Figure F.44: Mean strain over AOI in Y-direction

Mean strains over AOI as function of RH in young (laboratory mortar) specimen with CEM III/B + FA. Between test cycles the specimen was stored in temperature cycles (W = wetting (increasing RH), D = drying (decreasing RH)).

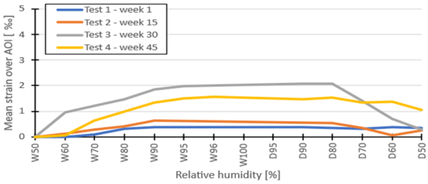

Figure F.45: Mean strain over AOI in X-direction

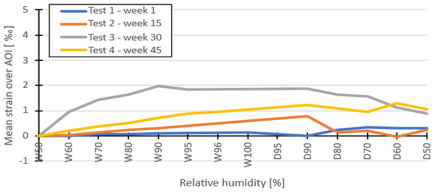

Figure F.46: Mean strain over AOI in Y-direction

Mean strains over AOI as function of RH in young (laboratory mortar) specimen with CEM III/B + FA. Between test cycles the specimen was stored in alternating wet-dry climate (W = wetting (increasing RH), D = drying (decreasing RH)).

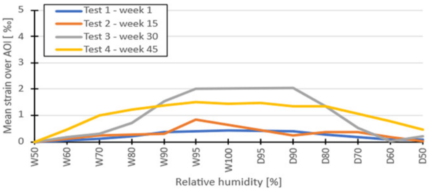

Figure F.47: Mean strain over AOI in X-direction

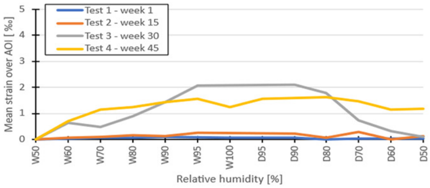

Figure F.48: Mean strain over AOI in Y-direction

Mean strains over AOI as function of RH in old (existing concrete) specimen with CEM III/C. Between test cycles the specimen was stored in dry climate (W = wetting (increasing RH), D = drying (decreasing RH)).

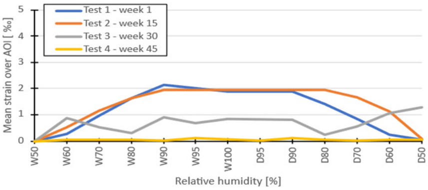

Figure F.49: Mean strain over AOI in X-direction

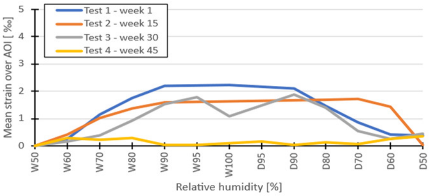

Figure F.50: Mean strain over AOI in Y-direction

Mean strains over AOI as function of RH in old (existing concrete) specimen with CEM III/C. Between test cycles the specimen was stored in wet climate (W = wetting (increasing RH), D = drying (decreasing RH)).

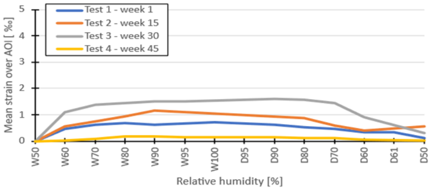

Figure F.51: Mean strain over AOI in X-direction

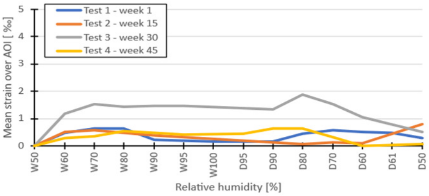

Figure F.52: Mean strain over AOI in Y-direction

Mean strains over AOI as function of RH in old (existing concrete) specimen with CEM III/C. Between test cycles the specimen was stored in temperature cycles (W = wetting (increasing RH), D = drying (decreasing RH)).

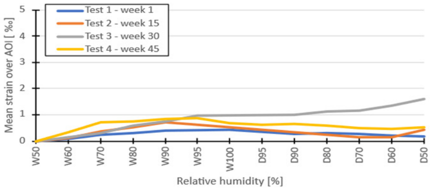

Figure F.53: Mean strain over AOI in X-direction

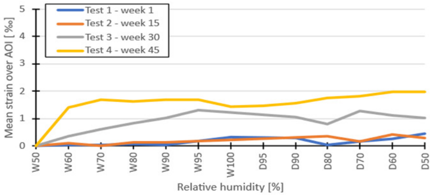

Figure F.54: Mean strain over AOI in Y-direction

Mean strains over AOI as function of RH in old (existing concrete) specimen with CEM III/C. Between test cycles the specimen was stored in alternating wet-dry climate (W = wetting (increasing RH), D = drying (decreasing RH)).

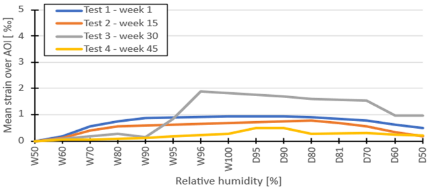

Figure F.55: Mean strain over AOI in X-direction

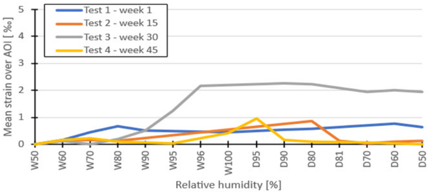

Figure F.56: Mean strain over AOI in Y-direction

Mean strains over AOI as function of RH in young (laboratory mortar) specimen with CEM III/C. Between test cycles the specimen was stored in dry climate (W = wetting (increasing RH), D = drying (decreasing RH)).

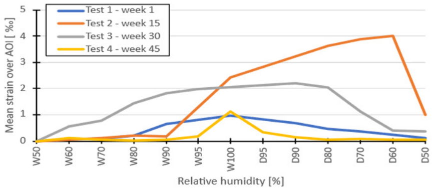

Figure F.57: Mean strain over AOI in X-direction

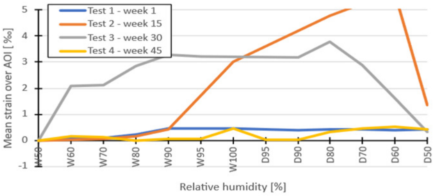

Figure F.58: Mean strain over AOI in Y-direction

Mean strains over AOI as function of RH in young (laboratory mortar) specimen with CEM III/C. Between test cycles the specimen was stored in wet climate (W = wetting (increasing RH), D = drying (decreasing RH)).

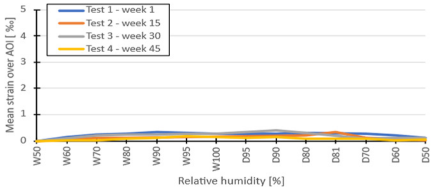

Figure F.59: Mean strain over AOI in X-direction

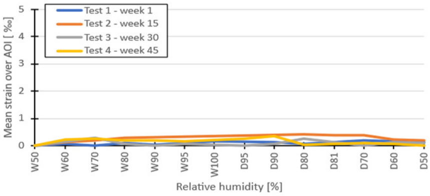

Figure F.60: Mean strain over AOI in Y-direction

Mean strains over AOI as function of RH in young (laboratory mortar) specimen with CEM III/C. Between test cycles the specimen was stored in temperature cycles (W = wetting (increasing RH), D = drying (decreasing RH)).

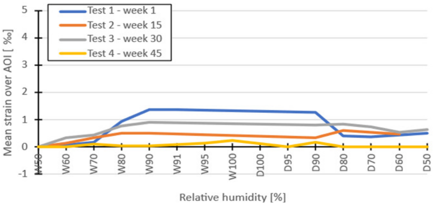

Figure F.61: Mean strain over AOI in X-direction

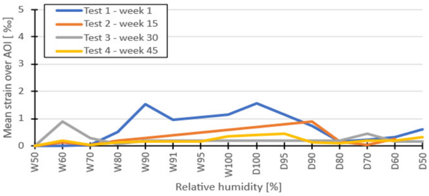

Figure F.62: Mean strain over AOI in Y-direction

Mean strains over AOI as function of RH in young (laboratory mortar) specimen with CEM III/C. Between test cycles the specimen was stored in alternating wet-dry climate (W = wetting (increasing RH), D = drying (decreasing RH)).

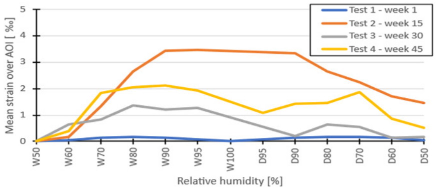

Figure F.63: Mean strain over AOI in X-direction

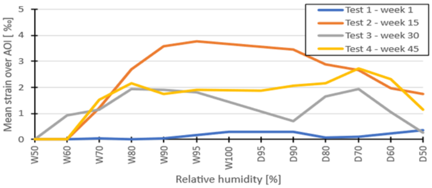

Figure F.64: Mean strain over AOI in Y-direction

Appendix G

Optical microscopy tests

G.1 Parameters for Ncorr analysis

An average sequence of 12 images is captured per specimen during a test cycle. These images are analysed with Ncorr, the parameters that were used in the analysis are given in Table G.1.

Table G.1: Ncorr - parameters for DIC analysis – optical microscopy

DIC parameters	
Subset radius	60
Subset spacing	8
Nr. of iterations	100
Nr. of threads	4
Format displacements	2592 x 1944 pixels 425 x 319 µm²
- **Units/pixel**	0.164
- **Units**	µm
Set strain parameters	
- **Strain radius**	1-10 depending on data match

G.2 Summary of test dates per specimen

Test cycle 1		
CEM I	12 & 13 November 2020	week 46 2020
CEM III/B	10 & 11 November 2020	week 46 2020
CEM III/B + FA	23 November 2020	week 48 2020
CEM III/C	26 November 2020	week 48 2020

Test cycle 2		
CEM I	23 January 2021	week 3 2021
CEM III/B	26 January 2021	week 4 2021
CEM III/B + FA	27 January 2021	week 4 2021
CEM III/C	27 January 2021	week 4 2021

Test cycle 3		
CEM I	6 April 2021	week 14 2021
CEM III/B	6 April 2021	week 14 2021
CEM III/B + FA	7 April 2021	week 14 2021
CEM III/C	8 April 2021	week 14 2021

Test cycle 4		
CEM I	15 June 2021	week 24 2021
CEM III/B	16 June 2021	week 24 2021
CEM III/B + FA	16 June 2021	week 24 2021
CEM III/C	17 June 2021	week 24 2021

G.3 Mean strains over AOI

Mean strains over AOI as function of RH in old (existing concrete) specimen with CEM I. Between test cycles the specimen was stored in dry climate (W = wetting (increasing RH), D = drying (decreasing RH)).

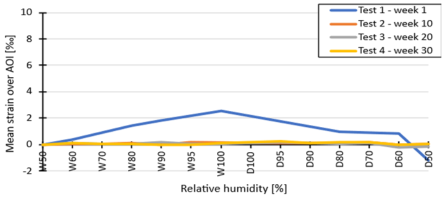

Figure G.1: Mean strain over AOI in X-direction

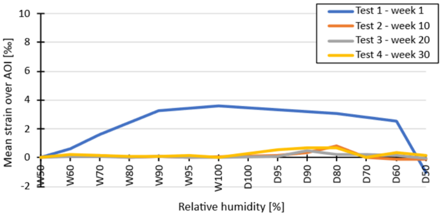

Figure G.2: Mean strain over AOI in Y-direction

Mean strains over AOI as function of RH in old (existing concrete) specimen with CEM I. Between test cycles the specimen was stored in wet climate (W = wetting (increasing RH), D = drying (decreasing RH)).

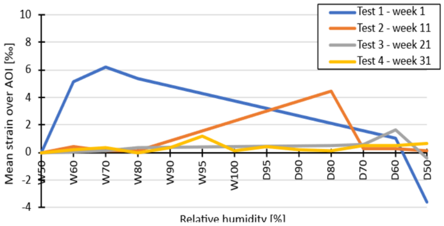

Figure G.3: Mean strain over AOI in X-direction

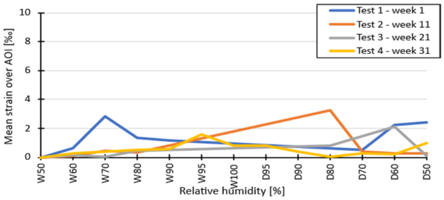

Figure G.4: Mean strain over AOI in Y-direction

Mean strains over AOI as function of RH in old (existing concrete) specimen with CEM I. Between test cycles the specimen was stored in temperature cycles (W = wetting (increasing RH), D = drying (decreasing RH)).

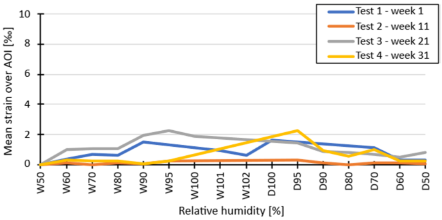

Figure G.5: Mean strain over AOI in X-direction

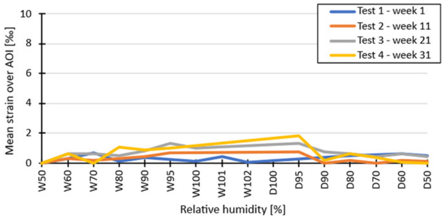

Figure G.6: Mean strain over AOI in Y-direction

Mean strains over AOI as function of RH in old (existing concrete) specimen with CEM I. Between test cycles the specimen was stored in alternating wet-dry climate (W = wetting (increasing RH), D = drying (decreasing RH)).

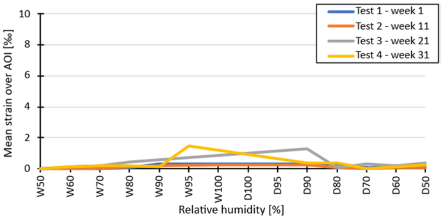

Figure G.7: Mean strain over AOI in X-direction

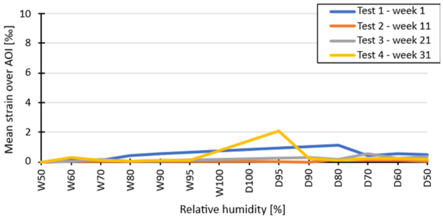

Figure G.8: Mean strain over AOI in Y-direction

Mean strains over AOI as function of RH in young (laboratory mortar) specimen with CEM I. Between test cycles the specimen was stored in dry climate (W = wetting (increasing RH), D = drying (decreasing RH)).

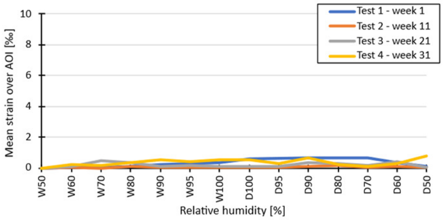

Figure G.9: Mean strain over AOI in X-direction

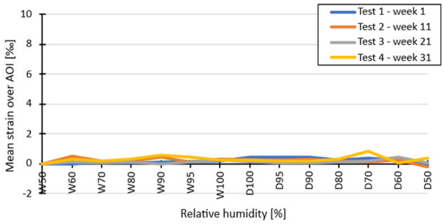

Figure G.10: Mean strain over AOI in Y-direction

Mean strains over AOI as function of RH in young (laboratory mortar) specimen with CEM I. Between test cycles the specimen was stored in wet climate (W = wetting (increasing RH), D = drying (decreasing RH)).

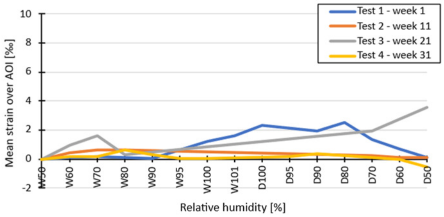

Figure G.11: Mean strain over AOI in X-direction

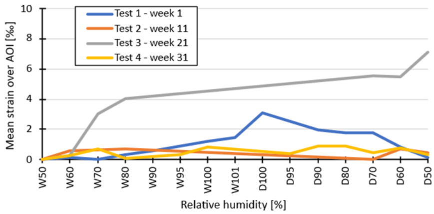

Figure G.12: Mean strain over AOI in Y-direction

Mean strains over AOI as function of RH in young (laboratory mortar) specimen with CEM I. Between test cycles the specimen was stored in temperature cycles (W = wetting (increasing RH), D = drying (decreasing RH)).

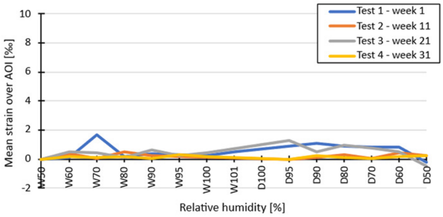

Figure G.13: Mean strain over AOI in X-direction

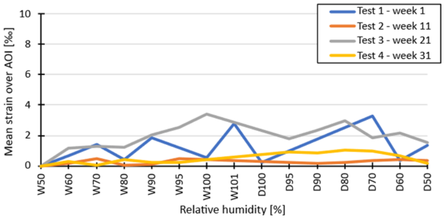

Figure G.14: Mean strain over AOI in Y-direction

Mean strains over AOI as function of RH in young (laboratory mortar) specimen with CEM I. Between test cycles the specimen was stored in alternating wet-dry climate (W = wetting (increasing RH), D = drying (decreasing RH)).

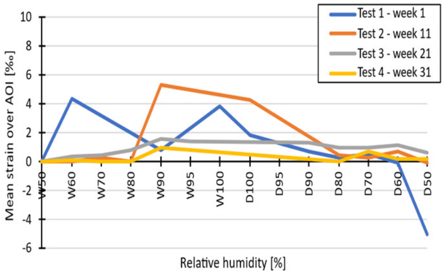

Figure G.15: Mean strain over AOI in X-direction

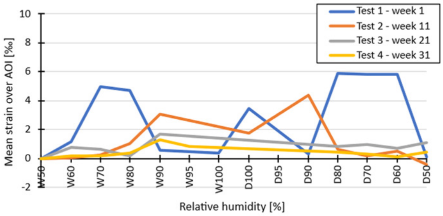

Figure G.16: Mean strain over AOI in Y-direction

Mean strains over AOI as function of RH in old (existing concrete) specimen with CEM III/B. Between test cycles the specimen was stored in dry climate (W = wetting (increasing RH), D = drying (decreasing RH)).

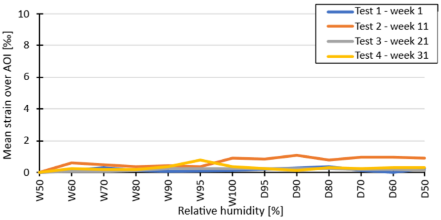

Figure G.17: Mean strain over AOI in X-direction

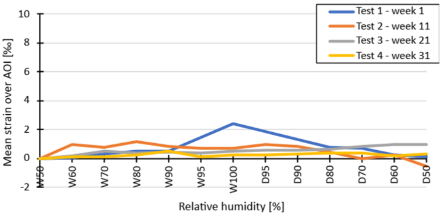

Figure G.18: Mean strain over AOI in Y-direction

Mean strains over AOI as function of RH in old (existing concrete) specimen with CEM III/B. Between test cycles the specimen was stored in wet climate (W = wetting (increasing RH), D = drying (decreasing RH)).

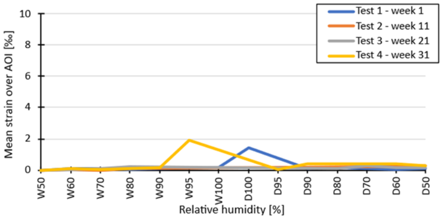

Figure G.19: Mean strain over AOI in X-direction

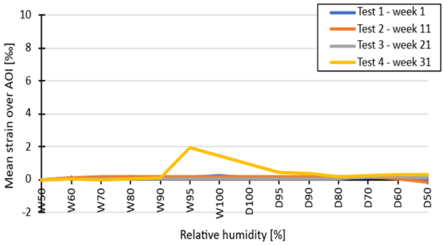

Figure G.20: Mean strain over AOI in Y-direction

Mean strains over AOI as function of RH in old (existing concrete) specimen with CEM III/B. Between test cycles the specimen was stored in temperature cycles (W = wetting (increasing RH), D = drying (decreasing RH)).

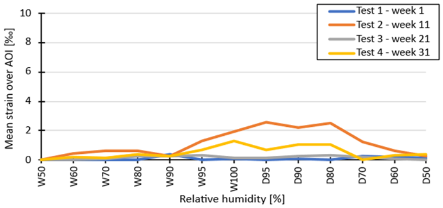

Figure G.21: Mean strain over AOI in X-direction

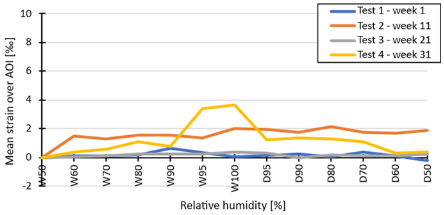

Figure G.22: Mean strain over AOI in Y-direction

Mean strains over AOI as function of RH in old (existing concrete) specimen with CEM III/B. Between test cycles the specimen was stored in alternating wet-dry climate (W = wetting (increasing RH), D = drying (decreasing RH)).

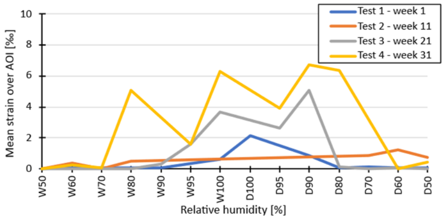

Figure G.23: Mean strain over AOI in X-direction

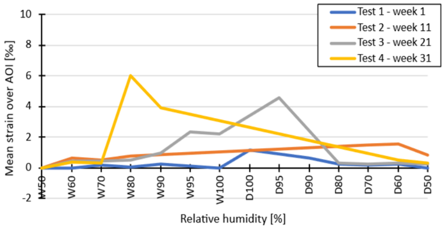

Figure G.24: Mean strain over AOI in Y-direction

Mean strains over AOI as function of RH in young (laboratory mortar) specimen with CEM III/B. Between test cycles the specimen was stored in dry climate (W = wetting (increasing RH), D = drying (decreasing RH)).

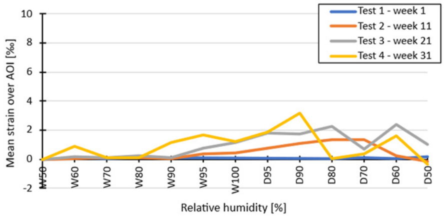

Figure G.25: Mean strain over AOI in X-direction

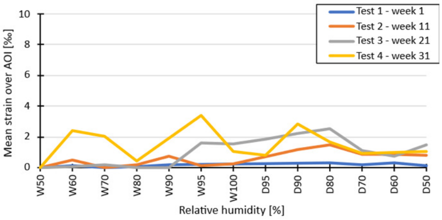

Figure G.26: Mean strain over AOI in Y-direction

Mean strains over AOI as function of RH in young (laboratory mortar) specimen with CEM III/B. Between test cycles the specimen was stored in wet climate (W = wetting (increasing RH), D = drying (decreasing RH)).

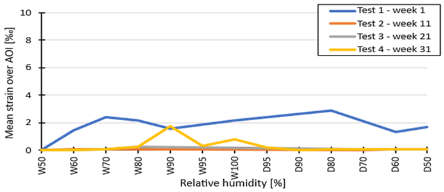

Figure G.27: Mean strain over AOI in X-direction

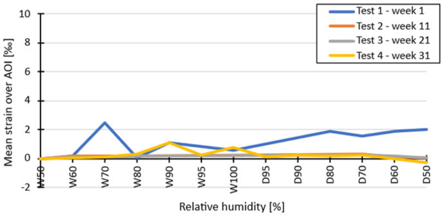

Figure G.28: Mean strain over AOI in Y-direction

Mean strains over AOI as function of RH in young (laboratory mortar) specimen with CEM III/B. Between test cycles the specimen was stored in temperature cycles (W = wetting (increasing RH), D = drying (decreasing RH)).

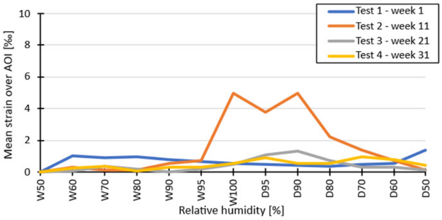

Figure G.29: Mean strain over AOI in X-direction

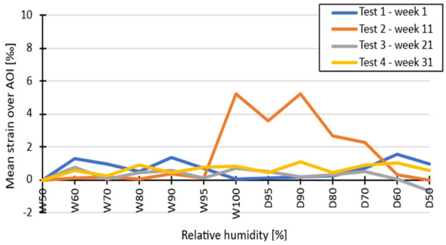

Figure G.30: Mean strain over AOI in Y-direction

Mean strains over AOI as function of RH in young (laboratory mortar) specimen with CEM III/B. Between test cycles the specimen was stored in alternating wet-dry climate (W = wetting (increasing RH), D = drying (decreasing RH)).

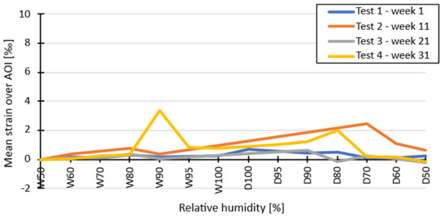

Figure G.31: Mean strain over AOI in X-direction

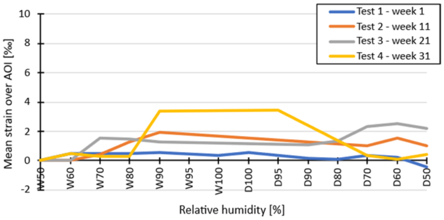

Figure G.32: Mean strain over AOI in Y-direction

Mean strains over AOI as function of RH in old (existing concrete) specimen with CEM III/B + FA. Between test cycles the specimen was stored in dry climate (W = wetting (increasing RH), D = drying (decreasing RH)).

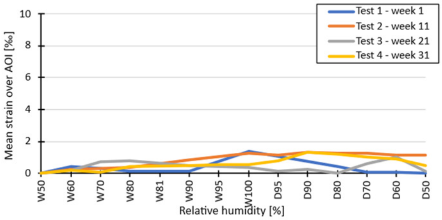

Figure G.33: Mean strain over AOI in X-direction

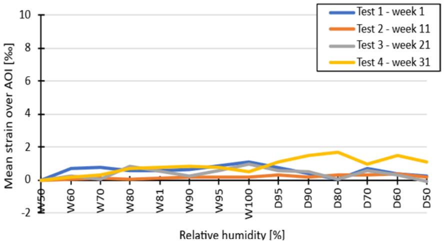

Figure G.34: Mean strain over AOI in Y-direction

Mean strains over AOI as function of RH in old (existing concrete) specimen with CEM III/B + FA. Between test cycles the specimen was stored in wet climate (W = wetting (increasing RH), D = drying (decreasing RH)).

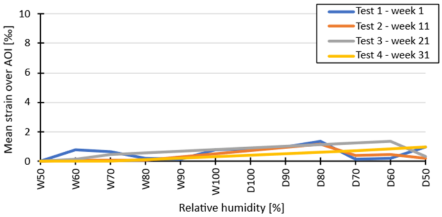

Figure G.35: Mean strain over AOI in X-direction

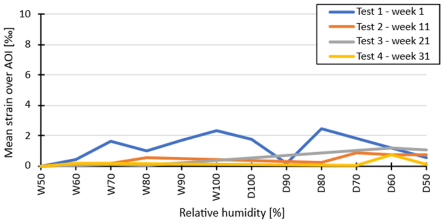

Figure G.36: Mean strain over AOI in Y-direction

Mean strains over AOI as function of RH in old (existing concrete) specimen with CEM III/B + FA. Between test cycles the specimen was stored in temperature cycles (W = wetting (increasing RH), D = drying (decreasing RH)).

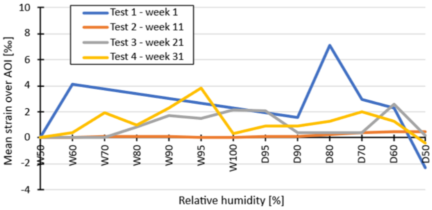

Figure G.37: Mean strain over AOI in X-direction

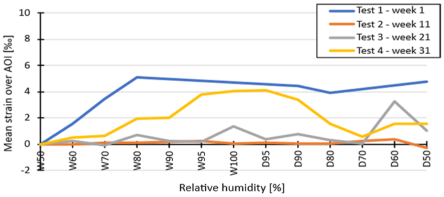

Figure G.38: Mean strain over AOI in Y-direction

Mean strains over AOI as function of RH in old (existing concrete) specimen with CEM III/B + FA. Between test cycles the specimen was stored in alternating wet-dry climate (W = wetting (increasing RH), D = drying (decreasing RH)).

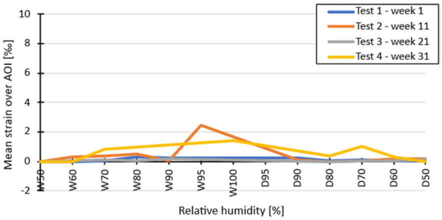

Figure G.39: Mean strain over AOI in X-direction

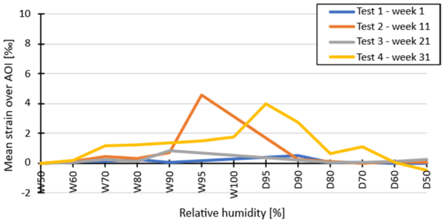

Figure G.40: Mean strain over AOI in Y-direction

Mean strains over AOI as function of RH in young (laboratory mortar) specimen with CEM III/B + FA. Between test cycles the specimen was stored in dry climate (W = wetting (increasing RH), D = drying (decreasing RH)).

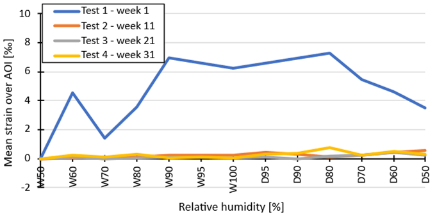

Figure G.41: Mean strain over AOI in X-direction

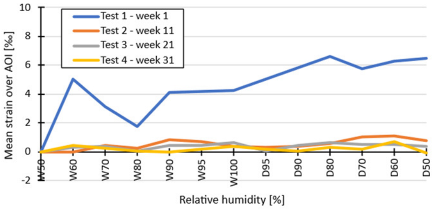

Figure G.42: Mean strain over AOI in Y-direction

Mean strains over AOI as function of RH in young (laboratory mortar) specimen with CEM III/B + FA. Between test cycles the specimen was stored in wet climate (W = wetting (increasing RH), D = drying (decreasing RH)).

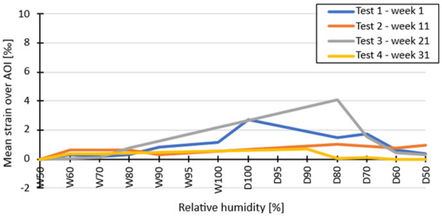

Figure G.43: Mean strain over AOI in X-direction

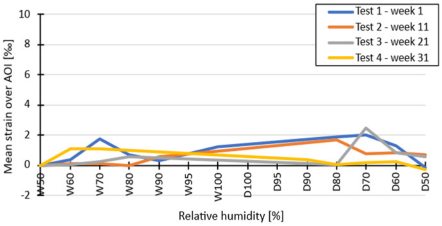

Figure G.44: Mean strain over AOI in Y-direction

Mean strains over AOI as function of RH in young (laboratory mortar) specimen with CEM III/B + FA. Between test cycles the specimen was stored in temperature cycles (W = wetting (increasing RH), D = drying (decreasing RH)).

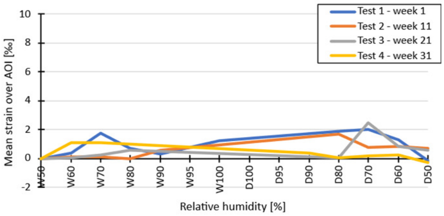

Figure G.45: Mean strain over AOI in X-direction

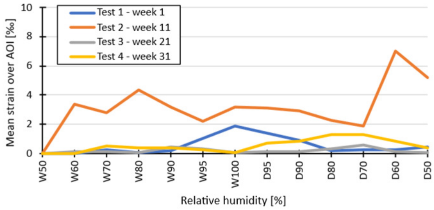

Figure G.46: Mean strain over AOI in Y-direction

Mean strains over AOI as function of RH in young (laboratory mortar) specimen with CEM III/B + FA. Between test cycles the specimen was stored in alternating wet-dry climate (W = wetting (increasing RH), D = drying (decreasing RH)).

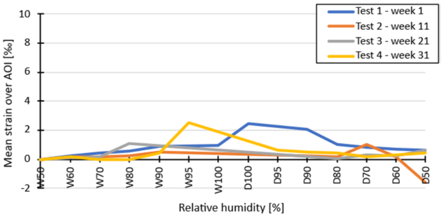

Figure G.47: Mean strain over AOI in X-direction

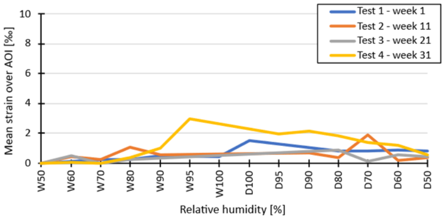

Figure G.48: Mean strain over AOI in Y-direction

Mean strains over AOI as function of RH in old (existing concrete) specimen with CEM III/C. Between test cycles the specimen was stored in dry climate (W = wetting (increasing RH), D = drying (decreasing RH)).

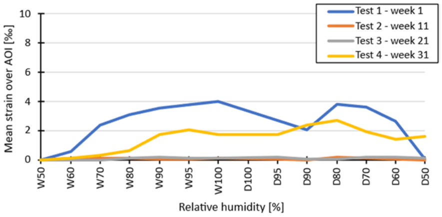

Figure G.49: Mean strain over AOI in X-direction

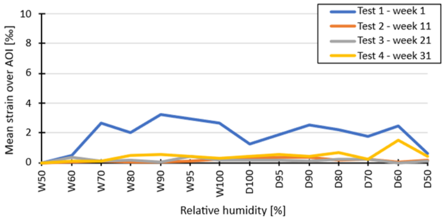

Figure G.50: Mean strain over AOI in Y-direction

Mean strains over AOI as function of RH in old (existing concrete) specimen with CEM III/C. Between test cycles the specimen was stored in wet climate (W = wetting (increasing RH), D = drying (decreasing RH)).

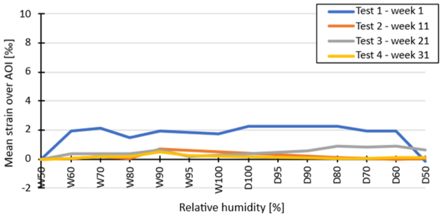

Figure G.51: Mean strain over AOI in X-direction

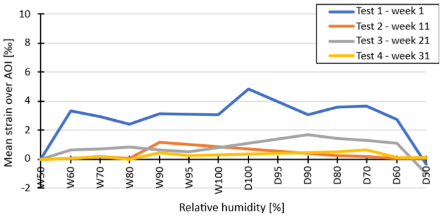

Figure G.52: Mean strain over AOI in Y-direction

Mean strains over AOI as function of RH in old (existing concrete) specimen with CEM III/C. Between test cycles the specimen was stored in temperature cycles (W = wetting (increasing RH), D = drying (decreasing RH)).

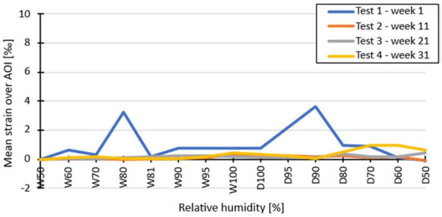

Figure G.53: Mean strain over AOI in X-direction

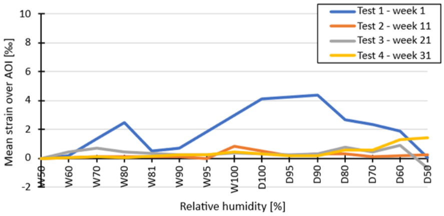

Figure G.54: Mean strain over AOI in Y-direction

Mean strains over AOI as function of RH in old (existing concrete) specimen with CEM III/C. Between test cycles the specimen was stored in alternating wet-dry climate (W = wetting (increasing RH), D = drying (decreasing RH)).

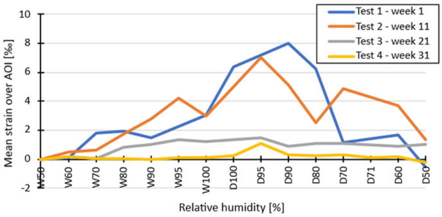

Figure G.55: Mean strain over AOI in X-direction

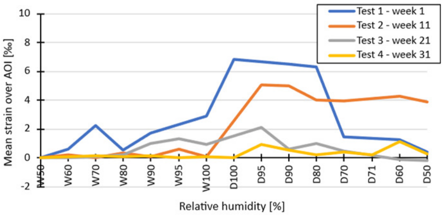

Figure G.56: Mean strain over AOI in Y-direction

Mean strains over AOI as function of RH in young (laboratory mortar) specimen with CEM III/C. Between test cycles the specimen was stored in dry climate (W = wetting (increasing RH), D = drying (decreasing RH)).

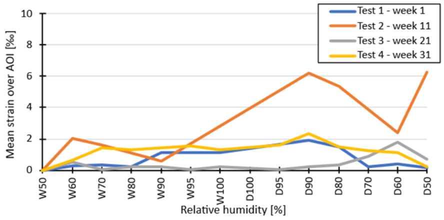

Figure G.57: Mean strain over AOI in X-direction

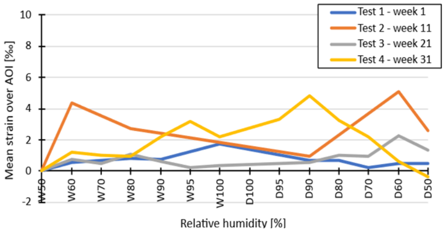

Figure G.58: Mean strain over AOI in Y-direction

Mean strains over AOI as function of RH in young (laboratory mortar) specimen with CEM III/C. Between test cycles the specimen was stored in wet climate (W = wetting (increasing RH), D = drying (decreasing RH)).

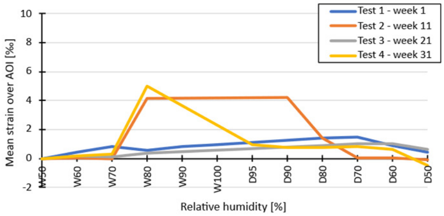

Figure G.59: Mean strain over AOI in X-direction

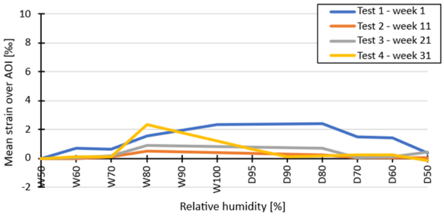

Figure G.60: Mean strain over AOI in Y-direction

Mean strains over AOI as function of RH in young (laboratory mortar) specimen with CEM III/C. Between test cycles the specimen was stored in temperature cycles (W = wetting (increasing RH), D = drying (decreasing RH)).

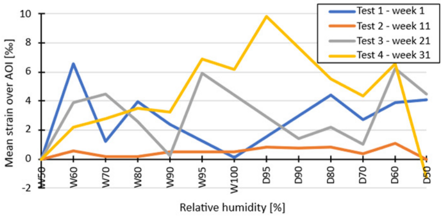

Figure G.61: Mean strain over AOI in X-direction

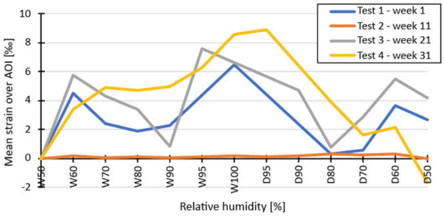

Figure G.62: Mean strain over AOI in Y-direction

Mean strains over AOI as function of RH in young (laboratory mortar) specimen with CEM III/C. Between test cycles the specimen was stored in alternating wet-dry climate (W = wetting (increasing RH), D = drying (decreasing RH)).

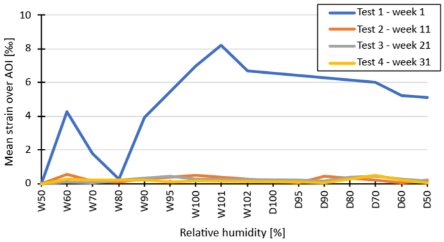

Figure G.63: Mean strain over AOI in X-direction

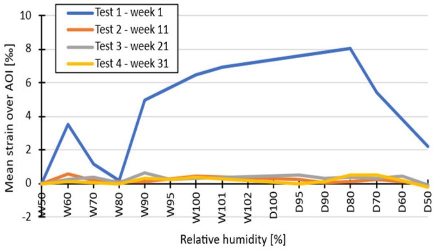

Figure G.64: Mean strain over AOI in Y-direction